FACULTY OF ENGINEERING
AND ARCHITECTURE

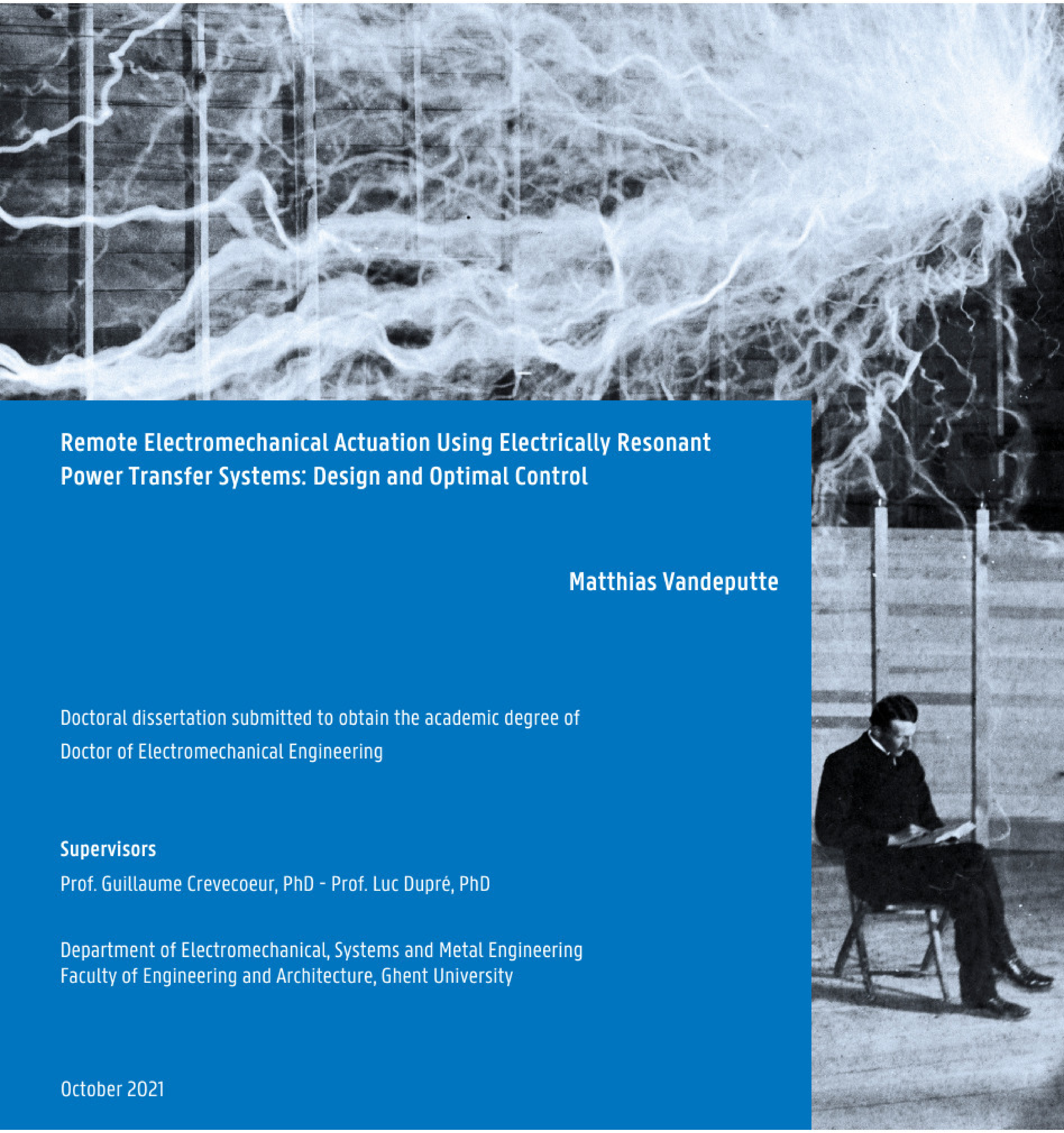

Remote Electromechanical Actuation Using Electrically Resonant Power Transfer Systems: Design and Optimal Control

Matthias Vandeputte

Doctoral dissertation submitted to obtain the academic degree of
Doctor of Electromechanical Engineering

Supervisors
Prof. Guillaume Crevecoeur, PhD - Prof. Luc Dupré, PhD

Department of Electromechanical, Systems and Metal Engineering
Faculty of Engineering and Architecture, Ghent University

October 2021

GHENT
UNIVERSITY

FACULTY OF ENGINEERING
AND ARCHITECTURE

Remote Electromechanical Actuation Using Electrically Resonant Power Transfer Systems: Design and Optimal Control

Matthias Vandeputte

Doctoral dissertation submitted to obtain the academic degree of
Doctor of Electromechanical Engineering

Supervisors
Prof. Guillaume Crevecoeur, PhD - Prof. Luc Dupré, PhD

Department of Electromechanical, Systems and Metal Engineering
Faculty of Engineering and Architecture, Ghent University

October 2021

GHENT
UNIVERSITY

ISBN 978-94-6355-526-5
NUR 959
Wettelijk depot: D/2021/10.500/74

Members of the Examination Board

Chair

Prof. Em. Daniël De Zutter, PhD, Ghent University

Other members entitled to vote

Mustafa Boyvat, PhD, Max Planck Institute for Intelligent Systems, Germany
Prof. Johan Gyselinck, PhD, Université libre de Bruxelles
Prof. Peter Sergeant, PhD, Ghent University
Prof. Emmeric Tanghe, PhD, Ghent University

Supervisors

Prof. Guillaume Crevecoeur, PhD, Ghent University
Prof. Luc Dupré, PhD, Ghent University

Voorwoord

Een doctoraat is een apart gegeven. Je hebt net je masterproef afgewerkt en nu begin je weer vanop nul, maar dan grootschaliger en een pak langer. Je omgeving is geïnteresseerd in wat je doet, maar om eerlijk te zijn, zelf weet je dat ook nog niet helemaal. Één ding staat vast aan de start van het doctoraat, over 4 à 5 jaar zal je (als alles goed gaat) een boek geschreven hebben waarin je al het werk zal samenvatten dat je tegen dan zal hebben verzet. Een culminatie van alle doorzetting, tegenslagen, doorbraken en writer's blocks van de voorbije jaren. Samen met jouw doorontwikkeling in de materie krijgt het proefschrift alsmaar meer vorm. Het is een vreemd gevoel hoe je op enkele jaren een doctoraat het jouwe maakt, je pad langzaam maar zeker vastlegt, maandenlang toewerkt naar het proefschrift, om dan finaal abrupt afscheid te nemen van wat je hebt gecreëerd. Een doctoraat vormgeven en tot een goed einde brengen is geen evidentie en ik kan er dan ook niet omheen dat ik op het einde van de rit veel personen in mijn omgeving te danken heb die het eindresultaat mee mogelijk hebben gemaakt.

Allereerst wil ik mijn promotor, Guillaume, bedanken. Al van de eerste dag van mijn masterproef heb je op een bijna onvoorwaardelijke manier in mij geloofd en mij gemotiveerd. Op de meer uitdagende momenten heb ik altijd op je kunnen rekenen voor een extra boost van inspiratie en drive. Daarnaast wil ik ook mijn copromotor, Luc, en al mijn andere collega's van EELAB bedanken. Arne, Annelies, Jasper, Mariem, Andries, Pieter, Tom, Wannes, Shima, Tom, Lynn, Rikkert, Thijs, Jordi,.. In onze grote bureau zijn er veel gezichten gepasseerd, maar ondanks de drukte was dat toch een zegen. Jullie waren voor mij geregeld het klankbord dat ik nodig had om mijn onderzoek in perspectief te plaatsen. De koffiepauzes en het we're-in-this-together-gevoel hebben mij gemotiveerd om een proefschift af te leveren waar ik trots op kan zijn.

I would also like to thank the members of my Jury. Thank you for willing to be part of my Jury and for the time and effort spent on reading my dissertation.

Als laatste wil ik mijn familie en in het bijzonder Iris bedanken. Jullie hebben altijd interesse getoond in wat ik doe ook al was het niet altijd evident om mijn uiteenzettingen te volgen. Ik apprecieer enorm hoe ik bij jullie mentaal tot rust kan komen en mijn batterijen kan opladen wanneer ik tijd met jullie doorbreng.

Matthias Vandeputte, 14 september 2021

Contents

Samenvatting

Draadloze energieoverdracht (*wireless power transfer*, WPT) is een overkoepelende term die de technologieën beschrijft die de transmissie van energie naar een ontvanger mogelijk maken zonder het gebruik van fysieke verbindingen zoals elektrische geleiders. De meest veelbelovende methode van draadloze energieoverdracht is gebaseerd op het principe van magnetische inductie. WPT heeft een lange weg afgelegd sinds haar ontdekking in het begin van de 19e eeuw. Prominente wetenschappers zoals Michael Faraday, Joseph Henry en Nikola Tesla hebben bijgedragen tot de ontwikkeling van inductieve draadloze energieoverdracht. Pas recent, in de laatste twee decennia, is de technologie rendabel geworden voor het gebruik in commerciële producten, zoals bijvoorbeeld elektrische tandenborstels en oplaadvlakken voor smartphones. Het groeiende marktaandeel van elektrische voertuigen maakt draadloze energieoverdracht interessant voor draadloos laden met hoog vermogen met behulp van oplaadpads die zijn geïntegreerd in parkeerplaatsen of zelfs in het wegoppervlak, zodat voertuigen rijdend kunnen gevoed worden. Recent ontwikkelde standaarden voor draadloos laden van elektronica en huishoudelijke toestellen (Qi standaard) en elektrische voertuigen (SAE J2954) tonen aan hoe ver de technologie is gematureerd. Hedendaagse WPT systemen hebben overdrachtsefficiënties boven de 90% en vermogenscapaciteiten van meer dan 11 kW.

Inductieve energieoverdracht is gebaseerd op de elektromagnetische interactie tussen magnetisch gekoppelde spoelen. Een tijdvariabele stroom door een spoel genereert een oscillerend magnetisch veld in zijn omgeving. Magnetische veldlijnen die door een nabijgelegen spoel passeren induceren een spanning in die spoel die de verandering van het magnetisch veld tegenwerkt. Deze geïnduceerde spanning in de ontvangerspoel kan gebruikt worden om een batterij op te laden of om direct een last te voeden die verbonden is met de ontvanger. Magnetische inductie maakt op deze manier draadloze energieoverdracht mogelijk over middelgrote luchtspleten.

De geïnduceerde spanning neemt toe voor hogere frequenties van de wisselstroom (*alternating current*, AC). Een hogere frequentie verhoogt echter ook de inductieve last die gezien wordt door de spanningsbron. Een goed gekozen capaciteit kan deze inductantie compenseren en de geobserveerde last sterk verlagen. Voor een gegeven wisselspanning kan de stroom significant oplopen wanneer de inductantie van de spoel exact wordt gecompenseerd. Dit fenomeen wordt resonantie genoemd en de combinatie spoel-capaciteit noemt men een resonator. Magnetische resonantie vormt de grondslag van efficiënte midrange resonante draadloze energieoverdracht (*resonant wireless power transfer*, RWPT).

Resonatoren versterken lokaal het magnetische veld, net zoals magnetische materialen dat doen. Op een macroscopische schaal kan een rooster van resonatoren zich gedragen als een geavanceerd materiaal (een *metamateriaal*) met eigenschappen die niet eigen zijn aan klassieke magnetische materialen. Hedendaags onderzoek is gericht op diepe integratie van resonatoren in elektromagnetische toepassingen. Een plaat of blok van metamateriaal kan bijvoorbeeld draadloze energieoverdracht versterken of personen in de buurt afschermen van sterke elektromagnetische velden. Ander recent onderzoek focust op de integratie van resonatoren in elektrische motoren. Het potentieel van metamaterialen heeft twee luiken. Enerzijds kunnen resonatoren magnetisch materiaal vervangen dat vaak zwaar, duur of bros is of energieverlies veroorzaakt. Anderzijds kan de fysieke interactie tussen resonatoren dynamische eigenschappen mogelijk maken die afwijken van standaard gelijkstroom- of wisselstroommotoren.

Hedendaags onderzoek rond RWPT-gebaseerde motoren is voornamelijk beperkt tot de afleiding van analytische formules en eindige elementen modellering (*finite element modeling*, FEM) met sterk uiteenlopende resultaten en conclusies. De ontwikkeling van resonantiegebaseerde motoren kent meerdere uitdagingen, namelijk: de weerstand van spoelen verandert drastisch in functie van de frequentie, de discrete capaciteiten vragen een bepaald volume in een geïntegreerd ontwerp, exacte resonante tuning (afstemming) is moeilijk te bereiken en te behouden, enzovoort. Deze thesis heeft als doel het onderzoeksveld rond direct geïntegreerde resonatoren in RWPT motoren vooruit te brengen. De grootste sprong ten opzichte van huidig onderzoek is de validatie van afgeleide analytische modellen en controlestrategieën op een fysiek prototype. Daarnaast analyseren we het effect van bewust foute afstemming (detuning) van resonatoren, wat wil zeggen dat de excitatiefrequentie niet overeenstemt met de resonantiefrequentie van een of meerdere spoelen in de opstelling. Tenslotte bespreken we hoe de capaciteitswaarde van een of meerdere resonatoren kan worden aangepast terwijl de motor in actie is, door het gebruik van een geschakelde capaciteit (*switch controlled capacitor*, SCC).

In Hoofdstuk 2 vatten we de ‘state of the art’ van resonante draadloze energieoverdracht samen. We bespreken de werking en tuning principes van de meest voorkomende resonatortypes en introduceren indicatoren die de effectiviteit van resonante systemen beschrijven. Deze indicatoren zullen ook van toepassing zijn voor de optimale ontwikkeling van resonantiegebaseerde motoren. Analytische modellen worden voorgesteld die kunnen gebruikt worden om belangrijke elektromagnetische interacties tussen resonatorspoelen af te leiden, zoals magnetische koppeling, krachten en koppels. We verkennen ook fundamentele aspecten in het ontwerp van resonatoren, zoals temperatuurs- en frequentieafhankelijke verliesmechanismen in samengepakte geleiders. De meeste gebruikte wisselstroomcapaciteiten worden opgesomd en hun belangrijkste voor- en nadelen worden vergeleken.

In Hoofdstuk 3 leiden we analytische uitdrukkingen af die de elektrische stromen beschrijven in een resonantiegebaseerde motor met meerdere spoelen. Op basis van deze stromen en de magnetische koppeling tussen de spoelen vinden we het koppel op een draaiende ontvangerspoel. In dit hoofdstuk bespreken we ook de ontwikkeling van de prototype opstelling waarmee we de analytische modellen voor de stroom en het koppel valideren. De basisopstelling bestaat uit drie luchtspoelen. Op het einde van het hoofdstuk bekijken we de mogelijkheid om een magnetische ferrietkern toe te voegen rond de as van de rotor en het positieve effect op het ontwikkelde koppel.

In Hoofdstuk 4 onderzoeken we de mogelijkheid om de resonatoren bewust foutief af te stemmen. We bespreken de vrijheidsgraden van deze detuning en het effect op de elektrische parameters. De uitdrukkingen voor de elektrische stromen en het koppel worden gereviseerd en het effect van de detuning op het koppel wordt doorgedreven onderzocht. We observeren dat het koppel drastisch toeneemt door de resonatoren te detunen, terwijl het afstemmen van de capaciteiten veel robuuster wordt. In dit hoofdstuk introduceren we ook nog twee performantie-indicatoren die de koppelefficiëntie en koppelcapaciteit beschrijven voor een gegeven machine.

In tegenstelling tot de frequentie is het veel moeilijker om capaciteitswaarden nauwkeurig aan te passen, zeker wanneer de machine actief is. Hoofdstuk 5 bespreekt de technologie die mogelijk maakt om de capaciteitswaarden actief aan te passen voor minstens één capaciteit in de resonantiegebaseerde motor. Voor sterke variaties van de capaciteitswaarde zijn de gewoonlijke afleidingen van de equivalente capaciteit onnauwkeurig. We ontwikkelen een semi-analytische methode om de stroom- en spanningsgolfvormen te voorspellen voor een ontvanger resonator met een SCC. In dit hoofdstuk bespreken we ook hoe we tegelijk elektrische variabelen zoals stromen en impedanties kunnen schatten op basis van sensordata.

Het laatste hoofdstuk vat de bijdragen samen van deze thesis aan het onderzoeksveld van resonatiegebaseerde motoren en verstrekt richtlijnen voor toekomstig onderzoek rond dit onderwerp.

Summary

Wireless power transfer (WPT) is a general term to describe technologies that enable the transmission of energy to a receiver without the need for physical connections such as electrical conductors. The most promising type of wireless transfer is based on the principle of magnetic induction. WPT has come a long way since the discovery of the magnetic induction phenomenon in the early 1800's. Prominent scientists like Michael Faraday, Joseph Henry and Nikola Tesla contributed to the development of inductive wireless power transfer. Only recently, in the last one or two decades, the technology of WPT became viable to use in commercial products, e.g., electrical toothbrushes and charging pads for smartphones. The growing market share of electrical vehicles makes the application of WPT interesting for high power charging by the use of charging pads in parking spots or even for integration in roads to enable the energy supply of driving vehicles. Recently developed standards for WPT in consumer products (Qi standard) and electric vehicle applications (SAE J2954) indicate the maturation of the technology. Present-day WPT systems show transfer efficiencies over 90% and power ratings over 11 kW.

Inductive power transfer is based on the electromagnetic interaction between magnetically coupled coils. A time-varying current in a coil generates an oscillating magnetic field in its vicinity. Magnetic field lines that pass through a nearby coil induce a voltage in that coil that counteracts the changing magnetic field. This induced voltage in the receiver coil can be used to charge a battery or to directly power a load that is connected to the receiver. Magnetic induction thus enables the wireless transfer of energy over moderate air gaps.

The induced voltage increases for higher frequencies of the alternating current (AC). A higher frequency, however, also increases the inductive load that is observed by the power source. A well-chosen capacitor can compensate this inductance and significantly reduce the observed load. For a given AC voltage, the current in the coil can significantly increase when the inductance of the coil is exactly compensated. This phenomenon is called resonance and the coil-capacitor combination is referred to as a resonator. Magnetic resonance forms the foundation of efficient mid-range resonant wireless power transfer (RWPT).

Resonators locally amplify the magnetic field, similar to magnetic materials. On a macroscopic scale, a lattice of resonator coils can behave as an advanced material (*meta-material*) with properties that are not found in classic magnetic materials. Contemporary research is aimed towards deep integration of resonators in electromagnetic applications. A slab of meta-material could for example amplify wireless power transfer or shield bystanders from strong electromagnetic fields. Other recent research focuses on the integration of resonators in electric motors. The potential of meta-materials is twofold. First, the resonators can substitute the magnetic material, which is often heavy, expensive, brittle or lossy. On the other hand, the physical interaction between resonators enable dynamical properties that are not found in standard DC or AC electric motors.

Current research regarding RWPT based motoring is mostly limited to the derivation of analytical expressions and finite element modeling (FEM) with widely varying results and conclusions. The development of an RWPT based motoring system is challenging for multiple reasons, e.g., the resistance of coils changes drastically as a function of the frequency, the discrete capacitors require space in the integrated design, exact resonant tuning is hard to achieve and maintain, etc. This thesis aims to advance the field of directly integrated resonators in RWPT motoring systems. The biggest leap compared to current research is the validation of the derived analytical models and control strategies on a physical prototype. Additionally, we analyze the effect of detuning the resonators from resonance, meaning that the excitation frequency does not match the resonance frequencies of (all) the resonators in the system. Finally we discuss how the capacitor value of one or more resonators can be adjusted on the fly, while the motor is operational, by the use of a switch controlled capacitor.

In Chapter 2 we summarize the state of the art of resonant wireless power transfer. We discuss the operation and tuning principles of the most common resonator types and introduce figures of merit that describe the efficacy of RWPT systems that will also be useful for the optimal design of RWPT based motoring systems. Analytical models are presented that can be used to derive important electromagnetic interactions between resonator coils, e.g., magnetic coupling, forces and torques. We also explore fundamental aspects of resonator design and sizing, such as temperature and frequency dependent loss mechanisms in bundled conductors. The most commonly

used AC capacitor types are listed together with a comparison of their most important advantages and disadvantages.

In Chapter 3, we derive analytical expressions that describe the currents in the RWPT system with multiple coils. Based on these currents and the magnetic coupling between the coils, we find the torque on a rotating receiver coil. In this chapter we also discuss the construction of the physical prototype on which the analytical current and torque expressions are validated. The base prototype consists of 3 air coils. At the end of the chapter we discuss the possibility of adding a magnetic ferrite core around the axle of the rotor body and its positive effect on the generated torque.

In Chapter 4, we explore the possibility of detuning the resonators. We discuss the degrees of freedom of the detuning process and their effect on the electrical parameters. The expressions for the currents and the torque are revised and the effect of the detuning on the torque is thoroughly investigated. We observe that the torque can drastically increase by detuning the resonators, while the tuning becomes significantly more robust. In this chapter, we also introduce two more performance metrics that describe the torque efficiency and capability for a given machine.

While the frequency of the power source is easily changed, it is much more difficult to vary capacitor values, especially when the motor is running. Chapter 5 discusses the technologies that allow for active detuning of at least one of the capacitors in an RWPT motoring setup. For wide capacitor ranges, the state-of-the-art derivations of equivalent capacitance significantly drop in accuracy. A new semi-analytical method is developed which accurately predicts the current and voltage waveforms in a receiver resonator with a switch controlled capacitor. In this chapter we also discuss how we can simultaneously estimate electrical properties such as currents and impedances based on sensor data.

The final chapter summarizes the contributions of this thesis to the field of RWPT based motoring and provides guidelines towards future research on this topic.

List of Acronyms

3D	three dimensional
AC	alternating current
DC	direct current
DOF	degrees of freedom
EM	electromagnetic
EMF	electromotive force
ESL	equivalent series inductance
ESR	equivalent series resistance
EV	electric vehicle
FEM	finite element modeling
FPGA	field-programmable gate array
HF	high frequency
IC	integrated circuit
I(C)PT	inductive(ly coupled) power transfer
IGBT	insulated-gate bipolar transistor
KVL	Kirchoff's voltage law
LC	inductor-capacitor
MLCC	multilayer ceramic capacitors
MMF	magnetomotive force
MOSFET	metal-oxide-semiconductor field-effect transistor
MSE	modified Steinmetz equation
ODE	ordinary differential equation
PEN	polyethylene naphthalate
PET	polyester
PP	parallel-parallel
PP	polypropylene
PPS	polyphenylene sulfide
PS	parallel-series
PTFE	polytetrafluoroethylene (Teflon)
RF	radio frequency
RFID	radio-frequency identification

RIC	resonant inductive coupling
RLC	resistor-inductor-capacitor
RMS	root mean square
(R)WPT	resonant wireless power transfer
Rx	receiver
S1, S2	switch 1 and 2
SAE	Society of Automotive Engineers
SCC	switch controlled capacitor
SCMR	strongly coupled magnetic resonance
SMA	shape memory alloy
SMD	surface mount device
SP	series-parallel
SS	series-series
TRL	technology readiness level
Tx	transmitter
WET	wireless energy transmission

List of Symbols and Notations

Latin symbols

symbol	name	unit
a	radius	m
$\mathbf{A}$	magnetic vector potential	$\mathrm{Wb/m}$
$B, \mathbf{B}$	Magnetic flux density (vector)	T
c	speed of light, 299 792 458	$\mathrm{m/s}$
C	capacitor	F
d	distance	m
D	diameter	m
$\mathbf{D}$	displacement field vector	$\mathrm{C/m^2}$
e	error	
E	induced voltage vector	V
E	energy	J
$\mathbf{E}$	Electrical field vector	V
f	frequency	Hz
F	force	N
h	height	m
$H, \mathbf{H}$	Magnetic field (vector)	$\mathrm{A/m}$
$i, \mathbf{i}, I$	current (vector, phasor)	A
j	imaginary unit element	-
$J, \mathbf{J}$	current density (vector)	$\mathrm{A/m^2}$
k	coupling factor	-
$l, \mathbf{l}$	length, line with tangential direction	m
$K, \mathbf{K}$	positional derivative (matrix) of mutual inductance	$\mathrm{H/rad}$
L	inductance	H
$m, \mathbf{m}$	magnetic moment (vector)	$\mathrm{A \cdot m^2}$
m	amount of strands	-
$M, \mathbf{M}$	mutual inductance (matrix)	H
n	amount of conductors	-
$\mathbf{n}$	normal vector	-

symbol	name	unit
p	polynomial coefficient	-
P	power	W
Q	quality factor	-
r, $\mathbf{r}$	position (vector)	m
r_0	radius of conductor	m
R	resistance	Ω
R_0	radius of bundle	m
S, $\mathbf{S}$	surface, surface with direction of normal	m^2
t	time	s
T	torque	Nm
T	temperature	K
$\mathbf{T}$	Maxwell tensor	$\mathrm{N/m^2}$
TE	torque efficiency	$\mathrm{Nm/W}$
TC	torque capability	$\mathrm{Nm/A^2}$
U	kQ factor	-
v, $\mathbf{v}$	voltage (vector)	V
V	volume	m^3
w	width	m
W	work	J
x	first carthesian coordinate	m
X	reactance	Ω
y	second carthesian coordinate	m
z	third carthesian or cylindrical coordinate	m
Z	impedance	Ω

Greek symbols

symbol	name	unit
α	attenuation	$\mathrm{rad/s}$
α_c	temperature coefficient	$\omega \cdot \mathrm{m/K}$
δ	thickness, depth	m
δ	switching instance	rad
δ_c	loss angle of a capacitor	-
ε	induced voltage	V
ε_0	permittivity of vacuum	$\mathrm{F/m}$
λ	wavelength	m
ζ	damping ratio	-
η	efficiency	-,%
μ_0	permeability of vacuum	$\mathrm{H/m}$

symbol	name	unit
θ	physical angle of rotation	rad
ϕ	angle, phase angle	rad
Φ	magnetic flux	Wb
Ψ	coupled magnetic flux	Wb
ρ	radial cylindrical coordinate	m
ρ_c	resistivity of copper	$\Omega \cdot \mathrm{m}$
ρ_ε	charge density $\mathrm{C/m^3}$	
σ	conductivity	$\Omega^{-1} \cdot \mathrm{m}^{-1}$
$\tau, \boldsymbol{\tau}$	torque on finite element	Nm
ω	electrical frequency	$\mathrm{rad/s}$

Units

A	ampere
C	coulomb
F	farad
H	henry
Hz	hertz
J	joule
K	kelvin
m	meter
N	newton
rad	radians
s	second
T	tesla
V	volt
W	watt
Ω	ohm
$^\circ$	degree
$^\circ C$	degrees celcius
%	percent

Common notations

$\mathbf{1}$	unit vector
i	scalar
I	complex value/phasor
$\mathbf{i}$	vector of complex values/phasors
$\mathbf{A}$	matrix

$f()$	scalar function
$\mathbf{f}()$	vector function
$\mathbf{A}()$	matrix function
$\bullet_0$	value corresponding to resonance
$\bullet_{\mathrm{AC}}$	value corresponding to AC operation
$\bullet_{\mathrm{DC}}$	value corresponding to DC operation
$\bullet_r$	value corresponding to the rotor
$\bullet_{\mathrm{ref}}$	reflected
$\bullet_s$	value corresponding to the stator
$\bullet_t$	value corresponding to the transmitter
$\bullet_{\mathrm{tot}}$	total
$\bullet^*$	optimal
$\hat{\bullet}$	peak amplitude
$\Delta\bullet$	difference
$\mathbf{x}$	state-space state vector
$\mathbf{A}$	state-space system matrix
$\mathbf{b}$	state-space input vector

Mathematical functions and operators

A^{-1}	matrix inverse
A^{H}	Hermitian or conjugate transpose
A^{T}	transpose
Re	real part
Im	imaginary part
$\lvert a\rvert$	absolute value
$\overline{a}$	average
$\dot{a}$	time derivative
$\angle$	phase angle of complex vector
∇	gradient
$\nabla\cdot$	divergence
$\nabla\times$	curl
$E()$	elliptical derivative of the second kind
$K()$	elliptical integral of the first kind

Chapter 1

Introduction

Electrical machines have been the standard for industrial and consumer motoring applications for over 100 years. Various motoring solutions exist for propulsion applications and conveying physical motion. In electrical machines they all rely on the force interactions in the low frequency electromagnetic domain, i.e. interactions between electric currents and magnetic fields generate electromechanical energy conversion. These standard electromagnetic motors are highly efficient (typically over 90% [1, 2]), with a high torque per volume ratio. Often, heavy and expensive rare-earth permanent magnets are used to generate a strong magnetic field, e.g., in synchronous permanent magnet motors and brushless DC motors. Another way to generate a magnetic field is by running a current through a wound coil, called an electromagnet. Magnetic materials, mostly laminated electrical steel, are used to guide the magnetic flux through the stator and rotor of the motor and to limit the magnetic reluctance of the closed flux path. Most downsides of electromagnetic motors are direct consequences of the magnetic material that enables the strong magnetic fields inside the motors:

- Rare-earth materials are as the name implies rare and expensive. Rare-earth permanent magnets are generally extremely brittle and vulnerable to corrosion.

- Permanent magnets and electrical steel are dense and constitute the biggest part of the weight of an EM motor. The total weight of a regular EM motor is composed of electrical steel (40-65%), aluminum (20-35%), copper (8-15%), regular steel alloy (4-10%) and permanent magnets (0-4%) [3–5].

- As the reluctance of air is much higher than that of electrical steel, the air gaps between the fixed stator and the rotating rotor body is typically between 0.3 and 1 mm depending on the size, power and speed rating of the motor [6–8]. These tight tolerances drive up the cost and complexity of an electric motor, while complicating the cooling of the internal components.

This dissertation aims to investigate the possibility of (partially) alleviating the need for magnetic materials to generate a high magnetic field at the level of the conductors. Some electric circuits, such as series connected coil-capacitor (LC) circuits (Figure 1.1(a)) are able to amplify incident oscillating magnetic fields without the need for magnetic materials. The energy of the oscillations in the circuit builds up faster than it is dissipated, resulting in an underdamped system. When the oscillation in the circuit is the strongest for the frequency of the external magnetic field or the series connected voltage source, the circuit is said to be in resonance and the circuit is referred to as a resonator. Figure 1.1(b) shows the typical root mean square (RMS) current amplitude profile for a resonator as a function of the excitation frequency (ω), with a distinct peak at the resonance frequency (ω_0). In this thesis, the amplitude of sinusoidal electrical quantities are always given in RMS unless explicitly stated.

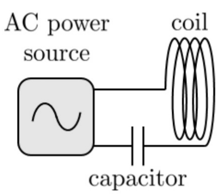

(a)

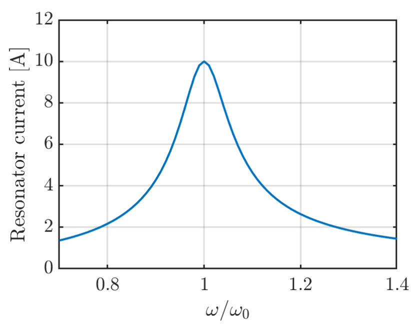

(b)

Figure 1.1: A resonator circuit, e.g., an LC-circuit (a), typically has a current peak at its resonance frequency (b).

A resonator can locally amplify external magnetic fields, just like magnetic materials such as electrical steel. Synthetic structures that macroscopically show material-like properties are called metamaterials [9–18].

Metamaterials and electromagnetic resonators have received increasing research interest in the domain of wireless power transfer (WPT). Wireless power transfer [19–29] is the idea of transferring energy over the air without the use of a physical connection such as a conducting wire. Recent advancements in resonator technology made resonators viable [21] and efficient to use for transferring power (in the order of kilowatts) over large air gaps without the need for magnetic materials. The maturation of magnetic resonance in high power applications has paved the way for more direct integration of resonators in electric motors and actuators. Integration of magnetic resonance in electric motors can overcome multiple downsides of contemporary electric motors and add advantages that come with WPT technology:

- Magnetic resonators can (partially) replace the heavy and expensive magnetic materials inside the electric motors.
- The receiving device becomes more mobile, because physical tethers are eliminated. The use of batteries can also be diminished, reducing the cost and weight of the device. Increased mobility and reduction in weight of a device makes it generally more convenient to use.
- Avoiding the use of wires also makes the device safer, eliminating the risks of tripping over the wire, damage to the wire and possible shock resulting from damage to the wire.
- Wirelessly powered devices can be constructed with a waterproof shell, such that the charging infrastructure is safe from water and debris. Encapsulated devices can also be used in hazardous environments or inside the body, e.g., cardiac pacemakers [30] and capsule endoscopy cameras [31].

1.1 Wireless power transfer

1.1.1 History of wireless power transfer

In the early 19th century, the theoretical description of electromagnetism advanced in a rapid pace. In 1826, Andre-Marie Ampere first described how an electrical current generates a magnetic field, which is now known as Ampere's circuital law. Michael Faraday and Joseph Henry independently observed electromagnetic induction in the early 1830's. In Faraday's experimental demonstration, a circuit with a battery and a toroidal transformer was closed and a transient current was observed at the secondary winding of the transformer. Faraday theorized that some sort of wave would travel through the material of the ring from one circuit to the other when the current changed in the first one. Later, Faraday discovered that a moving permanent magnet near a coil also induces a current in that coil. Despite his findings, Faraday failed to describe the mechanism behind the induced currents in a rigorous mathematical fashion.

Historically, Faraday was attributed with first observing that a changing magnetic field induces a current in a nearby coil. This induced current is a direct consequence of the electromotive force (EMF), which is the voltage that is generated in the conductor of the coil when the magnetic flux through that coil changes. In 1834, Emil Lenz refined this notion and described that the induced current will counteract the change of the magnetic field through the coil. Lenz's law is thus an extension of Faraday's law of induction, where the sign of the EMF and the resulting induced current is also determined. In 1861, James Clerk Maxwell started from the ideas of Faraday as a basis for his quantitative electromagnetic theory, which directly coupled electricity and magnetism in a unified framework. He described electromagnetic interactions by local differential equations in which the 'rate of change' of a quantity was directly described by its time derivative. The Maxwell-Faraday equation is one of four Maxwell equations which describe all classic electromagnetic interactions. It states that the curl of the locally induced electrical field ($\mathbf{E}$) equals the rate of change of the local magnetic field ($\mathbf{B}$):

$$\nabla \times \mathbf{E} = -\frac{\partial \mathbf{B}}{\partial t} \tag{1.1}$$

Note that $\mathbf{E}$ and $\mathbf{B}$ are dependent on both the spatial coordinates and time (t). The Maxwell-Faraday equation can also be converted to the integral form, by applying the Kelvin-Stokes theorem:

$$\oint_l \mathbf{E} \cdot \mathrm{d}\mathbf{l} = -\int_S \frac{\partial \mathbf{B}}{\partial t} \cdot \mathrm{d}\mathbf{S} \tag{1.2}$$

where l is the contour of the surface S which is enclosed by a conductor. This definition is easier to align with the definition of Faraday's law of induction, namely, *The electromotive force around a closed path is equal to the negative of the time rate of change of the magnetic flux enclosed by the path.* In 1884, the direction and amplitude of the energy carried by an electromagnetic wave was described by the Poynting vector and the Poynting theorem, named after its inventor John Henry Poynting.

While the aforementioned scientists laid the groundworks of the theory behind electromagnetism in the beginning of the 19th century, Nikola Tesla significantly advanced the field of wireless electromagnetic power transfer at the end of the 19th century. Tesla envisioned a commercial wireless power distribution system that could transfer power to households and factories without the need of wires. Tesla developed radio frequency (RF) resonant transformers, called Tesla coils, which produced high AC voltages. Tesla experimented with both inductive and capacitive near-field power transfer and demonstrated the illumination of light bulbs over multiple meters. The magnetic field strength of a transmitter drastically decreases with distance. Tesla realized that a receiving coil could harvest the transmitter's energy more effectively if he used a resonant LC circuit which was tuned to the excitation frequency of the transmitter. While Tesla failed to make a commercial product from his research, his methods remain the basis of contemporary near-field wireless power transfer.

Over the last 100 years, electrical components (such as metal-oxide-semiconductor field-effect transistors (MOSFET's), insulated-gate bipolar transistors (IGBT's) and capacitors) have become much more efficient, while microcontrollers and specialized integrated circuits (IC's) enabled accurate high frequency control of electrical oscillators. The research of wireless power transfer has matured in the last couple of decades, with high power inductive power transfer finally finding their way into industrial and consumer applications in the early 2000's. In 2007, Kurs et al. [20] demonstrated the transfer of 60 W at about 40% efficiency over a distance in excess of 2 meters. In 2008 the first open standard for wireless power transfer was launched, named Qi. The name 'Qi' is based on the Chinese term for invisible (spiritual) energy and literally translates to 'air'. The Qi standard [32–34] was developed by the Wireless Power Consortium as an open interface standard that defines wireless power transfer using inductive charging between planar coils over distances of up to 4 cm. The focus of this standard is wireless charging of home appliances on charging pads, e.g., smartphones, watches, toothbrushes, etc.

Between 2010 and 2017, the power delivery rating for Qi compliant consumer electronics such as smartphones grew from 5 W to 30 W and the standard was extended with multiple features, such as foreign object detection and device identification. Wireless power transfer has been developed for very low power applications, such as RFID tags [35,36], to high power applications such as the wireless charging of electric vehicles and buses [37–41]. In 2016, the Society of Automotive Engineers (SAE) launched the first global standard for wireless car charging (SAE J2954 [42]) which applies to wireless charging systems of up to 11 kilowatts. Since then, promising EV charging pads from WiTricity (11kW+), Qualcomm Halo (20 kW, Figure 1.2(a)) and BMW (3.2kW, 1.2(b)) have become available on the consumer market.

(a) **(b)**

Figure 1.2: High power WPT applications have found their way to the consumer market, such as charging pads for EV's from Qualcomm (a) and BMW (b).

Since the introduction of WPT devices to the consumer market, the demand for WPT components has exponentially increased to about 250 million transmitters and 500 million receivers in 2020 [43] (Figure 1.3(a)). The increasing number of filed patents [44] (Figure 1.3(b)) indicates that the wireless revolution has only just begun.

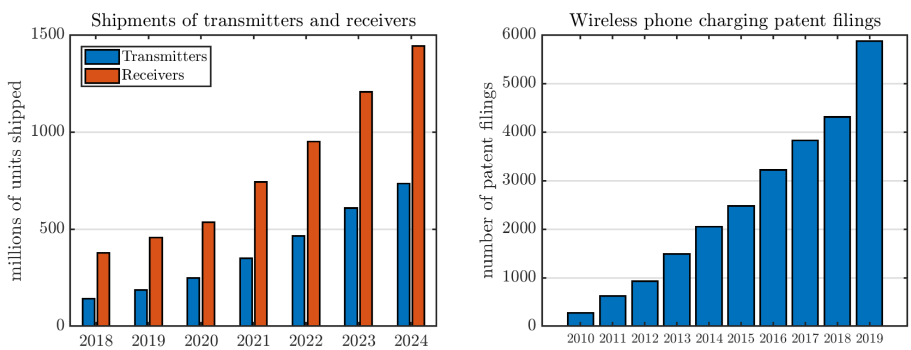

(a) **(b)**

Figure 1.3: The demand for WPT components has steadily grown since 2013 and is expected to grow even faster (a). The number of patent filings for wireless phone chargers indicates the growing development of WPT in consumer products (b).

1.1.2 Magnetic induction and resonance

Electromagnetic wireless power transfer is generally based on a time-varying electrical quantity, namely an electric or magnetic field, that induces a voltage and/or current in a receiver with the goal of transferring energy from the transmitter to the receiver. In commercial products, wireless power transfer systems are almost exclusively based on the principle of magnetic induction.

A current carrying open-ended coil generates a magnetic field in its vicinity. A direct current (DC) through that coil generates a non-varying magnetic field. No power can be extracted from that static magnetic field. If we however apply an alternating current (AC) in the coil, energy can be transmitted from this transmitter coil to a receiver. If the alternating magnetic flux of the transmitter coil is enclosed by a nearby receiver, a voltage is induced in that receiver coil which can in turn be used to power that device or charge its battery.

In literature, *wireless power transfer* has been described by many names. The naming mostly depends on trends, the focus of the design optimization or the technology behind the wireless power transfer. Historically, the focus of the design was on the inductive coupling between the transmitter and the receiver coils. Generally, the losses in the coil and the magnetic core material drive the design optimization of inductive power transfer. High magnetic coupling between the transmitter and receiver coils is primordial in increasing the efficiency of the power transfer. The transmitter and receiver coils are often constructed in the form of two halves of a transformer core, such that the magnetic flux path is mostly closed and stray fields are minimized. The focus on the inductive coupling between the system coils is reflected in the terms inductive(ly coupled) power transfer or I(C)PT. The inductance of the transmitter coil (L) is often compensated by a capacitor (C) in series or in parallel to the coil. The capacitor ensures that the load that is seen by the AC voltage source is real-valued and the voltage and current of the source are in phase. When the voltage and current waveforms are in phase, the stresses on and losses in the electrical components are reduced and the required voltage and current rating (VA rating) of the power source is lowered. For a series or parallel connected capacitor, the reactance of the coil is compensated when the frequency of the AC voltage (f) equals:

$$f = \frac{1}{2\pi\sqrt{LC}} \tag{1.3}$$

The frequency is then referred to as the resonance frequency of the coil-capacitor combination. While the current amplitude in an isolated resonator peaks at its resonance frequency, this is not always the case in the proximity of other resonators. Magnetic coupling with a receiver resonator (Rx) causes an additional voltage drop over the transmitter (Tx) coil, which can be converted to an equivalent *reflected impedance*. The reflected impedance is the highest at the resonance frequency of the receiver. When a resonant receiver with low resistance R and high quality factor $\left(Q = \frac{2\pi f L}{R}\right)$ is placed close to a resonant transmitter (Tx), the reflected impedance can cause a dip in the transmitter current around the resonance frequency, resulting in two local maxima in the transmitter and receiver current for frequencies that do not correspond to the resonance frequency of both resonators (see Figure 1.4(b)). This phenomenon is called *frequency splitting* [45]. At these current peaks, the delivered power

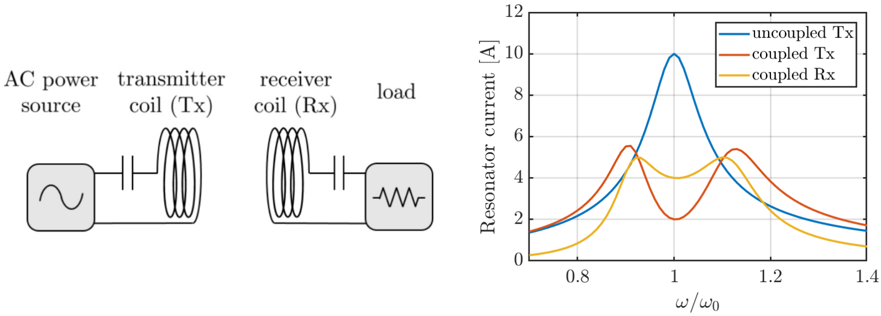

(a) **(b)**

Figure 1.4: When the transmitter (Tx) is strongly coupled with a receiver resonator (Rx) (a), the current in both coils reaches two distinct peaks at frequencies lower and higher than the resonance frequency (b).

is maximized. However, the transfer efficiency remains the highest at the resonance frequency. The transfer efficiency is the percentage of the ingoing power at the transmitter power source that is eventually absorbed by the receiver load. The design of strongly coupled (over the critical coupling) transmitter-receiver systems thus entails a trade-off between optimal efficiency and maximum power transfer.

Over time, the high power electrical components, such as IGBT's, MOSFET's and high frequency capacitors have become significantly more efficient, such that the losses and the equivalent series resistance of the LC coils have been lowered drastically. When tuning the LC coil to its resonance frequency, the decrease of the coil impedance causes a distinct peak in the current through the coil. The LC circuit is called a resonator and the resonant behavior of the LC coil can be considered the driving force behind the wireless power transfer. Because of this, the terms (resonant) wireless power transfer ((R)WPT), resonant inductive coupling (RIC) and strongly coupled magnetic resonance (SCMR) have become more prominent in describing inductive power transfer systems. Other terms for wireless power transfer are wireless power transmission, wireless energy transmission (WET) and electromagnetic power transfer. While other resonator types such as silicon ring resonators (photonics) [46] and conceptual dielectric resonators exist [47,48], LC circuits are currently the only resonator type that is considered viable in wireless transfer of electric energy. For this reason, inductive power transfer is often implied when using the term 'wireless power transfer'.

1.1.3 Near-field and far-field power transfer

Electromagnetic power transfer can be subdivided in two types, depending on the region in which the receiver is located.

- **Near-field region**: Near the transmitting device, i.e., at a distance shorter than one wavelength ($\lambda = c/f$, with c the speed of light in air), we can assume that the generated magnetic field is quasi-static. With that we mean that the magnetic field around the transmitter coil is directly proportional to the current in the conductor of the coil. The amplitude of the magnetic field strongly diminishes with respect to the distance to the coil. Resonant receivers can amplify the received magnetic field such that a useful amount of energy is extracted from the alternating magnetic field of the transmitter. Using magnetic resonance, the practical range increases from short range ($d \approx D_{\text{coil}}$) to medium range ($d \approx 10D_{\text{coil}}$).

- **Far-field region**: Further away from the transmitting device, the time retardation due to the finite speed of electromagnetic waves cannot be neglected. The electric and magnetic fields are perpendicular to each other and together they propagate as an electromagnetic wave. Electromagnetic waves, such as radio waves, microwaves and light waves, can be reflected and refracted, such that it is possible to focus the propagating waves in the direction of the receiver. Propagating waves radiate away from the transmitting device and the energy is lost whether or not a receiver coil picks up the oscillating magnetic field. This radiative loss can be converted into an equivalent series radiation resistance, but instead of heat, energy is dissipated in the form of electromagnetic radiation. Resonant inductive coupling systems where radiation losses cannot be neglected are often described using coupled mode theory [20, 49].

In this thesis, only near-field wireless power transfer is considered. The frequencies remain in the kHz range, far below microwave (GHz) or light wave (THz) frequencies, such that the wavelengths are tens of thousands times larger than the dimensions of the system. Additionally, we can simplify Ampere's circuital law and assume a magnetic quasi-static system. In practice this means that in Maxwell's equation (in the absence of magnetic and dielectric materials)

$$\nabla \times \mathbf{B} = \mu_0 \left(\mathbf{J} + \varepsilon_0 \frac{\partial \mathbf{E}}{\partial t} \right) \tag{1.4}$$

the time derivative of the electric field can be neglected. This allows us for example to apply the Biot-Savart law, which describes the magnetic field generated by a current carrying conductor, for AC currents. Equations (1.1) and (1.4) are two of four Maxwell's equations which are considered (together with the Lorentz force law) to be the fundamental equations for electromagnetism. For completion, the remaining two equations of Maxwell are given:

- **Gauss's law for electric fields**:

$$\oiint_S \mathbf{E} \cdot \mathrm{d}\mathbf{S} = \frac{1}{\varepsilon_0} \iiint_V \rho_\epsilon \mathrm{d}V \quad \Leftrightarrow \quad \nabla \cdot \mathbf{E} = \frac{\rho_\epsilon}{\varepsilon_0} \tag{1.5}$$

  The electrical flux of field $\mathbf{E}$ out of a closed surface S is equal to the enclosed electrical charge (with ρ_ϵ the volume charge density) divided by the permittivity of the vacuum ε_0.

- **Gauss's law for magnetic fields**:

$$\oiint_S \mathbf{B} \cdot \mathrm{d}\mathbf{S} = 0 \quad \Leftrightarrow \quad \nabla \cdot \mathbf{B} = 0 \tag{1.6}$$

  The magnetic flux through a closed surface is equal to zero. This is equivalent with saying that the magnetic field $\mathbf{B}$ is a solenoidal vector field with a divergence of zero. In contrast to electric fields, no magnetically charged 'sources' of magnetic fields (or monopoles) exist.

1.2 Building blocks of resonant wireless power transfer

Multiple advancements in circuit design, materials, electrical components and control strategies have enabled power transfer efficiencies of wireless power transfer systems that exceed 90%. To construct an effective and efficient RWPT system, many aspects of the resonator design need to be considered.

1.2.1 Resonator topologies

An LC resonator consists of an inductive coil and a capacitor which compensates the reactance of the inductor. If the coil is directly connected to a load or a power source, the capacitor can be connected in series or in parallel with the coil. Figure 1.5 shows the standard topology of a series (a) and parallel (b) compensated transmitter coil. A series compensated transmitter resonator has an equivalent resistance which is equal to the sum of the series resistance values of the coil and the capacitor. Close to the resonance frequency, the impedance becomes very low such that the current generated by the AC

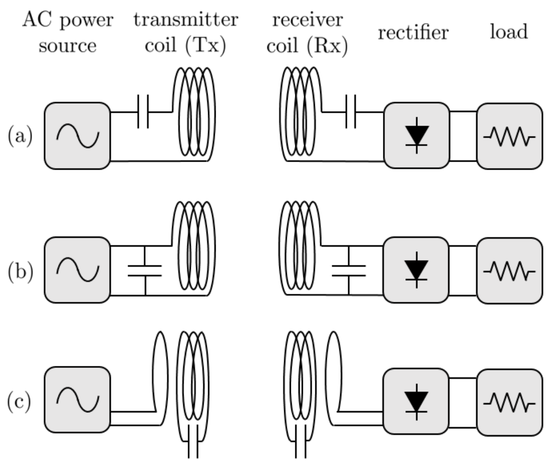

Figure 1.5: Resonant transmitter or receiver resonators can be classified under three categories. The reactance of an inductive coil can be compensated by a series (a) or parallel (b) connected capacitor. Alternatively, a short-circuited LC resonator can be placed near a conducting loop (c) to amplify the transferred inductive power.

voltage source reaches its peak value. A parallel compensated resonator also reaches its peak current in the coil at the resonance frequency. However, the impedance of the parallel connected coil and capacitor becomes very large around the resonance frequency of the coil. The AC voltage source sees a high impedance load and the current drops to its lowest value, while most of the current running through the coil circulates through the parallel capacitor.

Resonator coils can also be used in another way to amplify the magnetic field of the transmitter coil. A short-circuited series connected resonator coil is placed nearby a transmitter coil with significantly fewer (often only one) turns. The resonator picks up the magnetic field of the nearby transmitter loop/coil. The changing magnetic field induces a high current in the resonator coil and generates a much stronger magnetic field. This stronger magnetic field in its turn induces a counteracting voltage (EMF) in the transmitter loop. Consequently, the power source, connected to the transmitter loop, sees a high reflected impedance which is caused by the EMF that counteracts the current through the transmitter coil, as if a larger impedance was connected in series with the transmitter coil.

Figure 1.5(c) shows transmitter and receiver resonators that consist of 2 coils. If both the transmitter and resonator are constructed with a nearby short-circuited resonator, the transmitter-resonator pair is called a 4 coil RWPT system. Based on comparative research, the 2 coil system is generally considered the superior topology for high power transfer. The 4 coil system only shows benefits for higher frequencies or large dimensions. The resonator coil can be an open coil without a discrete capacitor. The parasitic capacitances between the windings function as the compensating capacitor. The resonance frequency of the coil is then tuned by physically changing the spacing between the turns. Parasitic capacitances are however very low, even for large coils, such that high frequencies or large dimensions are required to make this methodology practical. In the aforementioned experiment of Kurs et al. [20], the 4 coil system required coils of 60 cm in diameter to transfer 60 W at 10 MHz. The parasitic capacitance of single turn coils, also called split-ring resonators, is used for very high frequencies. Arrays of these split-ring resonators then act as metamaterial lenses which guide and amplify the magnetic field that is generated by a nearby transmitter.

1.2.2 Magnetic materials

In electric motors, the magnetic field is often generated by permanent magnets or current carrying copper coils. Laminated electrical steel is used to decrease the magnetic reluctance of the flux path such that the same magnetomotive force (MMF), generated by the current in the winding, results in a higher magnetic flux over the airgap. The pulsating flux generates an EMF inside the electrical steel. The resistive heat dissipation in a conducting material scales quadratically with the EMF and inversely proportionate with the resistivity of the material. Electrical steel is a good electrical conductor, such that the resistance is low and the power dissipated inside the magnetic material is potentially very high. The electrical steel is laminated in order to eliminate possible current paths. The flux can thus only be enclosed by a current path with the width of one lamination. The required maximum thickness of the lamination is directly related to the frequency of the flux pulsation. For frequencies in the kHz range or higher, it is impractical to keep using laminated steel to amplify the magnetic field inside the motor.

High frequency (HF) transformers are most commonly built using ferrite cores. Ferrites are ceramic compounds of the transition metals with oxygen and iron oxides, e.g., MnZn and NiZn, with high relative permeability and very high resistivity, thus limiting dissipation. Soft ferrites with low coercivity have been widely used as low dissipation inductor cores in RF applications (such as toroidal inductor cores) and HF transformer cores. Ferrites are often used in RWPT designs as a means to shape the magnetic field, by improving the magnetic coupling between coils and limiting stray fields [31, 50–53]. In ferromagnetic materials (such as magnetic iron and steel), the iron atoms and their magnetic fields align. In the ceramic grid of a ferrimagnetic material, iron atoms tend to oppose each other, with an asymmetrical tendency towards one direction. This results in a net magnetic field which is lower than that of a ferromagnetic material. Consequently, the maximum flux density of ferrimagnetic materials is significantly lower than that of ferromagnetic materials (1.9 T versus 0.6 T).

1.2.3 Capacitor tuning

The AC (non-polarized) capacitor is an essential component in RWPT systems. The current and voltage rating limits the power rating of the WPT system, while the dissipation factor determines the efficiency of the resonators. For AC power applications, film capacitors are often the optimal choice. Film capacitors are relatively cheap, with high voltage ratings, low dissipation factors and relatively high capacitance value, accuracy and stability. For high Q factors, it is often unavoidable that some sort of tuning is required to make sure the transmitter and receiver resonators are closely matched. Two physical tuning methodologies exist in literature to tune the capacitance value to the required resonance frequency:

- **Switched capacitor bank**: Multiple capacitors are connected in parallel. Capacitors can be switched on or off using an AC switch. One possible topology is a row of capacitors where each capacitor value is half the value of its neighbor. That way, the capacitance value can be controlled by steps equal to the smallest capacitor size, similar to how a decimal value can be represented as a binary number.

- **Switch controlled capacitor (SCC)**: SCC's are capacitors that are turned on and off multiple times per period. Most often, the capacitor is only charged up to a certain voltage and re-engages when the voltage over its terminals decreases under that voltage limit. This methodology allows for a continuous variation of the equivalent capacitor value.

1.3 Other RWPT technologies

1.3.1 Capacitive power transfer

While inductive power transfer is based on emitting and receiving of alternating magnetic fields, capacitive power transfer is based on the generation of electrical fields between electrodes, most often metal plates [54–59]. An alternating electrical field generates a variable charge in a receiver plate which

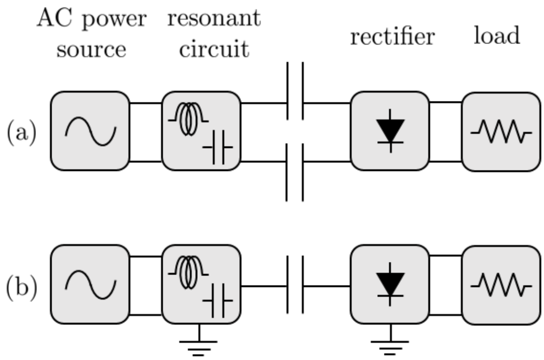

Figure 1.6: Capacitive power transfer systems generally need two pairs of capacitors (a) that couple the transmitter and receiver structures. Alternatively one of the capacitors can be substituted by a connection to the ground or a large passive plate (b) to allow for the displacement of the electrical charge to and from the capacitor plates.

causes an AC current in the receiver. Capacitive coupling can be applied in two ways:

- **Bipolar coupling**: The transmitter and receiver side are coupled by two pairs of capacitor plates (see Figure 1.6(a)). The capacitor plates of the transmitter side are driven in opposite phase, such that the charge can flow from one capacitor plate to the other. This way, the AC current has a return path in the circuit. This configuration is the most commonly used one for power transfer applications.

- **Unipolar coupling**: The transmitter and receiver are coupled through one pair of capacitor plates (Figure 1.6(b)). Both the transmitter and the receiver are connected to a large passive plate or the ground, such that the alternating charge on the plates can move in and out of the component. The ground acts as a return path of the AC current.

Capacitive wireless power transfer has multiple downsides compared to inductive power transfer. The metal plates need to be rather large and oriented towards each other, often limiting the added convenience of such a wireless transfer system. To obtain useful amounts of transferred power, extremely high voltages are required. These high voltages pose a safety risk for the user and nearby components. While the human body is mostly agnostic to magnetic fields [60](to a certain degree), strong electrical fields (and especially direct contact with charged conductor plates) are harmful for human tissue. One advantage of capacitive power transfer is the way electrical fields close compared to magnetic fields. Electrical fields can be large between the two plates with different potential, while the electrical field outside of this region is low. Magnetic fields of open ended coils tend to fill the space around the transmitter. The magnetic flux follows the path with the lowest reluctance. Similar to Pouillet's Law, the reluctance of air is lower if the flux can flow through a larger surface. For air coils, this means that the magnetic flux spreads out over the available air. This leakage flux can be guided by adding magnetic materials with lower reluctance which facilitate the closing of the magnetic flux path. This magnetic return path requires additional material, volume and weight.

1.3.2 Radiative power transfer

Far-field wireless power transfer requires propagating electromagnetic waves to transfer energy from a transmitter to a receiver. Electromagnetic waves such as microwaves or light waves can be 'beamed' or focused in a desired direction by smart design of the antenna or by refracting through a lens or reflecting on a (parabolic) dish. An antenna that emits a directed beam of electromagnetic waves is often referred to as a rectenna [61–63]. A laser is another example of a tightly bundled set of electromagnetic light waves. Proposed applications of power beaming are solar satellites that beam their harvested energy back to earth and drones that could theoretically never have to land or slow down to refuel.

1.3.3 Resonators as metamaterials

Resonant wireless power transfer enables the transfer of power over short to long distances without the need for physical connections or magnetic materials. The magnetic field of a transmitter excites a voltage in the receiver resonator. The resonant behavior of the receiver causes a large current to build in the conductor. This current then excites a strong local magnetic field. This newly generated magnetic field can be phase-shifted compared to the exciting magnetic field. If we represent the alternating magnetic field by a complex phasor, the phase-shifted amplification by the resonator can be represented by a complex relative permeability. Arrays of resonators can act as one large body with an equivalent material property. Such bodies are called metamaterials [9–18, 64]. Figure 1.7 shows two examples of metamaterial bodies found in literature [17, 64].

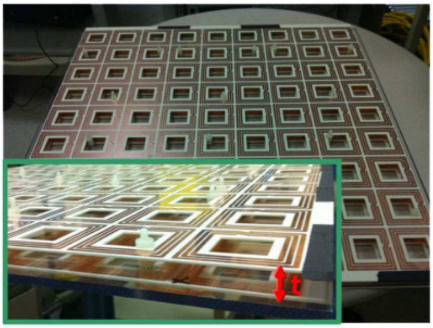

(a)

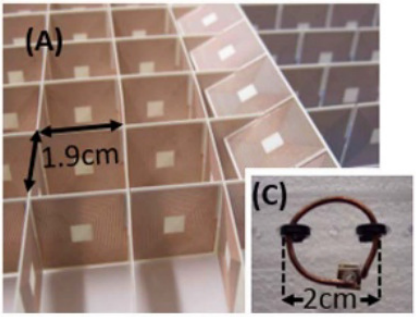

(b)

Figure 1.7: An array of resonators is called a metamaterial when it acts as one large body with an equivalent material property. Subfigures (a) and (b) are examples of metamaterial slabs found in literature [17, 64].

Metamaterials can have equivalent material properties that do not occur naturally, such as negative permeability. Metamaterials can for example be used as electromagnetic shields to block certain wavelengths [12, 13]. Resonator arrays can also be used as lenses for radiative electromagnetic waves [17]. Split-ring resonators often have their resonance frequency in the GHz or even THz range, which make them able to interact with microwaves and light waves. Resonator-based metamaterials have for example been studied to act as cloaking devices [14]. The metamaterial grid is designed to guide the light waves around a body to effectively make it invisible.

1.4 RWPT for actuation and motoring

Resonant wireless power transfer enables the induction of high currents at the receiver side. One of the applications of these induced currents is the supply of electromagnetic motors and actuators. RWPT can be used to feed electromagnetic motors and actuators on three levels of integration:

- Most often, the receiver coil of the RWPT system and the actuator sides are indirectly connected through an energy buffer, e.g., a battery (topology (a) in Figure 1.8) [65–68]. The induced current is rectified and the resulting DC voltage is then stepped up or down to the appropriate voltage to charge the battery using a DC-DC converter. While this method adds weight and cost to the receiving device, the battery buffer allows intermittent power transfer when it is more convenient for the user, such as charging of buses at bus stops or electric vehicles in parking spots.

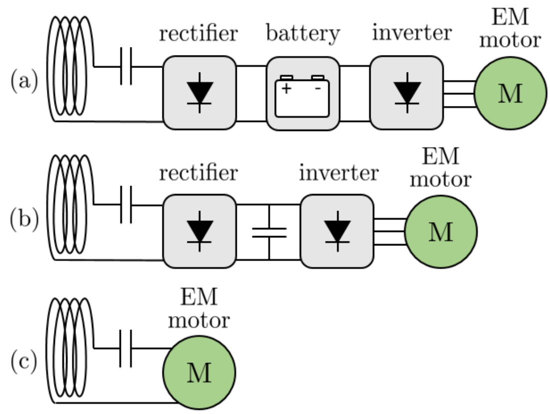

Figure 1.8: RWPT technology can be intergrated in electromagnetic (EM) motoring devices on three levels: by intermittently charging an intermediary buffer such as a battery (a), by AC-DC or AC-AC converting the induced current to the specific requirements of the EM motor (b) or by directly applying the induced current to generate electromagnetic forces and torques (c).

- A more direct energy conversion methodology (Figure 1.8(b)) is to rectify the induced voltage in an RWPT receiver coil and then use this DC voltage directly to actuate, for example, a DC-motor [29, 69–73] or a multiphase AC motor. In the case of multiple actuators, each actuator can have its own distinct resonance frequency, allowing for selective actuation of the receiving devices.

- The resonant behavior of LC coils can be applied to exert forces or torques directly (topology (c)) [74–88]. Resonators locally amplify the magnetic field, decreasing or outright eliminating the need for expensive and heavy magnetic materials. No intermediate electrical components are then required to convert the received power to appropriate voltages or frequencies.

This thesis investigates the direct applicability of RWPT in motoring systems. The focus of this research is thus on the third topology. The direct application of magnetic resonance in motoring systems has seen a significant growth in research interest since 2015. A semi-direct way to move actuators with resonant coils is to convert the heat generated by the current in LC receivers to selective actuation. In [74] the LC resonators selectively heat up a gas which expands an actuator while in other research a shape memory alloy (SMA) is heated to enable drug delivery from microsyringes [75, 76] or automatic multijoint folding of small robots [77].

Research regarding the direct application of RWPT mostly focuses on the generation of local magnetic fields and the force or torque interactions between resonators. Ebot and Yasutaka [78–81] developed a magnetic resonance based motor which has two distinct phases that are excited with a 90 degree phase shift. The variation of the excitation frequency is studied while varying the amount of pole pairs. Sakai [83–86] and Iachetti [82] based the design of an RWPT motor on the cage rotor design of a three phase induction machine. As the resonance frequency of the LC circuits is significantly higher than the speed of the rotor, the slip is close to 100%. In this research, the frequency is varied around the resonance frequency and multiple amounts of pole pairs are considered.

Liu [87] studied the lateral attraction and repulsion between two resonator coils and constructed an RWPT motor which consists of an array of quasi-lateral pole-pairs. The attraction and repulsion are a direct consequence of the frequency splitting phenomenon between two strongly coupled resonators. Boyvat [88] studied the lateral and rotational forces between externally excited resonators. The resonators are tuned to the same or different frequencies, while the frequency of the external magnetic field is varied continuously. It is shown that the torque on a rotating resonator is unidirectional for frequencies close the the resonance frequency of the resonators.

All direct applications of RWPT have solely been studied in analytical and finite element simulations, with the exception of [88], where the torque profile between two resonators was measured at the resonance frequency of the resonators. The simulated magnetic resonance based motors return a wide range of results regarding the expected torque and speed. Generally the expected torque of an RWPT based motor without magnetic material is low and multiple coils need to be tuned to approximately the same frequency to generate a measurable torque. This explains why it is difficult to validate the simulated behavior of an RWPT motor in a physical setup and why it has not been done to a larger extent.

1.5 Objectives and challenges

Research regarding the direct application of magnetic resonance is mostly limited to simulations of various kinds of motoring topologies. The novelty of the technology requires a rigorous analysis of the interaction between resonators and its applicability in motoring and actuation. The most important step in making RWPT motoring ready for commercialization is the development of experimental prototypes and accompanying design optimization procedures. This thesis aims to build a rigorous framework to understand the coil-coil interaction while making the technology ready for experimental validation. The goals which we aim to fulfill by the end of this manuscript and their particular challenges can be subdivided into four categories:

Insights and optimization

- Gaining a better understanding of the governing coil-coil mechanisms in RWPT by building an analytic framework. The framework must be parametric with respect to the geometrical and electrical physical quantities of the system.
- Further extending upon this framework and simultaneously optimizing the geometrical and electrical design parameters. Gained insights can be used as a guideline, while the constructed parametric models are applied as a basis for the optimization framework.
- Although research regarding RWPT based motors focuses mostly on eliminating magnetic material in the system, it is still important to study the potential benefits of combining magnetic resonant coils and magnetic material to generate torque. The addition of magnetic materials can amplify the magnetic field by lowering the reluctance of the flux path, while redirecting flux lines to improve the magnetic coupling between system coils.

Experimental validation

- The experimental validation of RWPT based motoring systems in literature is very limited. In this thesis we aim to convert every simulated finding into an experimental validation on a setup. Experimental validation is an important step in increasing the technology readiness level (TRL) of RWPT based motoring. The design of a physical setup brings multiple difficulties. We need to obtain a good understanding of the magnetic interaction between current carrying resonators and the resulting torque.
- It is important to analyze the loss mechanisms at the component level. Especially the losses in the conductors drastically increase for high frequencies. Additional losses due to e.g., the skin effect and the proximity effect quickly dominate the losses for increasing frequencies. A tradeoff will be identified between the current carrying capacity of the wires and the high frequency losses in the conductor.

Tuning and control optimization

- The selection and tuning of the capacitor in a resonant circuit is a critical aspect of the design of an RWPT motor. While in conventional electromagnetic motors, windings and magnetic material are tightly packed, using discrete capacitors requires additional space, especially for high capacitance values and power ratings. For high quality factors, capacitors need to be finely tuned. Depending on external effect such as temperature and magnetic interaction, the precise tuning can be affected and the resonance frequency of the LC resonators can shift.

- The unidirectional torque of RWPT motoring systems has been demonstrated at the resonance frequency of the resonators. It might however be beneficial to apply deviating frequencies to improve current generation in the resonator coils, similar to how the frequency splitting phenomenon causes increased currents for frequencies that deviate from the resonance frequency. In this thesis we want to identify the electrical degrees of freedom that govern the tuning of an RWPT motoring system and investigate their effect on the torque generation.

Increasing robustness

- Accurate tuning of multiple resonators is difficult, such that experimentally validating finely tuned simulated resonators can be challenging. Additionally it is not possible to drastically change the tuning of one or more resonators online. In this thesis we want to investigate the possibility of continuously varying the capacitance value in at least one resonator. We want to experimentally validate this continuous detuning of the capacitor and identify additional losses in such a variable capacitor.

- In a parametric simulation, all electrical parameters are assumed to be known exactly. Measured quantities will however deviate due to modeling uncertainties, e.g., non-linear effects such as magnetic saturation, and variability of electrical parameters due to outside effects such as temperature changes. In this thesis we want to investigate ways to align the parametric models with sensor data, by estimating electrical parameters and states online, especially ones that are difficult to physically measure, such as the current in a rotating coil.

1.6 Outline of the dissertation

The structure of this thesis follows the step by step development and optimization of an RWPT motoring system, based on the defined research objectives. Each chapter outlines a distinct aspect of the research in greater detail.

Chapter 2 provides an overview and synthesis of the state of the art regarding resonant wireless power transfer. Relevant electrical concepts, such as resonance, mutual inductance and reflected impedance are explained and important performance indicators such as quality factor, coupling factor and their effect on the transfer efficiency are derived. The most important resonant transmitter topologies are analyzed and compared. We derive analytical models for the magnetic field of air coils and coil-coil interactions such as magnetic coupling and forces and torques between air coils. In this chapter we also present important design considerations for RWPT based motoring. Based on the loss mechanisms in wound coils we derive optimal driving frequencies. Different AC capacitor types are compared and their applicability for RWPT motoring systems is discussed.

Analytical torque expressions for multicoil RWPT systems are derived in Chapter 3. The torque profiles for both voltage controlled and current controlled transmitter power sources are considered. A prototype of the RWPT motor is built to validate the electromechanical model. Additionally, a finite element model was constructed and an efficient methodology is derived for evaluating the performance of an RWPT motor. In this chapter we also study the potential benefit of combining resonators and magnetic material in the RWPT motor. A ferrite core is added in the rotor and we quantify its effect on the electrical parameters (e.g., the quality factor of the coils) and the torque generation.

In Chapter 4, we expand the torque expression for detuned system resonators. We discuss what degrees of freedom are present in detuning the RWPT motor and study their effect on the torque generation. The expanded expressions are validated on the prototype for three discrete capacitor detunings. We introduce new metrics to quantify the efficiency and torque limits of the RWPT motor. We show that detuned systems can reach higher average and maximum torques while the tuning is more robust.

Chapter 5 explains how a capacitor in a resonator can be continuously varied by the use of switching elements in order to detune an RWPT motor online. Two types of switch controlled capacitors are discussed and the relation between the control signal and the equivalent capacitor value is derived. For a large detuning range of the switched capacitor, the current and voltage waveforms cannot be assumed sinusoidal. By solving piecewise differential equations, accurate simulations of the electrical variables are developed. We also explain how the capacitor tuning can be estimated online based on sensor data of voltages and currents in the system.

Finally, Chapter 6 provides an overview of the research results of this thesis. We also discuss the possibilities and potential challenges for future research regarding this topic.

1.7 Research contributions

The thesis aimed to advance the understanding and development of RWPT motoring systems. The thesis emphasized mainly on the development of control strategies and electrical implementations in order to optimize the performance of a given system. The contributions of this work are aligned with the original research objectives:

- **Insights and optimization**: An analytical and parametric framework was constructed which enables the simulation of electrical and physical quantities. The performance of the RWPT motor is quantified in terms of commonly used figures of merit such as the quality factor, which allows optimal selection of the driving frequency. A finite element simulation model was constructed and an efficient evaluation methodology was developed to quickly quantify the performance of new RWPT motoring designs.

- **Experimental validation**: An experimental prototyping platform was constructed which enables accurate evaluation of the generated torque. Concrete design aspects were discussed regarding the construction of the coils and the selection of discrete AC capacitors. Offline and online measurements allow for the estimation of electrical quantities such as currents, resistance variations and resonator tuning.

- **Tuning and control optimization**: The detuning of RWPT motoring systems is rigorously analyzed in this thesis. The degrees of freedom for detuning are identified and the potential gains in maximum torque are studied as a function of variable frequency and capacitor tuning. Two additional performance indicators are introduced to quantify the efficacy of a given detuning setting.

- **Increasing robustness**: On a real setup, electrical parameters vary due to temperature variations, magnetic interactions, material degradation etc. while other electrical quantities are difficult to measure. Other quantities such as the equivalent capacitance of the switch controlled capacitor are hard to accurately predict, resulting in the need for online feedback. In this thesis, we introduce algorithms that enable online state estimation and control.

1.8 Scientific Publications

1.8.1 International SCI Journals

1. A. De Keyser, **M. Vandeputte**, and G. Crevecoeur. Convex mapping formulations enabling optimal power split and design of the electric drivetrain in all-electric vehicles. *IEEE Transactions on Vehicular Technology*, 66(11):9702-9711, 2017. (equal contribution) DOI: 10.1109/TVT.2017.2745101

2. **M. Vandeputte**, A. De Keyser, and G. Crevecoeur. Computationally efficient modeling for assessing the energy efficiency of electric drivetrains using convex formulations. *International Journal of Numerical Modelling: Electronic Networks, Devices and Fields*, 32(4):e2275, 2019. (equal contribution) DOI: 10.1002/jnm.2275

3. **M. Vandeputte**, L. Dupré, and G. Crevecoeur. Quasistatic torque profile expressions for magnetic resonance-based remote actuation. *IEEE Transactions on Energy Conversion*, 34(3):1255-1263, 2019. DOI: 10.1109/TEC.2019.2919789

4. **M. Vandeputte**, D. Bozalakov, L. Dupré, and G. Crevecoeur. Improving torque in a magnetic resonance based motoring system by detuning from resonance. *IEEE Transactions on Energy Conversion*, 2020. DOI: 10.1109/TEC.2020.3018192

1.8.2 Proceedings of International Conferences

1. **M. Vandeputte**, L. Dupré, and G. Crevecoeur. Series and parallel capacitor compensation of the transmitter in a magnetic resonance based motoring system. *In IECON 2019-45th Annual Conference of the IEEE Industrial Electronics Society*, volume 1, pages 1339-1344. IEEE, 2019. DOI: 10.1109/IECON.2019.8927283

2. M. Vandeputte, L. Dupré, and G. Crevecoeur. Effect of transmitter position on the torque generation of a magnetic resonance based motoring system. *In 2019 22nd International Conference on Electrical Machines and Systems (ICEMS)*, pages 1-5. IEEE, 2019. DOI: 10.1109/ICEMS.2019.8922545

1.8.3 Abstracts for International Conferences

1. A. De Keyser, **M. Vandeputte**, and G. Crevecoeur. Optimal torque actuations of an electric drivetrain using convex optimized power flows. *In 14th International Workshop on Optimization and Inverse Problems in Electromagnetism*, 2016.

2. **M. Vandeputte**. Resonator impedance optimization for quasi-static magnetic resonance based actuation. In 15th International Workshop on Optimization and Inverse Problems in Electromagnetism, 2018.

3. **M. Vandeputte**. High fidelity model based analysis of SCMR based motoring systems with ferrite rotor core. *In 2nd IEEE Conference Advances in Magnetics (AIM)*, 2020.
   (abstract accepted before cancellation of the conference)

Chapter 2

Resonant wireless power transfer for torque generation

2.1 Introduction

This chapter discusses the main driving mechanisms of resonant wireless power transfer for torque generation. The field of resonant wireless power transfer, which heavily relies on magnetic resonance, has matured in the last decades to the point that efficient, high power RWPT systems have become viable alternatives to wired electric power transfer, with transfer efficiencies over 90% [89]. Resonators are able to generate strong local magnetic fields and high currents despite the low magnetic coupling between coils due to large air gaps. This chapter begins with an outline on the current state of the art of RWPT (Section 2.2). The magnetic field of air coils and resulting electrical parameters are derived. Analytical electrical models and meaningful figures of merit are treated for the most important resonator topologies. In Section 2.3, derivations for the magnetic field of coils are adapted to provide better understanding of the electromagnetic coupling and force/torque interactions between moving air coils. This chapter lays the groundworks for the construction of the RWPT motoring prototype in the next chapter. The dominant loss mechanisms in air coils are studied and guidelines for the optimal driving frequency are derived in Section 2.4. Capacitors are primordial in resonators as they compensate the reactance of the coil inductance to make resonance possible. Section 2.5 provides an overview of the most commonly used AC capacitors and discusses the selection of the most suitable capacitor type for the RWPT motoring prototype.

2.2 Basics of resonant wireless power transfer

2.2.1 Air coil transmitters

A current running through an open ended coil generates a magnetic field around that coil and the coil is said to operate as an electromagnet. The simplest electromagnet circuit that we can consider is a voltage source connected directly to the terminals of a wound coil. Figure 2.1 illustrates the magnetic field lines for a current carrying coil.

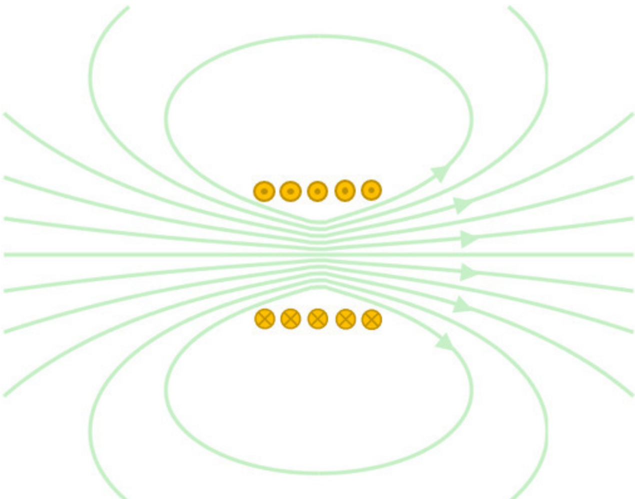

Figure 2.1: A current through an open ended coil generates a magnetic field around that coil. If the current through the coil is alternating, the coil acts as a magnetic field transmitter.

For a given DC voltage, the current through the coil is inversely proportional to the DC resistance of the coil.

$$i = \frac{V_{\mathrm{DC}}}{R_{\mathrm{DC}}} \tag{2.1}$$

If we connect an AC voltage source (v) to the terminals of the coil, an AC current i is generated. This AC current generates a magnetic field that is proportional to that current. A coil that is designed to generate an outward magnetic field is referred to as a transmitter coil.

2.2.2 Self inductance of coils

Lenz's law states that the varying magnetic field in the coil generates a voltage contrary to the change of magnetic field. This induced voltage is called the back electromotive force or back EMF and scales linearly with the change of the magnetic field and thus, by extension, the change of the current in the coil. The ratio of this induced voltage to the change in current is called the self-inductance of a coil and is generally denoted by the letter L.

$$v_L(t) = L\frac{\mathrm{d}i(t)}{\mathrm{d}t} \tag{2.2}$$

When we assume a periodic solution of Kirchoff's voltage law (KVL) for sinusoidal voltages and currents, we can lift the time dependent solution to the complex plane. Instead of sinusoidal functions of time, the voltage and current are now rotating vectors (so called phasors) on the complex plane. To find the time dependent solution, we only need to project the rotating vectors to the real axis. The phasors of a sinusoidal time signal are often denoted by capital letters while the time equivalent function is denoted by non capitalized letters.

$$V_L = j\omega L I_L \tag{2.3}$$

The oscillation frequency of the electrical variables can be described by f [Hz] or $\omega = 2\pi f$ [rad/s]. In the phasor representation, the back EMF V_L is said to lead the current through the coil (I_L) by $\frac{\pi}{2}$ radians. In this thesis, the phasor length corresponds to the root mean square (RMS) of the alternating variable. For sinusoidal functions, the peak amplitude is $\sqrt{2}$ times the RMS value.

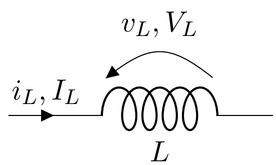

Figure 2.2: The current i_L (I_L) through an inductor L induces a back EMF v_L (V_L) opposite to the direction of the current.

2.2.3 Q factor of inductors

The inductive reactance $X_L = \omega L$ determines the amount of reactive power ($\omega L I^2$) that is absorbed by the coil. Per electrical cycle, the maximum magnetic energy that is stored in the coil equals LI^2, with I the RMS value of i. The performance of a coil design is often quantified by the dimensionless quality factor or the Q factor. The Q factor is the ratio of the inductive reactance X_L and the AC resistance of the coil.

$$Q = \frac{X_L}{R_{\mathrm{AC}}} = \frac{\omega L}{R_{\mathrm{AC}}} \tag{2.4}$$

The Q factor is also proportional to the maximum magnetic power stored in the coil and the power that is dissipated per cycle ($W_{\text{cycle}} = R_{\text{AC}} I^2 / f$):

$$Q = 2\pi \frac{LI^2}{W_{\text{cycle}}} = 2\pi f \frac{LI^2}{R_{\text{AC}} I^2} \tag{2.5}$$

The Q factor is directly related to the damping ratio $\zeta = \dfrac{1}{2Q}$ of an oscillator. The damping ratio determines whether or not the current in an oscillator or resonator coil will oscillate when stored energy is freely dissipated in the coil:

- A system with a low Q factor ($Q < 1/2; \zeta > 1$) is said to be overdamped and no oscillation will occur.
- A resonator with high Q factor ($Q > 1/2; \zeta < 1$) is underdamped such that the current oscillates while the energy dissipates from the coil.

2.2.4 Mutual inductance and coupling factor

According to Faraday's law of induction, a changing magnetic field is capable of inducing a voltage in a magnetically coupled loop or coil. More specifically, the voltage induced in the second coil ε_{21} by the current of the magnetic field of the first coil i_1 is equal to the change of the magnetic field flux that is enclosed by that receiving coil and opposite in sign. The enclosed flux is denoted as the coupled flux Ψ_{21}.

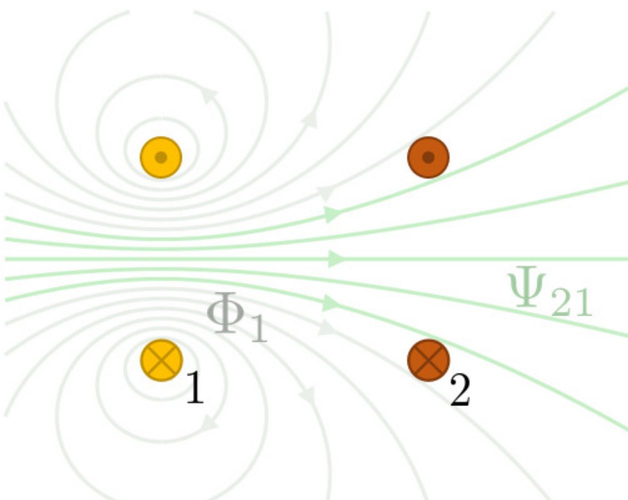

Figure 2.3: The coupled flux Ψ_{21} is the flux that is generated by the transmitter (coil 1) and enclosed by or coupled with the receiver (coil 2).

The magnetic flux generated by the first coil is proportional to the current in that coil. We can thus derive that the voltage induced in the second coil ε_{21} is also proportional to the rate of change of the current in the first coil $\frac{\mathrm{d}i_1}{\mathrm{d}t}$. The signs of the magnetic flux enclosed by the second coil and the current i_2 running through that coil follow the convention of the right hand rule. The induced voltage then has the same direction as the back EMF V_L in Figure 2.2. The ratio of the induced voltage in the second coil and the change of current in the first coil is denoted as the mutual inductance M_{21}.

$$\varepsilon_{21} = \frac{\mathrm{d}\Psi_{21}}{\mathrm{d}t} = M_{21}\frac{\mathrm{d}i_1}{\mathrm{d}t} \tag{2.6}$$

The mutual inductance is equal to the ratio of the coupled flux Ψ_{21} and the current that generated that flux i_1.

$$M_{21} = \frac{\Psi_{21}}{i_1} \tag{2.7}$$

The coupling factor k quantifies what percentage of the generated flux of one coil is magnetically coupled with or enclosed by the other coil. Inherently the coupling factor cannot be larger than one. The coupling factor is often said to be limited between 0 and 1 ($0 \leq k \leq 1$). However, if the reference of the coil currents is chosen in opposite directions or when the receiving coil is rotated 180 degrees such that it faces the other way, the induced voltage also switches sign. In this thesis we define that $-1 \leq k \leq 1$, which makes the derivations more rigorous. The k factor is directly related to the inductances in the circuit, namely the coupling factor is the ratio of the mutual inductance and the geometric mean of the self inductance values of the coils:

$$k_{12} = \frac{M_{12}}{\sqrt{L_1 L_2}} \tag{2.8}$$

2.2.5 Reflected impedance

We consider now a two coil system, where one coil is connected to an AC voltage source and the other coil is connected to a certain load impedance Z_L (Figure 2.4).

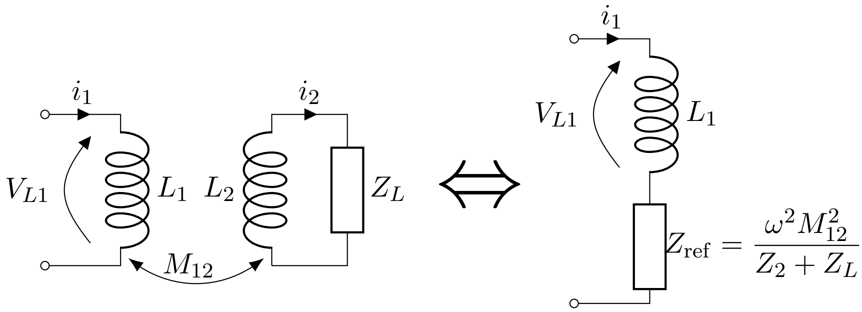

Figure 2.4: The interaction between the transmitter coil and the receiver coil can be translated to an equivalent reflected impedance in series with the transmitter coil.

We can construct the KVL in phasor representation for both coupled coils. We do not make any assumptions yet on the impedance of the receiver coil.

$$\begin{cases} V_s &= Z_1 I_1 + j\omega M_{12} I_2 \\ 0 &= Z_2 I_2 + Z_L I_2 + j\omega M_{12} I_1 \end{cases} \tag{2.9}$$

From the second equation of (2.9), we can write the current in the receiver coil as a function of the system parameters and the current in the transmitter coil:

$$I_2 = -\frac{j\omega M_{12}}{Z_2 + Z_L} I_1 \tag{2.10}$$

Substituting I_2 in the first equation of (2.9) returns:

$$V_s = Z_1 I_1 + \frac{\omega^2 M_{12}^2}{Z_2 + Z_L} I_1 \tag{2.11}$$

The magnetic coupling between the two coils makes it appear as if an additional impedance was connected in series with the transmitter coil. This virtual added impedance is called the reflected impedance. The power that is dissipated in the reflected impedance is equal to the power that would be dissipated in the second coil of the two coil system. Note that if the total receiver impedance $Z_2 + Z_L$ is inductive, the reflected impedance would be capacitive and vice versa.

2.2.6 Capacitors for reactance compensation

The KVL equation for the coil circuit can be written as

$$V_1 = R_1 I_1 + j\omega L_1 I_1 \tag{2.12}$$

The complex impedance of the coil is now equal to $Z_1 = R_1 + j\omega L_1$ and the current in the coil is inverse proportional to the amplitude of the impedance $|Z_1|$.

$$|I_1| = \frac{V_1}{|Z_1|} = \frac{V_1}{\sqrt{R_1^2 + \omega^2 L_1^2}} \tag{2.13}$$

Consequently, the current amplitude decreases for higher frequencies. To achieve higher currents for the same voltage, it would be beneficial to eliminate the inductive reactance ($X_{L1} = \omega L_1$) of the coil. This can be done by introducing a capacitor to the electrical circuit.

A capacitor generally consists of two conductive surfaces that are electrically isolated by a dielectric medium. When a current runs through the capacitor, an electric charge builds up on the conductive surfaces, a negative charge at one end and a positive charge on the other. Although current is said to pass through the capacitor, no electrons physically pass through the isolation layer. Instead, electrons build up on one side of the capacitor, while electrons are pulled away from the other side. This charge separation causes an electric potential or voltage that opposes the current through the capacitor. A dielectric isolation layer amplifies this opposing electric field. The capacitance (C) of a capacitor is defined as the amount of current that can pass through a capacitor until the opposing voltage increases by 1 volt.

$$v_C = \frac{1}{C}\int^t i_C \mathrm{d}t \tag{2.14}$$

Alternatively, the capacitance defines the change in voltage over time when a certain current runs through the capacitor.

$$\frac{\mathrm{d}v_C}{\mathrm{d}t} = \frac{1}{C} i_C \tag{2.15}$$

If we convert (2.15) to the phasor representation, it is clear that the opposing voltage V_C over the capacitor now lags the current I_C by $\frac{\pi}{2}$.

$$V_C = \frac{1}{j\omega C} I_C = -\frac{j}{\omega C} I_C = -jX_C I_C \tag{2.16}$$

The impedance ($-jX_C$) of the capacitor is opposite in sign compared to the inductor, such that we can use the capacitor to counteract the reactance of the inductor. Many different transmitter resonator topologies have been studied in literature, however, most topologies can be distilled to three basic implementations of resonators, namely the series compensated, parallel compensated and the 2 coil transmitter resonators.

2.2.7 Transmitter topologies

There are multiple ways to implement a capacitor in a circuit to compensate the reactance of an inductor in a transmitter coil. The most basic configurations are called the series and parallel compensation. The series and parallel configurations are most commonly used in 2 coil transmitter-receiver systems. Most resonant transmitter circuits can be reduced to a series or parallel compensated transmitter coil with an additional circuit which helps to stabilize the load that is seen by the power source. Examples of these topologies are the LCL [90,91], LCC [92], LLC [93] and LCLC [94] resonant converters. If both the transmitter and the receiver coil are series or parallel compensated, the transmitter-receiver system is called a 2 coil RWPT system. 4 coil transmitter-receiver topologies have also been explored in literature, for which both the transmitter and the receiver consist of 2 coils. One coil is then connected to the voltage source or the load directly, while a short-circuited resonator coil is placed nearby to amplify the local magnetic field.

Series compensated transmitter resonator

In a series compensated transmitter resonator, a capacitor is connected in series with the inductive coil. The impedance of the series connection of a coil L_1 and a capacitor C_1 equals

$$Z_{\text{tot}} = R_1 + j\omega L_1 + \frac{1}{j\omega C_1} = R_1 + j\left(\omega L_1 - \frac{1}{\omega C_1}\right) \tag{2.17}$$

When the capacitor fully compensates the inductance of the coil, the circuit's impedance equals the resistance of the coil. For this situation, the current is in phase with the voltage over the circuit and the current reaches its maximum amplitude. The coil is said to be in resonance.

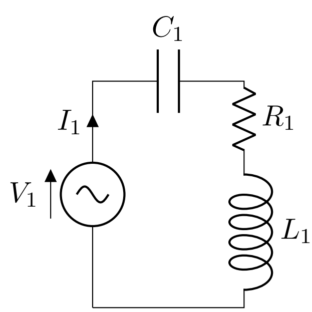

Figure 2.5: In a series compensated transmitter resonator, a capacitor is connected in series with the inductive coil.

The reactance of the inductor scales linearly with the frequency ($X_L = \omega L$), while the reactance of the capacitor is inversely proportional to the frequency $\left(X_C = \dfrac{1}{\omega C}\right)$, such that there is always a frequency for which the reactance of the circuit is zero ($\mathrm{Im}(Z_{\mathrm{tot}}) = 0$). The frequency for which the reactance of a coil is compensated is called the resonance frequency ω_0. The resonance frequency of the series connection of L_1 and C_1 is denoted by ω_{01}.

$$\omega_{01} = \frac{1}{\sqrt{L_1 C_1}} \text{ and } C_1^* = \frac{1}{\omega_{01}^2 L_1} \tag{2.18}$$

If the coil is magnetically coupled with a load, a virtual reflected impedance is connected in series with the inductor. The total transmitter impedance then equals

$$Z_{\mathrm{tot}} = R_1 + j\omega L_1 + \frac{1}{j\omega C_1} + Z_{\mathrm{ref}} = R_1 + Z_{\mathrm{ref}} \tag{2.19}$$

Parallel compensated transmitter resonator

The coil inductance can also be compensated by connecting a capacitor in parallel with the coil. The total transmitter impedance is then

$$Z_{\mathrm{tot}} = \frac{1}{j\omega C_1 + \dfrac{1}{j\omega L_1 + R_1}} \tag{2.20}$$

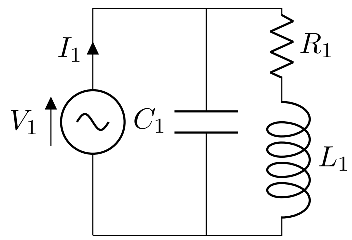

Figure 2.6: In a parallel compensated transmitter resonator, a capacitor is connected in parallel with the inductive coil.

By solving for the resonance condition $\mathrm{Im}(Z_{\mathrm{tot}}) = 0$, the capacitor value can be found by the expression

$$C_1^* = \frac{L_1}{\omega^2 L_1^2 + R_1^2} \tag{2.21}$$

Equivalently, the resonance frequency is expressed as

$$\omega_{01} = \sqrt{\frac{1}{L_1 C_1} - \frac{R_1^2}{L_1^2}} \tag{2.22}$$

For high Q factors, the resonance frequency can be accurately approximated as

$$\omega_{01} \approx \frac{1}{\sqrt{L_1 C_1}} \tag{2.23}$$

If we assume a resistive reflected impedance, then

$$C_1^* = \frac{L_1}{\omega^2 L_1^2 + (Z_{\mathrm{ref}} + R_1)^2} \tag{2.24}$$

and

$$Z_{\mathrm{tot}} = \frac{1}{j\omega C_1^* + \dfrac{1}{j\omega L_1 + R_1 + Z_{\mathrm{ref}}}} = R_1 + Z_{\mathrm{ref}} + \frac{\omega^2 L_1^2}{R_1 + Z_{\mathrm{ref}}} \tag{2.25}$$

Comparison between series and parallel compensated transmitter resonators

The series and parallel compensation methods are used to maximize the current in the coil, while eliminating the reactance of the coil. The series and parallel compensation methods have very different effects on the source load impedance and the current that is drawn from the source. In Section 2.2.3, it was explained that the resistance of an inductor coil highly affects the dynamic behavior of the current through that coil. Coils with a high Q factor cause underdamped current oscillations such that high AC currents can be generated in the resonator. For a series compensated transmitter resonator with a high Q factor, the total load impedance (Z_{tot}) approaches zero, while for a parallel compensated coil, the total load impedance approaches infinity. Figures 2.7 and 2.8 qualitatively compare the load impedance Z_{tot} and the source current I_{tot} for frequencies around the resonance frequency of the resonator ω_0 for increasing Q factors.

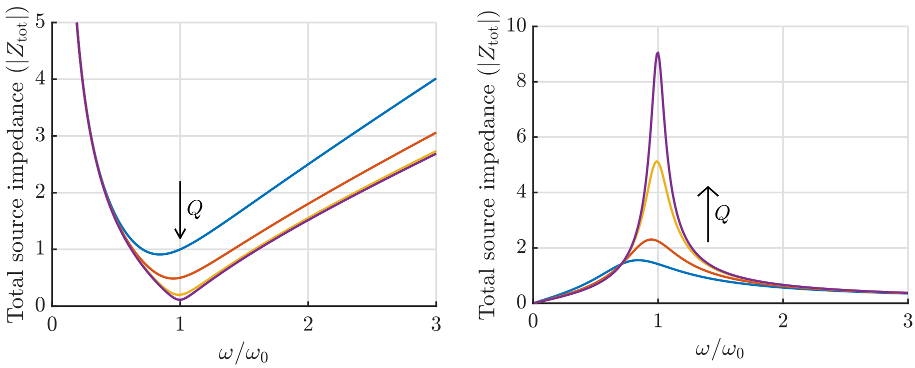

(a) **(b)**

Figure 2.7: Close to the resonance frequency of the resonator, the series compensation (a) results in a minimization of the load impedance Z_{tot}, while the parallel compensation (b) maximizes the load impedance.

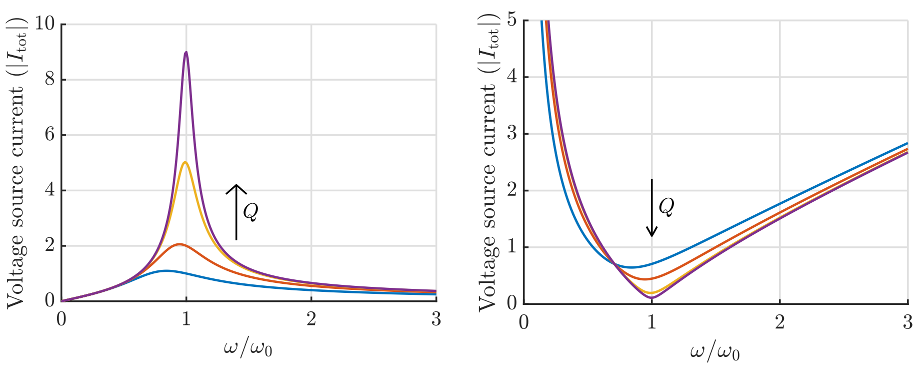

(a) **(b)**

Figure 2.8: Close to the resonance frequency of the resonator, the series compensation (a) results in a maximization of the load current I_{tot}, while the parallel compensation (b) minimizes the load current.

The load impedance of the series compensated coil shows a strong resemblance to the load current of the parallel compensated coil and vice versa. As the impedance and the load current are inverse proportional ($|I_{\mathrm{tot}}| \propto 1/|Z_{\mathrm{tot}}|$), we can conclude that the series and parallel compensation have inverse effects on the load impedance and current.

Both the transmitter and the receiver resonators can be compensated in series or parallel. Consequently, there are four possible topologies for 2 coil

RWPT systems, namely series-series (SS), series-parallel (SP), parallel-series (PS) and parallel-parallel (PP). Table 2.1 compares the characteristics of all four topologies. The equivalent series resistances (ESR) of the inductors are neglected. The excitation frequency is chosen to match the resonance frequency of the receiver coil and the load R_L is resistive.

$$\omega_0 = \omega_{02} = \frac{1}{L_2 C_2} \tag{2.26}$$

The reflected impedance to the transmitter coil is real-valued for series compensated receivers. For parallel compensated coils, the reflected impedance is partly capacitive. The value of C_1 is chosen such that the total transmitter load is real-valued. Only for the SS topology, capacitance value C_1 is not affected by the coupling with the receiver coil. The definition of the quality factor of the receiver changes when its compensating capacitor is connected in parallel with the load.

Table 2.1: The reflected impedance, Q factor and optimal primary capacitance are dependent on the topology of the 2 coil RWPT system.

Topology	$\mathbf{Re}(\boldsymbol{Z}_{\mathbf{ref}})$	$\mathbf{Im}(\boldsymbol{Z}_{\mathbf{ref}})$	$\boldsymbol{C_1}$	$\boldsymbol{Q_2}$
SS	$\frac{\omega_0^2 M_{12}^2}{R_L}$	0	$\frac{1}{\omega_0^2 L_1}$	$\frac{\omega_0 L_2}{R_L}$
SP	$\frac{M_{12}^2 R_L}{L_2^2}$	$-\frac{\omega_0 M_{12}}{L_2}$	$\frac{1}{\omega_0^2 \left(L_1 - \frac{M_{12}^2}{L_2}\right)}$	$\frac{R_L}{\omega_0 L_2}$
PS	$\frac{\omega_0^2 M_{12}^2}{R_L}$	0	$\frac{L_1}{\left(\frac{\omega_0^2 M_{12}^2}{R_L}\right)^2 + \omega_0^2 L_1^2}$	$\frac{\omega_0 L_2}{R_L}$
PP	$\frac{M_{12}^2 R_L}{L_2^2}$	$-\frac{\omega_0 M_{12}}{L_2}$	$\frac{L_1 - \frac{M_{12}^2}{L_2}}{\left(\frac{M_{12}^2 R_L}{L_2^2}\right)^2 + \omega_0^2 \left(L_1 - \frac{M_{12}^2}{L_2}\right)^2}$	$\frac{R_L}{\omega_0 L_2}$

For both the series and parallel compensated receiver resonator, the real part of the reflected impedance can be written as:

$$\mathrm{Re}(Z_{\mathrm{ref}}) = k_{12}^2 \omega_0 L_1 Q_2 \tag{2.27}$$

At the transmitter side, the reflected impedance is in series with the transmitter coil. The efficiency of the power transfer η is equal to the percentage of the active power that is dissipated in the reflected impedance and not in the resistance of the transmitter coil:

$$\eta = \frac{\mathrm{Re}(Z_{\mathrm{ref}})}{\mathrm{Re}(Z_{\mathrm{ref}}) + R_1} = \frac{k_{12}^2 Q_1 Q_2}{k_{12}^2 Q_1 Q_2 + 1} = \frac{U_{12}^2}{U_{12}^2 + 1} \tag{2.28}$$

The kQ factor ($k_{12}\sqrt{Q_1Q_2}$) is a dimensionless figure of merit which is often used to describe the efficacy of a WPT design. The kQ factor is often denoted as U. For two coupled coils, indicated by subscripts 1 and 2, then holds:

$$U_{12}^2 = k_{12}^2 Q_1 Q_2 = \frac{k_{12}^2 \omega^2 L_1 L_2}{R_1 R_2} = \frac{\omega^2 M_{12}^2}{R_1 R_2} \tag{2.29}$$

While the Q factor describes the ratio of the maximum energy stored in the total magnetic field Φ of a coil and the energy dissipated in the conductor of the coil, the kQ factor is the ratio of the energy stored in the coupled flux between two coils Ψ_{12} devided by the geometric mean of the dissipation in either coil.

2 coil transmitter resonator

The 2 coil resonator forms the basis of the 4 coil WPT system. 3 coil systems with a 2 coil transmitter resonators are also investigated in literature. In a 2 coil transmitter, a coil with a limited amount of turns (often only one) is connected to an AC voltage source. A short-circuited series compensated resonator coil with multiple turns is placed in very close proximity to the first coil.

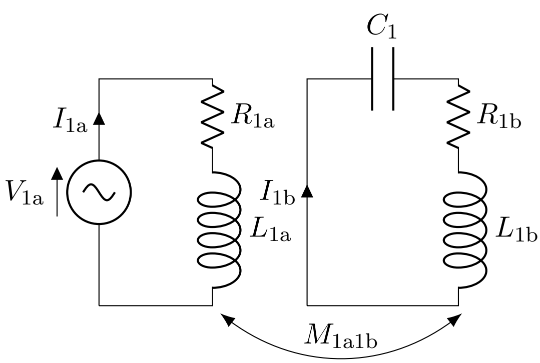

Figure 2.9: The 2 coil transmitter consists of one coil directly connected to a voltage source and a closely coupled short-circuited resonator coil.

A 2 coil transmitter or receiver is often considered when the resonator coil is an open coil for which the parasitic capacitance between the windings is used instead of a discrete capacitor [20]. Parasitic capacitances in air coils are very low, such that this approach is only feasible for large coils and high frequencies. The single loop coil and the resonator coil are denoted by subscripts $1a$ and $1b$ respectively.

We assume that the driving frequency matches the resonance frequency of the resonator coil ($\omega = \omega_0$). The KVL for the strongly magnetically coupled ($0 \ll k_{\mathrm{1a1b}} < 1$) coils can be written as

$$\begin{cases} V_{\mathrm{1a}} & = (R_{\mathrm{1a}} + jX_{\mathrm{L1a}})I_{\mathrm{1a}} + j\omega M_{\mathrm{1a1b}} I_{\mathrm{1b}} \\ 0 & = R_{\mathrm{1b}} I_{\mathrm{1b}} + j\omega M_{\mathrm{1a1b}} I_{\mathrm{1a}} \end{cases} \tag{2.30}$$

From the second equation of (2.30), the current in the resonator coil can be expressed as

$$I_{\mathrm{1b}} = -\frac{j\omega M_{\mathrm{1a1b}}}{R_{\mathrm{1b}}} I_{\mathrm{1a}} \tag{2.31}$$

and the resonator resistance is reflected to the loop coil.

$$V_{\mathrm{1a}} = \left(R_{\mathrm{1a}} + jX_{\mathrm{L1a}} + \frac{\omega^2 M_{\mathrm{1a1b}}^2}{R_{\mathrm{1b}}} \right) I_{\mathrm{1a}} \tag{2.32}$$

We now assume that R_{1b} is small enough so that we can neglect $R_{\mathrm{1a}} + jX_{\mathrm{L1a}}$, such that

$$V_{\mathrm{1a}} \approx \frac{\omega^2 M_{\mathrm{1a1b}}^2}{R_{\mathrm{1b}}} I_{\mathrm{1a}} = R_{\mathrm{1eq}} I_{\mathrm{1a}} \tag{2.33}$$

In a 2 coil resonator system, the current in the resonator is significantly higher compared to the loop coil, while the resonator coil usually has a relatively large amount of windings. Because of these reasons, the magnetic field of the loop coil can be neglected compared to the magnetic field generated by the resonator coil. It can be useful to link the excitation voltage V_{1a} directly to the resonator current as if the complete circuit only consists of one electrical loop. From (2.30) and (2.31), the excitation voltage can be written in terms of the resonator current and the system parameters:

$$V_{\mathrm{1a}} = (R_{\mathrm{1a}} + jX_{\mathrm{L1a}}) \frac{jR_{\mathrm{1b}}}{\omega M_{\mathrm{1a1b}}} I_{\mathrm{1b}} + j\omega M_{\mathrm{1a1b}} I_{\mathrm{1b}} \tag{2.34}$$

$$V_{\mathrm{1a}} = \left(\frac{jR_{\mathrm{1a}} R_{\mathrm{1b}}}{\omega M_{\mathrm{1a1b}}} - R_{\mathrm{1b}} \frac{L}{M_{\mathrm{1a1b}}} + j\omega M_{\mathrm{1a1b}} \right) I_{\mathrm{1b}} \tag{2.35}$$

Based on (2.33) and (2.31) we can approximate V_{1a} by:

$$V_{\mathrm{1a}} \approx \frac{\omega^2 M_{\mathrm{1a1b}}^2}{R_{\mathrm{1b}}} I_{\mathrm{1a}} = j\omega M_{\mathrm{1a1b}} I_{\mathrm{1b}} \tag{2.36}$$

The fictitious impedance that connects V_{1a} and I_{1b} is now an inductive load with impedance $j\omega M_{\mathrm{1a1b}}$ (see Figure 2.10). This observation is in line with the expectation that the current in a receiving resonator lags the voltage inducing current by $\frac{\pi}{2}$. The inductive load scales with the coupling factor k_{1a1b} and the geometric mean of the coil inductances ($M_{\mathrm{1a1b}} = k_{\mathrm{1a1b}} \sqrt{L_{\mathrm{1a}} L_{\mathrm{1b}}}$).

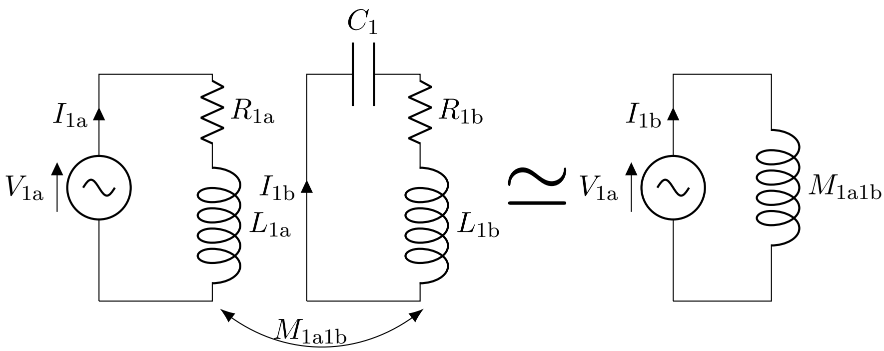

Figure 2.10: The current that is generated in the resonator of the 2 coil transmitter can be approximated by calculating the current of a fictitious inductive load equal to the mutual inductance between the loop and the resonator.

2.3 Electromechanical coil-coil interactions

2.3.1 Magnetic field of air coils

In order to design an RWPT system, it is important to understand the magnetic field generation of coils and the electrical (induced voltages) and physical (forces and torques) interaction between current carrying coils.

Circular filament coils

The field around a compactly wound coil can be closely approximated by a circular filament coil with radius a, shown in Figure 2.11.

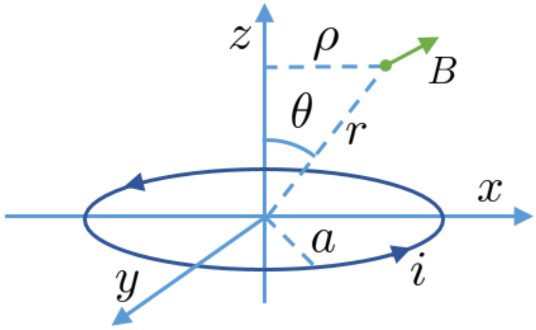

Figure 2.11: A compactly wound coil can be approximated by a circular filament coil with radius a.

For a straight conductor, the magnetic field is easily derived using Biot-Savart's law. Biot-Savart's law always satisfies the magnetostatic versions of Ampere's circuital law (1.4) and Gauss's law for magnetism (1.6). For circular conductors however it is easier to express the magnetic field vector **B** as the curl of its magnetic vector potential **A** [95, 96].

$$\mathbf{B} = \nabla \times \mathbf{A} \tag{2.37}$$

In spherical coordinates (r, θ_s, ϕ), the vector potential can be expressed as:

$$\mathbf{A}_\phi(r, \theta_s) = \frac{\mu_0 a i}{4\pi} \int_0^{2\pi} \frac{\cos\phi' d\phi'}{\sqrt{a^2 + r^2 - 2ar\sin\theta_s \cos\phi'}} \tag{2.38}$$

The subscript ϕ indicates that the vector potential is azimuthally symmetric and **A** points in the tangential direction. The integral can be rearranged into complete elliptical integrals of the first (K) and second (E) kind

$$\begin{cases} K(\kappa_B) & = \int_0^{\frac{\pi}{2}} \frac{1}{\sqrt{1 - \kappa_B^2 \sin^2(\lambda)}} \mathrm{d}\lambda \\ E(\kappa_B) & = \int_0^{\frac{\pi}{2}} \sqrt{1 - \kappa_B^2 \sin^2(\lambda)} \mathrm{d}\lambda \end{cases} \tag{2.39}$$

such that **A** can be simplified to

$$\mathbf{A}_\phi(r, \theta_s) = \frac{\mu_0}{4\pi} \frac{4ia}{\sqrt{a^2 + r^2 + 2ar\sin\theta_s}} \left[\frac{(2 - \kappa_B^2)K(\kappa_B) - 2E(\kappa_B)}{\kappa_B^2} \right] \tag{2.40}$$

with

$$\kappa_B^2 = \frac{4ar\sin\theta_s}{a^2 + r^2 + 2ar\sin\theta_s} \tag{2.41}$$

Elliptical integrals can be efficiently evaluated, as they are often hardcoded in softwarepackages such as MATLAB. In cylindrical coordinates (ρ, z, ϕ), (2.40) can be rewritten as:

$$\mathbf{A}_\phi(\rho, z) = \frac{\mu_0}{4\pi} \frac{4ia}{\sqrt{a^2 + \rho^2 + z^2 + 2a\rho}} \left[\frac{(2 - \kappa_B^2)K(\kappa_B) - 2E(\kappa_B)}{\kappa_B^2} \right] \tag{2.42}$$

The curl of (2.40) can be expressed in cylindrical coordinates (2.43) or in Cartesian coordinates (2.44) as follows:

$$\begin{cases} B_\rho(\rho,z) &= \dfrac{\mu_0 iz}{2\pi\alpha^2\beta\rho}\left[(a^2+r^2)E(\kappa_B)-\alpha^2K(\kappa_B)\right] \\ B_z(\rho,z) &= \dfrac{\mu_0 i}{2\pi\alpha^2\beta}\left[(a^2-r^2)E(\kappa_B)+\alpha^2K(\kappa_B)\right] \end{cases} \tag{2.43}$$

$$\begin{cases} B_x(x,y,z) = \dfrac{\mu_0 ixz}{2\pi\alpha^2\beta\rho^2}\left[(a^2+r^2)E(\kappa_B)-\alpha^2K(\kappa_B)\right] \\ B_y(x,y,z) = \dfrac{\mu_0 iyz}{2\pi\alpha^2\beta\rho^2}\left[(a^2+r^2)E(\kappa_B)-\alpha^2K(\kappa_B)\right] \\ B_z(x,y,z) = \dfrac{\mu_0 i}{2\pi\alpha^2\beta}\left[(a^2-r^2)E(\kappa_B)+\alpha^2K(\kappa_B)\right] \end{cases} \tag{2.44}$$

with

$$\begin{cases} \alpha^2 &= a^2+r^2-2a\rho = a^2+r^2-2a\sqrt{x^2+y^2} \\ \beta^2 &= a^2+r^2+2a\rho = a^2+r^2+2a\sqrt{x^2+y^2} \\ \kappa_B^2 &= 1-\dfrac{\alpha^2}{\beta^2} \end{cases} \tag{2.45}$$

Along the axis of the loop, the magnetic field equals

$$B_z(x,y,z) = \frac{\mu_0 ia^2}{2(a^2+z^2)^{3/2}} \tag{2.46}$$

The derivatives of the elliptic integrals are linear functions of the same elliptic integrals:

$$\begin{cases} \dfrac{dK(\kappa_B)}{d\kappa_B} &= \dfrac{E(\kappa_B)}{\kappa_B(1-\kappa_B^2)}-\dfrac{K(\kappa_B)}{\kappa_B} \\ \dfrac{dE(\kappa_B)}{d\kappa_B} &= \dfrac{E(\kappa_B)-K(\kappa_B)}{\kappa_B} \end{cases} \tag{2.47}$$

Similar to the magnetic field **B**, the spatial derivatives of the magnetic field ∇**B** can thus also be expressed as the sum of integrals of the first and second kind [95,96].

Magnetic dipoles

For distances far away from the center of the coil ($r \gg a$), the magnetic field of a coil can be approximated by that of a magnetic dipole at the location of the center of the coil ($r = 0$). A dipole is the limit case of a shrinking coil with a constant magnetic moment m. The magnetic moment of a current loop is the product of the current in the conductor of the loop (i) and the area enclosed by the loop (S) and is oriented in the normal direction of the surface:

$$\mathbf{m} = i\mathbf{S} \tag{2.48}$$

The normal of area S is oriented according to the right hand rule for the current through the conductor. To find the limit case of the shrinking coil, the radius of the coil decreases, while the current in the coil increases inverse proportional to the square of the radius of the coil. The vector potential $\mathbf{A}$ for a dipole can be expressed as

$$\mathbf{A}(\mathbf{r}) = \frac{\mu_0}{4\pi}\frac{\mathbf{m}\times\mathbf{r}}{r^3} \tag{2.49}$$

The magnetic field is equal to the curl of the vector potential

$$\begin{aligned}\mathbf{B}(\mathbf{r}) = \nabla\times\mathbf{A} &= \frac{\mu_0}{4\pi}\left[\frac{3\mathbf{r}(\mathbf{m}\cdot\mathbf{r})}{r^5} - \frac{\mathbf{m}}{r^3}\right] \\ &= \frac{\mu_0}{4\pi}\left[\frac{3\cdot\mathbf{1}_\mathrm{r}(\mathbf{m}\cdot\mathbf{1}_\mathrm{r}) - \mathbf{m}}{r^3}\right]\end{aligned} \tag{2.50}$$

In the second line of (2.50), $\mathbf{1}_\mathrm{r}$ is the unit vector in the direction from the dipole to the position $\mathbf{r}$. Figure 2.12 compares the magnetic field of a dipole (a) to the field of a circular filament coil (b) with the same magnetic moment.

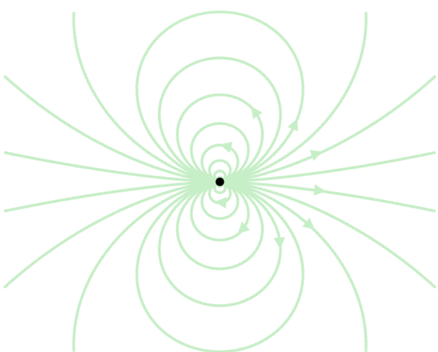

(a)

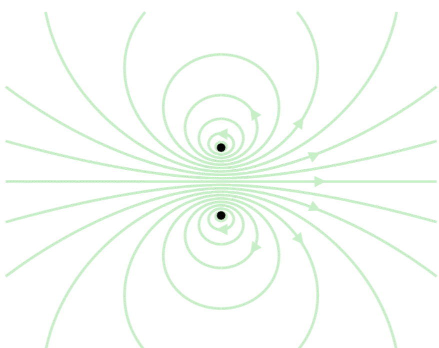

(b)

Figure 2.12: From a distance ($r \gg a$), the magnetic field of a dipole (a) closely approximates the magnetic field of a circular coil (b) with the same magnetic moment m.

Finite length straight conductors

Coils are often wound in rectangular shapes, e.g., in closely packed arrays of resonators. A rectangular coil is made up of several straight conductors, such that the magnetic field of a rectangular coil can be derived by summing the magnetic field contributions of the individual straight conductor sections. The magnetic field of a finite straight conductor (placed along the z-axis) is easily derived from Biot-Savart's law:

$$B_\phi = \frac{\mu_0 i}{4\pi\rho}(\cos\theta_1 + \cos\theta_2) \tag{2.51}$$

with θ_1 and θ_2 the angle between the wire and the imaginary lines connecting the endpoints of the wire with the position for which we want to find the magnetic field (see Figure 2.13). The tangential direction of the magnetic field then follows the right hand rule.

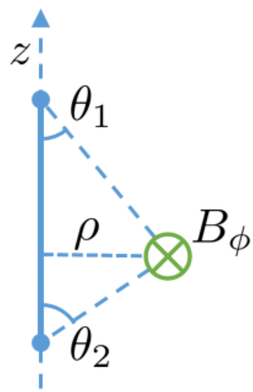

Figure 2.13: The magnetic field of a straight conductor with finite length.

2.3.2 Mutual induction between air coils

The electrical interaction between coupled air coils strongly depends on their geometries and their reciprocal positions. In this section, some basic expressions are listed for calculating the mutual inductance between coils.

Circular filament coils

The mutual induction between two coils is defined as the ratio of the coupled flux Ψ_{21} and the current that generated the flux i_1.

$$M_{21} = \frac{\Psi_{21}}{i_1} \tag{2.52}$$

The coupled flux Ψ_{21} is the part of the flux generated by current i_1 that passes through the surface that is enclosed by the second coil. In (2.37) **B** was defined as the curl of **A**. The Kelvin-Stokes theorem states that the line integral of a vector potential over a closed loop is equal to the surface integral of the normal component of the curl of that vector potential, such that:

$$\Psi = \iint_S \mathbf{B} \cdot \mathrm{d}\mathbf{S} = \iint_S \nabla \times \mathbf{A} \cdot \mathrm{d}\mathbf{S} = \oint_l \mathbf{A} \cdot \mathrm{d}\mathbf{l} \tag{2.53}$$

Generally it is much easier to evaluate a line integral of the magnetic vector potential **A** compared to a surface integral of the normal component of the magnetic vector field **B**. Kim et al. [97] used the magnetic vector potential to obtain expressions for the mutual induction between two misaligned coils. Grover et al. [98] originally used the direct Neumann integral approach (2.54) to derive the same formulas.

$$M_{12} = \frac{\mu_0}{4\pi} \oint_{l_1} \oint_{l_2} \frac{\mathrm{d}\mathbf{l}_1 \cdot \mathrm{d}\mathbf{l}_2}{r} \tag{2.54}$$

Babic et al. [99, 100] retrieved Grover's formula using the same method that Kim used. The general formula for the mutual inductance between two filament coils can be calculated by evaluating the following integral:

$$\begin{aligned} M &= \frac{2\mu_0}{\pi}\sqrt{a_1 a_2} \int_0^{\pi} \frac{[\cos\theta - \frac{d}{a_2}\cos\lambda]\Psi_M(\kappa_M)}{\kappa_M \sqrt{\gamma_M^3}} \mathrm{d}\lambda \\ &= \frac{2\mu_0}{\pi}\sqrt{a_1 a_2} \int_0^{\pi} \frac{f_1}{g_1} \mathrm{d}\lambda \end{aligned} \tag{2.55}$$

with

$$\begin{cases} \kappa_M^2 = \dfrac{4\alpha\gamma_M}{(1+\alpha\gamma_M)^2 + \xi_M^2} = \dfrac{f_2}{g_2} \\ \alpha_M = \dfrac{a_2}{a_1} \\ \beta_M = \dfrac{c}{a_1} \\ \gamma_M = \sqrt{1 - \cos^2(\lambda)\sin^2(\theta) - 2\dfrac{d}{a_2}\cos(\lambda)\cos(\theta) + \dfrac{d^2}{a_2^2}} \\ \xi_M = \beta_M - \alpha_M \cos(\phi)\sin(\theta) \\ \Psi_M(\kappa_M) = \left(1 - \frac{\kappa_M^2}{2}\right) K(\kappa_M) - E(\kappa_M) \end{cases} \tag{2.56}$$

Equation (2.55) describes the mutual inductance between two filamentary coils for which the second coil can be misaligned with 3 degrees of freedom (DOF), namely by an offset between the centers of the coils along the z-axis of the first coil (c), a radial misalignment between the center of the second coil and the z-axis of the first coil (d) and a rotation angle between the axes of both coils (θ), illustrated in Figure 2.14.

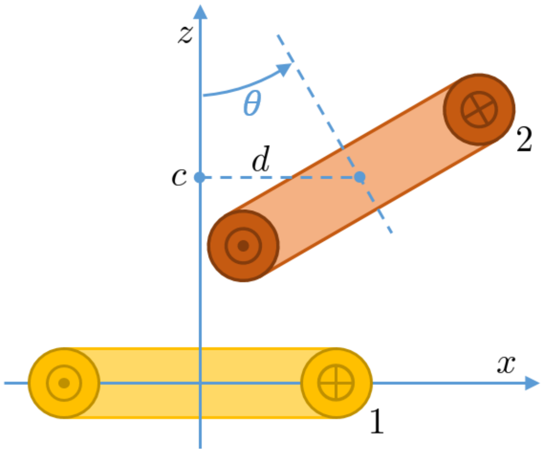

Figure 2.14: The relative position between two coils is described by 3 parameters (c, d, θ), corresponding to the degrees of freedom.

Note that both coil axes still intersect, such that one degree of freedom is not considered in the expression for the mutual inductance. In [99] Babic et al. also included this last DOF in a more general expression for the mutual inductance between inclined circular filaments arbitrarily positioned with respect to each other. The derivation is based on the vector potential and only requires sequential evaluation of terms, contrary to expressions that Grover obtained.

Magnetic dipoles

In WPT applications, the transmitter and receiver coils are often spaced far away from each other (i.e., the spacing between both coils is equal or larger than the diameters of both coils) such that one or all of the coils can be approximated by magnetic dipoles. When one of the coils can be approximated by magnetic dipoles, the mutual inductance between them is easily derived. We can assume that the magnetic field that is generated by the first coil and enclosed by the second (dipole) coil is locally uniform in both amplitude and direction. The coupled flux and the mutual inductance can then be approximated as

$$\Psi_{21} = n \iint_{S_2} \mathbf{B}_1 \cdot \mathrm{d}\mathbf{S} = n\mathbf{B}_1(\mathbf{r}_2) \cdot \mathbf{S}_2 \tag{2.57}$$

with n the amount of turns in the coil and

$$M_{21} = n\frac{\mathbf{B}_1(\mathbf{r}_2)}{i_1} \cdot \mathbf{S}_2 \tag{2.58}$$

$\mathbf{B}_1(\mathbf{r}_2)$ is the magnetic field of the filamentary coil in the reference frame of the coil and $\mathbf{r}_2$ is the relative position of the dipole in that reference frame. If both coils can be approximated by dipoles, the mutual inductance is

$$M_{21} = \frac{n\mu_0}{4\pi i_1}\left[\frac{3 \cdot \mathbf{1}_\mathrm{r}(\mathbf{m}_1 \cdot \mathbf{1}_\mathrm{r}) - \mathbf{m}_1}{r_2^3}\right] \cdot \mathbf{S}_2 \tag{2.59}$$

Finite length straight conductors

To know the mutual inductance between two coils for which the conductors consist of series connections of straight conductors, the easiest method is to use Neumann's formula:

$$M_{12} = \sum_{i=1}^{n_1}\sum_{j=1}^{n_2}\frac{\mu_0}{4\pi}\int_{l_{1i}}\int_{l_{2j}}\frac{\mathrm{d}\mathbf{l}_1 \cdot \mathrm{d}\mathbf{l}_2}{r} \tag{2.60}$$

Note that the directions of $\mathrm{d}\mathbf{l}_1$ and $\mathrm{d}\mathbf{l}_2$ are constant for these straight line segments, which simplifies the evaluation of the double integral.

2.3.3 Forces and torques on air coils

Forces on coils in (quasi) uniform fields

The translational force on a magnetic dipole is expressed by the dot product of the magnetic moment of the dipole and the gradient of the magnetic field:

$$\mathbf{F}_\mathrm{dip} = \nabla(\mathbf{m} \cdot \mathbf{B}) \tag{2.61}$$

Forces are reciprocal, such that (2.61) can be used to calculate the force between a dipole and any component that generates a magnetic field, as long as that generated field is known at the location of the dipole. The torque on the dipole in a magnetic field B (Figure 2.15(a)) can be written as the cross product of its magnetic moment and the local magnetic field.

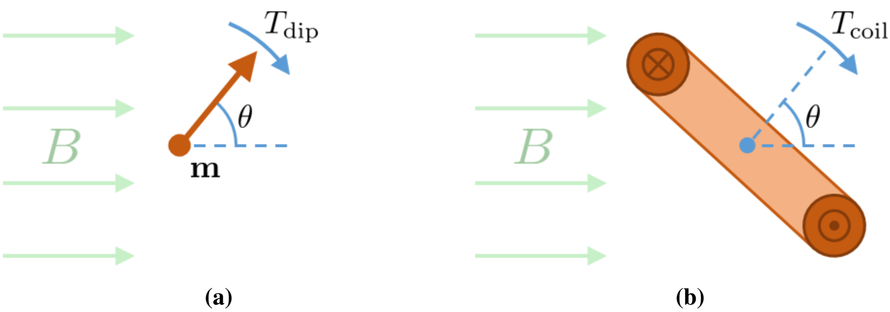

Figure 2.15: When a coil can be approximated by a dipole (a) or the external magnetic field is (quasi) uniform near the coil (b), the torque can be calculated as the cross product of the magnetic moment of the coil **m** and the external magnetic field **B**.

The torque vector is then pointed in the normal direction of the plane.

$$T_{\text{dip}} = \mathbf{m} \times \mathbf{B} \tag{2.62}$$

For a loop in a (quasi) uniform field, the torque is also expressed by (2.62), with its magnetic moment $\mathbf{m} = ni\mathbf{S}$:

$$T_{\text{coil}} = ni\mathbf{S} \times \mathbf{B} \tag{2.63}$$

Torque on a coil near a dipole

We now consider a dipole for which its magnetic moment vector lies on the xz plane of the coil.

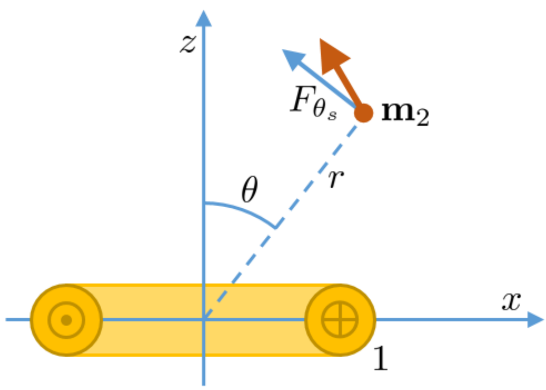

Figure 2.16: The torque on coil 1 equals the force on the dipole $\mathbf{m}_2$ in the tangential direction (F_{θ_s}) times the distance between the dipole and the center of the coil (r).

The coil rotates in the plane, around its y axis. The torque on the coil can be found by multiplying distance to the dipole by the tangential force on the dipole. The translational force in the xz plane on a dipole is expressed as $F_{\mathrm{xz}} = \nabla_{\mathrm{xz}}(\mathbf{m} \cdot \mathbf{B})$ with

$$\nabla_{\mathrm{xz}} \cdot \mathbf{B} = \begin{bmatrix} \frac{\mathrm{d}B_x}{\mathrm{d}x} & \frac{\mathrm{d}B_x}{\mathrm{d}z} \\ \frac{\mathrm{d}B_z}{\mathrm{d}x} & \frac{\mathrm{d}B_z}{\mathrm{d}z} \end{bmatrix} \tag{2.64}$$

the Jacobian of the x and z components of $\mathbf{B}$ (2.44) are

$$\begin{cases} \frac{\mathrm{d}B_x}{\mathrm{d}x} = \frac{\mu_0 i z}{2\pi\alpha^4\beta^3x^4} \{[a^4(-\gamma(3z^2+a^2)+8\rho^2x^2) \\ \qquad -a^2(5\rho^4x^2-4\rho^2z^2x^2+3z^4\gamma)-r^4(2x^4+\gamma z^2)]E(\kappa) \\ \qquad + \left[a^2(\gamma(a^2+2z^2)-3\rho^2x^2)+r^2(2x^4+\gamma z^2)\right]\alpha^2K(\kappa)\} \\ \frac{\mathrm{d}B_x}{\mathrm{d}z} = \frac{\mathrm{d}B_z}{\mathrm{d}x} = \frac{\mu_0 i}{2\pi\alpha^4\beta^3x} \{[(x^2-a^2)^2(x^2+a^2) \\ \qquad +2z^2(a^4-6a^2x^2+x^4)+z^4(a^2+x^2)]E(\kappa) \\ \qquad - \left[(x^2-a^2)^2+z^2(x^2+a^2)\right]\alpha^2K(\kappa)\} \\ \frac{\mathrm{d}B_z}{\mathrm{d}z} = \frac{\mu_0 i z}{2\pi\alpha^4\beta^3} \{\left[6a^2(x^2-z^2)-7a^4+r^4\right]E(\kappa)+\left[a^2-r^2\right]\alpha^2K(\kappa)\} \end{cases} \tag{2.65}$$

such that

$$F_{\mathrm{xz}} = \left[m_x\frac{\mathrm{d}B_x}{\mathrm{d}x} + m_y\frac{\mathrm{d}B_z}{\mathrm{d}x}, m_x\frac{\mathrm{d}B_x}{\mathrm{d}z} + m_y\frac{\mathrm{d}B_z}{\mathrm{d}z}\right] \tag{2.66}$$

To calculate the torque on the loop, we are interested in the tangential force F_{θ_s}, which is found by projecting the force F_{xz} on the tangential unit vector $\mathbf{1}_{\theta_s} = [-z, x]/r$:

$$F_{\theta_s} = \mathbf{1}_{\theta_s} \cdot F_{\mathrm{xz}}^{\mathrm{T}} = \frac{[-z, x]}{r} \cdot F_{\mathrm{xz}}^{\mathrm{T}} \tag{2.67}$$

The torque on the loop is then equal to this tangential force times the distance between the dipole and the center of the coil:

$$\begin{aligned} T &= r\mathbf{1}_{\theta_s} \cdot F_{\mathrm{xz}}^{\mathrm{T}} = [-z, x] \cdot F_{\mathrm{xz}}^{\mathrm{T}} \\ &= x\left(m_x\frac{\mathrm{d}B_x}{\mathrm{d}z} + m_y\frac{\mathrm{d}B_z}{\mathrm{d}z}\right) - z\left(m_x\frac{\mathrm{d}B_x}{\mathrm{d}x} + m_y\frac{\mathrm{d}B_z}{\mathrm{d}x}\right) \end{aligned} \tag{2.68}$$

Forces and torques between coils

The force between two magnetically coupled filament coils can be expressed as

$$\mathbf{F} = \nabla M_{12} i_1 i_2 = \left[\frac{\mathrm{d}M_{12}}{\mathrm{d}x}, \frac{\mathrm{d}M_{12}}{\mathrm{d}y}, \frac{\mathrm{d}M_{12}}{\mathrm{d}z}\right] i_1 i_2 \tag{2.69}$$

while the torque between the coils is:

$$T = \frac{\mathrm{d}M_{12}}{\mathrm{d}\theta} i_1 i_2 \tag{2.70}$$

To find the torque on the second coil, we need to calculate the spatial derivative of the mutual inductance M_{12}. The spatial derivative of the expression for the mutual inductance (2.55) can again be found by evaluating an integral:

$$\frac{\mathrm{d}M_{12}}{\mathrm{d}\theta} = \frac{2\mu_0}{\pi}\sqrt{a_1 a_2}\int_0^\pi \frac{f_1' g_1 - g_1' f_1}{g_1^2}\mathrm{d}\lambda \tag{2.71}$$

In (2.71), the derivative of a function to θ is denoted by a prime symbol ($'$). The spatial derivatives of the underlying function can be analytically expressed by substituting the following equations:

$$\begin{cases}
\alpha_M' = 0\\
\beta_M' = 0\\
\gamma_M' = \dfrac{-\cos^2(\lambda)2\sin(\theta)\cos(\theta) + 2\dfrac{d}{a_2}\cos(\lambda)\sin(\theta)}{2\gamma_M}\\
\xi_M' = -\alpha_M \cos(\phi)\cos(\theta)\\
(\kappa_M^2)' = 2\kappa_M \kappa_M' = \dfrac{f_2' g_2 - g_2' f_2}{g_2^2}\\
\dfrac{d\Psi_M}{d\kappa_M} = \left(1 - \frac{\kappa_M^2}{2}\right) d\dfrac{K(\kappa_M)}{d\kappa_M} - 2\kappa_M K(\kappa_M) - \dfrac{dE(\kappa_M)}{d\kappa_M}\\
\Psi_M' = \dfrac{d\Psi_M(\kappa_M)}{d\kappa_M}\kappa_M'\\
f_1' = -\sin(\theta)\Psi_M(\kappa_M) + [\cos\theta - \frac{d}{a_2}\cos\lambda]\Psi_M'\\
g_1' = \kappa_M'\sqrt{\gamma_M^3} + \dfrac{3}{2}\kappa_M\sqrt{\gamma_M}\gamma_M'\\
f_2' = 4\alpha_M\gamma_M'\\
g_2' = 2\alpha_M\gamma_M'(1 + \alpha_M\gamma_M) + 2\xi_M\xi_M'
\end{cases} \tag{2.72}$$

2.4 Design considerations for air coils

The design of an air coil affects a wireless power transfer system on multiple levels. Namely the physical, thermal, electrical and magnetic field design are all subject to the coil design.

- Physical design: the shape of the coil determines its weight, the space that is required to house the coil and the amount of copper that is needed to wind the coil. The shape of the coil can also limit the movability of nearby coils or other moving parts.
- Thermal design: the allowable current through the windings is limited by the resulting heat that will be generated in the windings. The wire thickness, stranding of the turns, the operating frequency and the section of the winding all influence the heat dissipation in the coil.
- Electrical design: the self inductance of the coil needs to be compensated to achieve electrical resonance in the circuit by e.g., a parallel or series connected capacitor. The sizing of this capacitor is inverse proportional to the self inductance of the coil. Additionally, the thermal dissipation in the coil can be translated to an equivalent series resistance. This additional resistance can limit the efficiency and maximum power transfer of the system.
- Magnetic design: The shape and size of the coil determine the magnetic coupling between coils in the system. Generally, a higher magnetic coupling between transmitter and receiver coils improves the efficiency of the power transfer.

A proper understanding of the particularities of the air coil design is thus essential to fully optimize the system design. In this chapter, analytical derivations and empirical formulas are used to better understand the governing mechanisms behind these four aspects of coil design. These derivations support the assumptions that are made in the development of the RWPT motoring prototype. To apprehend high fidelity behavior, we can rely on FEM models to optimize and design RWPT motoring systems in further detail.

2.4.1 Self inductance of air coils

The magnetic field that is generated by the conductors in a coil is partly coupled with the loops in the coil itself. In 2.2.2 it was explained how a back EMF is generated that counteracts the change of current in the coil (self inductance). Section 2.2.4, explained how the magnetic coupling with other current carrying coils induces an EMF in other magnetically coupled loops or coils (mutual inductance). A coil can be seen as a stack of single turn loops that are connected in series and that are strongly magnetically coupled with each other.

Single turn coils

The self-inductance of a circular wire loop has been derived in [101, 102]. If we denote the diameter of the wire as $2r_0$ and the radius of the loop as a, the self-inductance can be derived to be

$$L_{\text{loop}} = \mu_0 a \left[\ln\left(\frac{8a}{r_0}\right) - 1.75 \right] \tag{2.73}$$

Note that the self-inductance is only weakly dependent on the diameter of the wire. This is because most of the generated magnetic field is coupled with all the current paths in the loop and only a small part of the generated flux closes inside the conductor itself.

When stacking two turns and connecting them in series, the current in one turn (i_1) generates a flux that is partly coupled with the other turn (Ψ_{21}) and vice versa (Ψ_{12}). Note that due to the series connection of these turns, the currents i_1 and i_2 are equal. The change of the current in one loop generates a back EMF in the other loop. This back EMF now scales with the mutual inductance between both coils.

$$v_{21}(t) = -\frac{\mathrm{d}\Psi_{21}(t)}{\mathrm{d}t} = M_{21}\frac{\mathrm{d}i_1(t)}{\mathrm{d}t} \tag{2.74}$$

It can be proven that the reciprocal coupled fluxes Ψ_{21} and Ψ_{12}, and consequently the mutual inductances M_{21} and M_{12}, are equal. The total back EMF for the series connected loops is then

$$\begin{aligned} v_{\text{tot}}(t) &= L_1\frac{\mathrm{d}i_1(t)}{\mathrm{d}t} + M_{12}\frac{\mathrm{d}i_2(t)}{\mathrm{d}t} + L_2\frac{\mathrm{d}i_2(t)}{\mathrm{d}t} + M_{21}\frac{\mathrm{d}i_1(t)}{\mathrm{d}t} \\ &= (L_1 + L_2 + 2M_{12})\frac{\mathrm{d}i_1(t)}{\mathrm{d}t} \end{aligned} \tag{2.75}$$

and the equivalent self-inductance of the series connected loops is now equal to $L_{\text{tot}} = L_1 + L_2 + 2M_{12}$. By adding more turns to the coil, the coil inductance becomes

$$L_{\text{tot}} = \sum_{i=1}^{n} L_i + \sum_{i=1}^{n-1}\sum_{j=i+1}^{n} 2M_{ij} \tag{2.76}$$

with n the amount of turns in the coil. The first summation has n terms, while the second summation has $\frac{n(n-1)}{2}$ terms. For closely packed coils, the coupling factor $k = \frac{M_{12}}{\sqrt{L_1 L_2}}$ between two coils is close to 1. For coils with a high amount of turns, we can thus accurately replace the turns by filament wires with infinitesimal thickness. The inductance of the coil is then analytically approximated by the summation of the mutual inductances between the turns, and the self-inductances of the individual turns. The mutual inductance between two coaxial loops was already derived by Maxwell. For two coaxial coils with radii a_1 and a_2 and axial offset c, the mutual inductance can be calculated by:

$$M = \frac{2\mu_0}{\kappa_M}\sqrt{a_1 a_2}\left[\left(1 - \frac{\kappa_M^2}{2}\right)K(\kappa_M) + E(\kappa_M)\right] \tag{2.77}$$

which is a special case of (2.55). Coils can be wound in many shapes. The most commonly used forms are the previously considered circular wire loop, disk coils, pancake/flat spiral coils, circular coils with rectangular section, and thin-wall, finite length solenoids. For these forms, the self-inductance is calculated analytically and/or empirically approximated in literature [103–105].

The empirically fitted equation of Welsby (2.78) accurately describes coils with rectangular cross-sections (see Figure 2.17), thin-walled solenoids (small value of w) and disk coils (small value of h).

$$L = \frac{\mu_0 n^2 \pi a^2}{h} \frac{1}{1 + 0.9\frac{a}{h} + 0.32\frac{w}{a} + 0.84\frac{w}{h}} \tag{2.78}$$

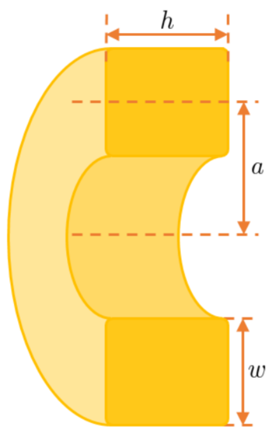

Figure 2.17: The shape of a coil with rectangular cross section is unambiguously determined by its average radius a, the width of the winding w and the height h of the stacked turns.

Wheeler's equation for thin-wall solenoids corresponds to Welsby's for $w = 0$:

$$L = \frac{10\mu_0 n^2 \pi a^2}{9a + 10h} \tag{2.79}$$

An interesting design optimization would be to optimize the inductance of a circular coil with rectangular cross-section and a given wire length. Maxwell approximated this optimal coil as one with square cross section for which holds that $2a = 3.7w$. Other researchers, including Brooks, refined this solution and stipulate that the optimum dimensions closely follow the rules $a = \frac{3}{2}h = \frac{3}{2}w$, such that the cross-section of the complete coil consists of 4 equally shaped squares. The so-called ”Brooks” coil has an approximated inductance of

$$L = 1.353\mu_0 a n^2 \tag{2.80}$$

A high inductance in itself is not very useful for wireless power transfer however. It only lowers the required capacitor value to compensate for the coil's self inductance. Tight packing of the coil winding increases the eddy currents in the conductor and thermally insulates the inner turns. Flat coil types such as rectangular and round spiral coils, pancake coils and disk coils have been studied in literature and empirical formulas exist to approximate their self inductance values. While flat coils are generally favored in RWPT systems, they are suboptimal choices for RWPT motoring systems. A densely packed coil section is required to generate measurable torque in a compactly designed RWPT based motoring system, such that these flat coil types fall out of the scope of this thesis.

2.4.2 Losses in air coils

Conduction losses

When current passes through a conducting material, a low resistance needs to be overcome, resulting in a reverse voltage. Because of this reverse voltage, power is dissipated in the conductor in the form of heat. The DC resistance of a conductor scales linearly with the specific resistivity of the conductor (ρ_c for copper) and its length l_c and is inversely proportional to the area of the cross section of the conductor (S_c). For a copper conductor, the DC resistance is given by Pouillet's law:

$$R_{\mathrm{DC}} = \frac{\rho_c l_c}{S_c} \tag{2.81}$$

The specific resistance of a conducting material is temperature dependent. For a large temperature range (T), the specific resistance can be linearly approximated. Often this approximation is done around room temperature (20°C), i.e.,

$$\rho_c(T) = \rho_{c20} + \alpha_{c20}\left[T - T_{20}\right] \tag{2.82}$$

with α_{c20} the temperature coefficient of copper at 20°C. Generally, the temperature coefficient is positive, such that the resistance of the conductor increases when the temperature of the conductor rises.

Skin effect

An AC current that runs through a round conductor forms a magnetic field inside the conductor. As the current changes over time, the magnetic field inside the conductor also changes. The changing tangential flux in the conductor induces an axial electric field (back EMF) which is stronger in the center of the conductor. The back EMF pushes the moving electrons to the perimeter of the conductor. As a consequence, the current density on the outside of the conductor increases. Another way of looking at it is that the change in tangential flux induces eddy currents that counteract the current in the center of the conductor and increase the current at the outside of the conductor. For a given current, the effective conducting area decreases, such that the resistance of the wire increases. Figure 2.18 shows an example of the non-uniform current density distribution inside a conductor with a diameter of 2 mm at 10 kHz.

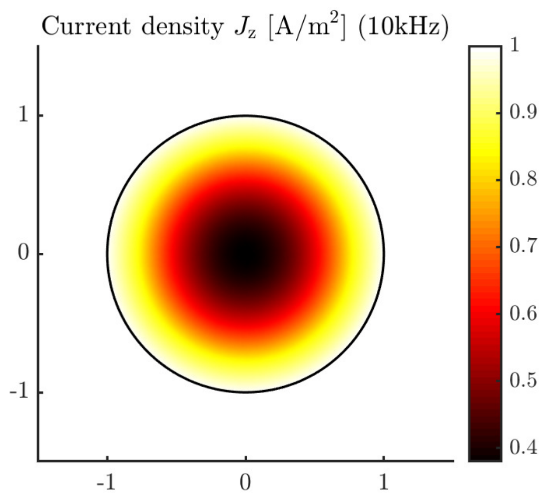

Figure 2.18: The induced back EMF inside the conductor counteracts the current in the center of the conductor, resulting in a higher current density near the surface ('skin') of the conductor.

The skin depth or penetration depth δ_s is a measure for the effective depth at which the current is present in the conductor. For frequencies far below the microwave range, δ_s is defined as

$$\delta_s = \sqrt{\frac{2\rho_c}{\omega\mu}} \tag{2.83}$$

For high frequencies, the AC resistance can be calculated by replacing the conductor by a cylindrical shell with depth δ_s.

$$R_{\text{AC,s}} \approx \frac{l_c \rho_c}{\pi (d - \delta_s)\delta_s} \approx \frac{l_c \rho_c}{\pi d \delta_s} \tag{2.84}$$

The exact current density in the conductor can be calculated using Bessel functions:

$$J_s(r) = \frac{k_s I}{2\pi R} \frac{J_0(k_s r)}{J_1(k_s R)} \tag{2.85}$$

with k_s the wave number of the conductor.

$$k_s = \frac{1 - j}{\delta_s} \tag{2.86}$$

and J_0 and J_1 the Bessel functions of the 0th and 1st order. The AC resistance can be written as the DC resistance multiplied by a factor in terms of Bessel functions.

$$R_{\text{AC,s}} = \text{Re}\left(\frac{m_s r_0}{2} \frac{J_0(m_s r_0)}{J_1(m_s r_0)}\right) R_{\text{DC,s}} \tag{2.87}$$

with m_s the conjugate of k_s.

$$m_s = \sqrt{\frac{j\omega\mu_0}{\rho_c}} = \frac{1 + j}{\delta_s} \tag{2.88}$$

The solution for the AC resistance is approximated as [106–108]

$$R_{\text{AC,s}} = R_{\text{DC,s}}(1 + y_s) \tag{2.89}$$

with

$$y_s = \frac{x_s^4}{192 + 0.8 x_s^4} \tag{2.90}$$

and

$$x_s = \sqrt{\frac{\omega \mu_0 l_c}{\pi R_{\text{DC,s}}}} \tag{2.91}$$

This approximation only holds for $x_s \le 2.8$. For frequencies in the kHz range, this condition is fulfilled. For $0.8 x_s^4 \ll 192$, the additional AC resistance can be approximated as

$$R_{\text{AC,s}} - R_{\text{DC,s}} = R_{\text{DC,s}} y_s \approx \frac{\omega^2 \mu_0^2 r_0^2 l_c}{192\pi \rho_c} \tag{2.92}$$

and the additional losses due to the skin effect are:

$$P_s = (R_{\text{AC,s}} - R_{\text{DC,s}}) I^2 \approx \frac{\omega^2 \mu_0^2 r_0^2 l_c}{192\pi \rho_c} I^2 \tag{2.93}$$

When the conductor heats up, the specific resistance ρ_c increases. From (2.81) and (2.92) we see that the DC resistance increases with temperature, while the equivalent resistance due to eddy currents decreases. For a given conductor, the AC resistance approximately scales with the square of the driving frequency ω. Note that this low frequency approximation slightly overestimates the losses in the coil, especially for very high frequencies. For higher frequencies, the eddy currents generate a magnetic field that counteracts the magnetic field generated by the uniformly distributed current density. For very high frequencies, the skin depth and the AC resistance approach an non-zero asymptotic value.

Proximity effect

The skin effect losses are calculated using the magnetic field in a single isolated conductor. When winding a coil, the magnetic field of nearby conductors can also strongly affect the generation of eddy currents in the conductor. The generation of eddy currents due to nearby current carrying conductors is called the proximity effect. Figure 2.19 illustrates how the current density is higher at the outside of the bundle of four copper wires of 2 mm in diameter at 10 kHz.

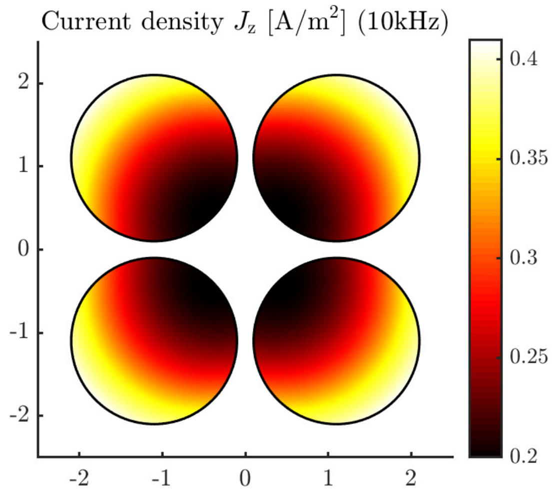

Figure 2.19: The transversal AC magnetic field of nearby conductors induces a back EMF which pushes the current flow to the outer edges of the bundle.

For densely wound coils with an increasing number of turns, the added AC resistance due to the proximity effect quickly overtakes the skin effect. The magnetic field generated by nearby conductors transversally passes through the conductor. For a conductor in a uniform low frequency transversal field, the eddy current loss can be approximated as [109]:

$$P_p = \frac{l\pi r_0^4(\omega B_t)^2}{4\rho_c} \tag{2.94}$$

With B_t the RMS amplitude of the transversal field and r_0 the radius of one conductor. To give a qualitative idea of the added AC resistance due to the proximity effect, we assume a circular cross section (with radius R_0) of a bundle of straight conductors (Figure 2.20).

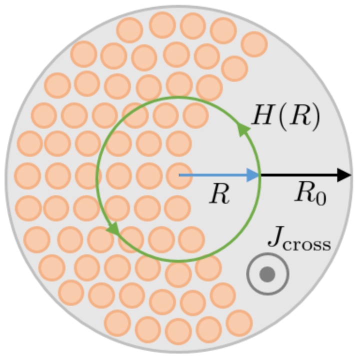

Figure 2.20: In a bundle of conductors with outer radius R_0, the transversal field $H(R)$ causes additional AC dissipation in the conductors.

The current density over the cross section is on average equal to

$$J_{\text{cross}} = \frac{nI}{\pi R_0^2} \tag{2.95}$$

Note that the current density over the cross-section will not change as all conductors are connected in series such that they always run the same current. The current distribution inside the conductors will however be affected by the local transversal magnetic field. We can now use Ampere's law to calculate the magnetic field as a function of the distance from the center of the cross-section of the coil.

$$\begin{aligned} 2\pi RH(R) &= J_{\text{cross}}R^2\pi \\ H(R) &= \frac{J_{\text{cross}}R}{2} = \frac{nIR}{2\pi R_0^2} \end{aligned} \tag{2.96}$$

Equivalent to the single conductor problem, the magnetic field scales linearly with the distance from the center of the cross-section. The conductors closest to the outer perimeter of the cross-section are mostly affected by transversal fields. To calculate the loss in the conductors, we are interested in the square of the magnetic field.

$$H(R)^2 = \left(\frac{J_{\text{cross}}R}{2}\right)^2 = \frac{n^2I^2R^2}{4\pi^2R_0^4} \tag{2.97}$$

The average transversal magnetic field squared is calculated by averaging over the cross-section of the coil:

$$\overline{H_t^2} = \frac{1}{S}\int_0^{R_0} 2\pi R H(R)^2 dR = \frac{1}{\pi R_0^2}\frac{n^2I^2}{2\pi R_0^4}\int_0^{R_0} R^3 dR = \frac{n^2I^2}{8\pi^2R_0^2} \tag{2.98}$$

Starting from (2.94), the AC dissipation in a conductor due to a transversal magnetic field is on average

$$P_p = \frac{l\pi r_0^4\omega^2}{4\rho_c}\overline{B_t^2} = \frac{l\pi r_0^4\omega^2}{4\rho_c}\mu_0^2\overline{H_t^2} = \frac{l\pi r_0^4\omega^2}{4\rho_c}\mu_0^2\frac{n^2I^2}{8\pi^2R_0^2} = \frac{n^2I^2\mu_0^2 l r_0^4\omega^2}{32\rho_c\pi R_0^2} \tag{2.99}$$

with

$$\overline{B_t^2} = \mu_0^2\overline{H_t^2} \tag{2.100}$$

the average value of the square of the magnetic field. The equivalent AC resistance due to the proximity effect can then be approximated as:

$$R_{\text{AC,p}} = \frac{P_p}{I^2} = \frac{n^2\mu_0^2 l r_0^4\omega^2}{32\rho_c\pi R_0^2} \tag{2.101}$$

Equation (2.101) shows that the equivalent AC resistance due to the proximity effect also scales approximately quadratically with the driving frequency, while it decreases for higher temperatures.

Litz wire

Equations (2.92) and (2.101) show that the AC dissipation due to skin effect and proximity effect both scale quadratically with the radius of the wire. It can be beneficial to split a conductor in parallel isolated strands to lower the eddy currents in the conductor. Litz wire [110, 111] is one type of multi-strand wire that is often used in RF applications (see Figure 2.21(a)).

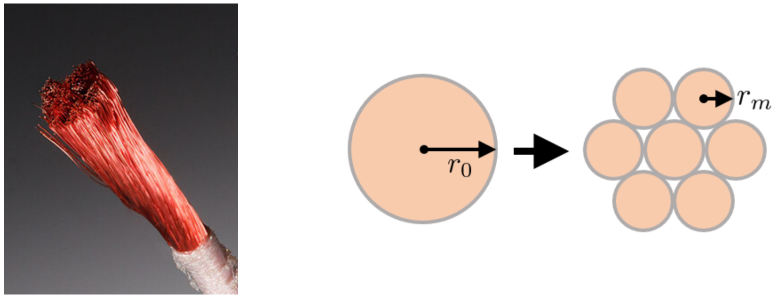

(a) **(b)**

Figure 2.21: In Litz wire, the conductor with radius r_0 is split in multiple isolated strands of radius r_m to mitigate AC losses.

The strands have a thickness that is lower than the skin depth such that AC losses are negligible. For the same cross section of copper, the AC dissipation is inversely proportional to the square of the amount of parallel strands used to construct a conductor. This is easily proven. When dividing the wire in m strands, the current per strand equals approximately I/m, while the radius of a strand equals $r_m = r_0/\sqrt{m}$, thus conserving the cross-section surface of the copper (Figure 2.21(b)). The AC dissipation per strand scales with $r_m^2 I^2$ for both the skin effect and the proximity effect. The dissipation per strand then scales with $(r_0/\sqrt{m})^2(I/m)^2$ or $r_0^2 I^2/m^3$, such that the total AC dissipation decreases by a factor m^2. Litz wire is very useful for eliminating AC losses in a coil, especially at high frequencies for e.g., RF applications. Multi-stranded wire however is very expensive compared to solid core wire. Terminating a Litz wire requires successful stripping of all isolation layers for each strand which makes the processing of Litz wire difficult. The biggest downside of Litz wire for power and motoring applications is the low copper per volume ratio due to the additional isolation layers per strand. The radial thermal conductivity of the wire is also lowered by the internal isolation layers. These spatial and thermal limitations severely impact the maximum current density of Litz wire, which is required for effective motoring applications.

Q factor

The performance of a coil in a wireless power transfer system is often expressed by the dimensionless quality factor, also denoted as the Q factor. The Q factor is a measure for how underdampened a resonator is. The Q factor is the ratio of the reactance and the resistance of the coil (see Section 2.2.3).

$$Q = \frac{\omega L}{R} \tag{2.102}$$

This also means that the Q factor equals the ratio of the energy stored in the magnetic field of the coil per cycle and the energy that is dissipated in the coil per cycle. The Q factor directly determines the oscillating current in a resonator.

The Q factor is highly frequency dependent. First, the reactance ωL of an inductor scales linearly with the frequency. The inductance of a coil does not change notably with frequency. From (2.92) and (2.101) we can approximate that the AC resistance of a coil scales quadratically with the driving frequency. The total coil resistance can then be written as $R_{\mathrm{DC}} + p\omega^2$, with R_{DC} and p positive values. The Q factor can thus be written as

$$Q = L\frac{\omega}{R_{\mathrm{DC}} + p\omega^2} \tag{2.103}$$

For a given coil, it is useful to know the optimal driving frequency, for which the Q factor is maximized. The peak value for Q can be found by equating its derivative to ω to zero.

$$\frac{dQ}{d\omega} = L\frac{R_{\mathrm{DC}} + p\omega^2 - 2p\omega^2}{(R_{\mathrm{DC}} + p\omega^2)^2} = L\frac{R_{\mathrm{DC}} - p\omega^2}{(R_{\mathrm{DC}} + p\omega^2)^2} = 0 \tag{2.104}$$

such that the optimal driving frequency is found for

$$\omega^* = \sqrt{\frac{R_{\mathrm{DC}}}{p}} \tag{2.105}$$

For this optimal driving frequency, the Q factor is

$$Q^* = L\frac{\sqrt{\frac{R_{\mathrm{DC}}}{p}}}{R_{\mathrm{DC}} + p\sqrt{\frac{R_{\mathrm{DC}}}{p}}^2} = L\frac{\sqrt{\frac{R_{\mathrm{DC}}}{p}}}{2R_{\mathrm{DC}}} = L\frac{1}{2\sqrt{pR_{\mathrm{DC}}}} \tag{2.106}$$

The resistance of the coil at the optimal driving frequency is then equal to

$$R_{\mathrm{AC}}^* = R_{\mathrm{DC}} + p(\omega^*)^2 = 2R_{\mathrm{DC}} \tag{2.107}$$

and the local derivative of the resistance to ω is

$$\left.\frac{\mathrm{d}R_{\mathrm{AC}}(\omega)}{\mathrm{d}\omega}\right|_{\omega^*} = 2p\omega^* = 2\sqrt{pR_{\mathrm{DC}}} \tag{2.108}$$

This is an interesting observation. Around the optimal value of the Q factor, the coil resistance is equal to two times the DC resistance and for small variations of ω around its optimal value of ω^*, the resistance of the coil can be approximated by a linear dependence on ω through the origin, namely

$$R_{\mathrm{AC}} \approx 2\omega\sqrt{pR_{\mathrm{DC}}} \tag{2.109}$$

2.5 Capacitor selection for RWPT motoring designs

Capacitors are essential for the reactance compensation in a wireless power transfer system. A physical capacitor exhibits non-ideal behavior in the form of losses, charge leakage and reactance variation. A non-ideal capacitor can be described by its lumped equivalent circuit (Figure 2.22).

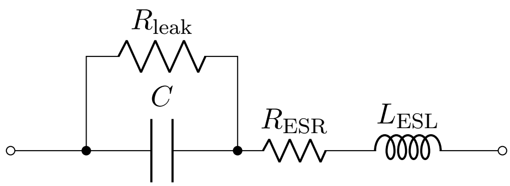

Figure 2.22: A non-ideal capacitor can be modeled by an equivalent circuit which includes its leakage resistance and its equivalent series resistance and inductance.

In this equivalent circuit, R_{leak} represents the path through which electrons manage to migrate through the isolation layer. For a DC bus capacitor, this value is very important because this parallel resistance directly determines the decrease of the state of charge over time. For high frequency AC applications, the conductive losses predominate over the leakage losses. R_{ESR} represents the equivalent series resistance of the capacitor, which represents the resistive losses when current passes through the capacitor. The dissipation in the capacitor is thus approximated by $R_{\mathrm{ESR}} I_C^2$. The equivalent series inductance (L_{ESL}) of the capacitor corresponds to the first resonance frequency of the capacitor ($\omega_C^2 = \frac{1}{C L_{\mathrm{ESL}}}$). For finely tuned AC applications such as wireless power transfer, a stable and reliable reactance value of the compensating capacitor is of very high importance, such that the applicable frequency range must be far below the (first) resonance frequency of the capacitor. For these frequencies, the series inductance can be neglected. For the high frequency application of the RWPT motoring system, we can neglect the leakage resistance and the equivalent series inductance in the equivalent capacitor circuit.

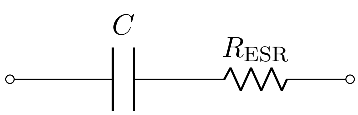

Figure 2.23: For well dimensioned capacitors for high frequency applications, the equivalent circuit can be simplified, leaving only the equivalent series resistance.

The dissipation in an AC capacitor is often expressed by the loss angle δ_C.

The loss angle represents the ratio of the series resistance and the capacitive reactance of the capacitor. Equation (2.110) is also a measure for the average dissipation in the capacitor compared to the maximum energy stored in the capacitor per cycle.

$$\tan \delta_C = \frac{R_{\mathrm{ESR}}}{X_C} = R_{\mathrm{ESR}} \omega C \tag{2.110}$$

The ESR of the capacitor varies with frequency due to the skin effect in the conductive foil, as well as other effects related to the dielectric characteristics. For capacitors with relatively low ESR, the Q factor of the capacitor is often given:

$$Q_C = \frac{X_C}{R_{\mathrm{ESR}}} = \frac{1}{\tan \delta_C} = \frac{1}{R_{\mathrm{ESR}} \omega C} \tag{2.111}$$

The Q factor is inversely proportional to the resistance of the component. For a series connection between an inductor and a capacitor, the new quality factor can be calculated as:

$$Q = \frac{1}{\dfrac{1}{Q_L} + \dfrac{1}{Q_C}} \tag{2.112}$$

In the RWPT motoring design, the dissipation in the coil dominates the losses in the capacitor, such that the Q factor can be approximated by the Q factor of the coil.

2.5.1 Capacitor types

Multiple types of capacitors are available for AC applications. AC capacitors are required to be non-polarized, such that positive and negative voltages can be generated over the terminals. In this section, the most commonly used AC capacitor are listed and their application potential for RWPT motoring is discussed.

Electrolytic capacitors

Electrolytic capacitors are constructed as a stack of an aluminium film (anode) with an isolating anodised oxide layer, a solid or liquid electrolyte and a conducting aluminium film which serves as the cathode. An electrolytic capacitor is inherently polarized and is mostly used in DC applications, such as reducing the voltage ripple in a DC bus. Non-polarized types do exist (e.g., Figure 2.24(a)) by combining two identical capacitors in back-to-back configuration. Non-polarized electrolytic capacitors require double the volume for the same capacitance value. This capacitor type is relatively cheap with a high capacitance per volume ratio, but with wide tolerances. The voltage rating is often low (about 35 V), but high voltage variants are available. Electrolytic capacitors are mostly useful in higher capacitance range ($> 1\mu$F). While the applicable frequency range is limited (up to about 100kHz), it is well within the required range of about 10kHz for the design of RWPT motoring systems. Electrolytic capacitors have relatively high leakage current and ESR. The limited lifetime and the failure mechanism make this capacitor type unsuitable for highly integrated designs.

Mica capacitors

The silver mica capacitor (Figure 2.24(b)) is the most commonly used type of mica capacitor. It consists of a mica sheet coated with metal on both sides, encased in epoxy. Multiple layers can be stacked to increase the capacitance value. Mica capacitors are mostly used in oscillators and filters because of their high stability and reliable capacitance value. They are rated for high voltages, have low losses and can be used for high frequencies. The capacitance value of mica capacitors is however limited to a couple thousand picofarads. They also require a high volume per capacitance and are relatively expensive.

Ceramic capacitors

Ceramic capacitors use ceramic material as a dielectric and silver coated contacts. They consist of a single disk or as multilayer ceramic capacitors (MLCC), see Figure 2.24(c). Ceramic capacitors are most often used as surface mount devices (SMD). They are relatively cheap and have a good high frequency performance and low losses. The capacitance values are however low (up to 100nF). Choosing a ceramic capacitor is mostly a tradeoff between stability (class 1) and capacitance value (class 2) which determines their application. Class 1 ceramic capacitors are mostly used in resonant circuits, while class 2 capacitors are mostly used for voltage smoothing and decoupling applications. For class 2 ceramic capacitors, the capacitance value can vary due to piezoelectric effects. All ceramic capacitors still have low capacitance per volume and they are sensitive to vibration and mechanical stress.

Film capacitors

There are two types of film capacitors, namely metalized paper/film and film foil capacitor, where conductors and dielectric are seperate films. Metalized film capacitors (Figure 2.24(d)) are significantly smaller in size and have self healing properties. Film capacitors are generally stable, with inherent low inductance and low ohmic losses. They are also cheap and suitable for high surge currents and AC power applications. Polypropylene (PP) and polyester

(PET) film capacitors have by far the largest market share, while polyphenylene sulfide (PPS), polyethylene naphthalate (PEN) and polytetrafluoroethylene or Teflon (PTFE) film capacitors still have their own niche applications. PET film capacitors have a higher capacitance per volume ratio. PP film capacitors are however more stable while having a significantly lower dissipation factor. Compact form factors range from several pF up to a few microfarads. While ceramic capacitors are capable of higher frequencies, the frequency range of film capacitors strongly exceeds the required range of 10kHz.

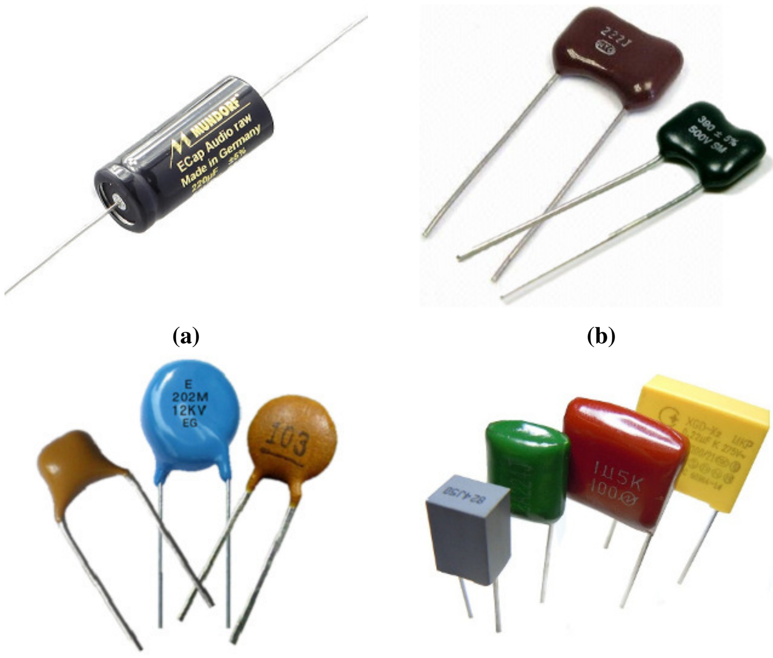

(a) **(b)** **(c)** **(d)**

Figure 2.24: Electrolytic capacitors (a), mica capacitors (b), ceramic capacitors (c) and film capacitors (d) are the most commonly used non-polarized capacitor types for AC applications.

The polypropylene film capacitors are relatively stable, with low losses, acceptable capacitance to volume ratio and high current and voltage capabilities. Additionally, they are relatively cheap and a high range of capacitance values are available. Because of these reasons, the polypropylene film capacitors were selected for use in the experimental RWPT motoring system.

2.6 Conclusion

In this chapter, we explored the state of the art regarding resonant wireless power transfer. In Section 2.2, the three main transmitter resonator topologies (series compensated, parallel compensated and 2 coil) were studied and the conditions for resonant tuning with a discrete capacitor were derived. Important dimensionless figures of merit, namely the quality factor (Q) and the kQ-factor U were introduced to quantify the effectiveness of a resonator coil and the efficiency of the energy transfer between two transmitter and receiver resonator coils. We studied analytical descriptions of the magnetic field of air coils in Section 2.3. These formulations were adapted to represent the mutual inductance between coils and the forces and torque that are generated between magnetically coupled air coils.

The findings in this chapter enable the design of an RWPT motoring prototype on which we can validate the parametric electrical models and the closed-form expressions for mechanical torque generation. The dominant loss mechanisms of air coils were studied and the three main causes of dissipation (conduction losses, skin and proximity effect) were discussed. For high frequency applications, the skin effect and proximity effect quickly dominate the DC resistance of the conductor. We remarked that the frequency dependent losses are approximately quadratic in ω. From this observation, the optimal driving frequency of a resonator coil was derived, by optimizing the quality factor. As this optimal driving frequency is in the range of 1-10kHz, a discrete capacitor is required to obtain resonant behavior. An overview was given of the four most common AC capacitor types. We concluded that the polypropylene film capacitor type is best suited for our RWPT motoring prototype. PP capacitors are stable, cheap and efficient while having an acceptable capacitance to volume ratio.

Chapter 3

RWPT motoring

In Section 2.2 the electrical interaction between a transmitter coil and one or more receivers was discussed. The forces between current carrying coils and external magnetic fields was explained in Section 2.3.3. In this chapter, both aspects are combined and the motoring possibilities of the current carrying coils in RWPT systems are explored. In 3.1 the rationale behind the motoring possibility of a RWPT system with two receivers is explained. In Section 3.2 closed-form torque expressions are derived for general multicoil RWPT systems. A prototype of the RWPT motoring system was constructed in 3.3, together with a FEM model of the system, to validate the closed-form torque expressions. In this chapter we also explore the potential benefit of combining magnetic resonance and magnetic materials in the RWPT motoring design. A ferrite core is added inside the rotor coil. The effect of the ferrite core on the Q factors of the coils, the magnetic coupling between the coils and the resulting torque gain is quantified at the end of this chapter.

3.1 Rationale behind RWPT based motoring

In this section, we explain how the excited currents in receiver resonators can be applied to generate torque in an RWPT system. A simplified RWPT motoring system is presented and the coil interactions are discussed for three (and by extension six) special coil orientations. Two identical series connected RLC resonators with area S, n turns and ESR $R_s = R_r$ are placed inside a uniform sinusoidal magnetic field $B = \sqrt{2}B_0 \sin(\omega t)$, with B_0 the RMS amplitude of the magnetic field. Figure 3.1 depicts the configurations of the considered resonators.

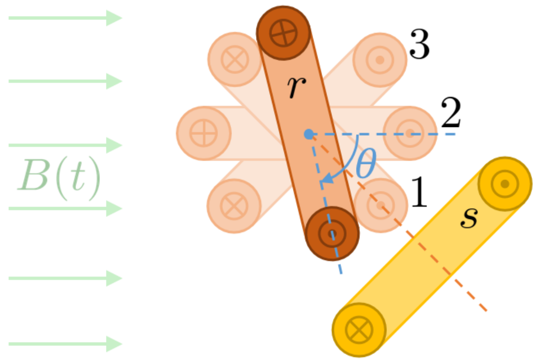

Figure 3.1: The torque on a rotating resonator for three (and by extension six) special orientations. The external magnetic field $B(t)$ interacts with the fixed stator resonator (s) and the rotor resonator (r) with variable orientation.

The frequency of the magnetic field coincides with the resonance frequencies of the resonator coils. One of the resonator coils is fixed in space at a 45 degree angle with the direction of the external magnetic field. This fixed coil is referred to as the stator coil. The second resonator coil is placed with its center on the axis of the stator coil and can freely rotate around its own center. The rotating resonator is referred to as the rotor resonator. The angle between the rotor and the uniform magnetic field is denoted by θ. The induced voltage in the stator is according to Faraday's law of induction equal to the time derivative of the coupled flux. For the stator, the coupled flux is equal to $\Psi_\mathrm{s} = B\sin(\pi/4)nS$, while the coupled flux for the rotor is dependent on the rotor angle θ ($\Psi_\mathrm{r} = B\sin(\theta)nS$). The induced voltages in the stator and rotor coils (in the RMS phasor representation) by the uniform magnetic field are then equal to

$$\begin{cases} \varepsilon_\mathrm{s} & = j\omega B_0 \sin\left(\frac{\pi}{4}\right) nS = j\omega B_0 \frac{\sqrt{2}}{2} nS \\ \varepsilon_\mathrm{r} & = j\omega B_0 \sin(\theta) nS \end{cases} \tag{3.1}$$

The phasor of B_0 is chosen to be oriented along the real axis of the complex plane. We will now consider the three specific rotor positions and observe the torque acting on the rotor coil.

Position 1

For the first position, namely $\theta = \pi/4$, both resonator coils are not magnetically coupled ($M_\mathrm{sr} = 0$). Both resonators behave as isolated receiver coils.

The KVL for the system is then

$$\begin{cases} j\omega B_0 \frac{\sqrt{2}}{2} nS & = R_s I_s \\ j\omega B_0 \frac{\sqrt{2}}{2} nS & = R_r I_r \end{cases} \tag{3.2}$$

Note that the currents in the resonator coils are in phase, while both currents are $\pi/2$ out of phase with the external magnetic field B. The instantaneous torque on the rotor coil can be described by (2.70), with

$$\begin{cases} i_r(t) = \mathrm{Re}(I_r e^{j\omega t}) = \sqrt{2}|I_r|\cos(\omega t + \phi_r) \\ i_s(t) = \mathrm{Re}(I_s e^{j\omega t}) = \sqrt{2}|I_s|\cos(\omega t + \phi_s) \end{cases} \tag{3.3}$$

and ϕ_r and ϕ_s the phases of the current phasors I_r and I_s. The expression of the average torque over one electrical cycle ($T_e = 1/f$) can be worked out as follows:

$$\begin{aligned} T_{\mathrm{av}} &= \frac{\mathrm{d}M_{\mathrm{sr}}}{\mathrm{d}\theta}\frac{1}{T_e}\int_t^{t+T_e} i_1(t)i_2(t)\mathrm{d}t \\ &= \frac{\mathrm{d}M_{\mathrm{sr}}}{\mathrm{d}\theta}\frac{2|I_r||I_s|}{T_e}\int_t^{t+T_e} \cos(\omega t + \phi_r)\cos(\omega t + \phi_s)\mathrm{d}t \\ &= \frac{\mathrm{d}M_{\mathrm{sr}}}{\mathrm{d}\theta}\frac{|I_r||I_s|}{T_e}\int_t^{t+T_e} [\cos(2\omega t + \phi_r + \phi_s) + \cos(\phi_r - \phi_s)]\mathrm{d}t \\ &= \frac{\mathrm{d}M_{\mathrm{sr}}}{\mathrm{d}\theta}|I_r||I_s|\cos(\phi_r - \phi_s) \\ &= \mathrm{Re}(I_{\mathrm{r}} I_{\mathrm{s}}^{\mathrm{H}})\frac{\mathrm{d}M_{\mathrm{sr}}(\theta)}{\mathrm{d}\theta} \end{aligned} \tag{3.4}$$

Because the rotor and stator currents are in phase for position 1, (3.4) is simplified to

$$T_{\mathrm{rs}} = \mathrm{Re}(I_{\mathrm{r}} I_{\mathrm{s}}^{\mathrm{H}})\frac{\mathrm{d}M_{\mathrm{sr}}(\theta)}{\mathrm{d}\theta} = -|I_{\mathrm{r}}||I_{\mathrm{s}}|\frac{\mathrm{d}M_{\mathrm{sr}}(\theta)}{\mathrm{d}\theta} > 0 \tag{3.5}$$

while the average torque on the rotor due to the uniform magnetic field can be expressed as

$$T_{\mathrm{rb}} = \mathrm{Re}(I_{\mathrm{r}})\cos(\theta)B_0 nS = 0 \tag{3.6}$$

The resonator currents are in phase, such that both coils want to align (i.e. a torque is exerted) in the direction of θ. The external magnetic field does not directly generate an average torque on the rotor, because the rotor current I_r is $\pi/2$ out of phase with the magnetic field B.

Position 2

If the rotor position is $\theta = 0$, the rotor is not magnetically coupled with the external magnetic field ($\Psi_r = B\sin(0)nS = 0$). Any current in the rotor coil is excited indirectly via the stator resonator coil. The stator acts as a relay between the external magnetic field and the rotor resonator. The whole system operates similar to a domino resonator system [25, 112, 113]. The set of KVL equations is now

$$\begin{cases} j\omega B_0 \frac{\sqrt{2}}{2} nS & = R_s I_s + j\omega M_{\mathrm{sr}} I_{\mathrm{r}} \\ 0 & = R_r I_r + j\omega M_{\mathrm{sr}} I_{\mathrm{s}} \end{cases} \tag{3.7}$$

which can be resolved to

$$\begin{cases} j\omega B_0 \frac{\sqrt{2}}{2} nS & = \left(R_s + \frac{\omega^2 M_{\mathrm{sr}}^2}{R_r} \right) I_s \\ I_r & = -j \frac{\omega M_{\mathrm{sr}}}{R_r} I_s \end{cases} \tag{3.8}$$

The magnetic interaction of the stator resonator with the rotor resonator is translated to a real valued reflected impedance. The stator current leads the external magnetic field again by $\pi/2$. The rotor current I_r in its turn leads the stator current I_s by $\pi/2$. The rotor current is now in antiphase with the external magnetic field. The torque on the rotor due to the interaction with the stator coil (T_{rs}) and the external magnetic field (T_{rb}) is

$$\begin{cases} T_{\mathrm{rs}} & = \mathrm{Re}(I_{\mathrm{r}} I_{\mathrm{s}}^{\mathrm{H}}) \frac{\mathrm{d}M_{\mathrm{sr}}(\theta)}{\mathrm{d}\theta} = 0 \\ T_{\mathrm{rb}} & = \mathrm{Re}(I_{\mathrm{r}}) \cos(0) B_0 nS = |I_{\mathrm{r}}| B_0 nS > 0 \end{cases} \tag{3.9}$$

The torque on the rotor is now only generated by the external magnetic field and is again oriented in the positive direction of θ.

Position 3

In the third rotor position $\theta = -\pi/4$ or $7\pi/4$, the rotor coil is fully aligned with the stator coil. The stator and rotor coil now behave as two identical strongly coupled receivers [26]. The KVL equations for this situation are

$$\begin{cases} j\omega B_0 \frac{\sqrt{2}}{2} nS & = R_s I_{\mathrm{s}} + j\omega M_{\mathrm{sr}} I_{\mathrm{r}} \\ j\omega B_0 \frac{\sqrt{2}}{2} nS & = R_r I_{\mathrm{r}} + j\omega M_{\mathrm{sr}} I_{\mathrm{s}} \end{cases} \tag{3.10}$$

As both coils have the same orientations and the coil resistances are the same ($R_s = R_r = R$), the set of KVL equations is evidently symmetrical. Consequently, both the stator and the rotor currents are equal in amplitude and in phase:

$$I_{\mathrm{r}} = I_{\mathrm{s}} = j\omega B_0 \frac{\sqrt{2}}{2} nS \frac{R - j\omega M_{\mathrm{sr}}}{R^2 + \omega^2 M_{\mathrm{sr}}^2} = \omega B_0 \frac{\sqrt{2}}{2} nS \frac{jR + \omega M_{\mathrm{sr}}}{R^2 + \omega^2 M_{\mathrm{sr}}^2} \tag{3.11}$$

The stator and rotor currents now lead the external magnetic field between 0 and $\pi/2$ radians. As the rotor and stator coils are optimally coupled, no torque is generated on the rotor by the interaction with the stator coil $\left(\frac{\mathrm{d}M_{\mathrm{sr}}(\theta)}{\mathrm{d}\theta} = 0\right)$. The torque on the rotor due to the interaction with the external magnetic field is again positive in the direction of θ:

$$T_{\mathrm{rb}} = \mathrm{Re}(I_{\mathrm{r}}) \cos\left(-\frac{\pi}{4}\right) B_0 nS = |\mathrm{Re}(I_{\mathrm{r}})| \frac{\sqrt{2}}{2} B_0 nS > 0 \tag{3.12}$$

When the rotor turns π radians, the geometry of the system stays the same, while the current (in the chosen convention) switches sign. It is easily shown that the torque on the rotor is also positive for the corresponding positions $\theta = 3\pi/4$, π and $5\pi/4$. From this observation, we can conclude that the interaction between two receiver resonators in a non-rotating magnetic field may allow for motoring operation, with unidirectional torque over a full rotation. In the next section, the coil interactions in a general resonator topology are rigorously analyzed and closed-form expressions for the torque for all rotor angles θ are derived.

3.2 Generalized RWPT based motoring

A generalized RWPT motoring system consists of an arbitrary number of three distinct circuit types, which are shown in Figure 3.2, namely the transmitter coil (t), stator coils (s) and rotor coils (r). The transmitter coil is connected to a voltage or current controlled power source. The stator coils and rotor coils are inductor-capacitor (RLC) series connections, of which the stator coils are fixed in space and the rotor coils are free to rotate around an axis. The rotation angle of the rotor is denoted as θ.

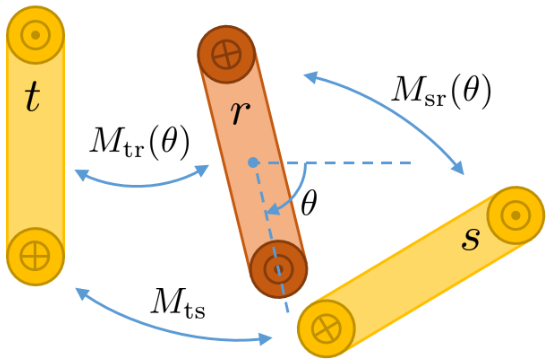

Figure 3.2: The general resonator topology consists of a transmitter coil (t) connected to a power source, a stator coil (s) that is fixed in space and one or more rotor coils (r) that can rotate around an axis.

3.2.1 State-space model for moving coils

When a current is present in a coil, a voltage is induced in another coil when these coils are magnetically coupled. The magnetic interaction can be described by Lenz's law, which states that the induced electromotive force (EMF) $\varepsilon_{\mathrm{ab}}$ in a conducting loop, e.g. t, by a current, e.g. i_r, is equal to the negative of the rate of change of the enclosed magnetic flux Ψ_{tr}. Ψ_{tr} is the flux excited by current i_r enclosed in the turns of coil t. If we assume that coil r can rotate, the EMF consists of the sum of the effects of movement (angle θ) and change in excitation current i_r, and can be derived by applying the chain rule:

$$\begin{aligned}\varepsilon_{\mathrm{tr}} &= \frac{\mathrm{d}\Psi_{\mathrm{tr}}}{\mathrm{d}t} \\ &= \frac{\mathrm{d}}{\mathrm{d}t}(M_{\mathrm{tr}}(\theta)\cdot i_r) \\ &= \frac{\mathrm{d}M_{\mathrm{tr}}(\theta)}{\mathrm{d}\theta}\frac{\mathrm{d}\theta}{\mathrm{d}t}i_r + M_{\mathrm{tr}}(\theta)\frac{\mathrm{d}i_r}{\mathrm{d}t} \\ &= K_{\mathrm{tr}}(\theta)\dot{\theta}i_r + M_{\mathrm{tr}}(\theta)\frac{\mathrm{d}i_r}{\mathrm{d}t}\end{aligned} \tag{3.13}$$

The first part of Equation (3.13) is called the motional EMF generated by the Lorentz force and the second part is the transformer EMF induced by the changing magnetic field. M_{tr} represents the mutual inductance between circuits t and r. The spatial derivative of $M_{\mathrm{tr}}(\theta)$ to the rotation angle θ is denoted as $K_{\mathrm{tr}}(\theta)$ and the rotational speed as $\dot{\theta}$. Note that the reciprocal mutual inductance values M_{tr} and M_{rt} are equal and the same holds for the spatial derivative, namely K_{tr} and K_{rt}. Based on (3.13), we can construct a state-space representation of the electrical states in the RWPT system. For each resonator coil, we express Kirchoff's voltage law (KVL). For the rotor resonator in Figure 3.2 the KVL is:

$$v_r = R_r i_r + L_r \frac{\mathrm{d}}{\mathrm{d}t} i_r + v_{C_r} + \varepsilon_{\mathrm{rs}} + \varepsilon_{\mathrm{rt}} \tag{3.14}$$

with v_r the voltage from an external power source ($=0$ if no source is present), R_r the equivalent series resistance (ESR), L_r the coil's self inductance and v_{C_r} being the voltage over the capacitor C_r (if a series-capacitor is present). For each capacitor, the associated differential equation is added to the set of differential equations:

$$C_r \frac{\mathrm{d}v_{C_r}}{\mathrm{d}t} = i_r \tag{3.15}$$

In order to convert these equations to matrix form, we define resistance matrix R_d, impedance matrix Z_d, voltage vector V_t and state vector x as follows:

$$R_d = \begin{bmatrix} R_t & 0 & 0 & 0 & 0 \\ 0 & R_s & 0 & 0 & 0 \\ 0 & 0 & R_r & 0 & 0 \\ 0 & 0 & 0 & 0 & 0 \\ 0 & 0 & 0 & 0 & 0 \end{bmatrix} \tag{3.16}$$

$$Z_d = \begin{bmatrix} L_t & M_{\mathrm{ts}} & M_{\mathrm{tr}}(\theta) & 0 & 0 \\ M_{\mathrm{ts}}^{\mathrm{T}} & L_s & M_{\mathrm{sr}}(\theta) & 0 & 0 \\ M_{\mathrm{tr}}(\theta)^{\mathrm{T}} & M_{\mathrm{sr}}(\theta)^{\mathrm{T}} & L_r & 0 & 0 \\ 0 & 0 & 0 & C_s & 0 \\ 0 & 0 & 0 & 0 & C_r \end{bmatrix} \tag{3.17}$$

$$V_t = \begin{bmatrix} v_t \\ 0 \\ 0 \\ 0 \\ 0 \end{bmatrix}; x = \begin{bmatrix} i_t \\ i_s \\ i_r \\ v_{Cs} \\ v_{Cr} \end{bmatrix} \tag{3.18}$$

Here, v_t is the voltage over the transmitter coil and x is the vector of all electrical states, namely, the currents in the coils and the voltages across the series-capacitors. If there are multiple (n_r) rotor coils present in the system, $M_{\mathrm{sr}}(\theta)$ is an $1 \times n_r$ vector. Equations (3.14) and (3.15) can now be written in matrix form:

$$V_t = Z_d \dot{x} + (R_d + \dot{Z}_d)x \tag{3.19}$$

3.2.2 General torque expression

In order to derive the general expression for the torque, we examine the energy transfer per unit of time ($\dot{E}$) in the system of coils. The energy E that is stored in the capacitors and the magnetic field can be expressed as:

$$E = \frac{1}{2} x^{\mathrm{T}} Z_d x \tag{3.20}$$

Application of the chain rule gives:

$$\dot{E} = \frac{1}{2} \dot{x}^{\mathrm{T}} Z_d x + \frac{1}{2} x \dot{Z}_d x + \frac{1}{2} x^{\mathrm{T}} Z_d \dot{x} \tag{3.21}$$

Equation (3.19) can be rewritten as:

$$Z_d \dot{x} = -(R_d + \dot{Z}_d) x + V_t \tag{3.22}$$

such that Equation (3.21) simplifies to:

$$\dot{E} = V_t^{\mathrm{T}} x - x^{\mathrm{T}} \left(R_d + \frac{1}{2} \dot{Z}_d \right) x \tag{3.23}$$

We can distinguish two components in Equation (3.23): the input power ($P_{\mathrm{in}} = v_t i_t = V_t^{\mathrm{T}} x$) and the dissipated power ($P_{\mathrm{diss}} = R_t i_t^2 + R_s i_s^2 + R_r i_r^2 = x^{\mathrm{T}} R_d x$). Mechanical work is the remaining term that relates to $\dot{E}$ due to the conservation of energy:

$$\dot{E} = P_{\mathrm{in}} - P_{\mathrm{diss}} - T\dot{\theta} \tag{3.24}$$

and therefore:

$$T\dot{\theta} = \frac{1}{2} x^{\mathrm{T}} \dot{Z}_d x \tag{3.25}$$

As Z_d is a function of the position θ, the time derivative of Z_d can be rewritten as:

$$T\dot{\theta} = \frac{1}{2} x^{\mathrm{T}} \frac{\partial [Z_d(\theta(t))]}{\partial t} x = \frac{1}{2} x^{\mathrm{T}} \dot{\theta} \frac{\partial [Z_d(\theta)]}{\partial \theta} x \tag{3.26}$$

Elimination of $\dot{\theta}$ in both sides of (3.26) results in the general expression for the torque:

$$T(t) = \frac{1}{2} x(t)^{\mathrm{T}} \frac{\partial [Z_d(\theta)]}{\partial \theta} x(t) \tag{3.27}$$

The torque is now shown to be independent of the speed $\dot{\theta}$. For the limit case of $\dot{\theta} = 0$, (3.27) also holds. The average torque over one cycle is then equal to:

$$T_{\mathrm{av}}(\theta) = \frac{1}{2} \mathbf{x}^{\mathrm{H}} \frac{\partial [Z_d(\theta)]}{\partial \theta} \mathbf{x} \tag{3.28}$$

with $\mathbf{x} = [I_t \; I_s \; I_r \; V_{Cs} \; V_{Cr}]^{\mathrm{T}}$ the RMS phasor representation of the states (x). $\mathbf{x}^{\mathrm{H}}$ is the conjugate transpose (or Hermitian transpose) of $\mathbf{x}$. Only the mutual inductance elements of Z_d are variable in θ, such that the capacitor voltages do not directly contribute to the torque in (3.28). The average torque per cycle can now be written as:

$$T_{\mathrm{av}}(\theta) = \frac{1}{2}\left(\mathbf{i}^{\mathrm{H}}\begin{bmatrix} 0 & 0 & K_{\mathrm{tr}}(\theta) \\ 0 & 0 & K_{\mathrm{sr}}(\theta) \\ K_{\mathrm{tr}}(\theta)^{\mathrm{T}} & K_{\mathrm{sr}}(\theta)^{\mathrm{T}} & 0 \end{bmatrix}\mathbf{i}\right) \tag{3.29}$$

with $\mathbf{i} = \begin{bmatrix} I_t & I_s & I_r \end{bmatrix}^{\mathrm{T}}$ the vector of the complex RMS phasors of i_t, i_s and i_r. K_{ab} was defined in Equation (3.13) as the angular derivative of M_{ab}.

3.2.3 Voltage and current controlled transmitters

A voltage or current controlled transmitter gives rise to magnetically coupled coils whose electrical state x in (3.18), together with the voltage over the transmitter coil V_t, follow dynamics (3.19). When considering a voltage controlled transmitter, V_t is a constant imposed value, whereas in case of a current controlled transmitter, V_t implicitly depends on the imposed current I_t and satisfies the electrical circuit laws in the transmitter coil. When deriving the general torque expression in Section 3.2.2, we defined $\mathbf{i}$ as the vector of the complex current phasors in the transmitter, stator and rotor coils. We will now express the current vector $\mathbf{i}$ as a function of the input, namely phasor V_t for a voltage controlled transmitter and I_t for a current controlled transmitter. Let us recall that in the frequency domain, the induced voltage expressed in (3.13) can be split up in an in-phase part with respect to the excitation coil current phasor I_b (motional EMF) and an out-of-phase part (transformer EMF):

$$E_{\mathrm{ab}} = K_{\mathrm{ab}}(\theta)\dot{\theta}I_b + j\omega M_{\mathrm{ab}}(\theta)I_b \tag{3.30}$$

with ω as the electrical angular speed, and $\omega = 2\pi f$ and f as the frequency of the power source. E is the complex phasor of ε. For the calculation of the quasi-static torque, we assume that $\dot{\theta} \ll \omega$, such that the element $K_{\mathrm{ab}}\dot{\theta}$ can be neglected in the calculation of the current vector $\mathbf{i}$ without significant loss in accuracy. This is equivalent to removing the $\dot{Z}_d x$ term in (3.19), such that:

$$V_t \approx Z_d\dot{x} + R_d x \tag{3.31}$$

Voltage controlled transmitter power source

When applying the KVL in the frequency domain, only one complex equation is required per coil. For a voltage controlled transmitter, Equation (3.31) turns into a set of three complex algebraic equations that connect the electrical states of the voltage controlled RWPT system:

$$Z_V \begin{bmatrix} I_t \\ I_s \\ I_r \end{bmatrix} = \begin{bmatrix} V_t \\ 0 \\ 0 \end{bmatrix} \Leftrightarrow \begin{bmatrix} I_t \\ I_s \\ I_r \end{bmatrix} = {Z_V}^{-1} \begin{bmatrix} 1 \\ 0 \\ 0 \end{bmatrix} V_t \tag{3.32}$$

with impedance matrix Z_V:

$$Z_V = \begin{bmatrix} R_t + j\omega L_t & j\omega M_{\mathrm{ts}} & j\omega M_{\mathrm{tr}}(\theta) \\ j\omega M_{\mathrm{ts}}^{\mathrm{T}} & R_s + \frac{1}{j\omega C_s} + j\omega L_s & j\omega M_{\mathrm{sr}}(\theta) \\ j\omega M_{\mathrm{tr}}(\theta)^{\mathrm{T}} & j\omega M_{\mathrm{sr}}(\theta)^{\mathrm{T}} & R_r + \frac{1}{j\omega C_r} + j\omega L_r \end{bmatrix} \tag{3.33}$$

It is important to note that the torque (3.29) scales quadratically with the amplitude of the transmitter voltage. We consider an RWPT system with one coil of each type, i.e. one transmitter, stator and rotor coil. In what follows, this topology will be referred to as the single rotor RWPT motoring system. For the considered system, all matrix elements of (3.33) have a 1×1 size, as there is only one transmitter, stator and rotor coil present in the system. In (3.32), the current vector **i** is expressed as a function of the transmitter voltage V_t and impedance matrix Z_V. Note that all stator and rotor coils are assumed to be tuned to resonant conditions ($j\omega L_a + \frac{1}{j\omega C_a} = 0$). Inserting the current vector from (3.32) in torque expression (3.29) gives the following simplified expression:

$$T_1(\theta) = \frac{1}{2} \frac{M_{\mathrm{ts}}\omega^2(K_{\mathrm{sr}}M_{\mathrm{tr}} - K_{\mathrm{tr}}M_{\mathrm{sr}})(\omega^2 M_{\mathrm{sr}}^2 + R_r R_s)}{\left(\begin{array}{c} [R_t(\omega^2 M_{\mathrm{sr}}^2 + R_r R_s) + \omega^2 M_{\mathrm{tr}}^2 R_s + \omega^2 M_{\mathrm{ts}}^2 R_r]^2 \\ + [\omega L_t(\omega^2 M_{\mathrm{sr}}^2 + R_r R_s) - 2\omega^3 M_{\mathrm{sr}} M_{\mathrm{tr}} M_{\mathrm{ts}}]^2 \end{array} \right)} |V_t|^2 \tag{3.34}$$

Current controlled transmitter power source

In the case of a controlled current in the transmitter coil, the applied voltage V_t is an indirect result of the imposed current I_t, such that the order of the system decreases by one:

$$V_t = (R_t + j\omega L_t)I_t + Z_t^{\mathrm{T}} \begin{bmatrix} I_s \\ I_r \end{bmatrix} \tag{3.35}$$

$$0 = Z_I \begin{bmatrix} I_s \\ I_r \end{bmatrix} + Z_t I_t \Leftrightarrow \begin{bmatrix} I_s \\ I_r \end{bmatrix} = -Z_I^{-1} Z_t I_t \tag{3.36}$$

with impedance matrix Z_I and Z_t:

$$Z_I = \begin{bmatrix} R_s + \dfrac{1}{j\omega C_s} + j\omega L_s & j\omega M_{\mathrm{sr}}(\theta) \\ j\omega M_{\mathrm{sr}}(\theta)^{\mathrm{T}} & R_r + \dfrac{1}{j\omega C_r} + j\omega L_r \end{bmatrix}$$
$$Z_t = \begin{bmatrix} j\omega M_{\mathrm{ts}} & j\omega M_{\mathrm{tr}}(\theta) \end{bmatrix}^{\mathrm{T}} \tag{3.37}$$

As with the voltage controlled transmitter power source, here we consider a single rotor RWPT motoring system. The torque expression (3.34) in case of having a voltage controlled transmitter scales quadratically with V_t; correspondingly, we can deduce from (3.29) together with (3.36) that the torque scales quadratically with the amplitude of the transmitter current I_t in the case of a current controlled transmitter. This results in the following simplified torque expression:

$$T_1(\theta) = \frac{M_{\mathrm{ts}}\omega^2(K_{\mathrm{sr}}M_{\mathrm{tr}} - K_{\mathrm{tr}}M_{\mathrm{sr}})}{\omega^2 M_{\mathrm{sr}}^2 + R_r R_s}|I_t|^2 \tag{3.38}$$

with $|I_t|$ the RMS amplitude of current i_t.

Reflected impedance to the transmitter coil

The rotor and stator currents were expressed in (3.36) as a matrix multiplication with the current vector I_t. The KVL for the transmitter (3.35) expresses the transmitter voltage V_t as the sum of the voltage drop over the transmitter coil itself and the induced voltage by the currents in the rotor and stator coils. As both the stator and rotor coil currents can be written in terms of the transmitter current, the externally induced voltages can be translated into a reflected impedance:

$$\begin{aligned} Z_{\mathrm{ref}} &= -Z_t^{\mathrm{T}} Z_I^{-1} Z_t \\ &= \frac{\omega^2 M_{\mathrm{ts}}^2(R_r) + \omega^2 M_{\mathrm{tr}}^2(R_s) - j2\omega^3 M_{\mathrm{ts}}M_{\mathrm{tr}}M_{\mathrm{sr}}}{\omega^2 M_{\mathrm{sr}}(\theta)^2 + R_r R_s} \end{aligned} \tag{3.39}$$

The amplitude of the transmitter voltage ($|V_t|$) is now the multiplication of the current amplitude ($|I_t|$) and the modulus of the total transmitter coil impedance:

$$|V_t| = |R_t + j\omega L_t + Z_{\mathrm{ref}}||I_t| \leftrightarrow |I_t| = \frac{|V_t|}{|R_t + j\omega L_t + Z_{\mathrm{ref}}|} \tag{3.40}$$

Equation (3.40) can be used to convert the torque expression for the current controlled system (3.38) to that of the voltage controlled system (3.34) and vice versa. If the rotor and stator coils are not magnetically coupled ($M_{\text{sr}} = 0$), the reflected impedance simplifies to the sum of the reflected impedance for single receiver resonators (2.11):

$$Z_{\text{ref}} = \frac{\omega^2 M_{\text{ts}}^2}{R_s} + \frac{\omega^2 M_{\text{tr}}(\theta)^2}{R_r} \tag{3.41}$$

This situation corresponds to the first position in Section 3.1.

3.2.4 Closed-form torque expressions for multiple resonator coils

Equation (3.29) can also be worked out into a closed-form expression for multiple resonator coils. We assume that all rotor coils have the same resistance ($R_{r_j} = R_r$) and that the mutual inductance between the rotor coils is zero or negligible. For a voltage controlled RWPT system with two uncoupled rotors, the torque profile can be expressed as follows:

$$T_2(\theta) = \frac{M_{\text{ts}}\omega^2 \sum\limits_{i=1}^{2}(K_{\text{sr}_\text{i}} M_{\text{tr}_\text{i}} - K_{\text{tr}_\text{i}} M_{\text{sr}_\text{i}})(\omega^2 \sum\limits_{i=1}^{2} M_{\text{sr}_\text{i}} + R_r R_s)|V_t|^2}{\left(\left[\omega^2 \sum\limits_{i=1}^{2} M_{\text{tr}_\text{i}}^2 R_s + \omega^2 M_{\text{ts}}^2 R_r + \omega^4 \frac{(M_{\text{sr}_1} M_{\text{tr}_2} - M_{\text{sr}_2} M_{\text{tr}_1})^2}{R_r}\right]^2 + \left[\omega L_t(\omega^2 \sum\limits_{i=1}^{2} M_{\text{sr}_\text{i}}^2 + R_r R_s) - 2\omega^3 M_{\text{ts}} \sum\limits_{i=1}^{2}(M_{\text{sr}_\text{i}} M_{\text{tr}_\text{i}})\right]^2\right)} \tag{3.42}$$

For a current controlled transmitter and multiple (n_r) rotor coils, (3.43) is obtained when neglecting the mutual induction between the rotor coils.

$$T_{n_r}(\theta) = \frac{M_{\text{ts}}\omega^2 \sum\limits_{i=1}^{n_r}\left[(K_{sr_i} M_{tr_i} - K_{tr_i} M_{sr_i}) \prod\limits_{i \neq j} R_{r_j}\right]}{\omega^2 \sum\limits_{i=1}^{n_r}\left[M_{sr_i}^2 \prod\limits_{i \neq j} R_{r_j}\right] + R_s \prod\limits_{j} R_{r_j}} \mathrm{i}_t^2 \tag{3.43}$$

If all rotor resistance values are assumed equal, (3.43) simplifies to:

$$T_{n_r}(\theta) = \frac{1}{2} \frac{M_{\text{ts}}\omega^2 \sum\limits_{i=1}^{n_r}(K_{sr_i} M_{tr_i} - K_{tr_i} M_{sr_i})}{\omega^2 \sum\limits_{i=1}^{n_r} M_{sr_i}^2 + R_r R_s} \mathrm{i}_t^2 \tag{3.44}$$

3.2.5 Current controlled single rotor RWPT motoring system

The torque profile of a current controlled system (3.38) can be studied qualitatively by assuming sinusoidal mutual inductance profiles. This approximation will be shown to be valid for the experimental setup (see Section 3.3). Figure 3.3 shows a schematic view of the RWPT motoring setup with one transmitter, stator and rotor coil. The rotational position of the stator is denoted by ϕ_{st}.

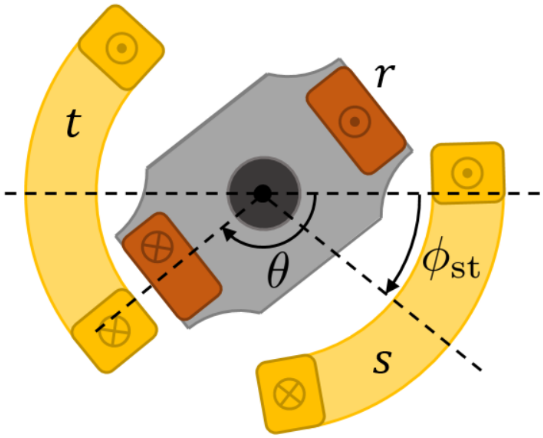

Figure 3.3: Schematic view of the 3 coil RWPT system.

For the approximated analysis, we only consider the first spatial harmonic of M_{tr} and M_{sr}. The angular dependence of the mutual inductances and associated spatial derivatives can then be described as:

$$
\begin{aligned}
M_{\mathrm{tr}_1}(\theta) &= -\hat{M}_{\mathrm{tr}}\sin(\theta) \\
M_{\mathrm{sr}_1}(\theta) &= -\hat{M}_{\mathrm{sr}}\sin(\theta-\phi_{\mathrm{st}}) \\
K_{\mathrm{tr}_1}(\theta) &= -\hat{K}_{\mathrm{tr}}\cos(\theta) = -\hat{M}_{\mathrm{tr}}\cos(\theta) \\
K_{\mathrm{sr}_1}(\theta) &= -\hat{K}_{\mathrm{sr}}\cos(\theta-\phi_{\mathrm{st}}) = -\hat{M}_{\mathrm{sr}}\cos(\theta-\phi_{\mathrm{st}})
\end{aligned}
\tag{3.45}
$$

with $\hat{M}_{\mathrm{tr}}$ and $\hat{M}_{\mathrm{sr}}$ the peak amplitudes of M_{tr_1} and M_{sr_1} and ϕ_{st} the physical angle shift between them. Substituting terms (3.45) in (3.38) gives rise to the following torque expression for a current controlled transmitter:

$$T_1(\theta) = \frac{1}{2}\frac{M_{\text{ts}}\omega^2\begin{bmatrix}\hat{M}_{\text{sr}}\cos(\theta-\phi_{\text{st}})\hat{M}_{\text{tr}}\sin(\theta) \\ \qquad -\hat{M}_{\text{tr}}\cos(\theta)\hat{M}_{\text{sr}}\sin(\theta-\phi_{\text{st}})\end{bmatrix}}{\omega^2[\hat{M}_{\text{sr}}\sin(\theta-\phi_{\text{st}})]^2+R_rR_s}|I_t|^2$$

$$= \frac{1}{2}\frac{\omega^2 M_{\text{ts}}\hat{M}_{\text{tr}}\hat{M}_{\text{sr}}\sin(\phi_{\text{st}})}{\omega^2\hat{M}_{\text{sr}}^2\sin^2(\theta-\phi_{\text{st}})+R_rR_s}|I_t|^2 \tag{3.46}$$

From (3.46) it is clear that the torque is unidirectional if the mutual inductance profiles can be approximated by their first spatial harmonic. The motoring direction is determined by the angle ϕ_{st}. In what follows, a quantification of the peak torque, the minimum torque and the average torque is made for the torque profile described in (3.46). As such, the peak torque can easily be found for $\sin(\theta-\phi_{\text{st}}) = 0$, which corresponds to the rotor not being magnetically coupled with the stator:

$$T_{1,\text{peak}} = \frac{\omega^2 M_{\text{ts}}\hat{M}_{\text{tr}}\hat{M}_{\text{sr}}\sin(\phi_{\text{st}})}{R_rR_s}|I_t|^2 \tag{3.47}$$

We can deduce from (3.47) that the maximum torque increases for increasing levels of coupling between the coils whereas an increase in coil resistance (inversely proportional to the Q factor) degrades the torque.

The minimum torque is found for $\sin(\theta-\phi_{\text{st}}) = \pm 1$:

$$T_{1,\text{min}} = \frac{\omega^2 M_{\text{ts}}\hat{M}_{\text{tr}}\hat{M}_{\text{sr}}\sin(\phi_{\text{st}})}{\omega^2\hat{M}_{\text{sr}}^2+R_rR_s}|I_t|^2 \tag{3.48}$$

The minimum torque is an important indication for the self-starting possibilities of the topology. Ideally, the minimum torque should exceed the sum of the friction torque and the load torque. The condition $\sin(\theta-\phi_{\text{st}}) = \pm 1$ is satisfied when the rotor and stator coils are aligned. In other words, magnetic interaction between the stator and rotor results in a degradation of the torque generation. The average torque over one cycle can be found as:

$$T_{1,\text{av}} = \frac{\sin(\phi_{\text{st}})\omega^2 M_{\text{ts}}\hat{M}_{\text{tr}}\hat{M}_{\text{sr}}|I_t|^2}{4\pi\omega^2\hat{M}_{\text{sr}}^2}\int_0^{2\pi}\frac{\mathrm{d}\theta}{\sin^2(\phi_{\text{st}}-\theta)+\frac{R_rR_s}{\omega^2\hat{M}_{\text{sr}}^2}}$$

$$= \frac{\sin(\phi_{\text{st}})\omega^2 M_{\text{ts}}\hat{M}_{\text{tr}}\hat{M}_{\text{sr}}|I_t|^2}{2\omega^2\hat{M}_{\text{sr}}^2}\frac{1}{\sqrt{\frac{R_rR_s}{\omega^2\hat{M}_{\text{sr}}^2}\left(1+\frac{R_rR_s}{\omega^2\hat{M}_{\text{sr}}^2}\right)}}$$

$$\triangleq \frac{\sin(\phi_{\text{st}})M_{\text{ts}}\hat{M}_{\text{tr}}|I_t|^2}{2\hat{M}_{\text{sr}}}\frac{U_{\text{sr,max}}^2}{\sqrt{U_{\text{sr,max}}^2+1}} \tag{3.49}$$

with

$$U_{\mathrm{sr,max}}^2 = \frac{\omega^2 \hat{M}_{\mathrm{sr}}^2}{R_r R_s} = \frac{\omega^2 \left(k_{\mathrm{sr,max}} \sqrt{L_r L_s}\right)^2}{\dfrac{\omega^2 L_r L_s}{Q_r Q_s}} = k_{\mathrm{sr,max}}^2 Q_r Q_s \tag{3.50}$$

The product of the coupling factor and the Q factor of resonator coils ($U = kQ$) is a common figure of merit for the efficiency of WPT systems [114, 115] (see Section 2.2.7). For RWPT, high values of U indicate high efficiency of the electromagnetic power transfer. For RWPT motoring systems, this strong interaction between the resonators counteracts the desired behavior, namely torque generation.

3.2.6 Dual rotor RWPT motoring system

The torque ripple (the difference between (3.47) and (3.48)) is significant for high Q factors of the coils. To alleviate the torque ripple, one might suggest to add a second rotor coil, which is rotated by 90 degrees compared to the first rotor coil (Figure 3.4).

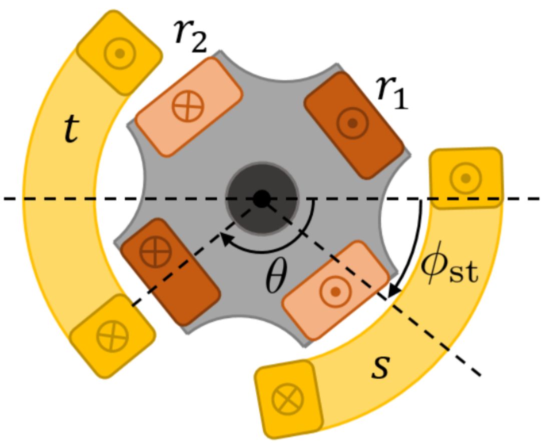

Figure 3.4: A second rotor coil is added in an attempt to lower the torque ripple.

In this way, the peak torque of one coil coincides with the minimum torque of the other coil. Similar to Section 3.2.5, the torque profile can be approximated by considering only the first spatial harmonic of M_{tr_2} and M_{sr_2}. The elements of (3.51) considering the added rotor coil are shifted over an angle of

$\frac{\pi}{2}$ compared to (3.45):

$$\begin{aligned} M_{\text{tr}_2}(\theta) &= -\hat{M}_{\text{tr}}\cos(\theta) \\ M_{\text{sr}_2}(\theta) &= -\hat{M}_{\text{sr}}\cos(\theta-\phi_{\text{st}}) \\ K_{\text{tr}_2}(\theta) &= \hat{M}_{\text{tr}}\sin(\theta) \\ K_{\text{sr}_2}(\theta) &= \hat{M}_{\text{sr}}\sin(\theta-\phi_{\text{st}}) \end{aligned} \tag{3.51}$$

When filling in these terms in (3.44), the following expression results:

$$\begin{aligned} T_2(\theta) &= \frac{\omega^2 M_{\text{ts}}\hat{M}_{\text{tr}}\hat{M}_{\text{sr}}[\sin(\phi_{\text{st}})+\sin(\phi_{\text{st}})]}{\omega^2\hat{M}_{\text{sr}}^2[\cos^2(\theta-\phi_{\text{st}})+\sin^2(\theta-\phi_{\text{st}})]+R_rR_s}|I_t|^2 \\ &= \frac{2\sin(\phi_{\text{st}})\omega^2 M_{\text{ts}}\hat{M}_{\text{tr}}\hat{M}_{\text{sr}}}{\omega^2\hat{M}_{\text{sr}}^2+R_rR_s}|I_t|^2 \end{aligned} \tag{3.52}$$

One can deduce from (3.52) that since the denominator for the torque is constant, the torque for the two rotor system is also constant when assuming sinusoidal mutual inductance profiles. Also, the direction of the torque depends on the sign of $\sin(\phi_{\text{st}})$. Therefore, the torque reaches a maximum absolute value for $\sin(\phi_{\text{st}}) = \pm 1$. For this condition, a rotor coil is aligned with the transmitter coil when there is no coupling with the stator coil. However, there is a trade-off in torque, as the coupling between the transmitter and stator M_{ts} is also affected by the angle ϕ_{st}.

We can conclude that the added rotor coil is capable of removing the torque ripple, but the magnetic interaction between the stator and at least one of the rotor coils at all times severely degrades the maximum achievable torque. The possibly high peak torque is eliminated, while the (now constant) torque of the two rotor system is only double the minimum torque of the single rotor system.

3.2.7 Comparison of average torque for single and dual rotor RWPT motoring systems

In Section 3.2.5 and 3.2.6, the torque profiles and their average values were derived for the single and dual rotor RWPT motoring systems respectively. If the ratio of these average torques (3.53) is larger than unity, the dual rotor setup would be beneficial not only for the elimination of the torque ripple, but also from an efficiency standpoint.

$$
\begin{aligned}
\frac{T_{2,\mathrm{av}}}{T_{1,\mathrm{av}}} &= \frac{2\sqrt{R_r R_s}\sqrt{\omega^2 \hat{M}_{\mathrm{sr}}^2 + R_r R_s}}{\omega^2 \hat{M}_{\mathrm{sr}}^2 + R_r R_s} \\
&= \frac{2\sqrt{R_r R_s}}{\sqrt{\omega^2 \hat{M}_{\mathrm{sr}}^2 + R_r R_s}}
\end{aligned}
\tag{3.53}
$$

The ratio $\frac{T_{2,\mathrm{av}}}{T_{1,\mathrm{av}}}$ will be larger than unity for:

$$
\frac{1}{3}\omega^2 \hat{M}_{\mathrm{sr}}^2 < R_r R_s \tag{3.54}
$$

or in terms of the dimensionless system parameter in the single rotor coil (3.50):

$$
U_{\mathrm{sr,max}}^2 < 3 \tag{3.55}
$$

Equation (3.55) describes a qualitative way to compare the single and dual rotor topologies considered in Sections 3.2.5 and 3.2.6: only for $U_{\mathrm{sr,max}}^2$ values under 3, the dual rotor system is considered to have the higher average quasi-static torque. For the setup used for the experimental validation in Section 3.3, $U_{\mathrm{sr,max}}^2$ was around 148 and thus, significantly larger than 3. From this condition, one can conclude that in the search for the highest coil quality factors and magnetic coupling between system coils (which in turn, increases the value of $U_{\mathrm{sr,max}}^2 = k_{\mathrm{sr,max}}^2 Q_s Q_r$ of the system), the single rotor topology will be more effective.

3.3 Development of an RWPT motoring prototype

To validate the derived formulas for the torque generation in an RWPT motoring system, a prototype is constructed. Of each coil type, one is present in the system. The prototype is designed with multiple insights in mind. The air gaps are limited to improve the magnetic coupling between the coils. Initially, there is no magnetic material present in the system, but a provision is made for a cylindrical core of magnetic material inside the rotor core (see Figure 3.5).

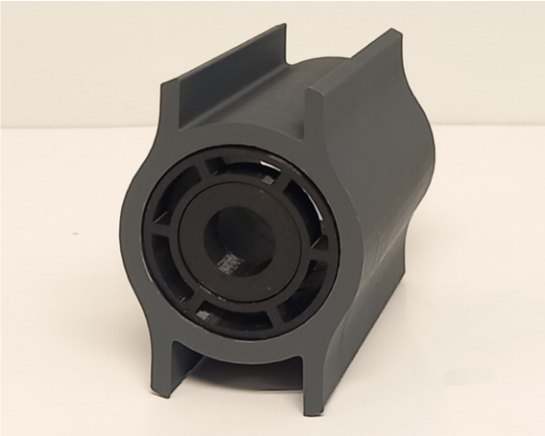

Figure 3.5: A provision is made in the rotor coil for a cylindrical core of magnetic material.

The outside dimensions of the motor are chosen to fit in a $10\mathrm{cm} \times 10\mathrm{cm} \times 10\mathrm{cm}$ volume. For the individual turns, a wire diameter of 0.8 mm is chosen. This wire diameter allows for ample current, while the maximum Q factor is reached between 5 and 10 kHz. The coil windings are made up of 200 turns per coil. For this amount of turns, the total current through the section of the windings is high enough to ensure a measurable torque, while the thickness of the winding is acceptable. A limited thickness is required to limit the leakage flux inside the winding, which allows for increased coupling between the coils. A limited winding thickness also allows for better heat dissipation and increases the current limit of the conductors. Solid core conductors were chosen instead of stranded Litz wire. The use of Litz wire would increase the cost and required section of the coils drastically, while limiting the maximum current due to the added thermal insulation. The additional AC resistance of the 0.8 mm solid core wire allows for frequencies up to 10 kHz, which is acceptable to show the efficacy of RWPT motoring.

For the amount of windings and the dimensions of the coils, the self inductance of the coils is estimated to be in the order of 5 mH. To counteract the self inductance of the coils between 5 and 10 kHz, the required film capacitors (50 - 200 nF) are significantly smaller than the coils themselves, which allows for an integrated design.

Figure 3.6 shows the front view of the RWPT motoring prototype system in the Solidworks environment.

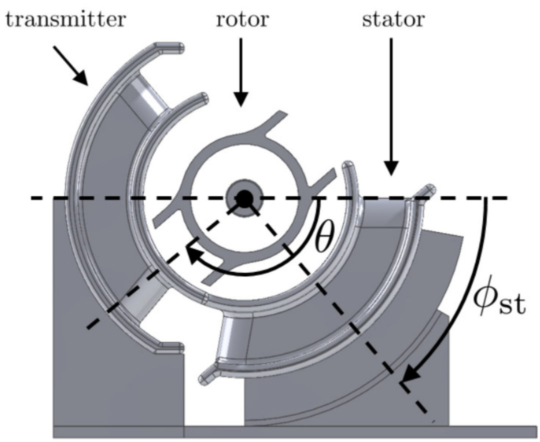

Figure 3.6: Frontview of the RWPT prototype in Solidworks.

The rotor core of the prototype system is 65 mm deep and the slots for the winding are 24 mm wide. 200 turns of 0.8 mm isolated copper wire require a total depth of about 90mm and a total rotor coil radius of about 34 mm. The axle of 13 mm diameter runs through the center of the rotor core. Between the axle and the rotor coil, there is a provision for a cylindrical rotor core of magnetic material with an outside diameter of 37 mm. The transmitter and stator windings are constructed identically. To limit the air gaps, the coils are wound in the shape of a cylindrical section around the rotor coil. The transmitter and stator coils are wound around a core that is 70 mm deep. The winding itself is about 100 mm deep. The cores cover a section of 100 degrees, while the pitch of the windings is about 115 degrees. The inner and outer radii of the cylindrical spaces for the windings are 39 and 57 mm respectively. Table 3.1 lists the geometrical parameters of the RWPT motoring coils. Rotation of the axisymmetric rotor core does not affect its shape relative to the stator and transmitter coils, such that their self inductance would not become dependent on the rotor angle.

Table 3.1: Geometrical parameters of the experimental setup

Component	Inner radius	Outer radius
transmitter/stator winding	39 mm	57 mm
rotor winding	22 mm	33 mm
ferrite core	6.5 mm	18.5 mm

Parameter	Value
total motor length	100 mm
transmitter/stator/rotor turns	200/200/200
wire diameter	0.8 mm
transmitter/stator coil span	$\pm 115°$
ϕ_{st}	0.72 rad $= \pm 41°$

Provisions are made to allow for limited changes in the geometry of the system. The transmitter can be moved away from the center of rotation, while the stator can be rotated around the rotor core. The rotor axle rests on two ball bearings on either side of the rotor core. The coil holders and the ball bearing housings are 3D printed in polylactic acid (PLA) on a Prusa MK2 3D printer.

Figure 3.7 shows the 3D model of the complete setup in Solidworks 2020. From left to right, a stepper motor, a torque transducer and the RWPT motoring system are shown. The real mechanical setup is shown in Figure 3.8.

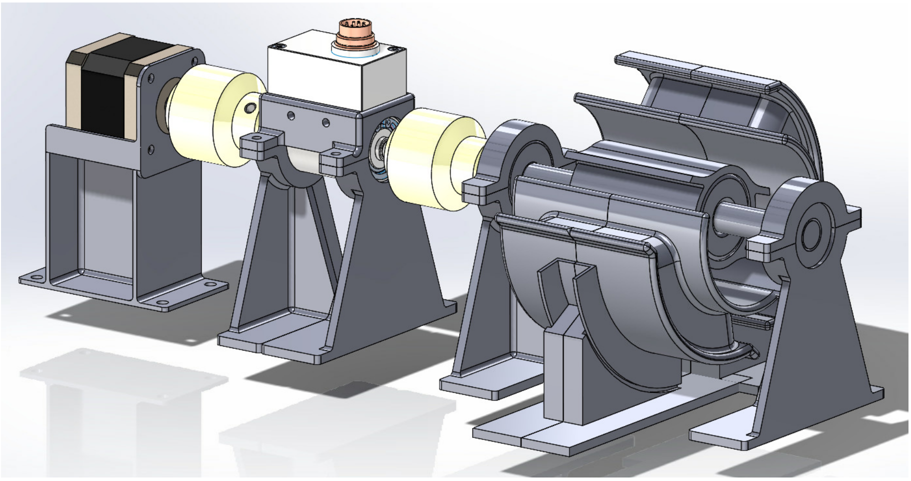

Figure 3.7: The RWPT motoring prototype was designed in Solidworks 2020. The 3D models of the supports were later used to 3D print them.

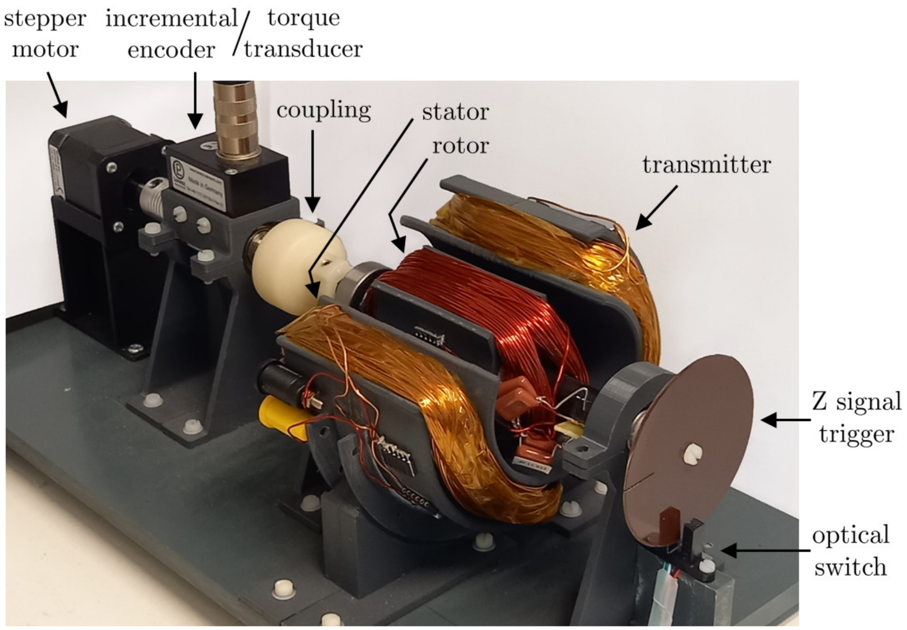

Figure 3.8: The experimental setup was used to validate the numerical and parametric electromechanical models.

The RWPT system is counteracted by a Trinamic QMOT QSH4218

(NEMA 17) two phase hybrid stepper motor (Figure 3.9(a)). The stepper motor has a holding torque of 270 Nmm which exceeds the expected peak torque of the RWPT system. The stepper motor is controlled by an A4988 driver board (Figure 3.9(b)) which is run in sixteenth step microstepping mode, resulting in a resolution of 3200 steps and a minimum step size of 0.1125 degrees. The stepper motor driver is controlled using the digital outputs of a dSpace MicroLabBox (DS1202) fast prototyping system with integrated dual core CPU and programmable FPGA. In between the stepper and RWPT motor, a Lorenz Messtechnik DR-2112 contactless torque transducer (Figure 3.9(c)) is placed with a nominal torque of 1 Nm ($\pm 0.1\%$) and built-in incremental encoder with 2×360 pulses. The torque transducer converts the deformation of a strain gauge to a voltage difference between -10V and +10V between two contacts, which corresponds to the nominal range of the transducer. The incremental encoder of the torque transducer does not account for drift, as the encoder only outputs A and B signals. A fiberglass disk with a fine slit is attached to the front end of the rotor axle. The disk fits in a slotted Optek OPB916 optical switch (Figure 3.9(d)). Every time the light passes through the slit and is picked up by the sensor, a Z signal is triggered and the position estimation is reset. The zero position of the encoder coincides with the rotor orientation for which the magnetic coupling between the transmitter and rotor coils is equal to zero ($M_{\mathrm{tr}} = 0$). Radial and axial forces can introduce additional stresses inside the axle of the torque transducer, which cause a bias in the torque readings.

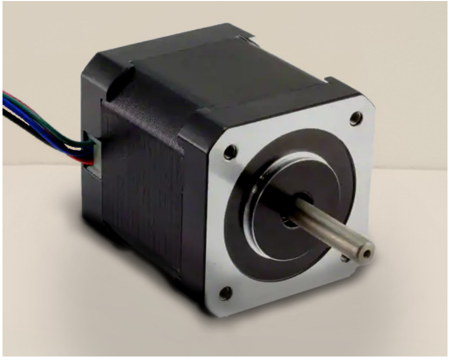

(a)

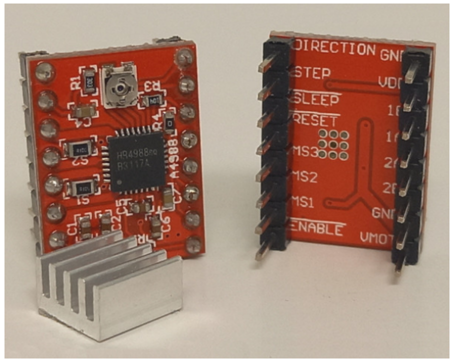

(b)

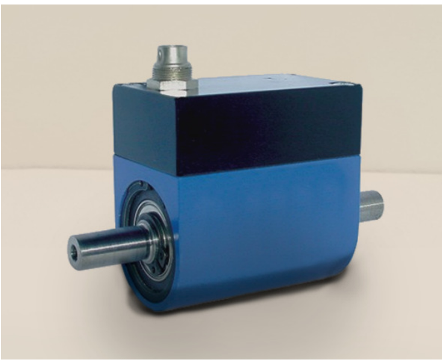

(c)

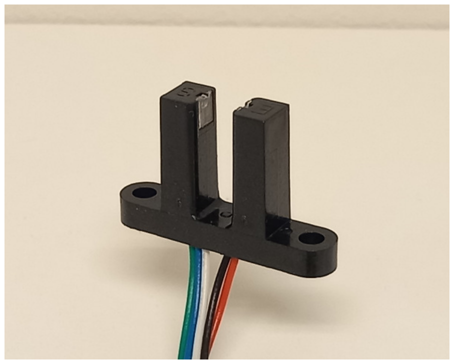

(d)

Figure 3.9: The Trinamic stepper motor (a) counteracts the RWPT motor and is controlled by an A4988 driver board (b). The torque is measured by a DR-2112 contactless torque transducer (c) with built-in incremental encoder. An Optek optical switch (d) provides the Z signal for the encoder.

To combat the transfer of radial and axial forces, the RWPT motoring system and the stepper motor are connected to the torque transducer by nylon curved tooth gear couplings. A Spitzenberger & Spies PAS 1000 4-quadrant amplifier is used as a voltage source for the transmitter. This linear amplifier can generate sinusoidal waveforms with a frequency of up to 10 kHz and an amplitude of up to 270 V RMS. The reference signal of the sinusoidal voltage is generated by an analog output channel of the dSpace MicroLabBox. Analog sensor data from the torque transducer, current and voltage probes and the encoder pulses are read through the analog and digital input channels respectively on the MicroLabBox and interpreted by software on a connected laptop. The stepper motor can be controlled in open loop, but the encoder is used to check the correct operation of the position control.

3.3.1 Q factor of the air coils

The resistance and inductance of the rotor and stator coils were measured using a Rohde & Schwarz HM8118 RLC meter for a wide range of frequencies. Figure 3.10 (left) and 3.11 (left) show how the rotor and stator coil resistances increase with the frequency. The quadratic trend line was fitted and shows very good correspondence to the measured data points. The right side plot in Figures 3.10 and 3.11 display the corresponding Q factors of the coils.

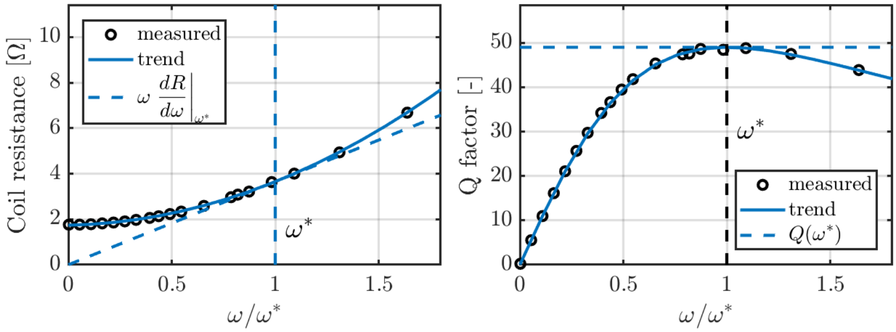

Figure 3.10: Measured resistance and Q factor values of the rotor air coil in the experimental setup. The Q factor is stable for a wide frequency band around its optimal value ($f_r^* \approx 9158$ Hz).

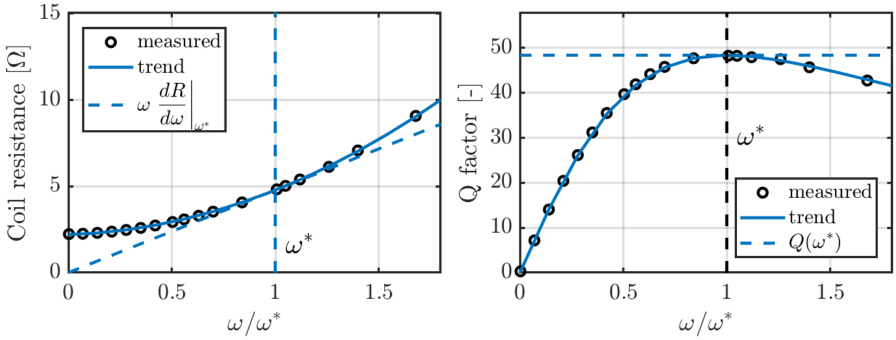

Figure 3.11: Measured resistance and Q factor values of the stator air coil in the experimental setup. The Q factor is stable for a wide frequency band around its optimal value ($f_s^* \approx 7146$ Hz).

The approximated expressions for the equivalent AC resistance due to skin effect (2.92) and proximity effect (2.101) in Section 2.4.2 indicated a quadratic dependency on the excitation frequency ω. Fitting a second degree polynomial shows that the addition of a small linear term strongly improves the accuracy of the regression model. This indicates that the derived quadratic loss models for the skin effect and proximity effect do not fully capture all loss mechanisms for the considered frequency range. This is due to the fact that we only used the quadratic term of the Bessel function approximation. Because of the added linear term, we need to revise the approximate formulas that were derived to find the optimal Q factor (2.103)-(2.109). The Q factor is now approximated as

$$Q = L\frac{\omega}{R_{\mathrm{DC}} + p_1\omega + p_2\omega^2} \tag{3.56}$$

with p_1 and p_2 the coefficients of the linear and quadratic terms of the resistance respectively. The peak value for the Q factor Q^*, and the corresponding frequency ω^*, is again found by equating its derivative to ω to zero.

$$\frac{dQ}{d\omega} = L\frac{R_{\mathrm{DC}} + p_1\omega + p_2\omega^2 - p_1\omega - 2p\omega^2}{(R_{\mathrm{DC}} + p_1\omega + p_2\omega^2)^2} = L\frac{R_{\mathrm{DC}} - p_2\omega^2}{(R_{\mathrm{DC}} + p_1\omega + p_2\omega^2)^2} = 0 \tag{3.57}$$

The linear term in the numerator cancels out, such that the optimal driving frequency remains

$$\omega^* = \sqrt{\frac{R_{\mathrm{DC}}}{p_2}} \tag{3.58}$$

For this optimal driving frequency, the Q factor is slightly lowered due to the added term p_1 in the denominator.

$$Q^* = L\frac{\sqrt{\frac{R_{\mathrm{DC}}}{p_2}}}{R_{\mathrm{DC}} + p_1\sqrt{\frac{R_{\mathrm{DC}}}{p_2}} + p_2\sqrt{\frac{R_{\mathrm{DC}}}{p_2}}^2} = L\frac{1}{2\sqrt{p_2 R_{\mathrm{DC}}} + p_1} \tag{3.59}$$

The resistance of the coil at the optimal driving frequency also has an additional term proportional to p_1:

$$R_{\mathrm{AC}}^* = R_{\mathrm{DC}} + p_1\omega^* + p_2(\omega^*)^2 = 2R_{\mathrm{DC}} + p_1\sqrt{\frac{R_{\mathrm{DC}}}{p_2}} \tag{3.60}$$

The linear term adds a constant value to the local derivative of the resistance to ω:

$$\left.\frac{dR_{\mathrm{AC}}(\omega)}{d\omega}\right|_{\omega^*} = p_1 + 2p_2\omega^* = p_1 + 2\sqrt{p_2 R_{\mathrm{DC}}} \tag{3.61}$$

For the peak values of the Q factor, the coil resistance remains about 2 times the DC resistance. Around this optimal frequency, the resistance of the coil can still be approximated by a straight line through the origin. Table 3.2 lists the measured coil parameters and their derived values.

Table 3.2: The rotor and stator coil parameters were measured for a wide frequency range and their optimal driving frequency f^* and Q factor Q^* were derived.

Parameter	Rotor	Stator
L	3.11 mH	5.15 mH
R_{DC}	1.74 Ω	2.20 Ω
p_1	3.06e-06 $\Omega s/\mathrm{rad}$	8.26e-06 $\Omega s/\mathrm{rad}$
p_2	5.25e-10 $\Omega s^2/\mathrm{rad}^2$	1.09e-09 $\Omega s^2/\mathrm{rad}^2$
f^*	9158 Hz	7146 Hz
Q^*	49.02	48.38

3.3.2 Optimal driving frequency

The torque formula (3.38) was derived for a current controlled transmitter in Section 3.2.3:

$$T(\theta) = \frac{M_{\mathrm{ts}}\omega^2(K_{\mathrm{sr}}M_{\mathrm{tr}} - K_{\mathrm{tr}}M_{\mathrm{sr}})}{\omega^2 M_{\mathrm{sr}}^2 + R_r R_s}|I_t|^2 \tag{3.62}$$

The magnetic field of the transmitter is thus invariant of the effect of the reflected impedance on the total transmitter impedance. We are interested in knowing what driving frequency is required to optimize the torque in the RWPT motoring system. For a nonzero value of the magnetic coupling between stator and rotor ($M_{\mathrm{sr}} \neq 0$) the torque expression can be rewritten as:

$$\begin{aligned} T(\theta) &= \frac{M_{\mathrm{ts}}\omega^2(K_{\mathrm{sr}}M_{\mathrm{tr}} - K_{\mathrm{tr}}M_{\mathrm{sr}})}{\omega^2 M_{\mathrm{sr}}^2\left(1+\frac{1}{U_{\mathrm{sr}}^2}\right)}|I_t|^2 \\ &= \frac{M_{\mathrm{ts}}(K_{\mathrm{sr}}M_{\mathrm{tr}} - K_{\mathrm{tr}}M_{\mathrm{sr}})}{M_{\mathrm{sr}}^2\left(1+\frac{1}{U_{\mathrm{sr}}^2}\right)}|I_t|^2 \\ &= \frac{M_{\mathrm{ts}}(K_{\mathrm{sr}}M_{\mathrm{tr}} - K_{\mathrm{tr}}M_{\mathrm{sr}})}{M_{\mathrm{sr}}^2\left(1+\frac{1}{k_{\mathrm{sr}}^2 Q_r Q_s}\right)}|I_t|^2 \end{aligned} \tag{3.63}$$

In (3.63), the square of the frequency cancels out in both the numerator and the denominator. The mutual inductances and their angular derivatives are all subject to the geometry of the design. Only the kQ factor U_{sr} is a function of the frequency. It is clear that the torque increases for higher values of U_{sr}^2. The magnetic coupling k is again dependent on the geometry of the system such that the torque is optimized when the Q factor of both coils (Q_r and Q_s) are at their optimal values.

When the mutual inductance between both receiver coils is close or equal to zero, the torque expression can be approximated as:

$$T(\theta) = \frac{M_{\text{ts}}\omega^2 K_{\text{sr}} M_{\text{tr}}}{R_r R_s}|I_t|^2 = \frac{M_{\text{ts}} K_{\text{sr}} M_{\text{tr}} Q_r Q_s}{L_r L_s}|I_t|^2 \tag{3.64}$$

This peak torque value is thus proportional to the quality factors of both receiver coils.

In Sections 2.4.2 and 3.3.1 it was explained that the resistance of a coil can be described as a quadratic dependency on the frequency. The optimal value of the Q factor is reached when the AC resistance is about double the DC resistance of the coil. Around the optimal frequency ω^*, the value of the Q factor is rather stable, meaning that a slight variation of the frequency does not severely impact the performance (Q) of the coil. As long as both the stator and the rotor coil have their optimal Q factor relatively close to each other, a frequency can be chosen such that both Q factors are close to their optimal value. In Section 2.4.2 and 3.3.1 it was also shown that around the optimal frequency, the resistance can be approximated by a linear relation between frequency and resistance $\left(R_r \approx \omega\frac{R_r^*}{\omega_r^*}; R_s \approx \omega\frac{R_s^*}{\omega_s^*}\right)$. The torque expression (3.38) can then be approximated by:

$$T(\theta) = \frac{M_{\text{ts}}(K_{\text{sr}} M_{\text{tr}} - K_{\text{tr}} M_{\text{sr}})}{M_{\text{sr}}^2 + \frac{R_r^* R_s^*}{\omega_r^* \omega_s^*}}|I_t|^2 \tag{3.65}$$

and the ω^2 term again cancels in both the numerator and the denominator. For frequencies around the optimal Q value, the torque is no longer a function of the frequency.

In conclusion, the optimal driving frequency of an RWPT motoring system corresponds to the frequency for which the Q factors of the receiver resonators are close to their optimal values. As long as both resonator coils have their optimal Q value close to each other ($\omega_r^* \approx \omega_s^*$), the optimal driving frequency is evidently chosen.

3.3.3 Capacitor selection and resonator tuning

From Figures 3.10 and 3.11 we can see that the Q factors of both coils are close to their optimal values between f_r^* and f_s^*. Based on the measured self inductance values of the coils, we can estimate proper capacitor values to ensure that the resonance frequencies lie within that range $\left(C_r = \dfrac{1}{\omega^2 L_r} \approx 120\mathrm{nF}\right)$. The resonance frequency of the series connected RLC coil is determined experimentally by connecting the RLC circuit to an AC voltage source with variable frequency and measuring the resulting current. The coil is in resonance when the voltage and the current are in phase. The stator capacitance is varied in steps of 0.5 nF until the stator's resonance frequency approximately coincides with the resonance frequency of the rotor. Table 3.3 summarizes the chosen capacitor values C, their corresponding ESR and loss angle δ_C and the estimated and measured resonance frequencies for both coils.

Table 3.3: The capacitor values of the stator and rotor resonators are tuned to ensure high Q factors and matching resonance frequencies.

Parameter	**Rotor**	**Stator**
C	118.5 nF	71.6 nF
δ_C	0.02%	0.02%
R_{ESR}	32 mΩ	54 mΩ
$\dfrac{1}{2\pi\sqrt{LC}}$	8290 Hz	8288 Hz
f_0	8289 Hz	8284 Hz

3.4 Electrical model validation

3.4.1 FEM assisted design optimization

Finite element modeling (FEM) has proven to be a valuable tool for optimizing a motor design. FEM allows for an accurate estimation of the magnetic field of coil windings, the estimation of the mutual inductance between coils and the evaluation of the exerted forces and torques on the coils. The RWPT motoring system is reconstructed in Comsol Multiphysics. The coils are built as a swept surface over a curved line. Figure 3.12 shows the 3D model of the swept surface coils in the Comsol environment (a) and a possible mesh of the 3D model (b).

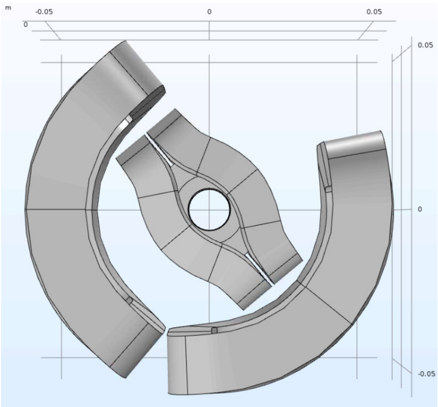

(a)

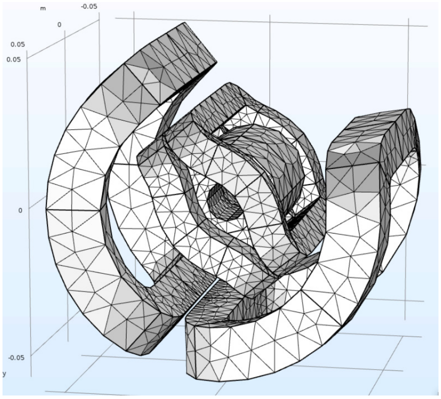

(b)

Figure 3.12: The RWPT motoring system is reconstructed in Comsol Multiphysics. A 3D model of the coils (a) is built and a mesh (b) is generated from the geometry.

For classic electrical machines, a 2D model often suffices. This is because the laminations of electrical steel and the limited air gap force the flux lines to be almost exclusively in the 2D plane, perpendicular to the rotor axle. In the RWPT setup, the limited amount of non-laminated magnetic material does not confine the flux lines in the 2D plane. For this reason, we chose to use a 3D FEM simulation. The mesh that is used for numerically validating the simulated and measured torque profiles is much finer than the illustrative one depicted in Figure 3.12(b). Comsol has multiple presets built-in which generate the 3D mesh with the physics calculations in mind. The mesh was refined using the presets until the RMS error of the mutual inductance M_{tr} (compared to the highest preset *extra fine*) for 8 uniformly spread rotor positions converged to about 1:1000 of the maximum mutual inductance value. Figure 3.13(a) shows the amount of tetrahedra that result from the mesh generation corresponding to the selected presets. Figure 3.13(b) shows the relative error for increasing refining presets. Based on this graph, the *normal* refining preset was selected.

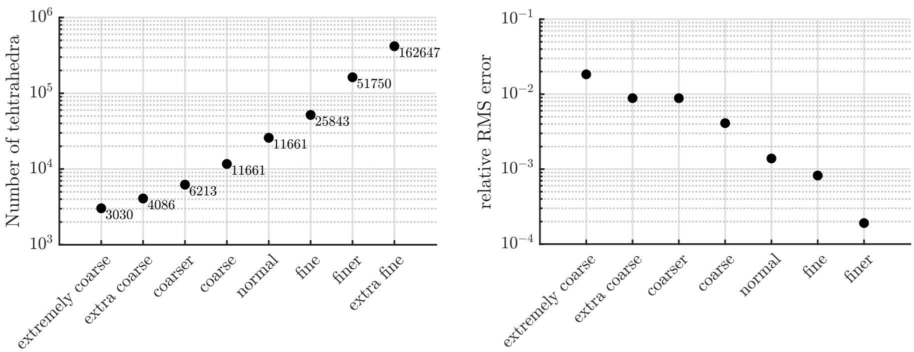

(a) **(b)**

Figure 3.13: The amount of tetrahedra resulting from the mesh generation for the available presets (a) and the relative RMS error on the mutual inductance M_{tr} resulting from simulation with these presets (b).

The FEM analysis is used to find stationary solutions in the frequency domain, resulting in complex valued solutions. This means that the oscillating electrical and magnetic quantities are described by their complex phasor representations. The stationary solution is found by assuming that the phasors do not change over time. The stationary solution is calculated for a fixed rotor position. While the rotor can easily be moved by adjusting rotor angle θ, the rotor does not move during the study. The (simplified) Maxwell equations for the discretized domains are sparsely coupled due to the shared boundaries between domains and the imposed boundary conditions. The most important electromagnetic laws that are imposed are presented.

- The displacement field vector **D** is equal to the electric field vector **E** times the electric permittivity of the medium.

$$\mathbf{D} = \varepsilon_0 \varepsilon_r \mathbf{E} \tag{3.66}$$

- The magnetic flux density vector **B** is defined by the magnetic field vector **H** times the permeability of the medium.

$$\mathbf{B} = \mu_0 \mu_r \mathbf{H} \tag{3.67}$$

- Ampere's circuital law (1.4) is simplified, ignoring the time derivative of the displacement field. The complex current density vector **J** is defined as the curl of the magnetic field vector **H**.

$$\nabla \times \mathbf{H} = \mathbf{J} \tag{3.68}$$

- According to Gauss' law (1.6), the magnetic flux density is a solenoidal vector field ($\nabla \cdot \mathbf{B} = 0$), so that it can be defined as the curl of a magnetic vector potential $\mathbf{A}$.
$$\mathbf{B} = \nabla \times \mathbf{A} \tag{3.69}$$

- On the outer boundary of the model, we assume magnetic insulation. This means that no magnetic flux crosses the outer boundary and the direction of the flux is parallel to the boundary surface. In terms of the vector potential $\mathbf{A}$, this is written as:
$$\mathbf{n} \times \mathbf{A} = 0 \tag{3.70}$$

- The current vector $\mathbf{J}$ and the electrical field vector $\mathbf{E}$ are related by the conductivity (σ) of the material.
$$\mathbf{J} = \sigma \mathbf{E} \tag{3.71}$$

The permittivity, permeability and conductivity are assumed fixed constants for each material type such that non-linear material behavior is neglected. The current density in the tetrahedra is imposed by the user and the resulting voltage drops and magnetic vector potential $\mathbf{A}$ are outputs of the study. The built-in *coil* module in Comsol allows for efficient electromagnetic modeling and simulation of coils. The winding section (S_{coil}) and number of turns per winding (n) is translated into an average current density perpendicular to the swept surface:
$$\mathbf{J}_{\text{coil}} = \frac{nI}{S_{\text{coil}}} \mathbf{1}_{\text{coil}} \tag{3.72}$$
$\mathbf{1}_{\text{coil}}$ is the unit vector perpendicular to the swept surface, in the direction of the coil windings. The losses due to eddy currents inside the conductors (i.e., skin and proximity effect) are also estimated based on the conductor radius and specific resistance ρ_c. The *coil* module also evaluates the amount of flux that is coupled with the coils.

3.4.2 Coil coupling validation

In the FEM model, the mutual inductance between coils can be estimated by applying a current in one coil and evaluating the coupled flux in another coil, using Equation (2.7). On the setup, the mutual inductance between two coils can be evaluated by exciting an alternating current through one coil (in this case 50V RMS at 5 kHz) and measuring the voltage over the open terminals of that second coil. The amplitude and phase of the voltage and current signals are extracted by performing an online Fourier transform in the FPGA. The higher time harmonics that are present are due to noise in the measurement. The

Fourier transform filters out all these higher harmonics. The mutual inductance is then derived as the ratio of the amplitude of the induced voltage in the rotor over the amplitude of the current in the exciting coil times the frequency ω:

$$M_{\mathrm{tr}}(\theta) = \frac{|E_{\mathrm{rt}}|}{\omega|I_{\mathrm{t}}|}; M_{\mathrm{sr}}(\theta) = \frac{|E_{\mathrm{rs}}|}{\omega|I_{\mathrm{s}}|} \tag{3.73}$$

The mutual inductance between the transmitter and the stator is measured on the setup ($M_{\mathrm{ts,meas}} = 0.728$ mH) and simulated using the FEM model ($M_{\mathrm{ts,sim}} = 0.694$ mH). Figure 3.14 compares the rotor angle dependency of the mutual inductance between transmitter and rotor (top) and between stator and rotor (bottom) and their angular derivatives. The estimated mutual inductance by the FEM model corresponds qualitatively to the measured values. The sideways shift of the mutual inductance profiles corresponds to the relative rotation of ϕ_{st} between the transmitter and the stator coil around the rotor axis.

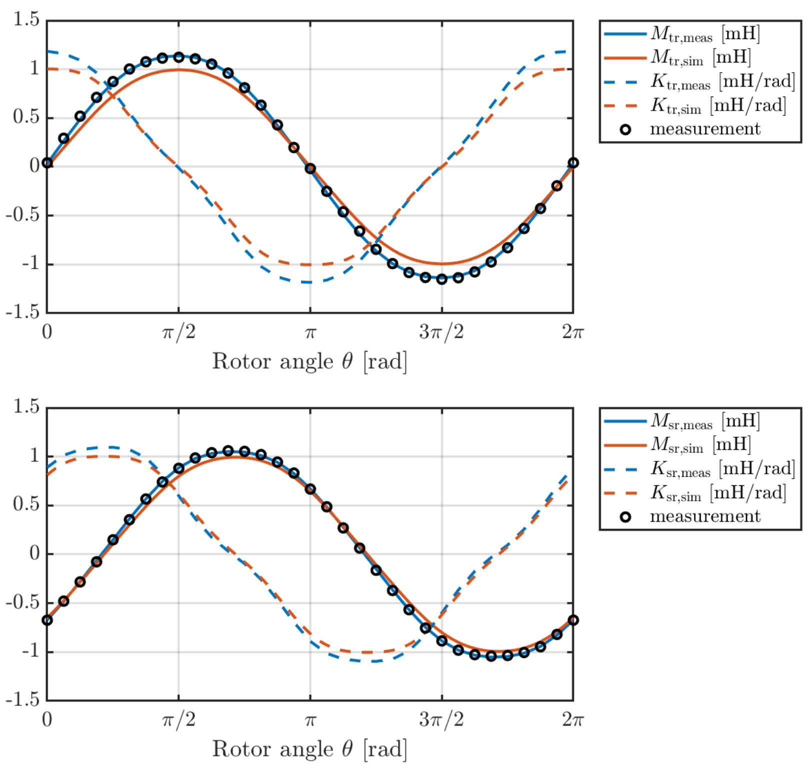

Figure 3.14: The estimated mutual inductance profiles by the FEM model correspond qualitatively to the measured values.

The mutual inductances M_{tr} and M_{sr} are close to sinusoidal for the considered RWPT motoring prototype. The angular derivative of the mutual inductances (K_{tr} and K_{sr}) are thus also close to sinusoidal, although higher spatial harmonics are amplified by the angular derivative.

In Section 3.2.5 we derived that the peak torque will occur for the rotor angle ϕ_{st} for which $M_{\mathrm{sr}} = 0$. For this position, the rotor and stator coils do not affect each other directly. If both the rotor and the stator resonators are in resonance, their currents are in phase, while both currents are out of phase with the transmitter current. Out of phase currents do not exert an average torque on each other. The torque between the stator and rotor coils can be expressed as $\frac{\mathrm{d}M_{\mathrm{sr}}(\phi_{\mathrm{st}})}{\mathrm{d}\theta}|I_r||I_s| \approx 0.0011|I_r||I_s|$. The current limit for both coils would need to exceed 30 A RMS before the torque is out of the range of the torque transducer. The transducer's nominal range is dimensioned to allow for an increase in torque due to geometrical changes or the addition of magnetic material in the rotor core.

3.4.3 System current validation

The setup is driven at a frequency between the resonance frequencies of the closely tuned rotor and stator coils (8286 Hz). A voltage of 100 V RMS is applied to the terminals of the transmitter coil. The current in all three coils was measured using high frequency current probes. The amplitude and phase of the voltage and current signals are again determined using an online Fourier transform. Figure 3.15 shows the measured amplitudes (top) and phases (bottom) of the transmitter, stator and rotor currents and compares them to their simulated counterparts. The resistance values were approximated by their quadratic regression models and the mutual inductance values were obtained by interpolating the measured mutual inductance profiles.

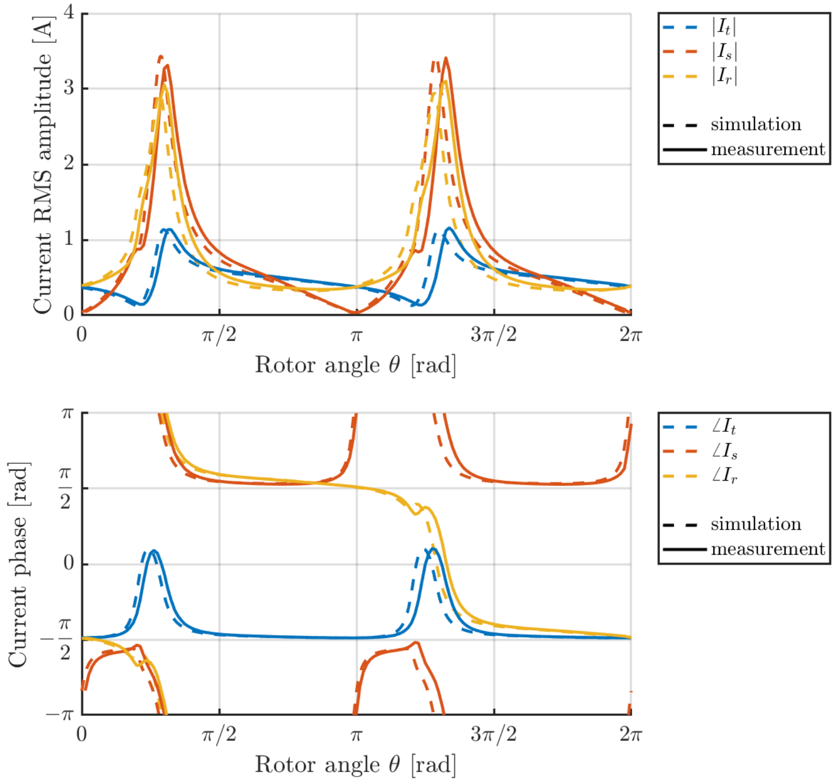

Figure 3.15: The measured current amplitudes (top) and phases (bottom) correspond well to the simulated values.

The sideways shift in the current measurements is explained by the limited accuracy of the optical sensor, which is used as the Z signal trigger of the encoder to recalibrate the position of the rotor. As expected, the stator and rotor currents reach their peak values for low magnetic coupling ($M_{\mathrm{sr}} \approx 0$). Around this zero coupling point, the phase of the rotor and stator shift by π radians. The rotor current phase shows a 2π shift after a full rotation, while the transmitter and stator current phases oscillate periodically for every half rotation. The transmitter current I_t generally lags behind the voltage V_t by $\pi/2$. When the stator and rotor coils are barely coupled, the current in the transmitter decreases drastically, indicating a high reflected impedance. A point is reached where the total transmitter impedance is slightly capacitive. We can directly validate the expression for the total transmitter impedance Z_{tot}, which is the series connection of the transmitter impedance and the reflected impedance

Z_{ref} (3.39):

$$Z_{\text{tot}} = R_t + j\omega L_t + \frac{\begin{bmatrix} \omega^2 M_{\text{ts}}^2 (R_r) + \omega^2 M_{\text{tr}}^2 (R_s) \\ - j2\omega^3 M_{\text{ts}} M_{\text{tr}} M_{\text{sr}} \end{bmatrix}}{\omega^2 M_{\text{sr}}(\theta)^2 + R_r R_s} \tag{3.74}$$

The total transmitter impedance can be found by dividing the phasor of the excitation voltage V_t by the phasor of the transmitter current:

$$Z_{\text{tot}} = \frac{V_t}{I_t} \tag{3.75}$$

Figure 3.16 compares the derived total transmitter impedance (3.75) with the analytical model (3.74).

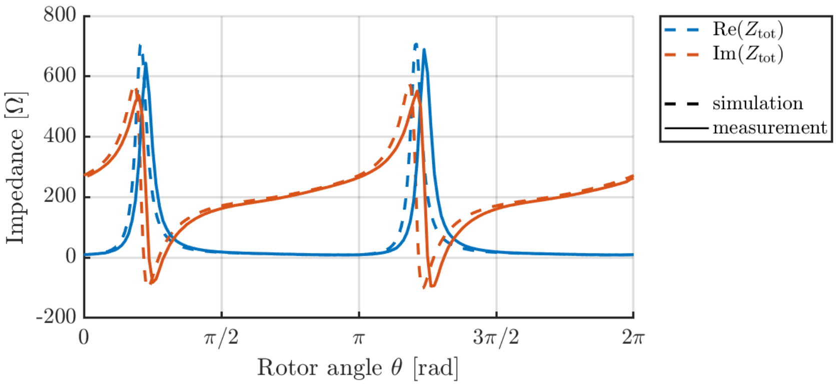

Figure 3.16: The derived total transmitter impedance corresponds well to its simulated counterpart. Z_{tot} shifts from capacitive to resistive and inductive values depending on the coupling of the transmitter with the resonator coils.

The total transmitter impedance varies from capacitive to inductive values, with a real value for $M_{\text{sr}} \approx 0$. The bias in the imaginary part of Z_{tot} is due to the self inductance of the transmitter coil L_t ($X_t = \omega L_t \approx 268\Omega$).

3.5 Torque model validation

3.5.1 Direct FEM based torque simulation

The FEM model can be applied to calculate the force vector $\mathbf{F}$ on the boundaries of the domains:

$$\mathbf{F} = \int_S \mathbf{n}_S \mathbf{T} \mathrm{d}S \tag{3.76}$$

with $\mathbf{n}_S$ the normal vector of surface S and $\mathbf{T}$ the Maxwell stress tensor. The torque vector τ on a domain (with reference to position $\mathbf{r}_0$) is proportional to the force vector $\mathbf{F}$ and distance of the boundary surface to position $\mathbf{r}_0$:

$$\boldsymbol{\tau} = \int_S (\mathbf{r} - \mathbf{r}_0) \times (\mathbf{n}_S \mathbf{T}) \mathrm{d}S \tag{3.77}$$

The torque around a given rotation direction $\mathbf{r}_{\mathrm{ax}}$ is found by projecting $\boldsymbol{\tau}$ on the unit vector of that axis:

$$\tau_{\mathrm{ax}} = \frac{\mathbf{r}_{\mathrm{ax}}}{|\mathbf{r}_{\mathrm{ax}}|} \cdot \boldsymbol{\tau} \tag{3.78}$$

The Maxwell stress tensor is calculated from the instantaneous currents and magnetic fields in the domains. In this section, we will streamline the calculation of the torque for a system with sinusoidal currents by rearranging the formula for the average torque found in Section 3.2.2. In (3.29) the torque on the rotor axle was described as:

$$T_{\mathrm{av}}(\theta) = \frac{1}{2} \left(\mathbf{i}^{\mathrm{H}} \begin{bmatrix} 0 & 0 & K_{\mathrm{tr}}(\theta) \\ 0 & 0 & K_{\mathrm{sr}}(\theta) \\ K_{\mathrm{tr}}(\theta)^{\mathrm{T}} & K_{\mathrm{sr}}(\theta)^{\mathrm{T}} & 0 \end{bmatrix} \mathbf{i} \right) \tag{3.79}$$

The torque expression can be worked out to

$$\begin{aligned} T(\theta) &= \frac{1}{2} \left(\left[\mathrm{Re}(\mathbf{i})^{\mathrm{T}} - j\mathrm{Im}(\mathbf{i})^{\mathrm{T}} \right] \mathbf{K} \left[\mathrm{Re}(\mathbf{i}) + j\mathrm{Im}(\mathbf{i}) \right] \right) \\ &= \frac{1}{2} \begin{bmatrix} \mathrm{Re}(\mathbf{i})^{\mathrm{T}} \mathbf{K} \mathrm{Re}(\mathbf{i}) + j\mathrm{Re}(\mathbf{i})^{\mathrm{T}} \mathbf{K} \mathrm{Im}(\mathbf{i}) \\ - j\mathrm{Im}(\mathbf{i})^{\mathrm{T}} \mathbf{K} \mathrm{Re}(\mathbf{i}) - j\mathrm{Im}(\mathbf{i})^{\mathrm{T}} \mathbf{K} \mathrm{Im}(\mathbf{i}) \end{bmatrix} \end{aligned} \tag{3.80}$$

The matrix of the angular derivative of the mutual inductance $\mathbf{K}$ is real valued and symmetrical, such that $\mathrm{Im}(\mathbf{i})^{\mathrm{T}} \mathbf{K} \mathrm{Re}(\mathbf{i}) = \mathrm{Re}(\mathbf{i})^{\mathrm{T}} \mathbf{K} \mathrm{Im}(\mathbf{i})$. Equation (3.80) can then be simplified to:

$$T(\theta) = \frac{1}{2} \left[\mathrm{Re}(\mathbf{i})^{\mathrm{T}} \mathbf{K} \mathrm{Re}(\mathbf{i}) + \mathrm{Im}(\mathbf{i})^{\mathrm{T}} \mathbf{K} \mathrm{Im}(\mathbf{i}) \right] \tag{3.81}$$

In this restructured equation, no complex values are present anymore. Both terms of (3.81) correspond to the equation for the torque between two DC current carrying coils. To find the torque in an RWPT motoring system, it is sufficient to simulate two DC current situations in the FEM model and add the results. To generalize the DC current expression, we rotate each phasor by ϕ_{rot}. The rotated vector is denoted by $\mathbf{i}' = e^{j\phi_{\mathrm{rot}}} \mathbf{i}$. The torque expression (3.79) can be rewritten as

$$T(\theta) = \frac{1}{2} \left(\mathbf{i}^{\mathrm{H}} \mathbf{K} \mathbf{i} \right) = \frac{1}{2} \left(e^{j\phi_{\mathrm{rot}}} \mathbf{i}'^{\mathrm{H}} \mathbf{K} \mathbf{i}' e^{-j\phi_{\mathrm{rot}}} \right) = \frac{1}{2} \left(\mathbf{i}'^{\mathrm{H}} \mathbf{K} \mathbf{i}' \right) \tag{3.82}$$

By the same restructuring of (3.81), the torque can be rewritten as:

$$T(\theta) = \frac{1}{2}\left[\mathrm{Re}(\mathbf{i}')^{\mathrm{T}}\mathbf{K}\mathrm{Re}(\mathbf{i}') + \mathrm{Im}(\mathbf{i}')^{\mathrm{T}}\mathbf{K}\mathrm{Im}(\mathbf{i}')\right] \tag{3.83}$$

This derivation proves that rotating the current phasors (or equivalently, changing the reference direction of the complex phasor plane) does not affect the decomposition of the torque formula into two DC current simulations. The real and imaginary parts of a current phasor correspond to the instantaneous value of a current with a time difference of $\Delta t = \frac{\pi}{2\omega}$, while rotation of the phasor is equivalent to shifting the AC current waveform in time. It is thus possible to simulate the AC rotor torque by evaluating two DC simulations, as long as the DC currents correspond to instantaneous AC currents, shifted by $\pi/2$. Evaluation of a DC simulation severely lowers the time needed to estimate the torque compared to a full AC simulation.

The simulated currents of Figure 3.15 are now decomposed into their real and imaginary parts. The two terms inside the brackets of (3.81) correspond to the DC torque generated by the real and imaginary parts of the current phasors ($T_{\mathrm{real,sim}}$ and $T_{\mathrm{imag,sim}}$). The average AC torque ($T_{\mathrm{av,sim}}$) is then equal to the average of both terms. Figure 3.17 compares the closed-form torque expressions with the FEM based simulated DC torque values.

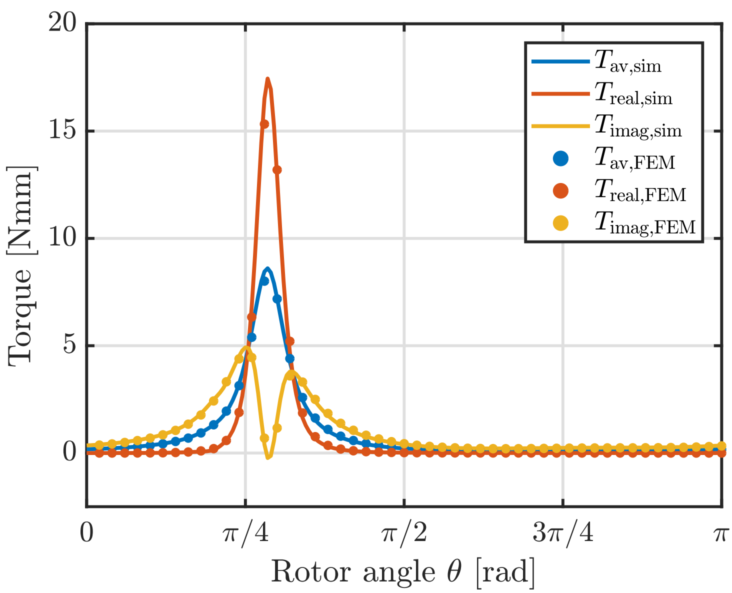

Figure 3.17: The average AC torque can be expressed as the average of two DC current torques.

The simulated torque profile corresponds to the closed-form expression, indicating that the simplified DC decomposition is equivalent to a full AC torque simulation.

3.6 Experimental torque validation

The stepper motor moves the rotor over a full rotation in steps of $\pi/80$ rad. For every stop, 100 V RMS is applied to the transmitter terminals, while the holding torque of the stepper motor counteracts the torque generated by the RWPT motoring system. The analog torque signal of the torque transducer (-10 V..+10 V) is converted to its nominal range (-1Nm..+1Nm) and recorded. The axial forces and the friction in the bearings introduce a bias in the torque measurements. To eliminate this bias, the same measurement is repeated without any voltage applied to the transmitter terminals (see Figure 3.18(a)). A sinusoidal bias is observed, corresponding to a slight misalignment of the rotor axle or an asymmetric weight distribution in the rotor core. Figure 3.18(b) shows the measured torque over half a rotation. The torque profile repeats for the second half of the rotation. The measured torque corresponds very well to the simulated torque profile.

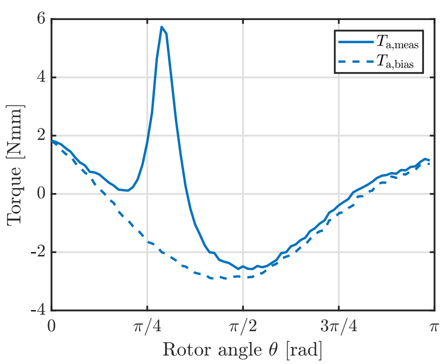

(a)

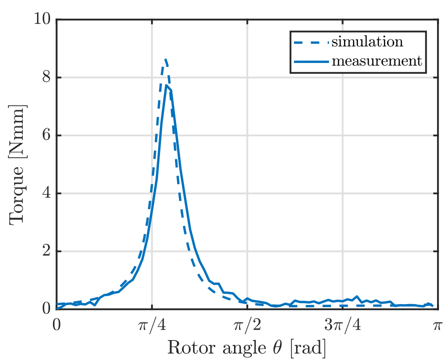

(b)

Figure 3.18: The measurement bias is identified for each rotor angle (a). The location and amplitude of the torque peak was accurately predicted by the analytical model (b).

3.7 Magnetic materials for RWPT motoring systems

Magnetic materials are generally added in electromagnetic motoring systems to improve the torque output. Magnetic materials can be added in the form of hard magnetic materials (with high coercivity and remanence) such as permanent magnets or soft magnetic materials (with low coercivity and remanence) such as electrical steel. The magnetic flux density B inside the material follows the magnetic field H. The magnetization characteristic of a material can be illustrated by hysteresis curves (see Figure 3.19). The coercivity of a material H_c is a measure for how much reverse magnetic field is required to demagnetize it. The remanence of a material is the magnetization B_r that is retained when the external magnetic field drops to zero.

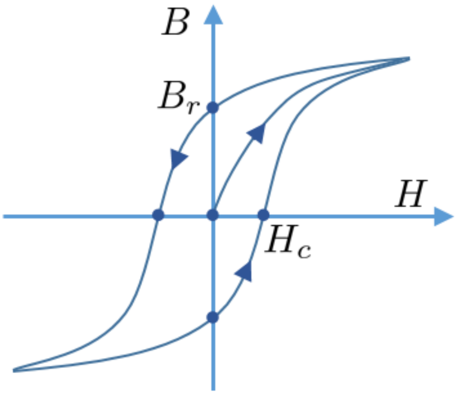

Figure 3.19: The magnetic flux density B inside a magnetic material follows the magnetic field H. The hysteresis curve of a magnetic material is (in part) characterized by its remanence B_r and its coercivity H_c.

Magnetic material allows to increase the magnetic coupling between coils and increase the flux density for a given current, by reducing the reluctance of the flux path. Electromagnetic forces are proportional to $I \times B$, such that the addition of magnetic material allows for higher torque densities.

The varying magnetic field in the magnetic material induces Foucault currents (or eddy currents) inside the material. Iron and steel generally have high conductivity, such that high losses are generated in the material. For this reason, stator and rotor cores are often laminated to limit the possible paths for the Foucault currents. For high frequencies, a lower penetration depth for the Foucault currents is observed, similar to the skin effect in a conducting wire. The penetration depth of a conductive sheet is expressed as:

$$\delta = \sqrt{\frac{2\rho}{\omega\mu_r\mu_0}} \tag{3.84}$$

Wireless power transfer requires frequencies of at least a few kHz, but often up to several MHz. For these frequencies, the Foucault losses are extremely high, even for very thin sheets of laminated cores. For wireless power transfer applications, soft ferrite material is more often incorporated to improve the magnetic properties of the designs [31,50–53]. Soft ferrites with low coercivity are also widely used as low dissipation inductor cores in RF applications and HF transformer cores. Ferrites are ceramic compounds of the transition metals with oxygen and iron oxides, e.g. MnZn and NiZn, with high relative permeability and very high resistivity, thus limiting dissipation. In RWPT, ferrite cores are used to strengthen the local magnetic field, which in turn increases the induced voltage in a receiver coil. Ferrites can also be used to effectively direct the flux paths through the system coils and to close the magnetic paths to limit stray fields around high power applications.

3.7.1 Ferrite material properties

The resistivity of ferrites (over 0.01 Ωm) is significantly higher than that of electrical steel (about $4.72 \cdot 10^{-7}$ $\Omega\mathrm{m}$ for 3% silicon content) or pure iron ($9.61 \cdot 10^{-8}$ $\Omega\mathrm{m}$). Electrical steel is an iron alloy which can have up to 6.5% silicon content. Commercial alloys stay under 3.2% to avoid negative material properties such as brittleness. For a given induced voltage, the eddy current losses are approximately proportional to the conductivity of the material, such that ferrites have much lower eddy current losses than steel. Due to their ferrimagnetic properties, ferrites inherently have a much lower magnetic saturation of up to 0.6 T, while ferromagnetic materials such as electrical steel can have saturation values up to 1.9 T. The relative permeability of ferrites varies widely from μ_r = 10..20000 [116] compared to about 4000..5000 for electrical steel [117–119] and 500 to 200 000 for pure iron, depending on the purity [120]. For AC applications, ferrites with low coercivity are used. This means that the induced magnetic flux density B easily follows variations in the magnetic field H, thus limiting the hysteresis losses.

In literature, the loss mechanisms in magnetic materials are grouped in three sections [121–126]:

- The change in magnetization in the material generates losses. For a non-zero coercivity, the magnetic induction B does not directly follow the magnetic field H. The required energy to make a full loop in the BH-plane is equal to the area enclosed by the loop:

  $$W_{\mathrm{h}}[\mathrm{W/m^3}] = \oint H dB \tag{3.85}$$

  For low frequencies, the BH-curve only depends on the peak value of the magnetic field and the dissipated power per cycle is considered quasi-static (independent of f). For higher frequencies and non-negligible saturation, the hysteresis losses in magnetic materials can be empirically described by the modified Steinmetz equation (MSE) [127]:

$$P_{\mathrm{h}}[\mathrm{W/m^3}] = C_h f^{\alpha_h} \hat{B}^{\beta_h} \tag{3.86}$$

with C_h, α_h and β_h material dependent empirical constants. α_h and β_h are non-integer values ($1 < \alpha_h < 3; 2 < \beta_h < 3$).

- For ferrimagnetic materials with low conductivity, the eddy current loss is described by a material property, neglecting the geometry of the ferrite core. This also means that the magnetic field of the eddy currents themselves are ignored. Under these conditions, the local eddy current losses in the core are expressed by a quadratic dependency on the induced voltage in the material [121, 127, 128]:

$$P_{\mathrm{e}}[\mathrm{W/m^3}] = C_2 \frac{f^2 \hat{B}^2}{\rho_f(f)} \tag{3.87}$$

with C_2 an empirically determined parameter which is dependent on the cross section and the conductivity of the core. $\hat{B}$ is the peak amplitude of the magnetic field. For frequencies over 10 kHz, the resistivity of the ferrite ($\rho_f(f)$) drops significantly [121, 124, 129].

- The residual losses W_{res} originate in dielectric effects [123], the release of energy by the precessing spins to the lattice (spin damping) and movement of the domain walls [121, 128, 130–132]. The Landau-Lifshiz-Gilbert equation can be used to model the spin damping, especially for very high frequencies (in the MHz range). The quantitative predictive power of the models for spin damping and domain wall effects is generally low and the residual loss W_{res} is often used as a term to cover all effects that cannot be modeled quantitatively [130]. The contribution of spin damping is limited for frequencies under 10 kHz [122].

In data sheets of ferrite material grades, the hysteresis loss is often described by a complex frequency dependent relative permeability with a negative imaginary component.

$$\mu_r = \mu' - j\mu'' \tag{3.88}$$

From this definition of the complex permeability, one can also define a loss angle ($\delta_\mu = \frac{\mu''}{\mu'}$), which represents the ratio of the hysteresis losses per cycle compared to the average magnetic energy stored in the material. A sinusoidal magnetic field H can be written in the phasor representation ($H = H_0 e^{j\omega t}$). The flux density B will then lag behind the magnetic field H:

$$B = (\mu' - j\mu'')H_0 e^{j\omega t} \tag{3.89}$$

and the area of the BH-curve will increase. The hysteresis loss per cycle is then equal to the enclosed area of this BH-curve. Figure 3.20 shows the approximated hysteresis curve for a magnetic material that is characterized by a complex permeability, for a fixed real part of the permeability μ' and increasing ratios of $j\mu''$ and μ'.

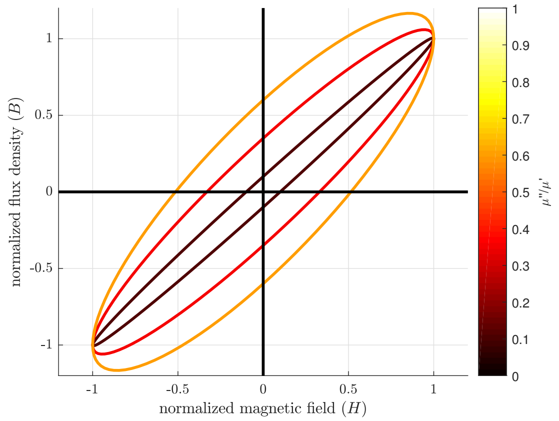

Figure 3.20: For a material with a complex permeablity, the magnetic flux density B lags behind the magnetic field H, resulting in an oval shaped BH curve.

The coordinates of the BH curve can be represented as

$$\langle H, B\rangle = \langle H_0 \cos(\omega t), \mu' H_0 \cos(\omega t) - \mu'' H_0 \sin(\omega t)\rangle \tag{3.90}$$

which can be subdivided in a flat linear trajectory

$$\langle H_{\text{lin}}, B_{\text{lin}}\rangle = \langle H_0 \cos(\omega t), \mu' H_0 \cos(\omega t)\rangle \tag{3.91}$$

and an ellipse shaped path

$$\langle H_{\text{el}}, B_{\text{el}}\rangle = \langle H_0 \cos(\omega t), -\mu'' H_0 \sin(\omega t)\rangle \tag{3.92}$$

The enclosed area of the BH-curve can thus be calculated as the area of an ellipse with a width of $2H_0$ and a height of $2\mu'' H_0$.

$$W_{\text{mag}}[\text{W}/\text{m}^3] = \oint H dB = \mu'' H_0^2 \pi \tag{3.93}$$

When the complex permeability approximation holds, the losses in the ferrite scale linearly with the imaginary part of the permeability μ'' and the frequency of the magnetic field, while they scale quadratically with the amplitude of the magnetic field. This corresponds to the MSE with $\alpha_m = 1$ and $\beta_m = 2$. On the microscopic scale, the material losses are caused by the damping of domain wall movement by eddy currents and spin relaxation. It is often argued that there is no physical distinction between eddy current losses and hysteresis losses (or static and dynamic losses) in the discrete domains of the material. On the macroscopic level, however, these mechanisms help to substantiate the rationale behind the shape of the empirical MSE models for the core losses.

If the magnetic field through a ferrite core is generated by a single current carrying coil, the magnetic field in the core is proportional to the current in that coil, such that the losses scale quadratically with the current in the coil. Note that for low enough frequencies, the eddy current losses also scale quadratically with the amplitude of the magnetic flux (and the current that causes it). This means that the combined losses in the ferrite core can be translated into an additional equivalent series resistance in the coil.

3.7.2 Q factor improvement

A ferrite core is added in the provisioned cylindrical space inside the rotor body, depicted in Figure 3.21.

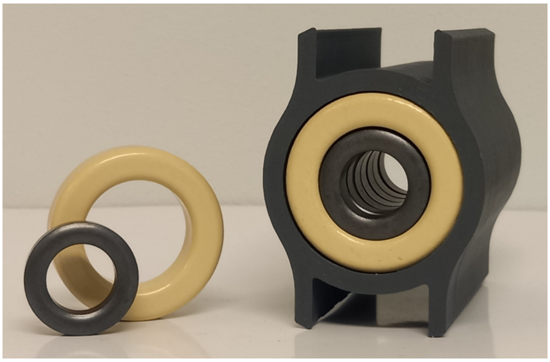

Figure 3.21: Toroidal ferrite cores are stacked to fill the cylindrical space in the rotor.

The ferrite core has a much lower magnetic reluctance than the air surrounding the coil. The magnetic flux of the coils thus increases, such that their self inductance values also increase. Figures 3.22 and 3.23 compare the resistance (left) and the Q factor (right) for the same rotor and stator coils with and without a ferrite core. The quadratic frequency dependency is again validated by an accurate fitted curve. The addition of a ferrite core increases the equivalent series resistance of the coil. The quality factors of the coils increase however because of the increased self inductance. The peak value of the Q factor also shifts to a lower frequency because the total AC resistance value reaches the double of the DC resistance for a lower frequency.

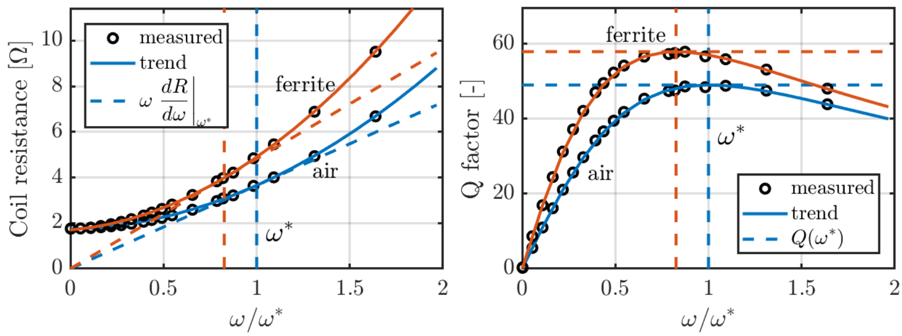

Figure 3.22: Measured resistance and Q factor values of the rotor coil in the experimental setup with and without ferrite core. The optimal Q factor increases in value and shifts to a lower frequency.

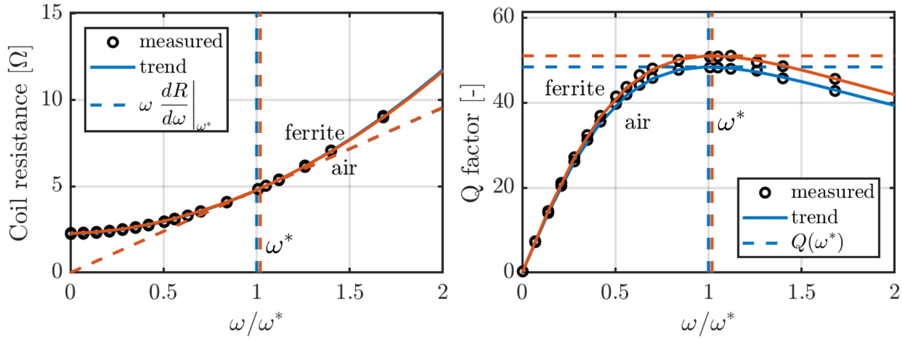

Figure 3.23: Measured resistance and Q factor values of the stator coil in the experimental setup with and without ferrite core. The resistance and Q factor of the stator are affected less than those of the rotor.

The measurements for the stator coil are also representative for the transmitter coil, as the relative position of the ferrite core to both the transmitter coil and the stator coil are the same. Table 3.4 summarizes the measured and derived coil parameters in the presence of a ferrite rotor core. The quality factors of the rotor and the stator are increased by 18% and 5% respectively. The linear frequency term p_1 increased significantly for the rotor compared to the air coil. This shows that the magnetization losses in the core also contribute to the equivalent series resistance of the coils.

Table 3.4: The rotor and stator coil parameters were measured on the setup with ferrite core and their optimal driving frequency f^* and Q factor Q^* were derived.

Parameter	Rotor	Stator
L	4.85 mH	5.44 mH
R_{DC}	1.69 Ω	2.26 Ω
p_1	1.24e-05 Ω/rad	7.73e-06 Ω/rad
p_2	7.50e-10 Ω/rad^2	1.08e-09 Ω/rad^2
f^*	7562 Hz	7284 Hz
Q^*	57.93	50.99

3.7.3 Coil coupling improvement

In Section 3.2.5 it was shown that the torque in an RWPT motoring system increases for higher Q factors of the coils and higher peak mutual inductance values between the system coils. While the ferrite introduces additional losses in the system for the same currents, the ferrite core also significantly increases the mutual inductance between the system coils. A large part of the magnetic flux of the coils is directed through the core. Coils that are in the close vicinity of the ferrite core thus tend to have higher magnetic coupling. Figure 3.24 compares the mutual inductance profiles between the coils in the FEM before and after a ferrite core is added inside the rotor coil. The mutual inductance between the rotor coil and the stationary coils is increased by 57%, while the coupling between the transmitter and the stator is increased by 23% to 0.895 mH.

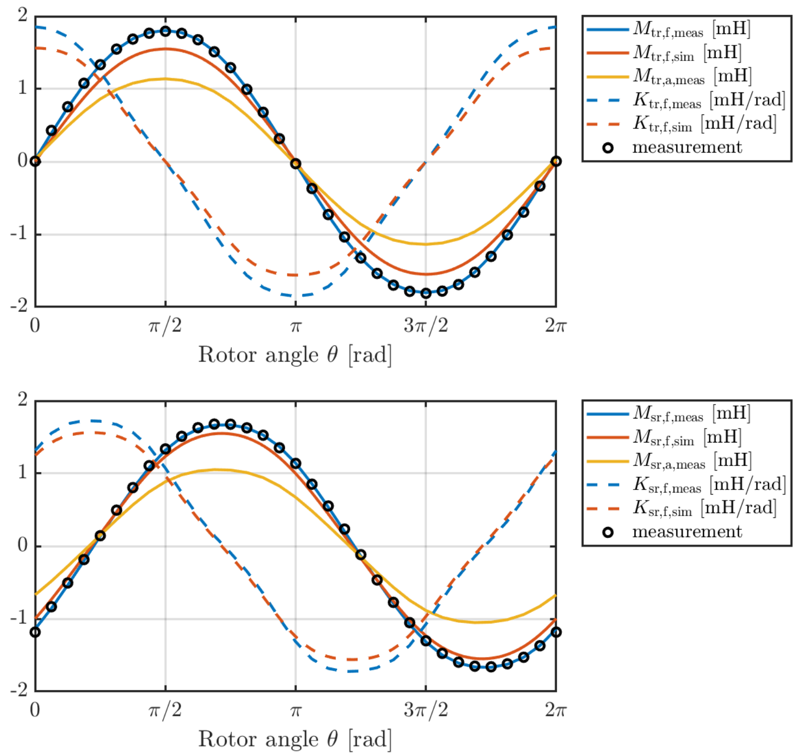

Figure 3.24: The mutual inductance profiles $M_{\mathrm{tr}}(\theta)$ (top) and $M_{\mathrm{sr}}(\theta)$ (bottom) were simulated in the FEM model and measured on the setup with ferrite rotor core. The measured mutual inductance profile without the air coil is also shown to illustrate the increase of magnetic coupling due to the added ferrite core.

Nonlinearity of ferrite losses for multiple coils

For a single current carrying coil near a core made of non-saturating magnetic material, we can assume that the local magnetic field inside the core always scales linearly with the current in that coil. When two current carrying coils are placed near a non-saturating magnetic core, the local magnetic fields (H) and the resulting flux densities (B) can still be linearly superposed for each spatial component (e.g. $B = [B_{1\mathrm{x}} + B_{2\mathrm{x}}, B_{1\mathrm{y}} + B_{2\mathrm{y}}]$). This linear property however does not hold for the amplitude of the magnetic field and flux density. This property is required to deduce a quadratic dependency between the current in a coil and the magnetic and electric losses inside the magnetic core. This is illustrated using a 2D FEM simulation of two infinitely long current carrying coils that are placed close to a magnetic core. Each coil consist of 10 turns and carries a current of 1 A. The magnetic material is characterized by a complex permeability ($\mu_r = 12000 - j120$). The real part of the permeability corresponds to the permeability of the ferrite core in the setup. The imaginary part of the permeability and the electric conductivity are highly variable for different ferrite materials. For this simulation, the imaginary part of the permeability and the electric conductivity ($2.5\Omega\mathrm{m}$) were manually chosen to make the resulting losses similar in value. Figure 3.25 shows the distribution of the hysteresis losses (left) and the eddy current losses (right) $[\mathrm{W/m^3}]$ when both coils carry a current of 1 A (in phase).

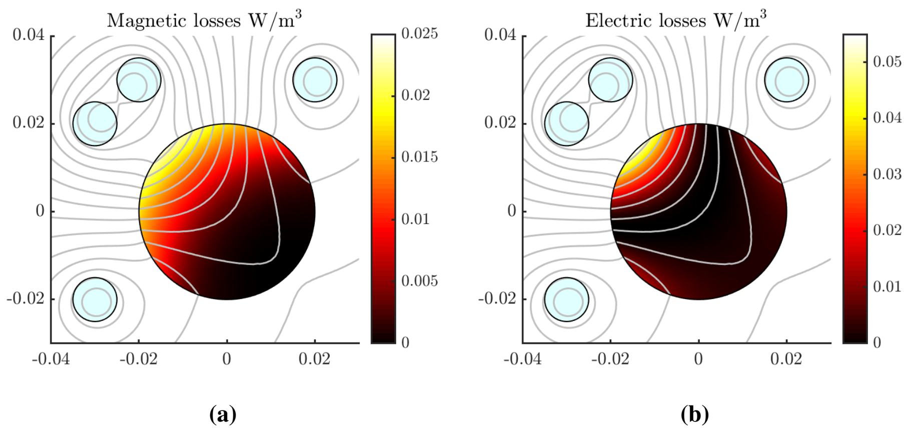

Figure 3.25: The distribution and magnitude of the hysteresis losses (a) and eddy current losses (b) in a ferrite coil in the proximity of two current carrying coils.

When we vary the phase difference between the currents in both coils, the total dissipation in the core also changes drastically. The losses are integrated over the section of the magnetic core for increasing phase difference between the currents in both coils (see Figure 3.26).

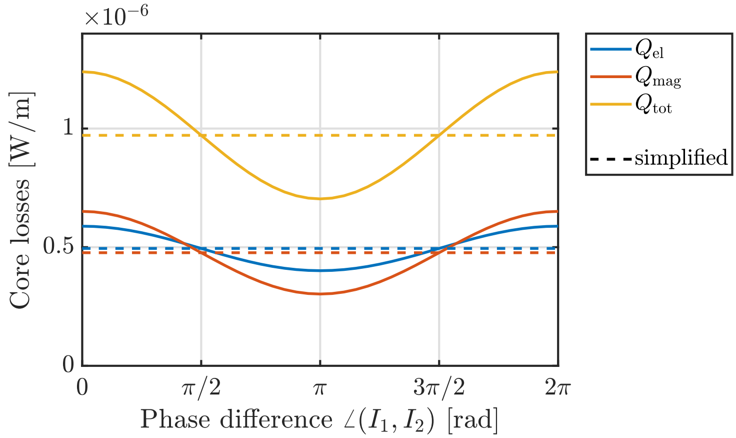

Figure 3.26: For fixed current amplitudes and varying phase shift between the coil currents, the magnetic and electrical losses vary significantly.

Even though the current amplitudes in both coils stay the same, the losses are highly variable. When the magnetic fields of both coils oppose each other, the local magnitude of the flux density decreases, such that the hysteresis and electrical losses also decrease. We can thus conclude that the dissipation in the magnetic core can no longer be attributed to both current carrying coils by an equivalent series resistance in both coils.

The simplified loss model represents the losses as dissipation in a series connected equivalent resistance. Because the real core losses are now dependent on the fields of nearby coils (and the current in those coils), the electrical model for the RWPT loses accuracy. In further analysis, we ignore the effect of nearby coils and the resistance of the coils is modeled using the quadratic fit of Figures 3.22 and 3.23. This is equivalent to calculating the losses for each coil separately, while the other coil has no current. In Figure 3.26, the dashed lines represent the sum of the losses for isolated coils. If we use an equivalent resistance to capture the magnetic core losses, the corresponding losses are close to the average expected value if the phase difference between the currents was unknown.

3.7.4 Retuning of the capacitors

The addition of the ferrite core increases the self inductance values of the rotor and stator coils, while their optimal Q factor shifts to lower frequencies. If rotor capacitor remains identical, the resonance frequency of the rotor shifts to 6630 Hz. The self inductance of the stator has not increased as much as the rotor, such that a larger capacitor value is required to tune its resonance frequency to that of the rotor. Table 3.5 lists the new capacitor values, their equivalent series resistance and the resulting resonance frequencies.

Table 3.5: The capacitor value of the stator is adjusted to match the lowered resonance frequency of the rotor.

Parameter	Rotor	Stator
C	118.5nF	106.7 nF
δ_C	0.02%	0.02%
R_{ESR}	41 mΩ	45 mΩ
$\frac{1}{2\pi\sqrt{LC}}$	6639 Hz	6606 Hz
f_0	6630 Hz	6632 Hz

3.7.5 System current validation

Following the same procedure as described in Section 3.4.3, the simulated current amplitudes and phases are validated on the RWPT motoring setup with a ferrite core for a transmitter voltage of 100V RMS. Figure 3.27 compares the simulated and measured coil currents.

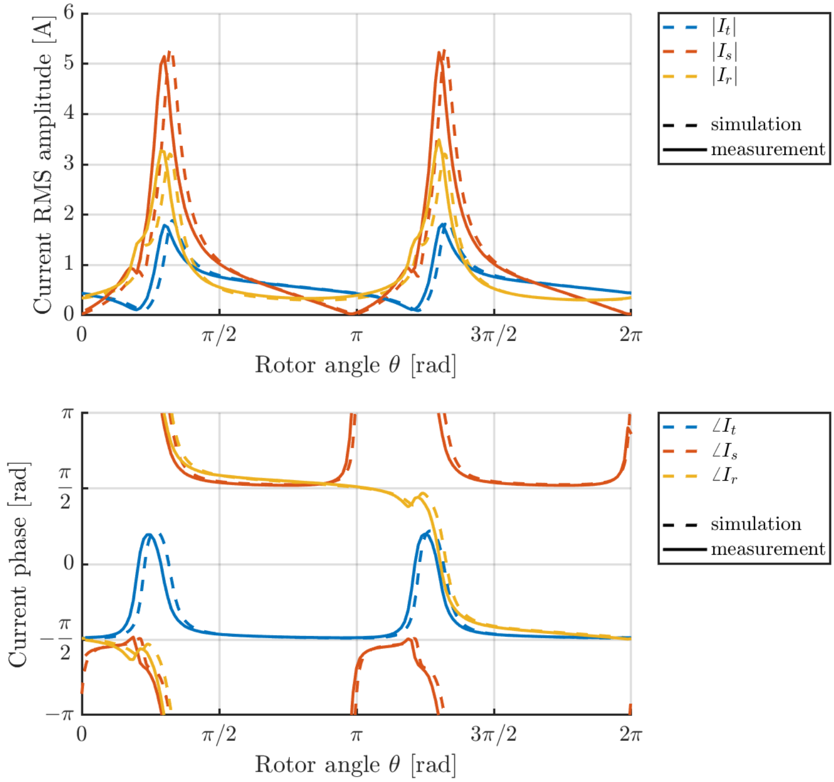

Figure 3.27: The measured current amplitudes (top) and phases (bottom) of the RWPT motoring system with ferrite core correspond well to the simulated values.

The phases of the currents follow a similar trajectory compared to the currents of the setup without a ferrite rotor core. The increased Q factors and mutual inductance values cause significantly higher peak currents in the coils. The increased mutual inductance values also increase the reflected impedance and consequently the total transmitter impedance (see Figure 3.28).

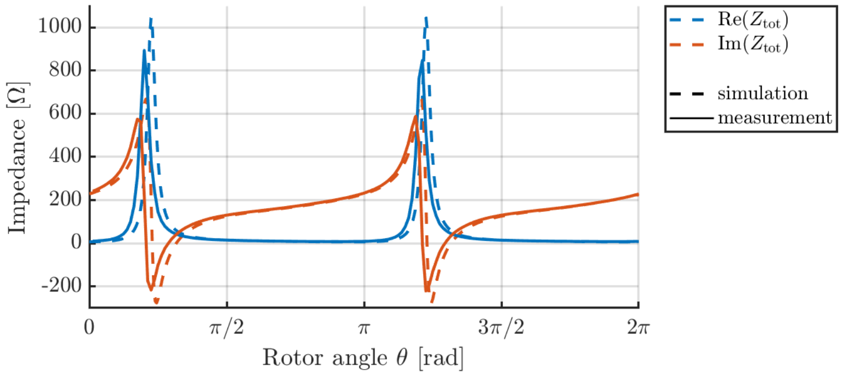

Figure 3.28: The increased current amplitudes and magnetic coupling result in a higher reflected impedance.

3.7.6 Torque model validation

The accuracy of the electrical model is still sufficient to analyze the effect of the ferrite core on the currents in the system. We do however observe a larger deviation (i.e. an overestimation) in the system currents. In Section 3.2.5 it was derived that the torque in an RWPT system increases with the magnetic coupling between the coils and the Q factor of the stator and rotor coils. Because of this, we expect an increase in the torque for the setup with a ferrite rotor core. To account for the potential bias in the measurements, the torque is again measures twice for each rotor position (see Figure 3.29(a)), once with the AC power source tuned off and once with the AC power source turned on. A similar sinusoidal bias is observed in the rotor with ferrite core. Figure 3.29(b) shows that the peak torque indeed increased by 144%. The slight overestimation of the currents in the coils also translates into a minor overestimation of the torque generated on the rotor.

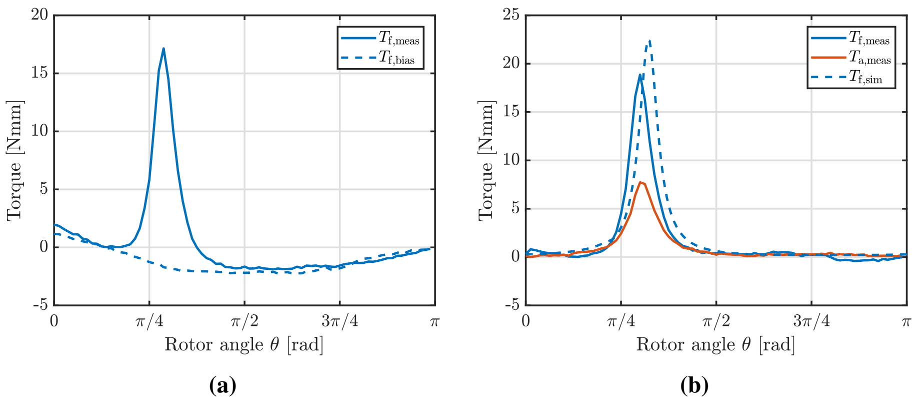

Figure 3.29: The peak torque increases by 144% when adding a ferrite rotor core (b).

3.8 Conclusion

In this chapter we developed an analytical model to simulate the currents and the torque generation in a multicoil resonator system. We showed that the torque is unidirectional for resonant tuning and motoring operation is possible. Torque profile expressions were derived for voltage and current controlled transmitter power sources. A three coil prototype was developed to experimentally validate the simulated coil currents and torque on the rotor coil. The prototype was reconstructed in a 3D FEM model. We derived efficient methods to evaluate the magnetic coupling between the coils and to evaluate the torque. We also explored the possibility of adding a cylindrical ferrite core inside the rotor coil and quantified its effect on the electrical parameters and the torque generation. Despite the additional eddy current losses and hysteresis losses (translated to an equivalent series resistance in the coils), the Q factors of the coils increase due to higher self inductance values. The higher Q factors and magnetic coupling between the coils result in an 144% increase in the peak torque value.

Chapter 4

Improving Torque in a Magnetic Resonance Based Motoring System by Detuning from Resonance

4.1 Introduction

Resonant wireless power transfer (RWPT) allows for efficient transfer of electrical energy over an air gap, by optimally tuning a receiver resonator. Next to transferring electrical energy to supply or charge a device, the previous chapter demonstrated that the induced current in receiver resonators can be directly applied to exert mechanical torque on a rotor axle. The peak torque however only occurs when both receiver coils are uncoupled because the magnetic coupling of two receiver resonators strongly affects their current. In this chapter, we investigate the effect of intentionally detuning the resonators coils in a RWPT motoring system on its torque generation capability.

To generate torque, the induced current should be sufficiently high and be (partly) in phase with the excitation current or the induced current of another resonator. Naturally, the transmitter and receiver currents are out of phase. A slight detuning of the system can bring the currents (more) in phase while reducing the current amplitudes. The detuning of the system thus constitutes a non-trivial trade-off between phase difference and current amplitude. Additionally, having receiver coils that are strongly coupled can significantly change their respective current amplitude and phase [26,45,133]. It was observed in the previous chapter that the rotor and stator current reached their highest values when both coils were not coupled ($M_{\mathrm{sr}} = 0$). For nonzero values of their magnetic coupling, both currents were strongly affected in both amplitude and phase, which resulted in significantly lower torque values for other rotor orientations. Due to these effects, it can no longer be assumed that resonant tuning of the receiver coils guarantees an optimal and robust torque generation for the RWPT motoring system. In this chapter, the effect of detuning from resonance on the rotor torque profile is investigated. Detuning of the resonators will prove to be essential in the design phase of the RWPT motoring system. Especially the torque in the previously suboptimal regions is strongly improved. It will also be shown that the behavior of the system is more robust with regards to the tuning of the coils when detuning is permitted.

In Section 4.2, the torque expression is expanded for a detuned RWPT motoring system. The possible detuning methodologies and their effect on the system parameters are described in Section 4.4. Section 4.5 discusses the effect of varying frequency on the torque for 3 discrete capacitor tunings. The torque is simulated in Section 4.5, using the formulas derived in Section 4.2, and validated on an experimental setup in Section 4.5.1. After validation of the torque expressions, we discuss the effect and performance of detuning on the torque by the use of several metrics in Section 4.6.1. Overall, the detuned system is more robust and significant gains in average (88%) and maximum torque (49%) are obtained.

4.2 Torque in a detuned RWPT based motoring system

4.2.1 State-space model

The considered RWPT motoring system again consists of three types of coils, namely the transmitter coil (t) and two resonator coils of which one is fixed in space (stator, s) and one is attached on a rotating axle (rotor, r), shown in Figure 4.1.

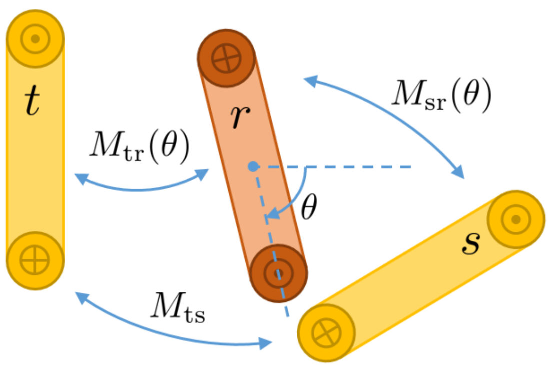

Figure 4.1: The RWPT motoring system consists of a transmitter coil (t), a fixed stator resonator (s) and a rotating rotor resonator (r).

The transmitter coil is driven by a current or voltage controlled AC power source at excitation frequency f. To obtain the currents in each coil, we need to solve Kirchoff's voltage law (KVL) with the complex phasors of the transmitter voltage and the coil currents at a given electrical angular frequency $\omega = 2\pi f$. The states of the RWPT motoring system from Figure 4.1 can be represented in the following form:

$$\begin{bmatrix} V_t \\ 0 \\ 0 \end{bmatrix} = \begin{bmatrix} R_t + j\omega L_t & j\omega M_{\mathrm{ts}} & j\omega M_{\mathrm{tr}}(\theta) \\ j\omega M_{\mathrm{ts}} & R_s + jX_s & j\omega M_{\mathrm{sr}}(\theta) \\ j\omega M_{\mathrm{tr}}(\theta) & j\omega M_{\mathrm{sr}}(\theta) & R_r + jX_r \end{bmatrix} \begin{bmatrix} I_t \\ I_s \\ I_r \end{bmatrix} \tag{4.1}$$

The model input V_t and the system states I_t, I_s and I_r are the complex phasors of the sinusoidal transmitter voltage v_t and system currents i_t, i_s and i_r. The mutual inductance M between the rotor coil and the transmitter (M_{tr}) and the stator (M_{sr}) is variable with respect to the rotor angle θ. X is the reactance of the RLC circuits, which is the sum of the coil inductance ($j\omega L$) and the capacitor reactance $\left(-j\dfrac{1}{\omega C}\right)$:

$$X = \omega L - \frac{1}{\omega C} \tag{4.2}$$

In the previous chapter, to generate torque in a RWPT motoring system the resonators are tuned to the same resonance frequency. The excitation frequency was then aligned with the resonance frequency of these coils $\left(\omega_0 = 2\pi f_0 = \frac{1}{\sqrt{LC}}\right)$, such that the reactance of both resonator coils (X_s and X_r) are canceled out. This methodology corresponds to standard RWPT. The KVL (4.1) then simplifies to the KVL (3.32) of the previous chapter. In this chapter however, the possibility of detuning the resonator coils is allowed, resulting in nonzero reactance terms.

We can find the stator and rotor currents in terms of the transmitter coil current by considering the last two rows of the KVL (4.1). We define the transmitter coupling matrix Z_t and impedance matrix for current control Z_I as

$$Z_t = \begin{bmatrix} j\omega M_{\mathrm{ts}} \\ j\omega M_{\mathrm{tr}}(\theta) \end{bmatrix} \qquad Z_I = \begin{bmatrix} R_s + jX_s & j\omega M_{\mathrm{sr}}(\theta) \\ j\omega M_{\mathrm{sr}}(\theta) & R_r + jX_r \end{bmatrix} \tag{4.3}$$

such that

$$\begin{bmatrix} I_s \\ I_r \end{bmatrix} = -Z_I^{-1} Z_t I_t \tag{4.4}$$

The first line of (4.1) shows the relation between the transmitter's sinusoidal excitation voltage v_t (with complex phasor V_t) and the transmitter current I_t. The stator and rotor currents I_s and I_r can be written as a function of I_t and the system impedances, such that the coil-coil interaction can again be translated to the transmitter coil in the form of a reflected impedance.

$$\begin{aligned} Z_{\mathrm{ref}} &= -Z_t^T Z_I^{-1} Z_t \\ &= \frac{\begin{bmatrix} \omega^2 M_{\mathrm{ts}}^2 (R_r + jX_r) + \omega^2 M_{\mathrm{tr}}^2 (R_s + jX_s) \\ - j2\omega^3 M_{\mathrm{ts}} M_{\mathrm{tr}} M_{\mathrm{sr}} \end{bmatrix}}{\omega^2 M_{\mathrm{sr}}(\theta)^2 + (R_r + jX_r)(R_s + jX_s)} \end{aligned} \tag{4.5}$$

If there is no significant magnetic coupling between the resonator coils ($M_{\mathrm{sr}} \approx 0$), then the reflected impedance can be written as:

$$Z_{\mathrm{ref}} = \frac{\omega^2 M_{\mathrm{ts}}^2}{R_s + jX_s} + \frac{\omega^2 M_{\mathrm{tr}}(\theta)^2}{R_r + jX_r} \tag{4.6}$$

The amplitude of the transmitter voltage (V_t) is now the multiplication of the current amplitude (I_t) and the modulus of the total transmitter coil impedance:

$$|V_t| = |R_t + j\omega L_t + Z_{\mathrm{ref}}||I_t| \leftrightarrow |I_t| = \frac{|V_t|}{|R_t + j\omega L_t + Z_{\mathrm{ref}}|} \tag{4.7}$$

4.2.2 Torque expression for a detuned system

The torque between two current carrying coils equals $\frac{1}{2} i_1 i_2 \frac{\mathrm{d}M_{12}(\theta)}{\mathrm{d}\theta}$, such that the total rotor torque can be written as the sum of the interactions with both the transmitter (M_{tr}) and the stator coil (M_{sr}):

$$T(\theta,t) = \frac{1}{2} i_t i_r \frac{\mathrm{d}M_{\mathrm{tr}}(\theta)}{\mathrm{d}\theta} + \frac{1}{2} i_s i_r \frac{\mathrm{d}M_{\mathrm{sr}}(\theta)}{\mathrm{d}\theta} \tag{4.8}$$
$$= \frac{1}{2} i_t i_r K_{\mathrm{tr}}(\theta) + \frac{1}{2} i_s i_r K_{\mathrm{sr}}(\theta) \tag{4.9}$$

$K_{\mathrm{tr}}(\theta)$ and $K_{\mathrm{sr}}(\theta)$ are defined as the positional derivatives of the mutual inductances $M_{\mathrm{tr}}(\theta)$ and $M_{\mathrm{sr}}(\theta)$, respectively. Since the system currents are sinusoidal, the average torque over one electrical period can be written as:

$$T(\theta) = \frac{1}{2}\mathbf{i}^{\mathrm{H}} \frac{\mathrm{d}\mathbf{M}(\theta)}{\mathrm{d}\theta}\mathbf{i} = \frac{1}{2}\mathbf{i}^{\mathrm{H}}\mathbf{K}(\theta)\mathbf{i} \tag{4.10}$$

with $\mathbf{i} = \begin{bmatrix} I_t & I_s & I_r \end{bmatrix}^T$ the vector of the complex phasors of the sinusoidal currents i_t, i_s and i_r. Matrices $\mathbf{M}(\theta)$ and $\mathbf{K}(\theta)$ are defined as

$$\mathbf{M}(\theta) = \begin{bmatrix} 0 & M_{\mathrm{ts}} & M_{\mathrm{tr}}(\theta) \\ M_{\mathrm{ts}} & 0 & M_{\mathrm{sr}}(\theta) \\ M_{\mathrm{tr}}(\theta)^{\mathrm{T}} & M_{\mathrm{sr}}(\theta)^{\mathrm{T}} & 0 \end{bmatrix} \tag{4.11}$$

$$\mathbf{K}(\theta) = \frac{\mathbf{M}(\theta)}{\mathrm{d}\theta} = \begin{bmatrix} 0 & 0 & K_{\mathrm{tr}}(\theta) \\ 0 & 0 & K_{\mathrm{sr}}(\theta) \\ K_{\mathrm{tr}}(\theta)^{\mathrm{T}} & K_{\mathrm{sr}}(\theta)^{\mathrm{T}} & 0 \end{bmatrix} \tag{4.12}$$

By expanding torque expression (4.10) with nonzero reactance terms, we obtain Equation (4.13), making the effect of detuning the resonator coils even more explicit.

$$T(\theta) \;=\; |I_t|^2\omega^2 \frac{\begin{bmatrix} M_{ts}(K_{\mathrm{sr}}M_{\mathrm{tr}} - K_{\mathrm{tr}}M_{\mathrm{sr}})(\omega^2 M_{\mathrm{sr}}^2 + R_r R_s + X_r X_s) \\ + K_{\mathrm{tr}}M_{\mathrm{sr}}^2 M_{\mathrm{tr}} X_s - K_{\mathrm{tr}} X_r M_{\mathrm{tr}} R_s^2 - K_{\mathrm{tr}} X_r M_{\mathrm{tr}} X_s^2 \\ - K_{\mathrm{sr}} M_{\mathrm{sr}} M_{\mathrm{tr}}^2 X_s - K_{\mathrm{sr}} X_r M_{\mathrm{sr}} M_{\mathrm{ts}}^2 \end{bmatrix}}{(\omega^2 M_{\mathrm{sr}}^2 + R_r R_s - X_r X_s)^2 + (R_r X_s + R_s X_r)^2} \tag{4.13}$$

The denominator of (4.13) is also the norm of the denominator of the reflected impedance (4.5). The torque expression can be easily written as a function of the transmitter voltage by substituting $|I_t|$ by the right hand side of (4.7). If we assume resonant tuning of both the stator and the rotor circuit, we can omit all reactance terms, such that (4.13) simplifies to (4.14).

$$T(\theta) = \frac{\omega^2 M_{\mathrm{ts}}(K_{\mathrm{sr}}M_{\mathrm{tr}} - K_{\mathrm{tr}}M_{\mathrm{sr}})}{\omega^2 M_{\mathrm{sr}}^2 + R_r R_s}|I_t|^2 \tag{4.14}$$

Note that in (4.13) and (4.14), the dependence of θ for the terms M_{tr}, M_{sr}, K_{tr} and K_{sr} was omitted for clarity.

4.3 Frequency variation for a tuned system

Equation (4.13) describes the torque profile of a general detuned system. Before we analyze the possible degrees of freedom in detuning the RWPT motoring system, we first reconsider the system of the previous chapter. There, the rotor and stator resonators are tuned to the same resonance frequency. Without changing the hardware, namely the series connected capacitors, we can detune both resonators simultaneously by adjusting the excitation frequency ω. For frequencies higher than the resonance frequency of the resonators, their series reactance shifts to more inductive values, while for lower frequencies, the coil impedances become capacitive.

Figures 4.2(a) and 4.2(b) show the simulated torque profile for a current and voltage controlled RWPT motoring system. The excitation frequency is varied from 6230 to 7030 Hz in steps of 200 Hz. Both control strategies show that the peak torque changes both in position and value. Shifting to a lower frequency allows for a significant increase in the peak torque, while higher frequencies result in lower peak torque values. In Section 3.2.5 it was shown that the torque is unidirectional when the frequency coincides with the resonance frequencies of the resonators. If the frequency is significantly increased or decreased compared to the resonance frequency f_0, part of the torque profile returns a negative value. This effect is the strongest for increased frequencies. For these tuning conditions, the torque is no longer unidirectional, such that motoring behavior cannot be guaranteed.

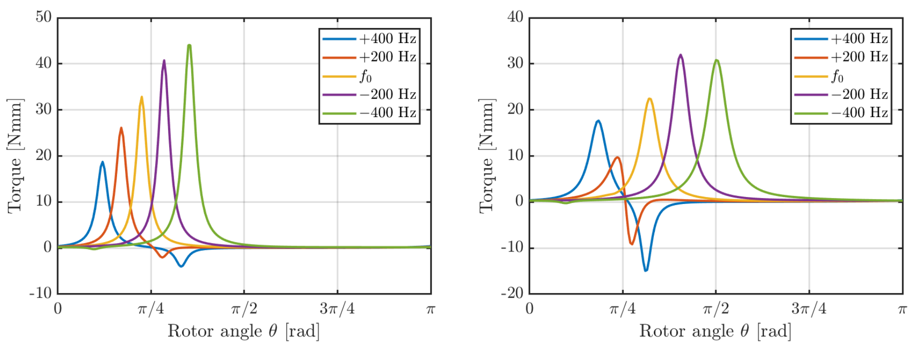

(a) **(b)**

Figure 4.2: The torque profile for a current controlled (a) and voltage controlled (b) transmitter is highly variable when changing the frequency.

4.4 Detuning the RWPT system

As stated before, changing the excitation frequency is only one possible way of detuning the reactance values of the resonator coils. When inspecting (4.13) we see that for nonzero reactances and thus allowing general detuning, the resulting torque strongly depends on these reactance values. In (4.2), the reactance of a coil was expressed as a function of the excitation frequency (ω) and the series connected capacitor (C), so we can change the reactance of a resonator by changing the excitation frequency of the transmitter or the value of the capacitor. The resonator is tuned to resonance if the frequency or the capacitor is chosen such that:

$$\omega_0 = \frac{1}{\sqrt{LC}} \longleftrightarrow C_0 = \frac{1}{\omega^2 L} \tag{4.15}$$

It is important to note that the reactance is strictly monotonous in both C and ω:

$$\frac{\mathrm{d}X}{\mathrm{d}C} = \frac{1}{\omega C^2} > 0 \text{ and } \frac{\mathrm{d}X}{\mathrm{d}\omega} = L + \frac{1}{\omega^2 C} > 0 \tag{4.16}$$

Figure 4.3 shows the reactances of the resonators as a function of ω/ω_0 and C/C_0.

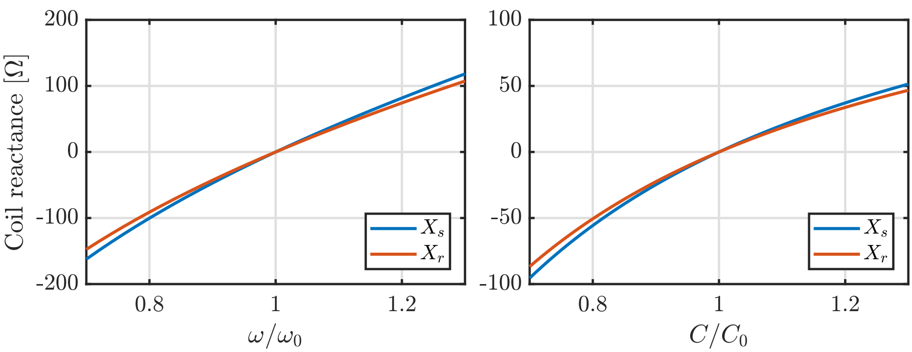

Figure 4.3: The stator and rotor reactance values X_s and X_r are strictly monotonous in ω (left) and C (right).

Around the resonance frequency ω_0, the resonator reactance can be approximated as:

$$X \approx \left.\frac{\mathrm{d}X}{\mathrm{d}\omega}\right|_{\omega_0} (\omega - \omega_0) = \left(L + \frac{1}{\omega_0^2 C}\right)(\omega - \omega_0) = 2L(\omega - \omega_0) \tag{4.17}$$

or

$$X \approx \left.\frac{\mathrm{d}X}{\mathrm{d}C}\right|_{C_0} (C - C_0) = \frac{1}{\omega_0 C_0^2}(C - C_0) \tag{4.18}$$

Because the reactance of an RLC circuit is strictly monotonous in ω and C, as illustrated in Figure 4.3, one of both parameters can be chosen freely, while the other is changed until the desired reactance is reached. This also means that the stator and rotor reactances X_s and X_r can always be set to predefined values by varying only 2 variables and keeping the third one fixed in the set $\{\omega, C_s, C_r\}$. The excitation frequency can be continuously adjusted by changing the control signal of the amplifier. The resonator capacitors C_s and C_r can be changed in a discrete fashion, namely offline by changing the hardware side of the setup, or online by connecting or disconnecting parallel capacitors using AC switches. For the given setup the excitation frequency is varied because its value can be freely adjusted without hardware changes, while the stator capacitor is swapped offline.

In Section 3.3.2 it was shown that the optimal torque coincides with the peak values of the Q factor of the coils, which resulted in an optimal driving frequency ω^*. It was also shown that for frequencies for which the resistance of the coils can be approximated by a straight line through the origin (4.19), the torque is barely affected. This means that for a wide range of frequencies, the torque is not significantly degraded by decreasing values of the Q factors.

$$R_r \approx \omega \frac{R_r^*}{\omega_r^*} \tag{4.19}$$

4.5 Discrete stator capacitor detuning

4.5.1 Experimental validation of detuned RWPT model

The detuning of the RWPT system can be captured by two degrees of freedom, namely by changing the frequency and the stator capacitor value. The electrical model and the torque model are validated for continuously variable frequencies and three discrete capacitor values. The capacitor values are chosen such that the resonance frequency of the stator is higher (f_{s1}), equal (f_{s2}) or lower (f_{s3}) than the resonance frequency of the rotor resonator f_r. Table 4.1 lists the three capacitor values and their corresponding resonance frequencies and loss factors.

Table 4.1: The series connected capacitor of the stator is detuned from resonance to obtain three discrete detuning settings.

Parameter	C_{s1}	C_{s2}	C_{s3}
capacitance (C)	95.8 nF	106.7 nF	116.9 nF
resonance frequency (f_s)	6997 Hz	6630 Hz	6334 Hz
dissipation factor (δ_C)	0.02%	0.02%	0.02%

The experimental validation of the analytical model is done on the RWPT motoring setup with ferrite rotor core that was used in the previous chapter (see Section 3.6 and 3.7.6). The rotor angle θ is varied in steps of $\pi/80$. For each rotor position, the frequency is varied in steps of 10 Hz from 5304 to 8614 Hz, which correspond to 80% and 130% of the resonance frequency of the rotor f_r. The amplitude of the transmitter current I_t is controlled to 0.2 A RMS. Figure 4.4 compares the measured and simulated torque profile for varying frequencies and for each of the three stator capacitor values.

The torque profile for C_{s2} (Figure 4.4(c) and (d)) at the resonance frequency ($f = f_r = f_{s2} = 6630$ Hz) corresponds to the torque profile of the RWPT system with resonant tuning in Section 3.7.6. At the resonance frequency, the current controlled torque has its peak value for $M_{\mathrm{sr}} = 0$ (or $\theta = \phi_{\mathrm{st}} + k\pi$), with ϕ_{st} the positional shift between $M_{\mathrm{tr}}(\theta)$ and $M_{\mathrm{sr}}(\theta)$ and the angle for which $M_{\mathrm{sr}}(\phi_{\mathrm{st}}) = 0$. This is due to the fact that the denominator of the torque as a function of current (4.14) is minimal for $M_{\mathrm{sr}} = 0$. When changing the excitation frequency, the peak torque varies smoothly, while its position shifts away from $\phi_{\mathrm{st}} + k\pi$. The peak torque position now corresponds to the minimum norm of the denominator of (4.13). For a wide range around the resonance frequency of both resonators, the torque has a positive value for the whole rotation. For larger deviations, the torque can be negative for some part of the rotation. At frequencies under the resonance frequency, the peak torque value can be higher compared to resonant tuning. This was also demonstrated in Figure 4.2.

For the detuned stator capacitors C_{s1} and C_{s3}, the peak torque ridge is discontinuous, with a gap of negative torque values between the resonance frequencies of both resonators f_r and $f_{s1/3}$. This gap in the torque profile shows that the torque peak for a resonant tuned RWPT motoring system is not very robust, as a slight variation of the resonant tuning results in a dip or negative torque values around the resonance frequency. For the lower capacitor value C_{s1} (Figure 4.4(a) and (b)), the maximum torque increases, while for the higher capacitor value C_{s3} (Figure 4.4(e) and (f)), the maximum torque decreases, but higher opposite torques (with negative value) are possible.

The transmitter voltage V_t is a direct result of the transmitter current control, where I_t was controlled to 0.2 A RMS. V_t can be calculated from the first equation of the KVL (4.1). For this, the resonator currents I_s and I_r can be determined by solving the second and third equations of (4.1), which was done in Equation (4.4). The transmitter voltage can also be determined by calculating the reflected impedance Z_{ref} (4.5) and multiplying the transmitter current I_t with the total transmitter impedance Z_{tot} (4.7). Figure 4.5 shows the measured and simulated values of the transmitter voltage. The transmitter current I_t and voltage V_t are directly measured on the setup using a current and voltage probe. The online Fourier transform is applied on the sinusoidal signals to extract their amplitude and phase, resulting in their phasor representation.

The total transmitter impedance Z_{tot} can be retrieved by dividing the voltage phasor by the current phasor.

$$Z_{\text{tot}} = \frac{V_t}{I_t} \tag{4.20}$$

Figure 4.6 displays the derived and simulated total transmitter impedance. As the current is controlled to a constant amplitude, the voltage and the total transmitter impedance only differ by a constant factor ($|V_t|/|Z_{\text{tot}}| = 0.2\text{A}$). The total transmitter impedance ($Z_{\text{tot}} = R_t + j\omega L_t + Z_{\text{ref}}$) follows a trend similar to the torque and the resonator currents. This is because the torque expression (4.13), the reflected impedance Z_{ref} (4.5) and the resonator currents (4.4) share the same denominator. For high torques, high currents are required. If high currents are induced in the resonators, they also induce back EMF's in the transmitter coil, resulting in a higher reflected impedance. The stator current I_s was also measured with a current probe and calculated from (4.1) and (4.4). The measured and simulated I_s values are added in Figure 4.7 to illustrate the correlation between the resonator currents, Z_{ref} and the torque on the rotor.

The system coils are constructed very simularly, with the same amount of turns and the same wire diameter. We can thus assume that the current limit for all three coils is the same. The labels correspond to the order of the currents in the KVL (4.1), namely I_t (1), I_s (2) and I_r (3). Figure 4.8 (left) indicates which coil current is the highest depending on the frequency and the rotor angle for each stator capacitor setting, while the corresponding current amplitude is shown on the right side. For high torques, the resonator currents are always significantly higher than the transmitter current (0.2 A RMS). The stator capacitor tuning determines which resonator has the highest current for a given rotor position.

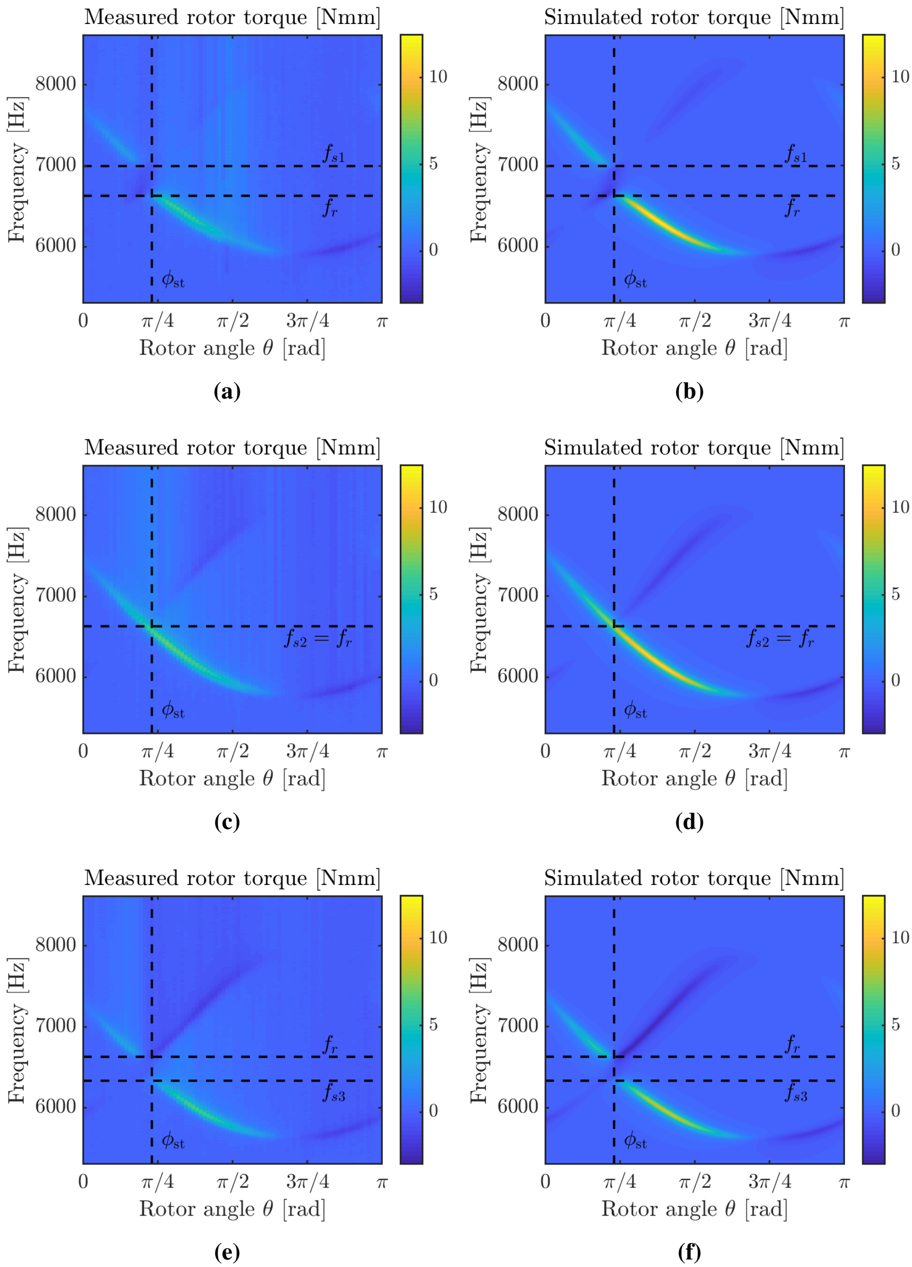

Figure 4.4: The measured (left) and simulated (right) torque for C_{s1} (a)-(b), C_{s2} (c)-(d) and C_{s3} (e)-(f).

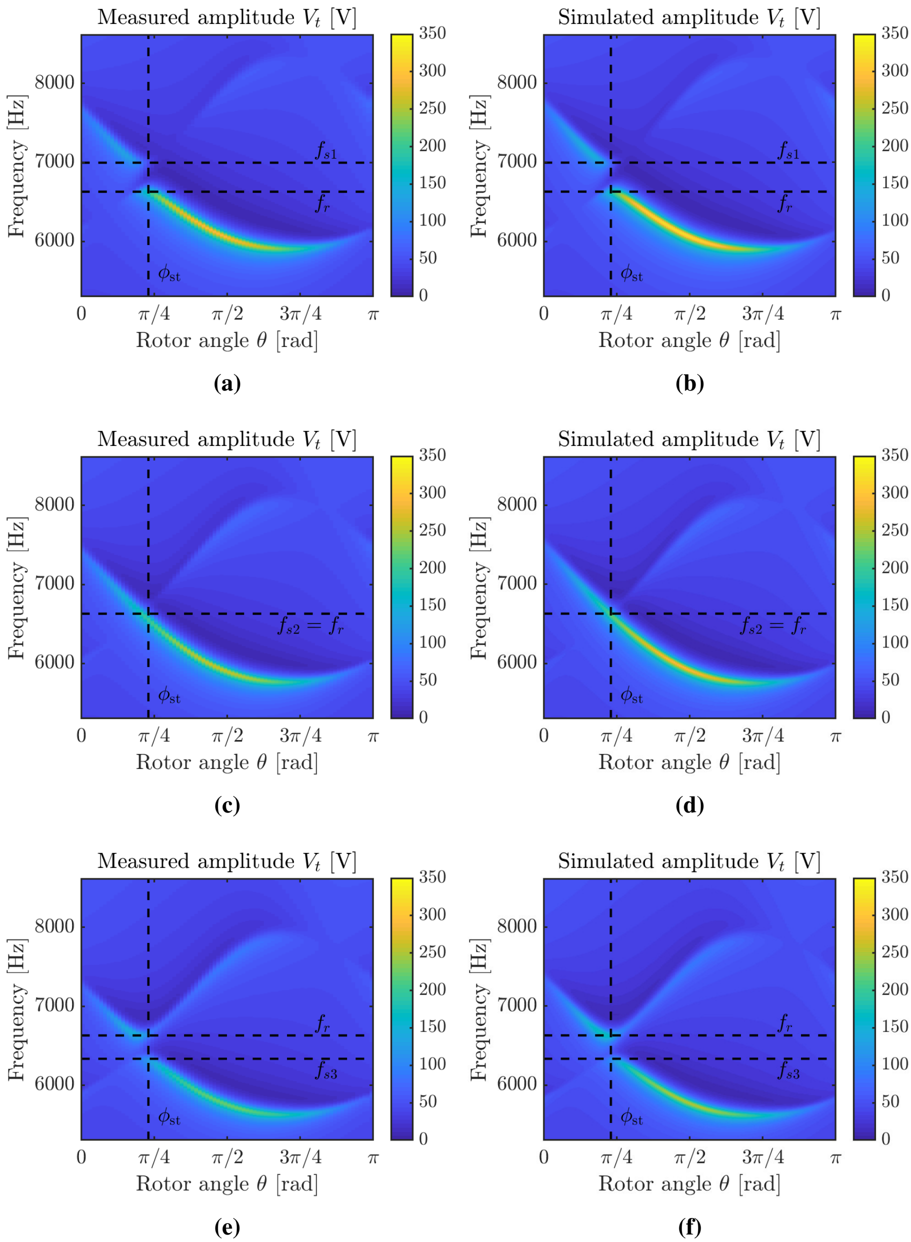

Figure 4.5: The measured (left) and simulated (right) transmitter voltage for C_{s1} (a)-(b), C_{s2} (c)-(d) and C_{s3} (e)-(f). The transmitter voltage is a direct result of the current control.

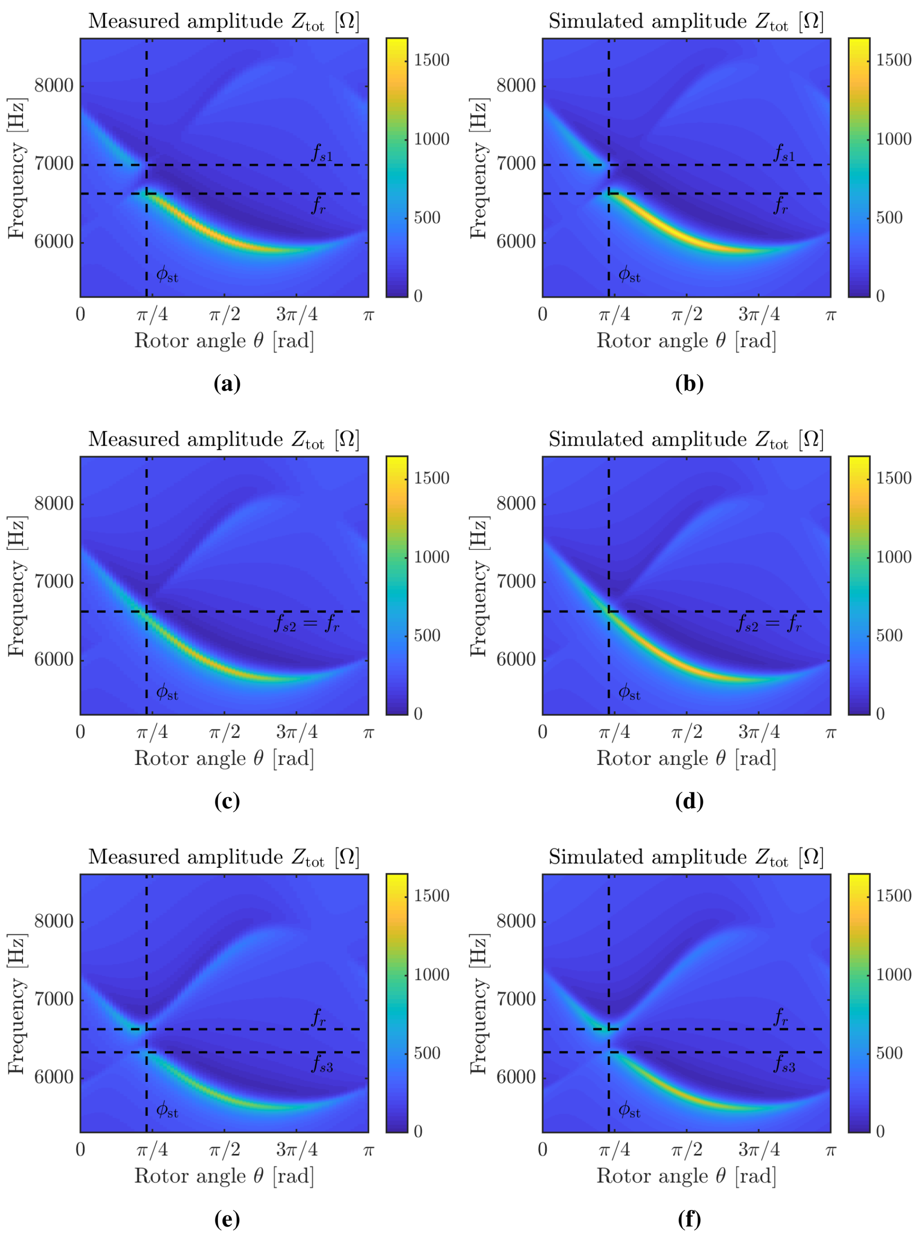

Figure 4.6: The measured (left) and simulated (right) total transmitter impedance for C_{s1} (a)-(b), C_{s2} (c)-(d) and C_{s3} (e)-(f). In the experimental validation, Z_{tot} is derived from the phasors of V_t and I_t.

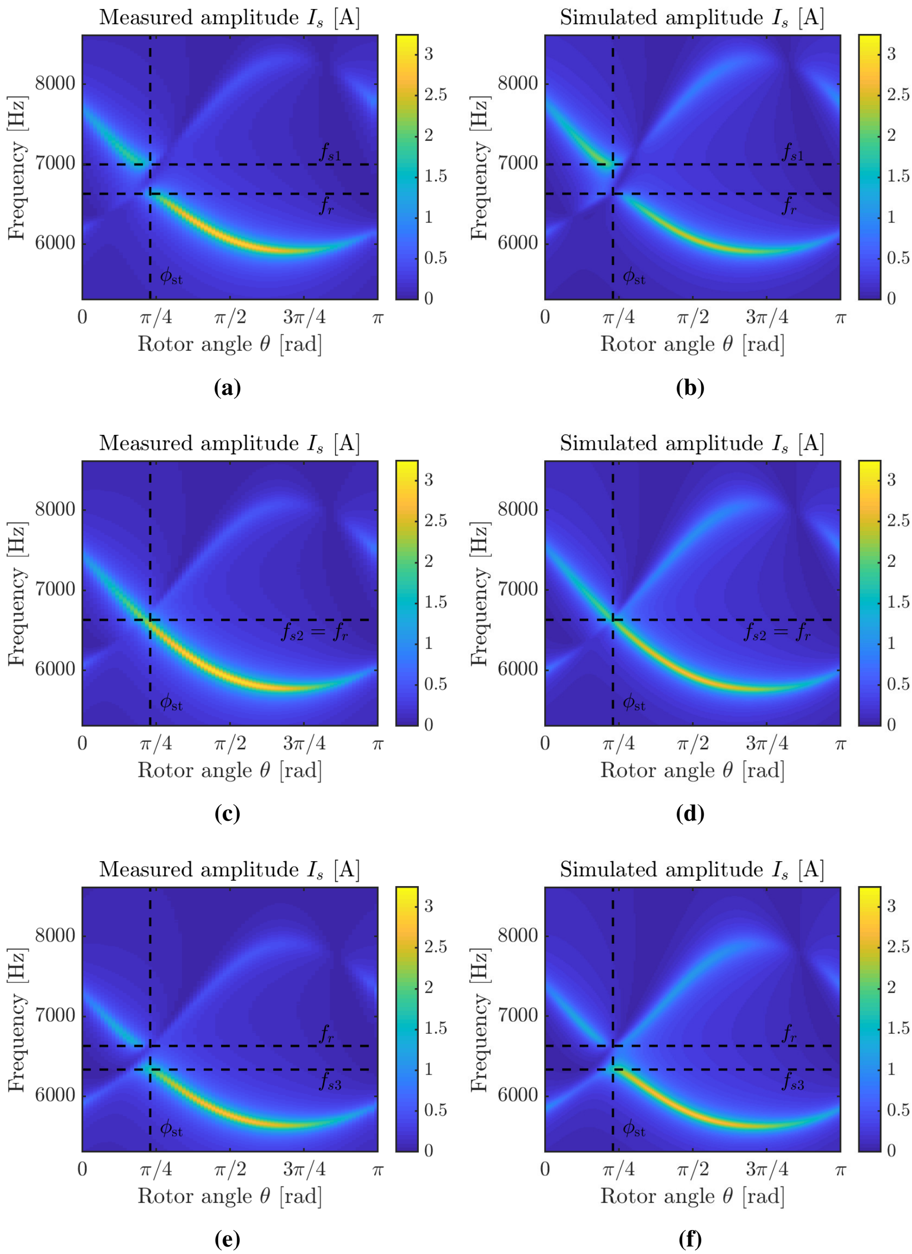

Figure 4.7: The measured (left) and simulated (right) stator current for C_{s1} (a)-(b), C_{s2} (c)-(d) and C_{s3} (e)-(f).

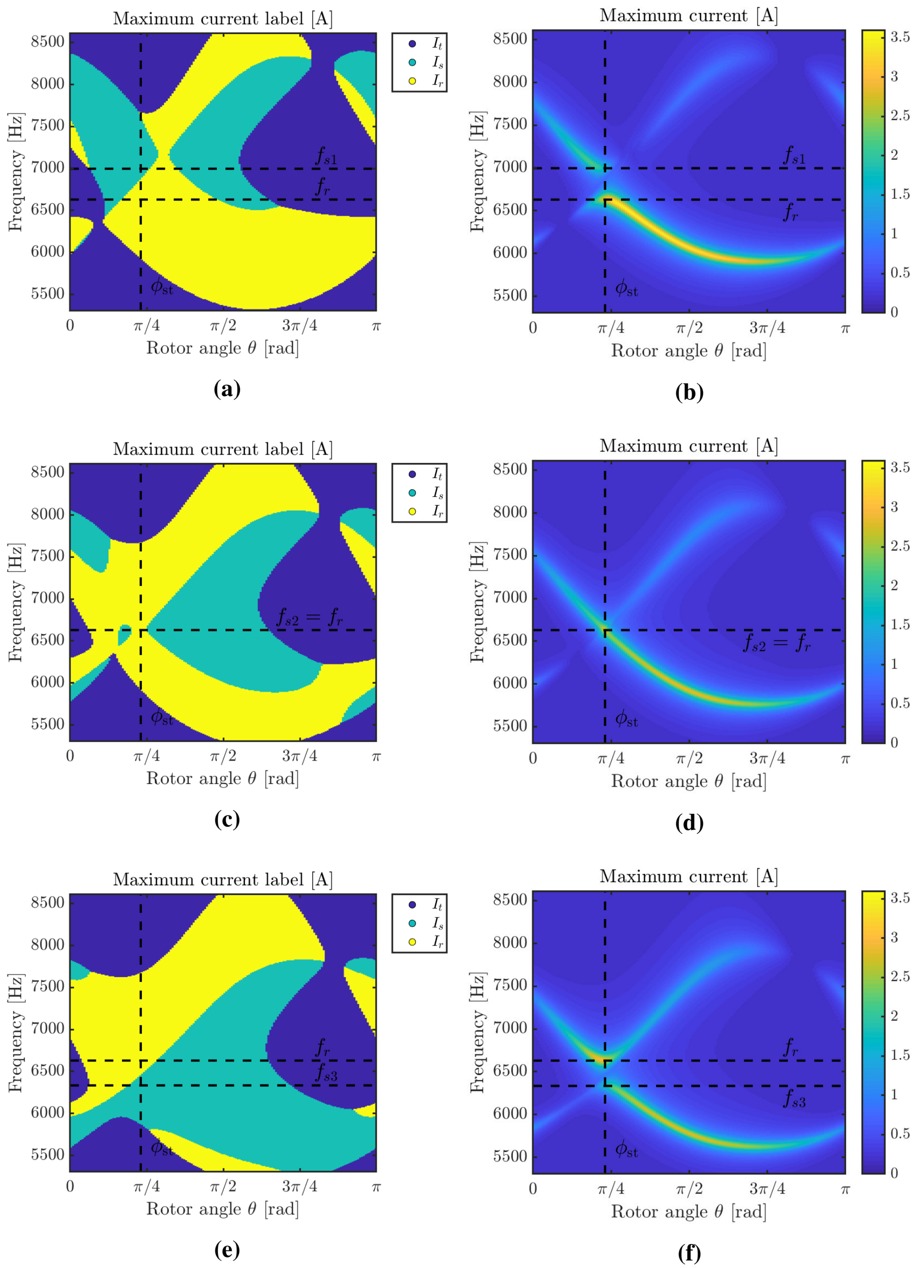

Figure 4.8: The label of the highest current (left) and the corresponding maximum RMS current amplitude (right) for C_{s1} (a)-(b), C_{s2} (c)-(d) and C_{s3} (e)-(f).

4.6 Continuous capacitor detuning

In the previous section, it was shown that detuning the stator capacitor (in 3 discrete steps) can increase the torque or allow for negative torques. In this section, we will explore the effects of continuous detuning of the stator capacitor.

4.6.1 Fixed detuning

First, the detuning of the excitation frequency and the stator capacitor is considered to be fixed for a full rotation. The three left panes of Figure 4.9 show the maximum (a), minimum (c) and average torque (e) for the three discrete stator capacitor settings from the previous section. These profiles correspond to the side view of the torque simulations in Figure 4.4. In the three right panes of Figure 4.9, the stator capacitor is continuously varied from 50% to 150% of the resonant tuning C_{s2}. Figures 4.9(b), (d) and (f) show the maximum, minimum and average torque over one rotation of the rotor for a given excitation frequency and stator capacitor tuning (C_s/C_{s2}). The discrete capacitor detuning settings are marked with horizontal dashed lines.

The average torque over one rotation is a measure for the motoring capability of the RWPT system. If the motoring system is only used for a small part of the rotation, for example when used as an actuator or a valve, the maximum and minimum torque value can be useful. Except for resonant tuning, the average and maximum torque are close to zero for a frequency in between the resonance frequencies of the stator and rotor coils ($f_s < f < f_r$ or $f_r < f < f_s$). So both resonator need to be tuned to either behave capacitive or inductive. For resonant tuning ($f_r = f_s$; $C_s = C_{s2}$), the average torque can be increased by 51%, while the maximum torque can be increased by 38% for a lowered frequency. If we allow detuning of the stator capacitor, the average torque can be increased by 88% and the maximum torque by 49% for a lowered frequency and lowered stator capacitor value. Note that these values are not reached for exactly the same detuning conditions.

If the RWPT system is used as a motor, negative torque during rotation is undesired, as the rotor can be stuck in stable points. In that case, we want to avoid minimum torque values under zero and stay in the most yellow region in Figure 4.9(d)). The minimum torque can also be useful if the RWPT system is intended to move in two directions. The optimal detuning is now opposite to that of the maximum torque, namely an increased stator capacitor value and a higher excitation frequency.

Suppose that we aim for a resonant non-detuned system, with torque expression (4.14). From Figures 4.9(b) and 4.9(f) it is clear that slight (unintended) detuning of the stator coil could almost completely eliminate the torque at the resonance frequency of the rotor. The average and maximum torque of a detuned system on the other hand is stable around its optimal setting.

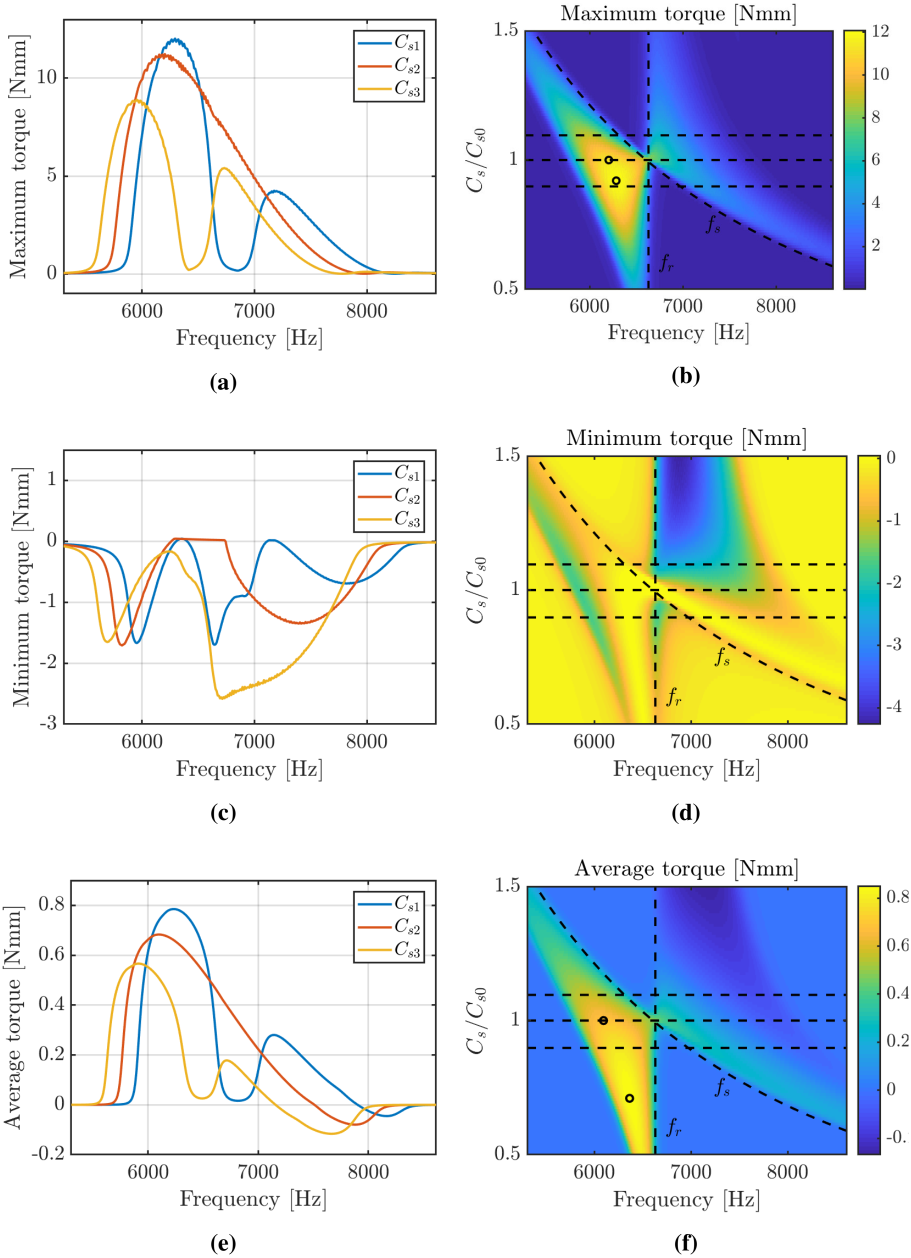

Figure 4.9: The maximum, minimum and average torque for varying detuning parameters f and C_s (right) and for the three discrete capacitor values (left).

4.6.2 Additional performance metrics

Until now, we discussed the possible torque gains when detuning a current controlled RWPT motoring system. In Section 4.5.1, we explained that there is a high correlation between the torque and the currents in the coils. Higher currents however result in additional heat dissipation losses (P_d) in the coils. For our quasi-static system, all ingoing active power is dissipated as heat in the coils.

$$P_d = R_t|I_t|^2 + R_s|I_s|^2 + R_r|I_r|^2 = \mathrm{Re}(V_t I_t^{\mathrm{H}}) \tag{4.21}$$

We propose a first new performance metric, namely the ratio of the torque and the dissipated power, which we call the torque efficiency (TE):

$$TE[\mathrm{Nmm/W}] = \frac{T}{R_t|I_t|^2 + R_s|I_s|^2 + R_r|I_r|^2} = \frac{T}{\mathrm{Re}(V_t I_t^{\mathrm{H}})} \tag{4.22}$$

The RWPT motoring system is controlled to a fixed transmitter current. For high torques, the resonator currents increase significantly. To get the most out of our setup without exceeding the current limits of the coils, we could control the transmitter current in such a way that the highest current is limited to a certain threshold. We then compare the torque to the highest current in the system as a measure for the torque capability of the system. In Section 4.2.2 it was shown that the torque is proportional to the square of the system currents. An objective measure for the torque capability (TC) is equal to the torque divided by the square of the highest current in the system.

$$TC[\mathrm{Nmm/A^2}] = \frac{T}{\max(|I_t|, |I_s|, |I_r|)^2} \tag{4.23}$$

Figure 4.10 shows the maximum, minimum and average torque efficiency (left) and torque capability (right) for varying detuning conditions. The minimum values correspond to negative torques. From Figure 4.10(a)-(d) it is clear that for the new performance metrics, positive and negative torque have very similar performance ranges. When comparing the two performance metrics, we see that the maximum torque efficiency (a) is smoother with wider ranges of slow-changing performance. The torque capability (b) on the other hand has a sharp peak performance ridge which falls within the optimal range of the torque efficiency. If we tune the system to have optimal torque capability, the torque efficiency is expected to be high as well.

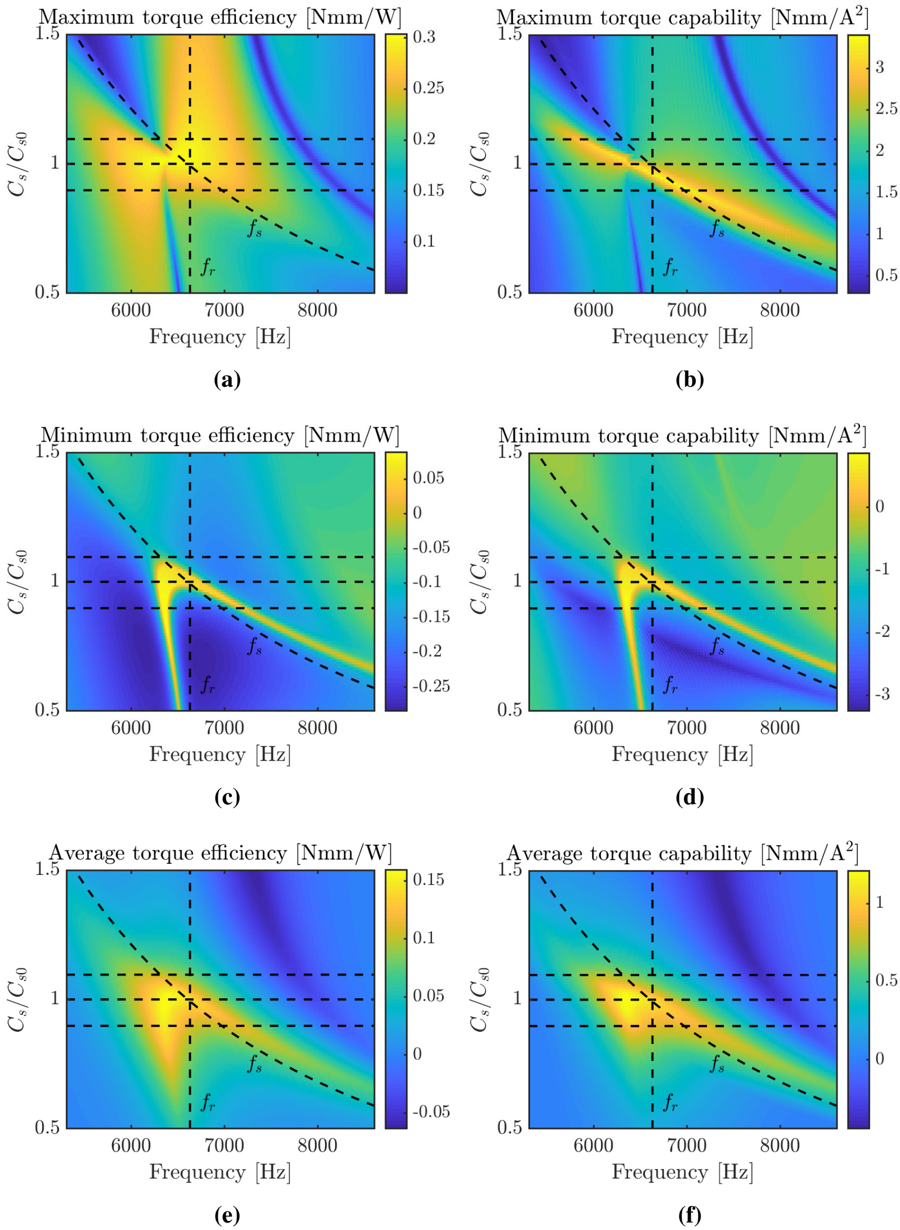

Figure 4.10: The maximum, minimum and average torque efficiency (left) and torque capability (right) for varying detuning parameters f and C_s.

4.7 Online capacitor and frequency detuning

The analysis in Figures 4.9 and 4.10 and Section 4.6.1 assumes that the frequency is fixed for a whole rotation. We could however vary the frequency depending on the rotor angle. Figure 4.11 shows the maximum and minimum torque that can be obtained for every rotor angle by varying the frequency for the same three stator capacitor values (left) or a wide range of stator capacitor values (right).

If the stator capacitor is tuned for resonance ($C_s = C_{s,\omega_r}$ and $\omega_s = \omega_r$), the maximum torque for each rotor angle (red) has a smooth behavior. The dashed red line shows the torque profile if the excitation frequency was fixed to the resonance frequency of the rotor and stator ($\omega = \omega_s = \omega_r$). When the stator is detuned, the maximum torque drops significantly for $M_{sr} = 0$, resulting in two local maxima. Figure 4.11 again shows that a slight unintended detuning of the stator coil causes a significant decrease in maximum torque around $\theta = \phi_{\mathrm{st}} + k\pi$. For the given system, the maximum torque for $\theta = \phi_{\mathrm{st}} + k\pi$ decreases by more than 50% for a 2% detuning of the stator capacitor value.

The possible gain in maximum torque by adjusting the excitation frequency and optionally the stator capacitor was discussed in Section 4.6.1. The same peak values are marked in Figure 4.11(b). By increasing the stator capacitor value, the minimum achievable torque decreases. There is a wide region where the torque can be positive or negative depending on the tuning of the stator capacitor and the excitation frequency.

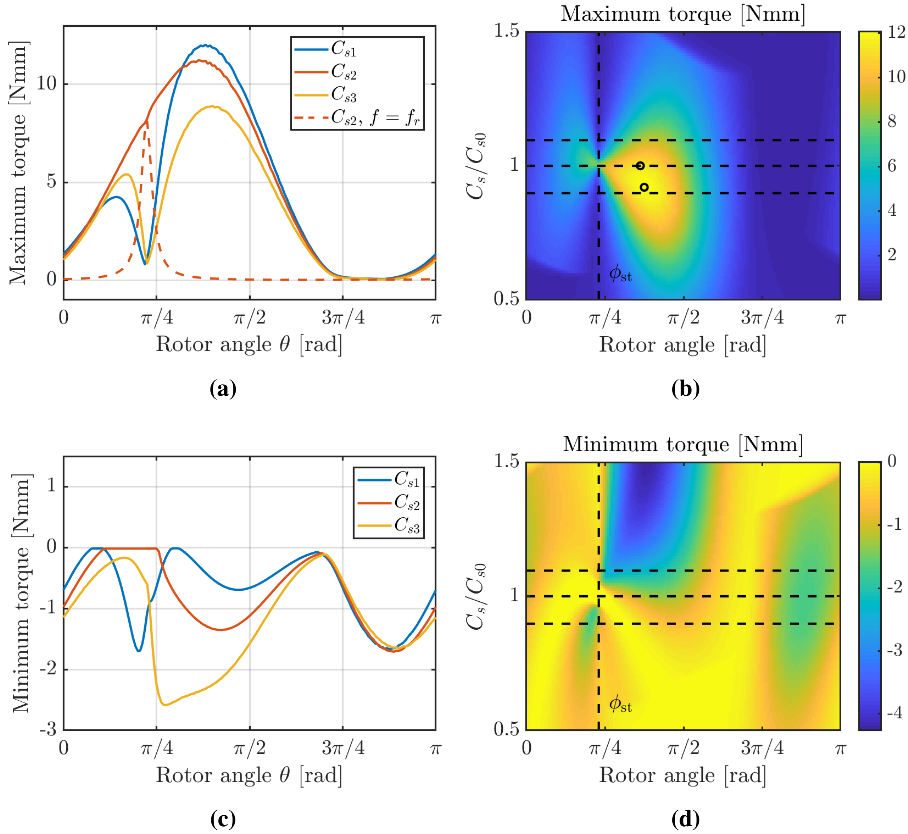

Figure 4.11: The maximum (b) and minimum (d) torque for each rotor angle are simulated for a varying stator capacitor value C_s and excitation frequency ω. The same metrics are shown for three discrete values for C_s in (a) and (c).

For a given RWPT motoring design with full detuning capability, we are also interested in the achievable torque efficiency and torque capability for a given rotor angle. Figure 4.12 shows the maximum and minimum simulated TE ((a) and (c)) and TC ((b) and (d)) for a given rotor angle as a function of the stator capacitance C_s. Figure 4.13 compares the maximum and minimum TE and TC and their corresponding capacitor and frequency setpoints. The maximum and minimum TE and TC are qualitatively similar, smooth functions of the rotor angle. The corresponding capacitor value C_s and frequency f are shown in Figures 4.13(c)-(f). The optimal capacitor values can be visually derived from Figures 4.11(a)-(d). The optimal frequencies and capacitor values are (piecewise) continuous functions of the rotor angle. The boundaries on the capacitor value and the frequency determine for which rotor angles these optimal values show discontinuities and clipping. When designing the RWPT system, we should identify the trade-off between the maximum performance of the system and the boundaries of f and C_s.

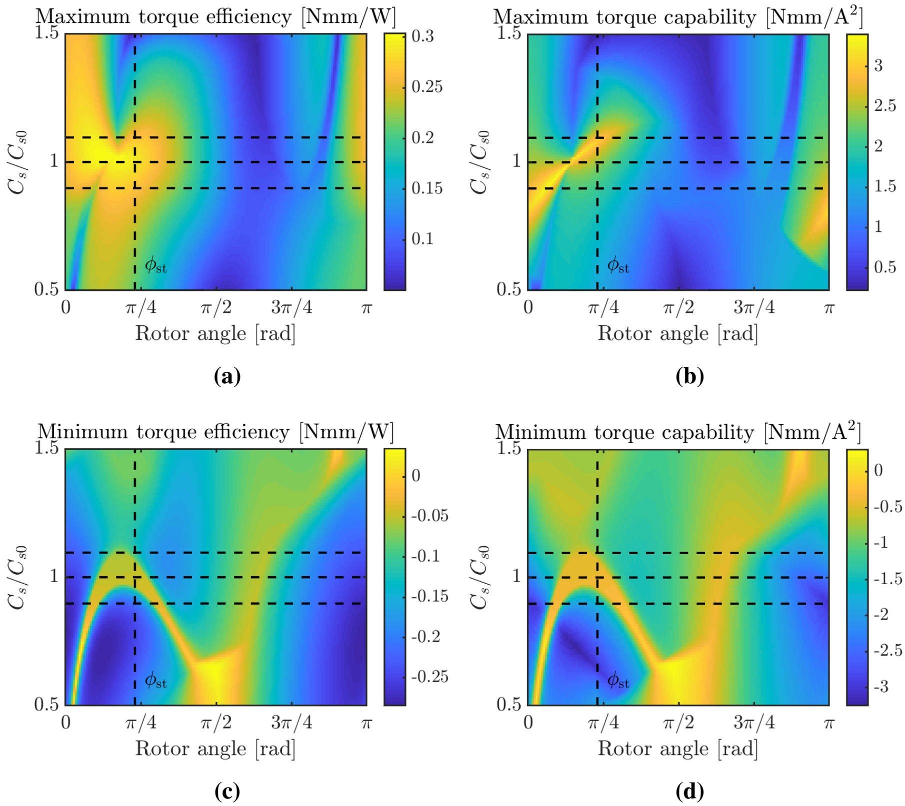

Figure 4.12: The maximum and minimum simulated TE ((a) and (c)) and TC ((b) and (d)) for a given rotor angle as a function of the stator capacitance C_s.

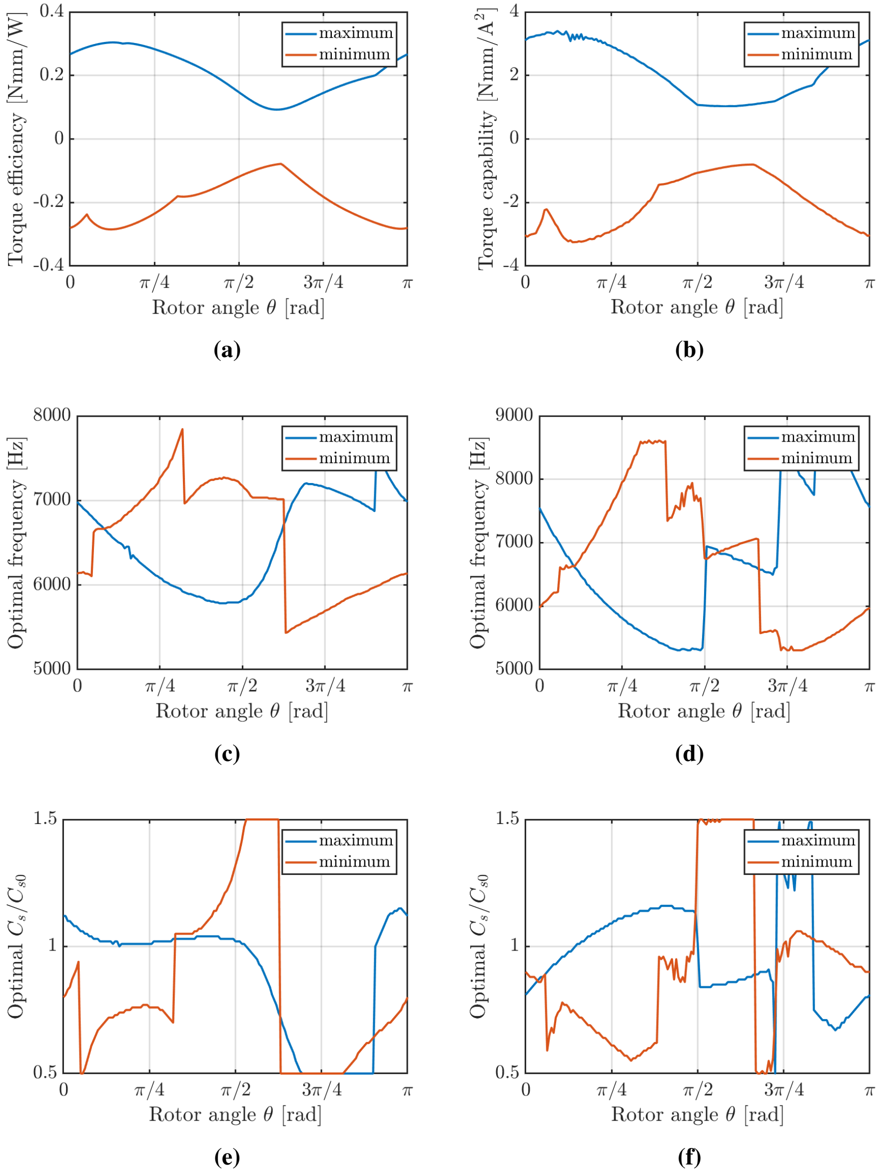

Figure 4.13: The minimum and maximum torque efficiency (a) and torque capability (b) and their corresponding frequency (c)-(d) and capacitor values (e)-(f).

4.8 Rotor current estimation

Online monitoring of system variables becomes more difficult when the considered components are moving. Especially the current measurement in the rotor coil is significantly more difficult compared to the fixed transmitter and stator coils. While methods exist to directly measure the current in a rotating coil, the implementation of these methods adds complexity and cost to the design of the system. It is important to know the amplitude of the rotor current for multiple reasons:

- Validation of the precise tuning of the rotor coil.
- Estimation of the losses and varying ESR of the rotor coil.
- Estimation of the torque due to the interaction between the coil currents.

A dynamic torque transducer is a very expensive component. Due to this cost, it is not practical to add such a sensor when manufacturing RWPT motors in large quantities. It would thus be beneficial if we could estimate the torque accurately based on the system currents. The experimental validation in Section 4.5.1 shows that the system currents and the resulting torque are not estimated with high accuracy if we only consider the electrical model of the system. It can be useful to add feedback of electrical measurements to improve the estimation of system variables.

The electrical interaction between the system coils is described by three complex equations, based Kirchoff's voltage law:

$$\begin{cases} V_t &= (R_t + j\omega L_t)I_t + j\omega M_{\mathrm{ts}} I_s + j\omega M_{\mathrm{tr}}(\theta) I_r \\ 0 &= j\omega M_{\mathrm{ts}} I_t + (R_s + jX_s) I_s + j\omega M_{\mathrm{sr}}(\theta) I_r \\ 0 &= j\omega M_{\mathrm{tr}}(\theta) I_t + j\omega M_{\mathrm{sr}}(\theta) I_s + (R_r + jX_r) I_r \end{cases} \tag{4.24}$$

The mutual inductance profile, as a function of the rotor angle θ, has been measured offline. The output voltage V_t of the amplifier can be measured online (or derived from the control signal), together with the transmitter and stator currents I_t and I_s. Based on the three complex equations, we now have three different expressions for the rotor current I_r:

a) $I_r = \dfrac{V_t - (R_t + j\omega L_t)I_t - j\omega M_{\mathrm{ts}} I_s}{j\omega M_{\mathrm{tr}}(\theta)}$

b) $I_r = \dfrac{-j\omega M_{\mathrm{ts}} I_t - (R_s + jX_s) I_s}{j\omega M_{\mathrm{sr}}(\theta)}$

c) $I_r = \dfrac{-j\omega M_{\mathrm{tr}}(\theta) I_t - j\omega M_{\mathrm{sr}}(\theta) I_s}{(R_r + jX_r)}$

Figures 4.14(a)-(c) show the resulting output of the rotor current estimation for varying frequencies and rotor angles.

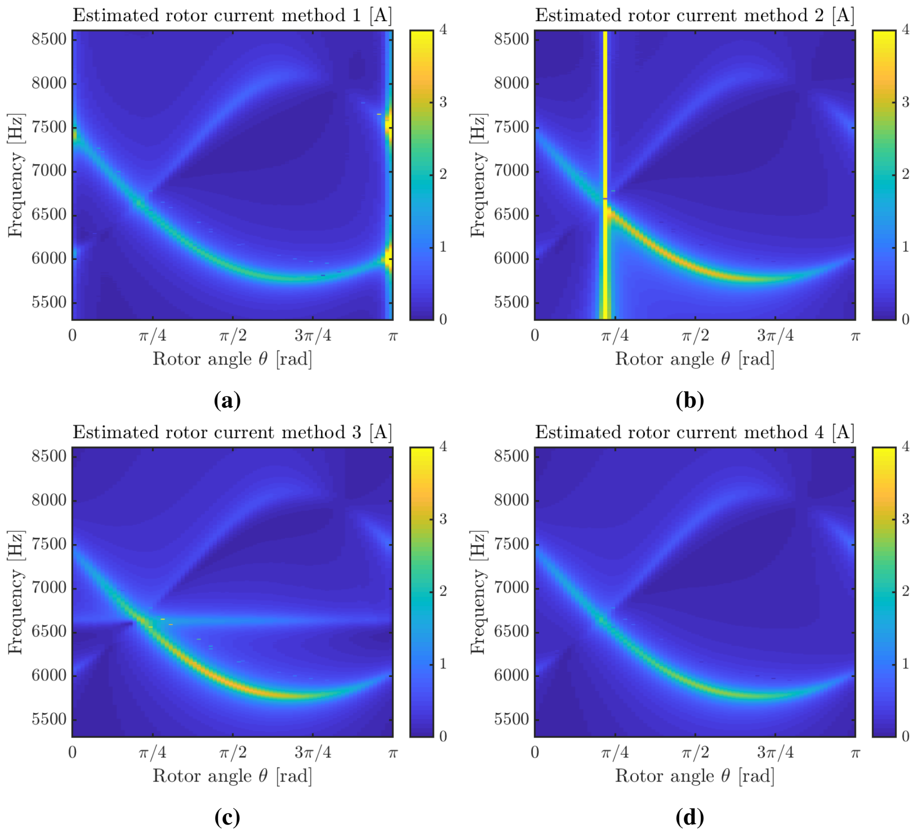

Figure 4.14: The rotor current can be estimated using four methods, which are based on the KVL equations of the system coils.

The first method becomes less accurate when the magnetic coupling between the transmitter and the rotor (M_{tr}) approaches zero. In Figure 4.14(a), the current estimation becomes highly unstable for rotor angles $\theta = 0$ and $\theta = \pi$, which is illustrated by vertical lines at these rotor angles. Similarly, the second method becomes unstable for low mutual inductance values between the stator and the rotor ($M_{\mathrm{sr}} \approx 0$), which results in inaccurate results around $\theta = \phi_{\mathrm{st}} + k\pi$, which are again illustrated by vertical lines on the figure. The first two methods show instability for low values of the denominator. The third suffers from a similar shortcoming. Namely, the estimation of the rotor current is too high for low impedance values of the rotor coil. These low impedance values correspond to frequencies close to the resonance frequency of the rotor and is visible by a horizontal deviation around the resonance frequency (6630 Hz). Methods (b) and (c) show an overestimation of the rotor current which is most likely due to an underestimation of the series resistance values of the resonator coils.

The set of linear equations in (4.24) show three equations which describe the same rotor current I_r, while all other variables are measured offline or online. As we theoretically only need one linear equation to find this one variable, (4.24) is an overdetermined set of equations. All three equations show inaccurate regions which mostly do not overlap. By combining the three estimates of the rotor current intelligently, the rotor current can be estimated more accurately for the whole operating range. Every model and measurement has intrinsic inaccuracies. By combining multiple models for the same current and including more measured variables, the overall accuracy of the current estimator will improve.

A straightforward method of solving an overdetermined linear set of equations is to minimize the sum of squares of the error in each equation:

$$I_r^* = \arg\min_{I_r}(|e_1|^2 + |e_2|^2 + |e_3|^2) \tag{4.25}$$

with

$$\begin{cases} e_1 &= -V_t + (R_t + j\omega L_t)I_t + j\omega M_{\text{ts}} I_s + j\omega M_{\text{tr}}(\theta) I_r \\ e_2 &= j\omega M_{\text{ts}} I_t + (R_s + jX_s)I_s + j\omega M_{\text{sr}}(\theta) I_r \\ e_3 &= j\omega M_{\text{tr}}(\theta) I_t + j\omega M_{\text{sr}}(\theta) I_s + (R_r + jX_r) I_r \end{cases} \tag{4.26}$$

This method corresponds to minimizing the sum of the squares of the deviations in Kirchoff's voltage law, which states that the sum of all voltages in a closed loop should be equal to zero. Note that for an overdetermined system it is rare that all errors are reduced to exactly zero. The minimization of the sum of squared error corresponds to the ordinary least squares problem which is used to estimate the unknown parameters in a linear regression model. The definition of the errors in (4.26) are converted to a linear system of the form

$$A\mathbf{x} = \mathbf{b} \tag{4.27}$$

with **x** the set of variables that we wish to estimate and matrix A and vector **b** independent of **x**. In this case, A, **b** and **x** are defined as:

$$\begin{cases} A &= \begin{bmatrix} j\omega M_{\mathrm{tr}}(\theta) \\ j\omega M_{\mathrm{sr}}(\theta) \\ R_r + jX_r \end{bmatrix} \\ \\ \mathbf{b} &= \begin{bmatrix} V_t - (R_t + j\omega L_t)I_t - j\omega M_{\mathrm{ts}} I_s \\ -j\omega M_{\mathrm{ts}} I_t - (R_s + jX_s) I_s \\ -j\omega M_{\mathrm{tr}}(\theta) I_t - j\omega M_{\mathrm{sr}}(\theta) I_s \end{bmatrix} \\ \\ \mathbf{x} &= I_r \end{cases} \tag{4.28}$$

We now wish to minimize the error vector which is defined as:

$$\min_{I_r} \|\mathbf{e}\| = \min_{I_r} \|A\mathbf{x} - \mathbf{b}\| \tag{4.29}$$

The solution of this minimization procedure can be expressed by

$$I_r^* = (A^{\mathrm{T}} A)^{-1} A^{\mathrm{T}} \mathbf{b} \tag{4.30}$$

for real-valued linear equations and by

$$I_r^* = (A^{\mathrm{H}} A)^{-1} A^{\mathrm{H}} \mathbf{b} \tag{4.31}$$

for complex valued linear equations, where A^{H} denotes the Hermitian or conjugate transpose of A. The expression $(A^{\mathrm{H}}A)^{-1}A^{\mathrm{H}}$ is called the Moore-Penrose inverse of A, which is a generalized type of matrix inverse that is applicable to most non-square matrices. The inverse of $A^{\mathrm{H}}A$ only exists if A has full column rank. In this case, the stochasticity and complex nature of the elements in A make it highly unlikely that the rank of A is not full. As the mutual inductance profiles M_{tr} and M_{sr} are zero for different angles of θ, there are a maximum of two zero terms in matrix A.

Figure 4.14(d) shows the result of the optimization function of the overdetermined system (4.25). The unstable solutions around $\theta = \{0, \phi_{\mathrm{st}}, \pi, \phi_{\mathrm{st}} + \pi, ..\}$ and $\omega = \omega_r$ have been eliminated by combining the different KVL equations. We can give the KVL equations different weight by multiplying the expression of the error by a weighting factor w:

$$I_r^* = \arg\min_{I_r} (|w_1 e_1|^2 + |w_2 e_2|^2 + |w_3 e_3|^2) \tag{4.32}$$

An argument could be made that the last two KVL equations are less reliable as the impedance of the resonators cannot be accurately known close to resonant conditions. In this work we do not further investigate this arbitrary weighing of the error. The main goal was to return a stable solution for all operating conditions, which we achieved.

4.9 Conclusion

The previous chapter showed that for a resonant tuning, the RWPT motoring system has a highly variable torque profile which reaches its peak value only at one certain angle. In this chapter, we demonstrated that the RWPT motoring system strongly benefits from detuning of the resonators. The electrical state-space model and the torque expressions were expanded with reactive terms that correspond to the detuned RLC circuits. For the 3 coil system, we identified 2 degrees of freedom that quantify the detuning of the resonators. The frequency and the stator capacitance value are chosen as the variable parameters corresponding to these detuning DOF.

The simulated system was validated for three stator capacitor values and a frequency sweep. It is shown that a high torque can now be reached for a much larger range of rotor angles instead of only one specific rotor angle. By varying the stator capacitor and lowering the driving frequency, the average and maximum torque over one rotation are increased by 88% and 49% respectively.

For resonant tuning, the average and maximum torque over one rotation are very sensitive to mistuning. Especially a tuning for which one resonator behaves inductive, while the other behaves capacitive should be avoided. When moving the tuning of the stator and rotor coils away from resonance, the average and maximum torque for one rotation become much more robust against slight mistuning.

The peak torque has a high correlation with the peak current amplitudes in the system. In Section 4.6.2, we suggested two performance indicators, namely the torque efficiency (TE) and the torque capability (TC), which allow us to quantify the quasi-static torque generation with respect to the dissipated power and the current limits.

Direct measurement of the current in the moving rotor coil requires additional cost and complexity. In Section 4.8 we discussed a robust method for estimating the rotor current based on the rotor position, the control signal of the AC voltage source and sensor data.

Chapter 5

Active capacitor detuning with state estimation

5.1 Introduction

In the previous chapter, the detuning of an RWPT motoring system was explored. It was determined that a 3 coil system with two resonators has two degrees of freedom for its detuning, namely the excitation frequency and the series connected capacitor of one of the resonators. It was shown that the optimal torque, torque efficiency or torque capability of an RWPT motoring system require a detuning which is highly dependent on the rotor angle. While the frequency is easily adjusted by changing the frequency of the control signal of the amplifier, it is challenging to finely tune the capacitance of the series connected capacitor, especially while the motor is operated. This chapter explores the possible ways in which the capacitor can be varied online in either a discrete (by the use of a switched capacitor bank) or continuous way by the use of AC transistor switches. The capacitance value of a capacitor describes how much the voltage over the capacitor changes in time when current passes through it. By prohibiting the charging or discharging of the capacitor during parts of one period by opening a switch, the equivalent capacitance can be changed. Sections 5.2.2 and 5.2.3 explain two types of switch controlled capacitors. It will be shown that zero voltage switching (ZVS) is made possible by phase-shifting the control signal of the integrated switches. Section 5.3 explains how the current and voltage waveforms can be reconstructed for SCC's with large capacitor ranges. In Section 5.4.2, we show how the equivalent impedance of the switch controlled capacitor can be estimated together with other system states, such as the rotor current.

5.2 Switched capacitor types

5.2.1 Discrete capacitor bank

A capacitor bank consists of a series of capacitors that are connected in parallel. The charging and discharging of the capacitors can be disabled by opening solid-state AC switches, typically back-to-back IGBT's or MOSFET's or electromechanical relays. In order to limit the number of discrete capacitors for a given capacitor range and tuning accuracy, capacitors of different capacitance values are used. The total capacitance is the sum of the capacitance values of the enabled capacitors. The most efficient distribution of these capacitor values is a binary weighted set [134–136]. For a binary weighted set, the capacitance value of the nth capacitor is double the value of the $(n-1)$th capacitor (see Figure 5.1).

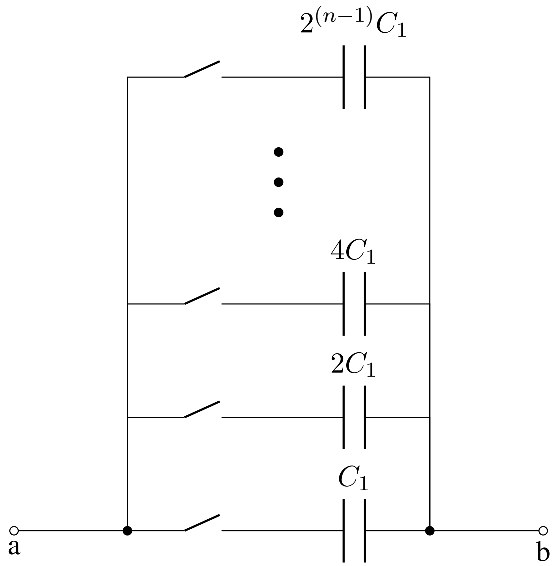

Figure 5.1: A switchable bank of binary weighted capacitors.

The total capacitance of a capacitor bank of n binary weighted parallel capacitors has a range up to $(2^n - 1)C_1$, with a step size of C_1. The Q factor of a coil is a measure for the bandwidth for which resonance occurs. For high Q factors, the required number of capacitors n easily rises to 5 or more [136]. Fine tuning of a switching capacitor bank thus requires multiple discrete capacitors, solid state switches and their accompanying controllers. Failure or instability of the capacitors can result in band gaps for which tuning is impossible.

5.2.2 Series connected switch controlled capacitor

The capacitance value of a capacitor indicates how much the voltage over its terminals increases when current passes through it. If we use an AC switch to partially limit the charging or discharging of the capacitor, this can be translated into a lower or higher equivalent capacitor value, depending on the configuration. In this chapter, we are only interested in the equivalent capacitor value for the first harmonic of the voltage and current. In resonant circuits, higher voltage harmonics are filtered out such that they do not cause significant higher harmonic currents. Switch controlled capacitors only require one AC switch and one auxiliary capacitor to enable continuous control of the equivalent capacitor value. In this chapter we discuss two ways in which an AC switch is used to change the equivalent capacitance. The first method uses a switch to short circuit the capacitor for some parts of the period. Specifically, the voltage is kept at zero for a certain interval, such that the charging of the capacitor is delayed. Because of the delayed charging, the peak voltage of the capacitor is lower and the capacitor is discharged earlier. This type of SCC can be connected in series with another capacitor that always conducts the current [93, 137–139]. Figure 5.2 shows the electrical scheme of a SCC (C_{sw}) connected in series with a permanently conducting capacitor (C_{fix}).

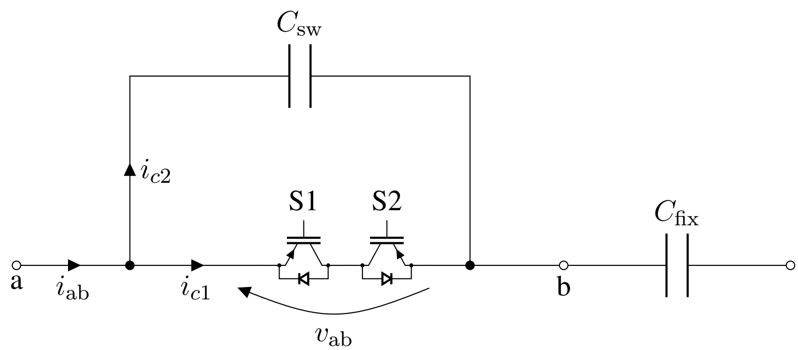

Figure 5.2: The series connected SCC is short circuited for certain intervals per period. This way charging of the capacitor is delayed.

The SCC is operated as follows:

- When the capacitor is discharged and the voltage over terminals a and b is zero, switches $S1$ and $S2$ are closed, such that the current passes through this short circuit.
- While the current i_{ab} is decreasing, the switches are opened. The current is forced through the capacitor and a counteracting voltage is generated.

- When the current crosses zero, the capacitor voltage reaches its peak value. When the current changes sign, the capacitor starts discharging.
- As soon as the voltage over the capacitor reaches zero, $S1$ and $S2$ are opened again, prohibiting a further decrease of the capacitor voltage.

When the switches open, no voltage is present over their terminals, such that zero voltage switching is achieved. When the switches close, however, a sudden short circuit is made between the capacitor terminals. As there is no inductor placed in series with the switched capacitor, the control needs to be very accurate in order to prevent current surges through the capacitor and the switches. Passive soft switching can still be achieved by using the bypass diode in the IGBT's. Instead of opening and closing $S1$ and $S2$ simultaneously, we now alternate their control signals. When $S1$ is closed and $S2$ is open, the bypass diode of $S2$ allows for positive currents (i_{c1}) to pass through. On the other hand, when $S1$ is opened and $S2$ is closed, negative currents can pass through. The conducting behavior is now slightly altered:

- When the capacitor is discharged and the current i_{c1} is positive, switch $S1$ is closed and $S2$ is opened, such that the current passes through this short circuit.
- While the current is decreasing, the switch control signals are inverted. The current is blocked by the bypass diode of $S1$ and is forced through the capacitor.
- When the current crosses zero, the capacitor voltage reaches its peak value. When the current changes sign, the capacitor starts discharging, but the diode of $S1$ does not conduct as long as the capacitor voltage is positive.
- As soon as the voltage over the capacitor reaches zero, the diode of $S1$ starts conducting the negative current, prohibiting a further decrease of the capacitor voltage.

The ZVS of the second stage is now ensured by the diode operation of the IGBT's. Figure 5.3 shows the control signals of $S1$ and $S2$ and the current and voltage waveforms of the SCC. The switching instance is defined with respect to the zero-crossing of the current as δ. The time that C_{sw} conducts current is denoted by δ_{12}. From the symmetry of the waveform we can prove that $\delta_{12} = 2\pi - 2\delta$.

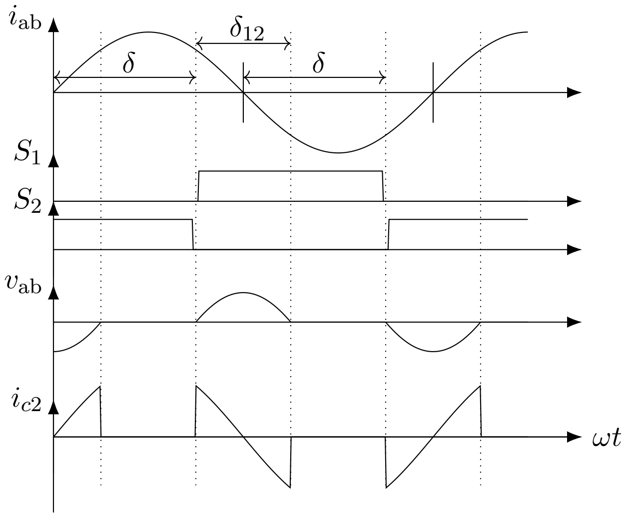

Figure 5.3: The current and voltage waveforms of the electrical states in the series connected switch controlled capacitor.

Improper switching instance control

The switching instance δ needs to be between $\pi/2$ and π to prohibit surge currents through the capacitor and transistors. For switching instances in the range of $0 \leq \delta < \pi/2$, the capacitor charges for longer than it can discharge, resulting in a surge current when the control signals are switched (Figure 5.4(a)). For switching instances later than π, the capacitor does not start charging at δ. Only later, when the current switches sign, the capacitor starts charging for a short interval until the control signals invert and a surge current through the transistors depletes the capacitor again (Figure 5.4(b)).

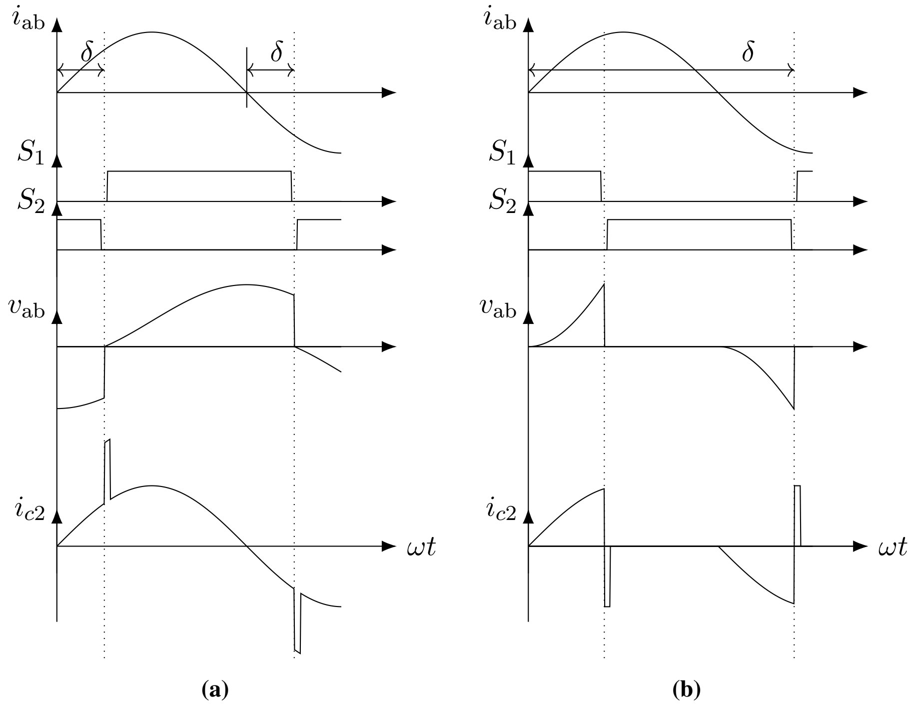

Figure 5.4: When the switching instance is too early (a) or too late (b), the capacitor still holds a charge when the short circuit is closed, resulting in a current surge through the capacitor.

Capacitance range of a series connected SCC

The equivalent capacitance of the SCC is determined by the length of the intervals for which the capacitor is able to charge and discharge. When the switched capacitor C_{sw} permanently conducts current and the current through the AC switch is always blocked (e.g., for $\delta = \pi/2$), the equivalent capacitor value of the SCC is evidently equal to C_{sw}. When the transistors always allow for current to pass (resulting in a short circuit), the voltage over terminals a and b does not change due to passing current, such that the equivalent capacitance is infinite. When a fixed capacitor (C_{fix}) is connected in series with the SCC, the equivalent capacitance varies between:

$$\begin{cases} C_{\mathrm{min}} & = \dfrac{C_{\mathrm{fix}} C_{\mathrm{sw}}}{C_{\mathrm{fix}} + C_{\mathrm{sw}}} \\ C_{\mathrm{max}} & = C_{\mathrm{fix}} \end{cases} \tag{5.1}$$

The series connection of the SCC lowers the total capacitance of the circuit. The possible range for the capacitance ΔC is then:

$$\begin{aligned}\Delta C &= C_{\text{max}} - C_{\text{min}} \\ &= C_{\text{fix}} - \frac{C_{\text{fix}}C_{\text{sw}}}{C_{\text{fix}} + C_{\text{sw}}} \\ &= C_{\text{fix}}\frac{C_{\text{fix}}}{C_{\text{fix}} + C_{\text{sw}}}\end{aligned} \tag{5.2}$$

The restructured expression for ΔC in the last line of (5.2) shows that for a small capacitance range, a large auxiliary capacitor C_{sw} is required.

Equivalent capacitor value

In this section, we derive the correspondence between the equivalent capacitance C_{eq} of a short circuited SCC and the switching instance δ. We are only interested in the equivalent capacitance for the first time harmonic. The higher harmonics of the current are naturally filtered out in an LC resonator. For this reason, we assume that the current through the resonator is sinusoidal, with $\hat{I}_{\text{ab}}$ the peak amplitude of the current through the SCC:

$$i_{\text{ab}} = \hat{I}_{\text{ab}} \sin(\omega t) \tag{5.3}$$

We observe the waveform of the voltage over the capacitor terminals a and b. At first, the capacitor is completely discharged and the voltage v_{ab} is zero. At the switching instance δ, the control signals of the transistors are inverted and the current is forced through the capacitor. The capacitor charges from $\omega t = \delta$ and v_{ab} reaches its peak value when the current i_{ab} crosses zero. The capacitor discharges again until $\omega t = 2\pi - \delta$. From that point, the diode of $S1$ conducts the current again because the voltage over the diode is non-positive. The voltage over the terminals remains zero between $2\pi - \delta$ and $\pi + \delta$. The same pattern repeats every π radians, with alternating signs of the capacitor voltage, such that:

$$v_{\text{ab},[\pi-\delta,\delta]} = 0 \tag{5.4}$$

At $\omega t = \delta$ the capacitor starts charging, starting from 0 V. The voltage over the terminal is then obtained by integrating the sinusoidal current:

$$\begin{aligned}v_{\text{ab},[\delta,2\pi-\delta]} &= \frac{1}{C_{\text{sw}}}\int_{\delta}^{\omega t} i_{\text{ab}}\text{d}(\omega t) \\ &= \frac{\hat{I}_{\text{ab}}}{\omega C_{\text{sw}}}[-\cos(\omega t) + \cos(\delta)]\end{aligned} \tag{5.5}$$

Starting from this half period, we can use the Fourier transform to find the peak amplitude of the first harmonic of v_{ab}, namely $\hat{V}_{\mathrm{ab}}$. As the capacitor voltage lags the current by $\pi/2$, we only need the cosine term of the Fourier transform.

$$\begin{aligned}\hat{V}_{\mathrm{ab}} &= \frac{2}{\pi}\left|\int_{\pi-\delta}^{2\pi-\delta} v_{\mathrm{ab}}\cos(\omega t)d(\omega t)\right| \\ &= \frac{2}{\pi}\left|\int_{\delta}^{2\pi-\delta} v_{\mathrm{ab},[\delta,2\pi-\delta]}\cos(\omega t)d(\omega t)\right| \\ &= \frac{\hat{I}_{\mathrm{ab}}}{\omega C_{\mathrm{sw}}}\frac{2}{\pi}\left|\int_{\delta}^{2\pi-\delta}[-\cos(\omega t)+\cos(\delta)]\cos(\omega t)d(\omega t)\right| \\ &= \frac{\hat{I}_{\mathrm{ab}}}{\omega C_{\mathrm{sw}}}\left|\frac{2\delta}{\pi}-2-\frac{\sin 2\delta}{\pi}\right|\end{aligned} \tag{5.6}$$

For $\pi/2 \leq \delta \leq \pi$, the Fourier transform returns a negative value, which indicates that the voltage indeed lags the current. The equivalent capacitive reactance $\frac{1}{\omega C_{\mathrm{eq}}}$ is now calculated as the ratio of the peak amplitudes of the first harmonics of the current $\hat{I}_{\mathrm{ab}}$ and the voltage $\hat{V}_{\mathrm{ab}}$.

$$\begin{aligned}\frac{1}{\omega C_{\mathrm{eq}}} &= \frac{\hat{V}_{\mathrm{ab}}}{\hat{I}_{\mathrm{ab}}} \\ C_{\mathrm{eq}} &= \frac{\hat{I}_{\mathrm{ab}}}{\omega \hat{V}_{\mathrm{ab}}} \\ &= \frac{C_{\mathrm{sw}}}{2-\frac{2\delta}{\pi}+\frac{\sin 2\delta}{\pi}}\end{aligned} \tag{5.7}$$

It is easily shown that the equivalent capacitance is a monotonous function of δ for $\pi/2 \leq \delta \leq \pi$. Figure 5.5 shows the equivalent capacitance for the SCC connected in series with a fixed capacitor and $C_{\mathrm{fix}} = C_{\mathrm{sw}}$. We observe that the minimum and maximum values correspond to the values in (5.1).

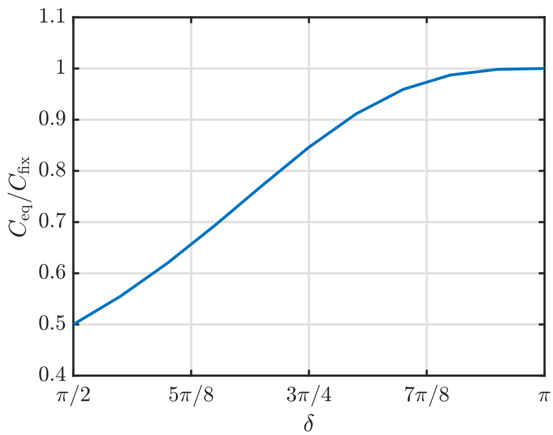

Figure 5.5: The equivalent capacitance of the series connected SCC varies monotonously with the switching instance δ.

5.2.3 Parallel switch controlled capacitor

Another way to integrate an SCC is by connecting a switched capacitor branch in parallel with a fixed capacitor [30, 92, 136, 140], illustrated in Figure 5.6. When the parallel SCC does not conduct current, the incoming current i_{ab} increases or decreases the voltage over the fixed capacitor C_{fix}. For some interval(s) of the period, the switches are closed and the incoming current i_{ab} is divided between both capacitors. In those intervals, the effective capacitance is higher and the voltage slope is decreased.

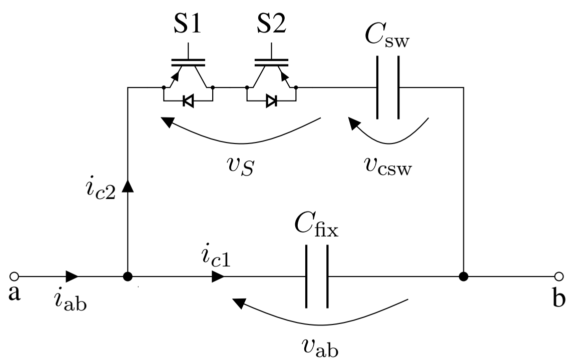

Figure 5.6: When the parallel connected SCC conducts current, the voltage in the fixed capacitor varies slower for the same current.

Figure 5.7 shows the waveforms for the correctly operated parallel SCC.

The auxiliary capacitor is charged up to a certain level and then disconnected until the voltage of the fixed capacitor decreases back to that level. ZVS is again made possible by leveraging the parallel diodes of the transistors:

- When the current is positive, $S1$ is closed and $S2$ is opened, such that current is allowed to pass through the auxiliary capacitor C_{sw}.
- While the current is positive but decreasing, the control signals of the switches are inverted at switching instance δ. The diode of $S1$ now prohibits further charging of the voltage v_{csw}. The voltage over the switches then follows the voltage difference between C_{fix} and C_{sw}.
- The voltage over C_{fix} rises more steeply (due to the lower effective capacitance) until it reaches its maximum value when current i_{ab} crosses zero. From then on, C_{fix} discharges until the voltage over its terminals equals the voltage over C_{sw}.
- When the voltage of C_{fix} drops to the voltage over C_{sw}, the bypass diode of $S1$ starts conducting. The current is again distributed between both capacitors, increasing their effective capacitance.

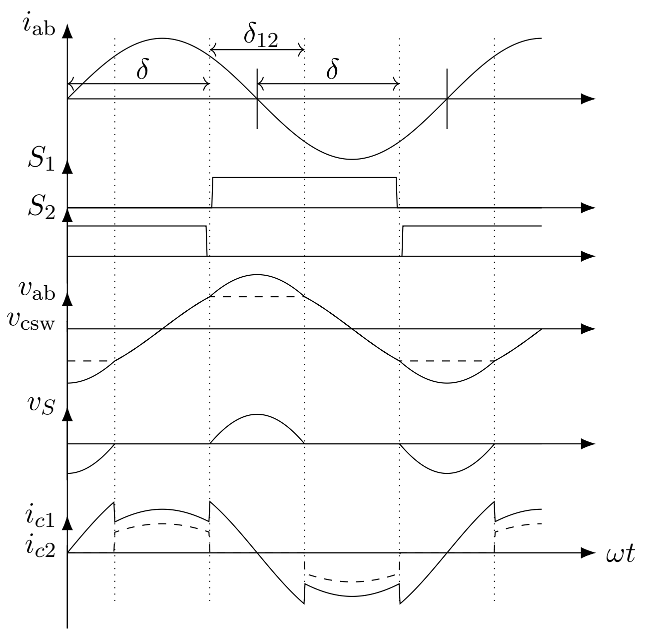

Figure 5.7: The current and voltage waveforms of the electrical states in the parallel switch controlled capacitor.

The time that the auxiliary capacitor is not conducting is again denoted by δ_{12}. Similar to the series connected SCC, we can prove that $\delta_{12} = 2\pi - 2\delta$.

The parallel diodes prevent surge currents to run between the capacitors when their voltage difference is non-zero, as long as $\pi/2 \leq \delta < \pi$.

When the switching instance δ is equal to $\pi/2$, the switched capacitor is always conducting current and the effective capacitance is equal to the sum of both capacitance values. For $\delta = \pi$, there is no opportunity for current to pass through the switched capacitor, such that the capacitance of the parallel branch is negated. The minimum and maximum capacitance values for the parallel SCC are:

$$\begin{cases} C_{\text{min}} = C_{\text{fix}} \\ C_{\text{max}} = C_{\text{fix}} + C_{\text{sw}} \end{cases} \tag{5.8}$$

Contrary to the series connected SCC, the addition of the SCC now increases the total capacitance. The capacitance range can be expressed as:

$$\begin{aligned} \Delta C &= C_{\text{max}} - C_{\text{min}} \\ &= C_{\text{sw}} \\ &= C_{\text{fix}} \frac{C_{\text{sw}}}{C_{\text{fix}}} \end{aligned} \tag{5.9}$$

For a small variation of the capacitor tuning, only a small parallel capacitor C_{sw} is required.

Equivalent capacitance value

In what follows, we derive the equivalent capacitance of the SCC as a function of the switching instance δ. First we express the voltage waveform of v_{ab} as a function of ωt. We again assume a sinusoidal resonator current i_{ab} with peak amplitude $\hat{I}_{\text{ab}}$.

Some time before the switching instance δ, both capacitors share the incoming current. As the capacitor voltage lags the current by $\pi/2$ rad, and based on the time-symmetry of the waveform, this interval starts at $\pi - \delta$. The voltage in this interval crosses zero at $\omega t = \pi/2 + k\pi$, when the current reaches its peak value. From these boundary conditions, the voltage over the terminals in the interval $\omega t \in [\pi - \delta, \delta]$ can be uniquely determined:

$$v_{\text{ab},[\pi-\delta,\delta]} = \frac{1}{C_{\text{max}}} \int_{\pi/2}^{\omega t} i_{\text{ab}} \mathrm{d}(\omega t) = -\frac{\hat{I}_{\text{ab}}}{\omega C_{\text{max}}} \cos(\omega t) \tag{5.10}$$

At instance δ, the current through C_{sw} is blocked until the voltage over C_{fix} decreases back to that level at $\omega t = 2\pi - \delta$ (due to symmetry). The voltage over C_{fix} is continuous at the switching instance, resulting in a unique solution for the voltage over the terminals:

$$\begin{aligned} v_{\text{ab},[\delta,2\pi-\delta]} &= v_{\text{ab},[\pi-\delta,\delta]}(\delta) + \frac{1}{C_{\text{min}}}\int_{\delta}^{\omega t} i_{\text{ab}}\text{d}(\omega t) \\ &= \left(\frac{\hat{I}_{\text{ab}}}{\omega C_{\text{min}}} - \frac{\hat{I}_{\text{ab}}}{\omega C_{\text{max}}}\right)\cos(\delta) - \frac{\hat{I}_{\text{ab}}}{\omega C_{\text{min}}}\cos(\omega t) \end{aligned} \tag{5.11}$$

The waveforms over the interval $[\pi-\delta, 2\pi-\delta]$ then repeat with alternating signs. We can again calculate the peak amplitude of the first harmonic of the voltage $\hat{V}_{\text{ab}}$ over the terminals using the Fourier transform:

$$\hat{V}_{\text{ab}} = \frac{2}{\pi}\int_{\pi-\delta}^{2\pi-\delta} v_{\text{ab}}\cos(\omega t)\text{d}(\omega t) \tag{5.12}$$

After some calculation, the peak voltage amplitude can be expressed as:

$$\hat{V}_{\text{ab}} = \frac{\hat{I}_c}{\omega C_{\text{min}}} + \left(\frac{\hat{I}_c}{\omega C_{\text{min}}} - \frac{\hat{I}_c}{\omega C_{\text{max}}}\right)\left(1 + \frac{\sin(2\delta)}{\pi} - \frac{2\delta}{\pi}\right) \tag{5.13}$$

The equivalent capacitance value C_{eq} is then calculated from the ratio of the peak amplitudes of the voltage and the current.

$$\begin{aligned} \frac{1}{C_{\text{eq}}} &= \frac{\omega\hat{V}_{\text{ab}}}{\hat{I}_{\text{ab}}} \\ &= \frac{1}{C_{\text{min}}} + \left(\frac{1}{C_{\text{min}}} - \frac{1}{C_{\text{max}}}\right)\left(1 + \frac{\sin(2\delta)}{\pi} - \frac{2\delta}{\pi}\right) \end{aligned} \tag{5.14}$$

We can ascertain that the equivalent capacitance C_{eq} varies from C_{min} for $\delta = \pi/2$ to C_{max} for $\delta = \pi$. The equivalent capacitance is again a monotonous function of δ, which is illustrated in Figure 5.8 for $C_{\text{fix}} = C_{\text{sw}}$.

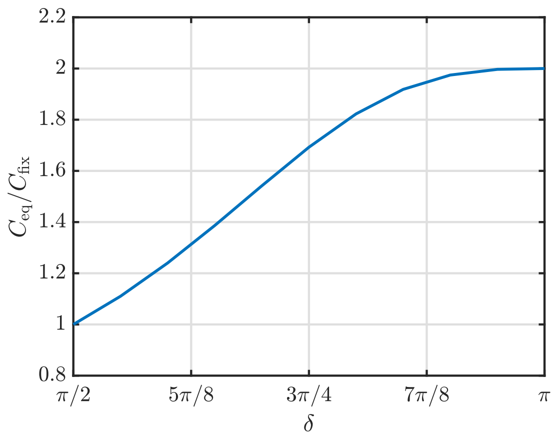

Figure 5.8: The equivalent capacitance for a parallel SCC is a monotonous function of switching instance δ.

5.3 Wide range parallel SCC

The derivation of the equivalent capacitance in Sections 5.2.2 and 5.2.3 were based on the assumption of a sinusoidal current and ignored the forward voltage of the diodes in the AC switch. For small capacitor variations (ΔC), the momentary capacitance value does not vary much, such that the voltage waveform is minimally deformed. Around its resonance frequency, a LC resonator operates as a bandpass filter, filtering out higher harmonics of the current. In Section 4.7 of the previous chapter it was shown that the torque performance of the RWPT motoring system is drastically improved when we allow strong detuning from the resonance frequency. Additionally the capacitance value of at least one of the resonators needs to be controlled in a large range around the resonant tuning. For these operating modes, the assumption of a purely sinusoidal current breaks down. In this section, we will consider a more realistic scenario for RWPT systems. A sinusoidal voltage v_{in} with frequency ω is connected in series with a RLC circuit with a parallel switch controlled capacitor (see Figure 5.9). This sinusoidal voltage can be caused by a voltage amplifier or be induced by the AC current in a (strongly) coupled coil. We do not assume that the excitation frequency of v_{in} corresponds to the resonance frequency of the LC circuit.

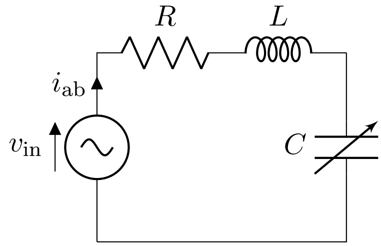

Figure 5.9: A sinusoidal voltage source is connected in series with an RLC circuit with variable capacitor.

From the previous section, we know that there is one interval per half period where the auxiliary capacitor C_{sw} conducts current (interval 2 in Figure 5.10). This means that we can split a half period into two sections, one for which the effective capacitance is $C_1 = C_{\mathrm{min}} = C_{\mathrm{fix}}$ and one for which the effective capacitance is $C_2 = C_{\mathrm{max}} = C_{\mathrm{fix}} + C_{\mathrm{sw}}$. The switching instance marks the start of interval (1). We now define δ' as the electrical angle (ωt) between the zero crossing of v_{in} and the switching instance. The start of interval (2) at δ_{12} is a result of the dynamics of the circuit, namely when the voltage over the fixed capacitor lowers to the level of the SCC.

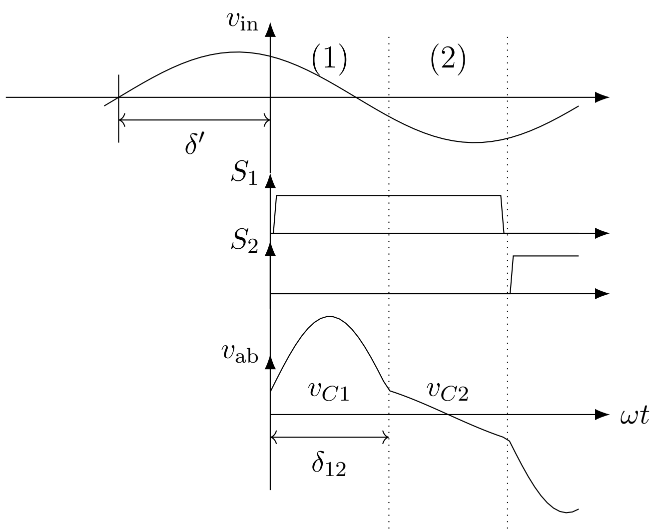

Figure 5.10: Every half period can be subdivided into two intervals, where the switching capacitor C_{sw} does (2) or does not (1) conduct current.

We will now explicitly solve the waveforms of the voltage over (v_{ab}) and current through the capacitor (i_{ab}). First, we derive the KVL for the circuit in Figure 5.9 for the first interval, where only the fixed capacitor conducts the current i_1:

$$\hat{V}_{\text{in}} \sin(\omega t + \delta') = Ri_1 + L\frac{\mathrm{d}i_1}{\mathrm{d}t} + v_{C1} \tag{5.15}$$

The current through the capacitor can be written as the time derivative of the voltage over the capacitor.

$$\frac{\mathrm{d}v_{C1}}{\mathrm{d}t} = \frac{i_1}{C_1} \tag{5.16}$$

By substituting (5.16) in (5.15), we obtain a second order ordinary differential equation (ODE) with a sinusoidal excitation.

$$\hat{V}_{\text{in}} \sin(\omega t + \delta') = LC_1\frac{\mathrm{d}^2v_{C1}}{\mathrm{d}t^2} + RC_1\frac{\mathrm{d}v_{C1}}{\mathrm{d}t} + v_{C1} \tag{5.17}$$

A similar second order ODE as a function of the current can be obtained by taking the time derivative of (5.17):

$$\omega\hat{V}_{\text{in}} \cos(\omega t + \delta') = L\frac{\mathrm{d}^2i_1}{\mathrm{d}t^2} + R\frac{\mathrm{d}i_1}{\mathrm{d}t} + \frac{i_1}{C_1} \tag{5.18}$$

Taking the time derivative of a function does degrade the general applicability of the solution. We will thus solve for the capacitor voltage in (5.17) and then use the time derivative in (5.16) to obtain the current through the capacitor.

5.3.1 Transient response of the RLC circuit with parallel SCC

Nonhomogeneous solution of the ODE

An ODE with a non-zero excitation has a solution which is the sum of one nonhomogeneous solution and a linear combination of the homogeneous solutions. For the nonhomogeneous solution, we require a transient response that abides the ODE with non-zero excitation. To find this solution, we assume that the response of v_{C1} is sinusoidal with the same frequency as the excitation v_{in}, such that we can solve the equation in the complex phasor representation. The ODE is now converted into a complex valued polynomial equation of the second order:

$$\begin{aligned} V_{\text{in}} &= |V_{\text{in}}|e^{j\delta'} = (1 - \omega^2 LC_1 + j\omega RC_1)V_{C1p} \\ V_{C1p} &= \frac{V_{\text{in}}}{1 - \omega^2 LC_1 + j\omega RC_1} \end{aligned} \tag{5.19}$$

The particular solution of the ODE can then be derived from the phasor V_{C1p}:

$$v_{C1p} = \hat{V}_{C1p} \sin\left(\omega t + \angle V_{C1p}\right) \tag{5.20}$$

From (5.16) we can derive the nonhomogeneous solution for the current phasor:

$$i_{C1p} = \omega C_1 \hat{V}_{C1p} \cos\left(\omega t + \angle V_{C1p}\right) \tag{5.21}$$

Homogeneous solution of the ODE

The homogeneous solution of an ODE is the transient response in the absence of the sinusoidal excitation:

$$0 = LC_1 \frac{\mathrm{d}^2 v_{C1}}{\mathrm{d}t^2} + RC_1 \frac{\mathrm{d}v_{C1}}{\mathrm{d}t} + v_{C1} \tag{5.22}$$

The solution(s) to this equation result in a zero value on the left side of the ODE. Adding a linear combination of the homogeneous solution(s) to the particular solution does not affect the validity of the ODE. To simplify the derivation of the homogeneous solution of the ODE (5.17), we first introduce two parameters that are closely related to the electrical behavior of the RLC circuit:

- The resonance frequency ω_1 of the LC circuit with capacitor C_1

  $$\omega_1[\mathrm{rad/s}] = \frac{1}{\sqrt{LC_1}} \tag{5.23}$$

- The attenuation α_1 of the RLC circuit is a measure of the energy loss in an oscillating circuit.

  $$\alpha_1[\mathrm{rad/s}] = \frac{R}{2L} \tag{5.24}$$

  The attenuation is closely related to the more commonly used damping ratio ζ_1 of the RLC circuit.

  $$\zeta_1[-] = \frac{\alpha_1}{\omega_1} = \frac{R}{2}\sqrt{\frac{C_1}{L}} = \frac{1}{2Q_1} \tag{5.25}$$

We can rewrite (5.17) as a function of these parameters:

$$0 = \frac{1}{\omega_1^2}\left(\frac{\mathrm{d}^2 v_{C1}}{\mathrm{d}t^2} + 2\alpha_1 \frac{\mathrm{d}v_{C1}}{\mathrm{d}t} + \omega_1^2 v_{C1}\right) \tag{5.26}$$

The transient response v_{C1} can be found by finding the roots of the characteristic equation

$$s^2 + 2\alpha_1 s + \omega_1^2 = 0 \tag{5.27}$$

The roots of the equation are:

$$s_{1/2} = -\alpha_1 \pm \omega_1\sqrt{\zeta_1^2 - 1} \tag{5.28}$$

For an underdamped system ($\zeta_1 < 1$), the roots are complex, resulting in an oscillating behavior. The generalized homogeneous solution v_{C1h} is then:

$$v_{C1h} = A_{1s} e^{-\alpha_1 t} \sin(\omega_1\sqrt{1-\zeta_1^2}t) + A_{1c} e^{-\alpha_1 t} \cos(\omega_1\sqrt{1-\zeta_1^2}t) \tag{5.29}$$

For high Q factors, the damping ratio ζ_1 and the attenuation α_1 are very low such that $\sqrt{1-\zeta_1^2} \approx 1$ and the attenuation is negligible for transients shorter than one period ($\alpha_1 t \approx 0$). Equation (5.29) can be simplified to the sum of a sine and a cosine of frequency ω_1:

$$v_{C1h} \approx A_{1s}\sin(\omega_1 t) + A_{1c}\cos(\omega_1 t) \tag{5.30}$$

The same procedure can be used to find the inhomogeneous solution and the homogeneous solutions for the second interval, where both capacitors conduct the current ($C = C_2$). The generalized solutions for both intervals are given by

$$\begin{cases} v_{C1} = \hat{V}_{C1p}\sin\left(\omega t + \angle V_{C1p}\right) + A_{1s}\sin(\omega_1 t) + A_{1c}\cos(\omega_1 t) \\ v_{C2} = \hat{V}_{C2p}\sin\left(\omega t + \angle V_{C2p}\right) + A_{2s}\sin(\omega_2 t) + A_{2c}\cos(\omega_2 t) \end{cases} \tag{5.31}$$

By substituting (5.16) in (5.31), we can derive the solution for the currents i_2 and i_2:

$$\begin{cases} i_1 = \dfrac{1}{C_1}\left[\omega\hat{V}_{C1p}\cos\left(\omega t + \angle V_{C1p}\right) + \omega_1 A_{1s}\cos(\omega_1 t) - \omega_1 A_{1c}\sin(\omega_1 t)\right] \\ i_2 = \dfrac{1}{C_2}\left[\omega\hat{V}_{C2p}\cos\left(\omega t + \angle V_{C2p}\right) + \omega_2 A_{2s}\cos(\omega_2 t) - \omega_2 A_{2c}\sin(\omega_2 t)\right] \end{cases} \tag{5.32}$$

5.3.2 Reconstructing the physical response of the SCC

In a switch controlled capacitor, the voltage and current over a half period is a concatenation of two piecewise functions. The first interval starts when the control signal is inverted such that only the fixed capacitor is able to conduct the current. If we shift this switching instance to $t = 0$, the phase shift of the excitation signal δ' is equal to the electrical angle ($\omega\Delta t$) between the zero crossing of v_{in} and the switching instance. Somewhere in the interval $\omega t \in [0, \pi]$, the voltage v_{C1} over the fixed capacitor drops below the voltage of the switched capacitor C_{sw}. From then on, both capacitors conduct the current and the transient solution v_{C2} becomes active until the next switching instance at $\omega t = \pi$.

By imposing the phase shift δ' between v_{in} and the switching instance at $t = 0$, we can identify 5 degrees of freedom (DOF) that determine the physical waveform of the voltage over and current through the switched capacitor:

- The 4 linear terms of the homogeneous solutions for v_{C1}, v_{C2}, i_2 and i_2.

$$A_{1s},\ A_{1c},\ A_{2s} \text{ and } A_{2c}$$

- The moment in time (δ_{12}) where both capacitors start conducting and the transient response follows $v_{\mathrm{ab}} = v_{C2}$ and $i_{\mathrm{ab}}(t) = i_2$.

We can also identify five physical boundary conditions for both intervals which have to be met:

1. The voltage over the fixed capacitor is always continuous. Because of this, the voltages of intervals 1 and 2 are equal at the transition point δ_{12}.

$$v_{C1}(\delta_{12}) = v_{C2}(\delta_{12}) \tag{5.33}$$

2. The second half of the period is a repetition of the first half but with opposite sign. The continuity condition for the capacitor value also holds for the boundaries of the interval.

$$v_{C2}(\pi) = -v_{C1}(0) \tag{5.34}$$

3. The presence of the series inductor requires a continuous current i_{ab}. The currents of intervals 1 and 2 are also equal at the transition point δ_{12}.

$$i_1(\delta_{12}) = i_2(\delta_{12}) \tag{5.35}$$

4. The same continuity condition for the current also holds for the boundaries of the interval, where the current values are equal and opposite in sign.

$$i_2(\pi) = -i_1(0) \tag{5.36}$$

5. The switched capacitor C_{sw} starts conducting when the voltage v_{C1} decreases to the same value it had before the switching instance.

$$v_{C1}(\delta_{12}) = v_{C1}(0) \tag{5.37}$$

If we keep into account the forward voltage drop (v_f) over the diode, the last condition is adjusted. While both capacitors charge simultaneously, the voltage of C_{sw} stays v_f lower than the voltage over the fixed capacitor C_{fix} (v_{ab}). Figure 5.11 shows an exaggerated voltage waveform for an SCC with a non-negligible forward voltage drop.

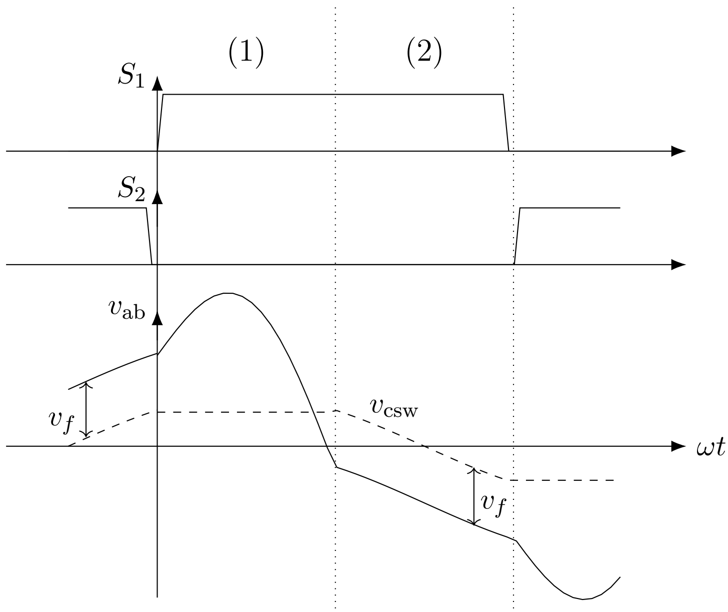

Figure 5.11: The voltage v_{ab} needs to drop by $2v_f$ before C_{sw} can start conducting again.

When C_{sw} is disengaged at $t = 0$, the voltage over C_{fix} (v_{ab}) increases while the current is positive. When the current switches sign, the voltage decreases until it drops below $v_{\text{csw}} - v_f$ and the switched capacitor starts conducting current again. The voltage over C_{sw} now remains v_f higher than v_{ab} while both capacitors discharge. The voltage v_{ab} is $2v_f$ lower when the second capacitor starts conducting at δ_{12}. The last boundary condition (5.37) is adjusted to:

$$v_{C1}(\delta_{12}) = v_{C1}(0) - 2v_f \tag{5.38}$$

We now wish to find the solutions for the parameters such that all five equality constraints are met. The value of the switching instance δ' fully determines the nonhomogeneous solutions for the voltage (5.20) and current (5.21) for both intervals. The nonhomogeneous solutions and the parametrized homogeneous solutions are added together and inserted in the five equations. A numerical solver tries to minimize the error on all five equality constraints. First, five error terms are defined as a function of the parameters:

$$\begin{cases} e_1 &= v_{C1}(\delta_{12}) - v_{C2}(\delta_{12}) \\ e_2 &= v_{C2}(\pi) + v_{C1}(0) \\ e_3 &= i_1(\delta_{12}) - i_2(\delta_{12}) \\ e_4 &= i_2(\pi) + i_1(0) \\ e_5 &= v_{C1}(\delta_{12}) - v_{C1}(0) - 2v_f \end{cases} \tag{5.39}$$

The numerical solvers tries to find the parameters for which the sum of the squared errors is minimal.

$$[A^*_{1s}, A^*_{1c}, A^*_{2s}, A^*_{2c}, \delta^*_{12}] = \arg\min(|e_1|^2+|e_2|^2+|e_3|^2+|e_4|^2+|e_5|^2) \quad (5.40)$$

There are five constraints and five parameters. Four of these parameters are linear scaling factors, which improves the chance of finding a solution for which all constraints are satisfied ($e_1 = .. = e_5 = 0$). The MATLAB function *vpasolve* is used to find the correct parameter values. The initial guess for the parameters is set to

$$[A_{1s}, A_{1c}, A_{2s}, A_{2c}, \delta_{12}] = [0, 0, 0, 0, \pi/2]$$

The methodology is tested for an RLC circuit with electrical parameters that correspond to the stator of the experimental setup (see Table 5.1). The capacitor values C_1 and C_2 correspond to 25% and 150% of the resonant tuning.

Table 5.1: The electrical parameters of the simulated RLC circuit correspond to those of the stator resonator in the experimental setup.

Parameter	**Value**
f	6630 Hz
L	5.44 mH
R	4.51 Ω
C_1	26.48 nF
C_2	158.89 nF
$\hat{V}_{\text{in}}$	20 V
v_f	0.7 V
δ'	$2\pi[0.36, 0.385, 0.41]$ rad

Figure 5.12 shows the voltage and current waveforms for three values of δ' that are obtained by the numerical solver. The blue waveforms correspond to a system for which we neglect the forward voltage drop (0.7 V) of the diodes. The value of δ' indirectly determines the transition point δ_{12}. Lower δ' values appear to also result in lower δ_{12} values. For δ'_1, the current amplitude is much higher, indicating that the tuning is close to resonant. The top of the current waveform is concave and the function appears close to sinusoidal. For δ'_2, the top of the current waveform is flattened and for the highest switching instance, δ'_3, the top of the current waveform even becomes convex. This observation proves that our assumption of a non-sinusoidal current was correct.

The inclusion of the forward voltage of the diode results in waveforms of lower amplitude, especially close to resonance. This is because close to resonance, the voltage drop over the series impedance decreases to values that are close to the additional voltage drop due to the diode. For strongly detuned RLC circuits (2 and 3), the voltage drop over the impedance is significantly larger than 0.7 V, such that the impact of the forward voltage on the current and voltage amplitude is limited. A very slight sideways shift to the right is observed which corresponds to the exaggerated waveform of Figure 5.11.

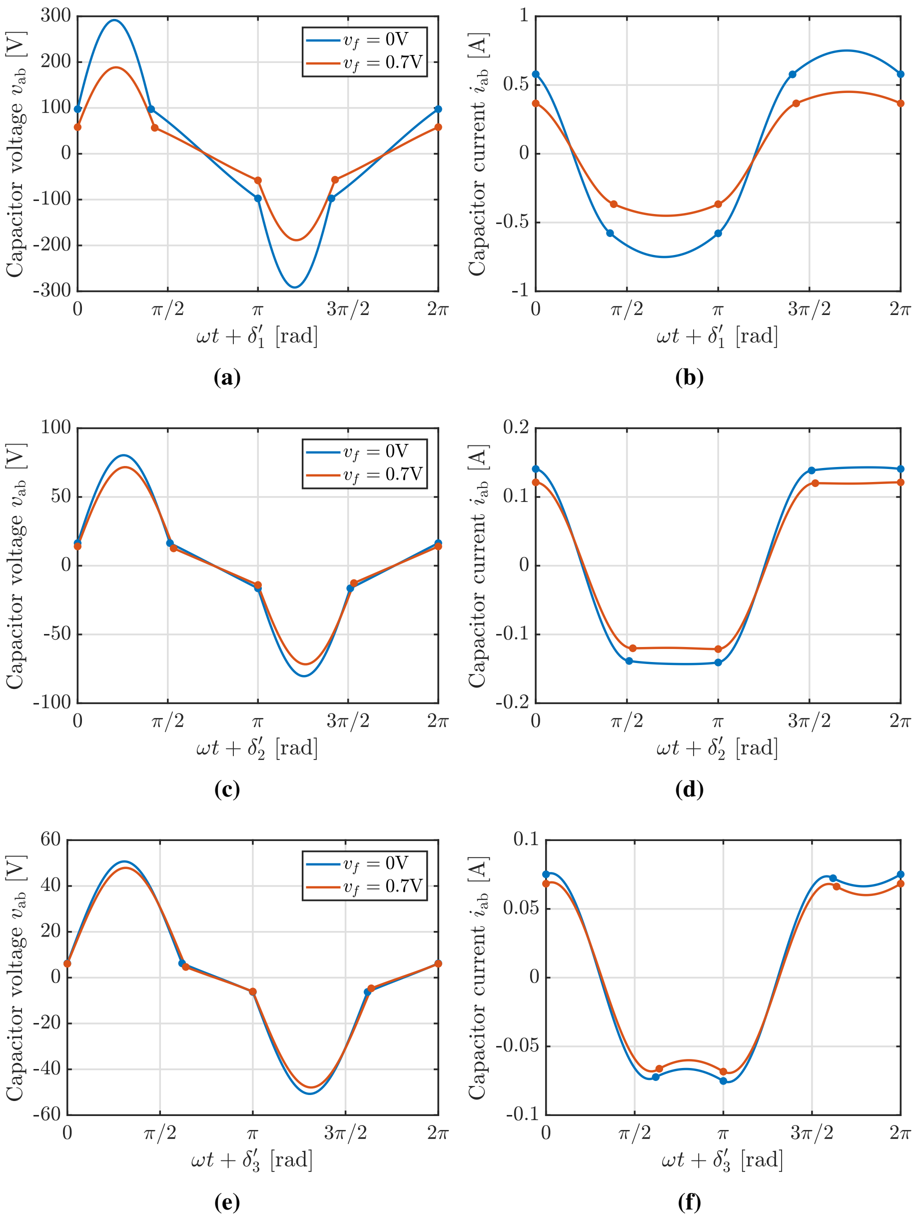

Figure 5.12: The voltage over (v_{ab}) and current through (i_{ab}) the parallel SCC in the RLC circuit.

Power loss estimation for a widerange SCC

Similar to the derivation of the equivalent capacitance of Section 5.2.3, we can derive the equivalent resistance and reactance of the RLC circuit by only considering the first harmonic of the current with phasor I_{ab}:

$$\begin{cases} R_{\mathrm{eq}} &= \mathrm{Re}\left(\frac{V_{\mathrm{in}}}{I_{\mathrm{ab}}}\right) \\ X_{\mathrm{eq}} &= \mathrm{Im}\left(\frac{V_{\mathrm{in}}}{I_{\mathrm{ab}}}\right) \end{cases} \tag{5.41}$$

As the source voltage only consists of a first harmonic, we can prove that the higher current harmonics do not contribute to the active power in the system and

$$P_{\mathrm{in,av}} = \mathrm{Re}\left(V_{\mathrm{in}} I_{\mathrm{ab}}^{\mathrm{H}}\right) = \frac{1}{2}\hat{V}_{\mathrm{in}}^{2} \frac{R}{R_{\mathrm{eq}}^{2} + X_{\mathrm{eq}}^{2}} \tag{5.42}$$

Table 5.2 lists the equivalent resistance, reactance and losses calculated for the three values of δ'.

Table 5.2: The equivalent resistance, reactance and losses calculated for the three switching instances.

Parameter	**1a**	**1b**	**2a**	**2b**	**3a**	**3b**
δ'	δ_1'	δ_1'	δ_2'	δ_2'	δ_3'	δ_3'
v_f	0 V	0.7 V	0 V	0.7 V	0 V	0.7 V
R_{eq}	23.6 Ω	39.1 Ω	118.1 Ω	138.8 Ω	217.8 Ω	236.7 Ω
X_{eq}	-5.8 Ω	-8.3 Ω	9.8 Ω	15 Ω	94 Ω	107.7 Ω
$P_{\mathrm{in,av}}$	8 W	4.9 W	1.7 W	1.4 W	0.8 W	0.7 W

The diode reduces the current amplitude, resulting in a higher impedance. The slight sideways shift in the current waveform due to the diode also contributes to the more inductive reactance values.

5.4 State estimation for RWPT systems with an SCC

In the previous chapter, we discussed that some electrical states of the RWPT system are useful to know but hard to measure when the system is running. The rotor current is a good example of a quantity that is hard to measure while the rotor is turning. In Section 4.8 we discussed how we can estimate the rotor current based on measurements of other electrical quantities, either online (e.g., other coil currents) or offline (e.g., the mutual inductance between coils). In this section we discuss how we can estimate the equivalent impedance of the RLC circuit with an SCC. With this information, we can adjust the switching instance to ensure resonant tuning or to obtain the optimal detuning for torque generation, discussed in the previous chapter.

In the previous section we derived a method to estimate the equivalent impedance of a single RLC circuit connected to a voltage source. We know (or measure) the voltage amplitude, frequency and phase. Additionally we measure the current through the series connected components and derive the phasor of the current I_{ab} using the online Fourier transform. The equivalent impedance is calculated as

$$Z_{\mathrm{eq}} = R_{\mathrm{eq}} + jX_{\mathrm{eq}} = \frac{V_{\mathrm{in}}}{I_{\mathrm{ab}}} \tag{5.43}$$

5.4.1 State estimation and control in a 2 coil system

With our RWPT motoring system in mind, we are interested in the active detuning of a short circuited resonator coil, in particular the stator coil. We consider a 2 coil setup, with a transmitter coil connected to an AC voltage source and one receiver resonator (see Figure 5.13), namely the stator.

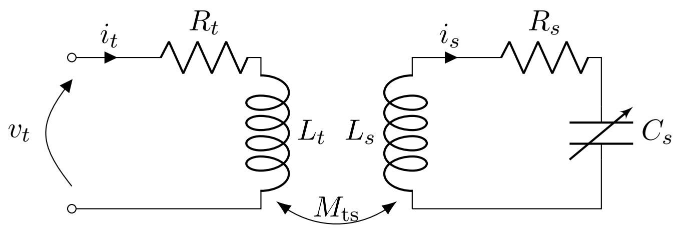

Figure 5.13: The 2 coil setup consists of the transmitter coil and the stator resonator with variable capacitance.

We leave the rotor with ferrite core in place, but we open the conductor, such that no current can flow through the rotor coil. The input voltage v_{in} (see Figure 5.9) is then equal to the induced voltage in de stator coil due to the current in the transmitter coil:

$$V_{\mathrm{in}} = -j\omega M_{\mathrm{ts}} I_t \tag{5.44}$$

And the KVL of the stator coil in the phasor representation is

$$0 = j\omega M_{\mathrm{ts}} I_t + (R_{\mathrm{s,eq}} + jX_{\mathrm{s,eq}}) I_s \tag{5.45}$$

When we measure the current waveforms of the transmitter and the receiver (stator), the impedance of the resonator coil is easily derived as

$$R_{\mathrm{s,eq}} + jX_{\mathrm{s,eq}} = \frac{-j\omega M_{\mathrm{ts}} I_t}{I_s} \tag{5.46}$$

with I_t and I_s the complex phasors of the first time harmonics of the transmitter and stator currents.

The simulated waveforms for the wide range parallel SCC are validated on the 2 coil setup. On the setup, we measure both the transmitter and the stator current. Using the Fourier transform, we derive the phase of the first harmonic of the stator current. The switching instance δ_{12} is varied in order to control the equivalent capacitance $C_{\mathrm{s,eq}}$ to the desired value $C_{\mathrm{s,set}}$. Figure 5.8 shows that the equivalent capacitance is a monotonous function of δ_{12} $(= 2\pi - 2\delta)$. From the definition of the reactance of the coil (5.47), we can find the equivalent capacitance (5.48).

$$X_{\mathrm{s,eq}} = \omega L_s - \frac{1}{\omega C_{\mathrm{s,eq}}} \tag{5.47}$$

$$C_{\mathrm{s,eq}} = \frac{1}{\omega^2 L_s - \omega X_{\mathrm{s,eq}}} \tag{5.48}$$

Figure 5.14 shows the flowchart of the simple control algorithm which is used to control the capacitor value $C_{\mathrm{s,eq}}$. The timeseries of the transmitter and stator current pass through the online Fourier transfer. Every period, new complex current phasors (I_t and I_s) are returned. From these phasors, the equivalent stator impedance $Z_{\mathrm{s,eq}}$ and capacitance $C_{\mathrm{s,eq}}$ are derived sequentially. For a given setpoint capacitor $C_{\mathrm{s,set}}$, the corresponding switching instance δ_{base} is estimated by inverting the monotonous (simplified) function for the equivalent capacitance (5.14). A zero crossing detector triggers when the stator current passes through zero. The control signal of the switches are inverted δ_{set} after the zero crossing of the current. If the estimated $C_{\mathrm{s,eq}}$ is lower/higher than the desired value $C_{\mathrm{s,set}}$, the switching instance correction δ_{corr} is increased/decreased by $2500\Delta C_{\mathrm{s,err}}$. This value is manually tuned to ensure fast response times without amplifying variance of the state estimation. The settling time of the controller is under 0.1 s for large steps. The wide range parallel SCC consists of a fixed capacitor of 27.5 nF and a switched capacitor of 220.4 nF. The SCC is controlled to equivalent capacitance values of 90, 120 and 150 nF.

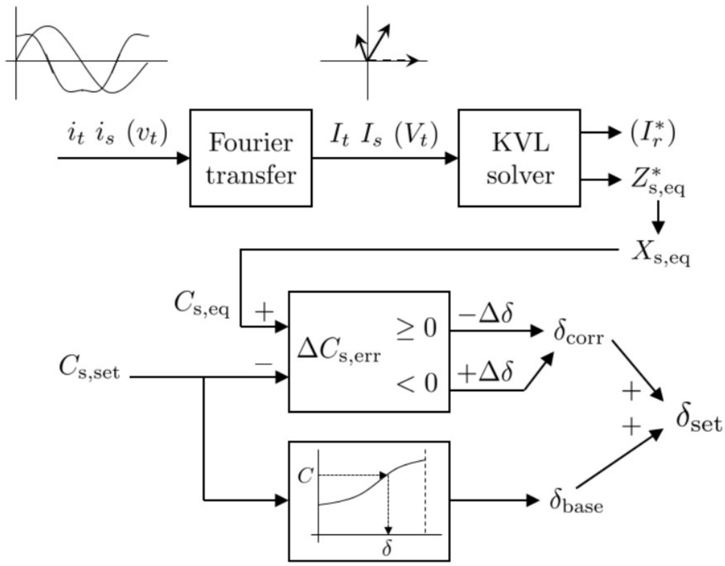

Figure 5.14: The state estimation and control scheme for the SCC in the RWPT setup.

We also measure the voltage waveform v_{ab} with a voltage probe so that we can compare the simulated voltage and current. Based on the voltage waveforms, the voltage drop over the freewheeling diode is estimated to be about 2.85 V. The AC switch in the setup uses high power silicon carbide (SiC) IGBT's which are known to have a high voltage drop over their freewheeling diodes. For AC switching applications it is recommended to use MOSFET's instead of IGBT's if the required currents and voltages allow it. If the MOSFET's inherent freewheel diode is conducting (after the zero-voltage switching), turning the MOSFET back on can eliminate most of the voltage drop. Table 5.3 lists the electrical parameters that are required for the waveform simulation.

Table 5.3: The required parameters for the waveform solver are measured on the physical setup.

Parameter	**Value**
f	5 kHz
C_1 @5 kHz	27.5 nF
C_2 @5 kHz	247.9 nF
L_s @5 kHz	5.44 mH
R_s @5 kHz	3.63 Ω
v_f	2.85 V

Now that the electrical parameters of the SCC are known, we manually vary the switching instance δ' in the waveform simulation, until the peak value of the simulated SCC voltage v_{ab} is equal to the measured peak value. Figure 5.15 compares the simulated and measured voltage and current waveforms for the switchable capacitor. The waveforms are timeshifted such that 0 rad corresponds to the switching instance δ'. For the considered capacitor setpoints, the peak of the current waveform is convex (90 nF), flat (120 nF) or concave (150 nF). The shapes of the voltage waveforms and the location of the switching instance δ_{12} for the simulation and the measurement correspond very well. The current waveforms vary slightly in amplitude and phase compared to the measurements, but qualitatively the shape of the current waveforms is predicted well by the solver.

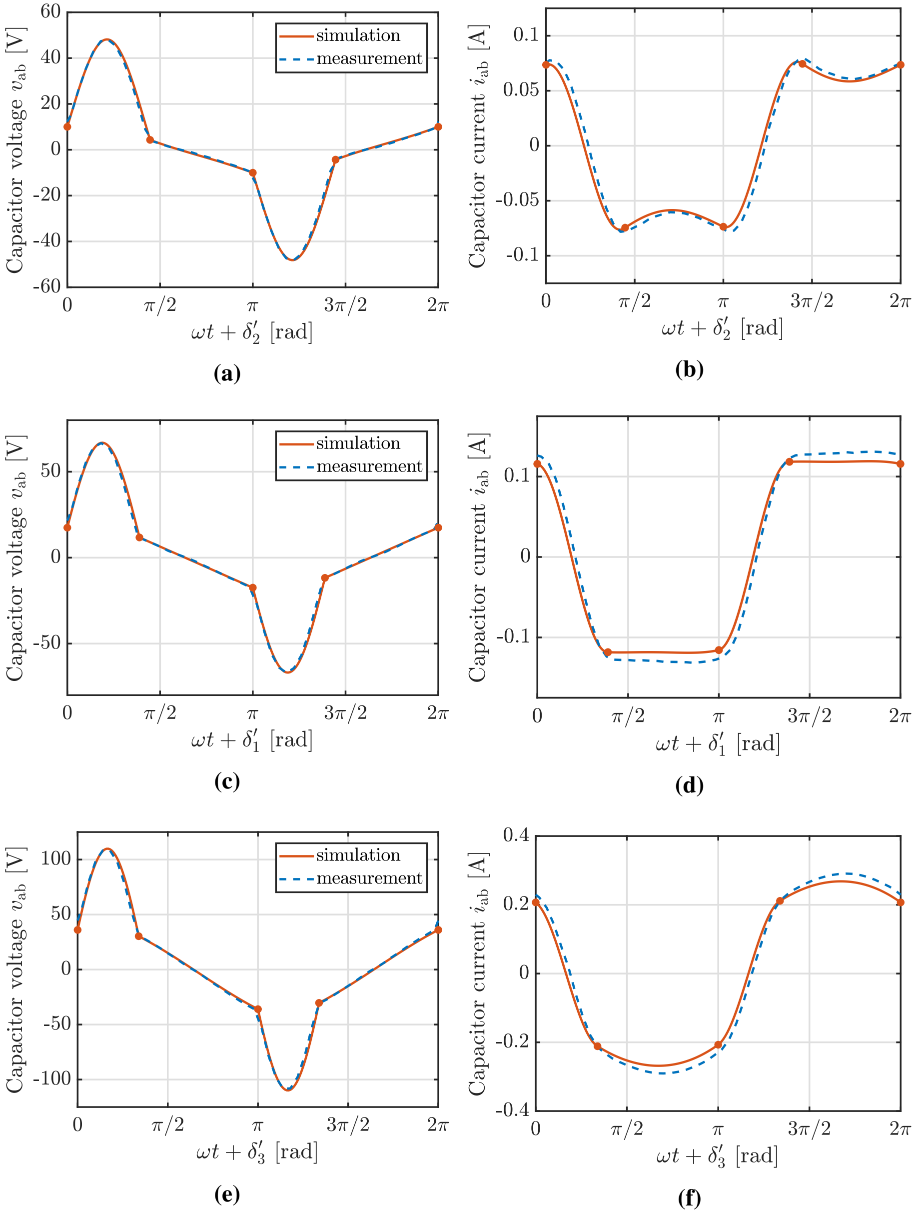

Figure 5.15: Simulation and measurement of the voltage over (v_{ab}) and current through (i_{ab}) the parallel SCC in the 2 coil setup.

The switching instance δ_{12} is a direct solution (δ_{12}^*) of the ODE solver in Section 5.3.2, while δ' was an input of the solver. We can also derive the switching instances δ' and δ_{12} from the measured current and voltage waveforms. Table 5.4 compares the simulated and measured switching instances for the three capacitor setpoints.

Table 5.4: The measured and simulated switching instances for the same peak SCC voltage v_{ab}.

C_{set}	$\boldsymbol{\delta'}$ **meas**	$\boldsymbol{\delta'}$ **sim**	$\boldsymbol{\delta_{12}}$ **meas**	$\boldsymbol{\delta_{12}}$ **sim**
90 nF	4.15 rad	4.12 rad	1.38 rad	1.40 rad
120 nF	4.28 rad	4.21 rad	1.19 rad	1.22 rad
150 nF	4.41 rad	4.29 rad	1.03 rad	1.06 rad

5.4.2 State estimation and control in a 3 coil system

In the previous section we showed that the ODE solver is capable of reconstructing the physical voltage and current waveforms in a detuned RLC resonator. The induced voltage in the resonator was derived directly from the measured transmitter current. We are interested in controlling the equivalent capacitor of the stator resonator while the rotor resonator is present. Preferably, we do not measure the current in the rotor coil. In Section 4.8 we derived a procedure to estimate the rotor current in a detuned RWPT system based on an overdetermined system of three KVL equations in the phasor representation. The rotor current was found by minimizing the sum of the squared error voltages for all three coils. In this section, the known stator capacitor is replaced by a variable SCC. We will discuss a similar method that allows us to simultaneously estimate the rotor current and the equivalent capacitance of the SCC in the stator. The KVL for the three coils is given by

$$\begin{bmatrix} V_t \\ 0 \\ 0 \end{bmatrix} = \begin{bmatrix} R_t + j\omega L_t & j\omega M_{\mathrm{ts}} & j\omega M_{\mathrm{tr}}(\theta) \\ j\omega M_{\mathrm{ts}} & R_s + jX_s & j\omega M_{\mathrm{sr}}(\theta) \\ j\omega M_{\mathrm{tr}}(\theta) & j\omega M_{\mathrm{sr}}(\theta) & R_r + jX_r \end{bmatrix} \begin{bmatrix} I_t \\ I_s \\ I_r \end{bmatrix} \tag{5.49}$$

The transmitter and stator currents, I_t and I_s, are measured on the setup. The AC voltage of the power source V_t can be measured or derived from the control signal. In the KVL (5.49), only the rotor current I_r and the stator impedance $R_s + jX_s$ are unknown. The three complex KVL equations are linear functions of these two unknown variables, resulting in an overdetermined linear system of equations:

$$A_3\mathbf{x}_3 = \mathbf{b}_3 \tag{5.50}$$

with

$$\begin{cases} A_3 & = \begin{bmatrix} j\omega M_{\mathrm{tr}}(\theta) & 0 \\ j\omega M_{\mathrm{sr}}(\theta) & I_s \\ Z_r & 0 \end{bmatrix} \\ \mathbf{b}_3 & = \begin{bmatrix} V_t - Z_t I_t - j\omega M_{\mathrm{ts}} I_s \\ -j\omega M_{\mathrm{ts}} I_t \\ -j\omega M_{\mathrm{tr}}(\theta) I_t - j\omega M_{\mathrm{sr}}(\theta) I_s \end{bmatrix} \\ \mathbf{x}_3 & = \begin{bmatrix} I_r^* \\ \\ Z_{\mathrm{eq}}* \end{bmatrix} \end{cases} \tag{5.51}$$

We can again minimize the sum of the squared errors using the complex Moore-Penrose inverse of A_3 (see Section 4.8).

$$\begin{bmatrix} I_r^* \\ \\ Z_{\mathrm{eq}}* \end{bmatrix} = (A_3^{\mathrm{H}} A_3)^{-1} A_3^{\mathrm{H}} \mathbf{b}_3 \tag{5.52}$$

The state estimation procedure is validated on the physical setup. The rotor coil is now closed such that current can pass through the coil. The rotor coil is fixed in one position for which the stator and rotor current values are similar in magnitude ($\theta = 0.79$ rad). The rotor current is measured using a current probe to validate the estimated rotor current. Figure 5.16 shows the measured current waveforms for the same capacitor setpoints ($C_{\mathrm{set}} \in$ [90 nF, 120 nF, 150 nF]).

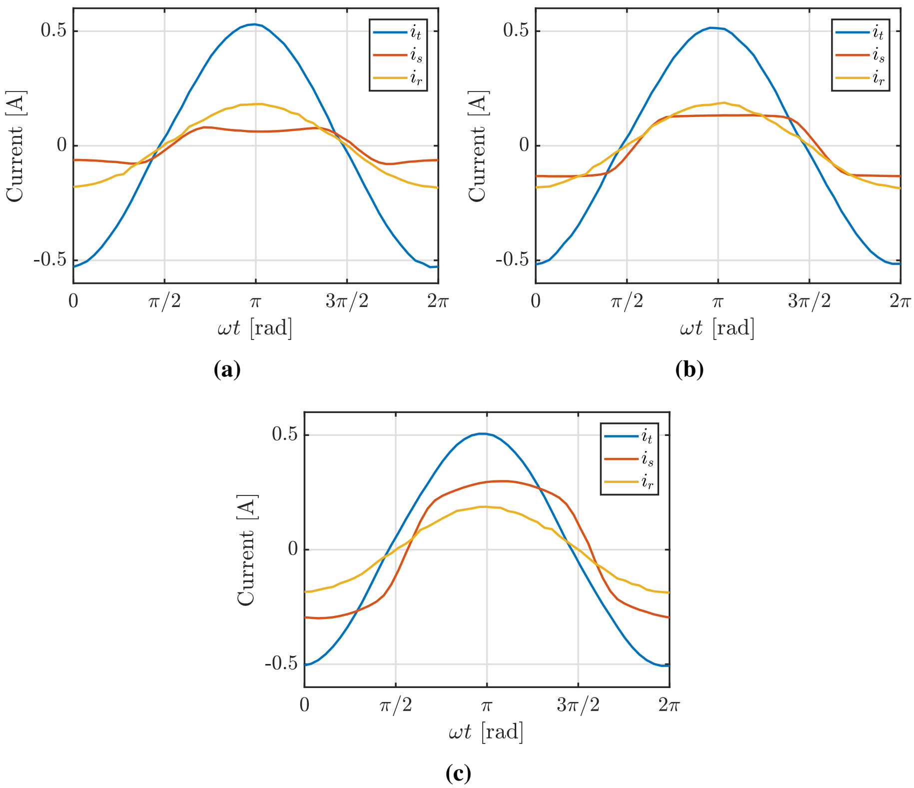

Figure 5.16: Measured current through the transmitter (i_t), stator (i_s) and rotor (i_r) coils for three setpoints for C_{set}: 90 nF (a), 120 nF (b) and 150 nF (c).

Because both the transmitter and rotor currents are close to sinusoidal, the induced voltage in the stator is also close to sinusoidal. The same shapes for the stator current peaks (convex, flat, concave) return for the given setpoints.

The current waveform of the rotor (i_r) is passed through the online Fourier transform to extract the complex phasor of the first time harmonic (I_r). Table 5.5 compares the estimated and measured complex phasors of the rotor current for all three capacitor setpoints. The transmitter voltage phasor is oriented along the real axis.

Table 5.5: The complex phasor of the rotor current that was measured directly (I_r) or estimated indirectly (I_r^*).

C_{set}	I_r	I_r^*
90 nF	$5.77 - j180$ mA	$4.84 - j192$ mA
120 nF	$5.68 - j183$ mA	$4.67 - j191$ mA
150 nF	$4.53 - j185$ mA	$3.85 - j187$ mA

5.5 Conclusion

In the previous chapter we showed that the performance of an RWPT motoring system improves when we detune the resonators. For this we need a variable frequency and at least one wide range variable capacitor. In this chapter we discussed three common methods for active capacitor tuning. Switch controlled capacitors can be varied for a wide range while only requiring one AC switch and two discrete capacitors. We discussed the operation (with zero voltage switching), the voltage waveform and equivalent capacitance value for limited range series and parallel connected SCC's. For the RWPT motoring application we chose the parallel connected SCC. For a wide capacitance range we cannot assume a sinusoidal capacitor current. We derived a semi-analytical method to find the voltage and current waveforms of an RLC circuit with a wide range parallel SCC. A numerical solver combines the solutions of piecewise second order ODE's while obeying electrical boundary conditions. The non-ideal voltage drop over the bypass diodes of the IGBT's are included in the model. We validated the simulated waveforms on the 3 coil setup with ferrite rotor core. The equivalent capacitance of the SCC is estimated based on model parameters and sensor data, with and without current in the rotor coil. We expanded the state estimator from the previous chapter to simultaneously estimate the stator impedance and the rotor current.

Chapter 6

Conclusion and future perspectives

The work in this thesis was performed as part of strategic research activity with the aim of exploring the mechanisms that cause forces and torques between resonator coils. In Chapter 1, the research was positioned within the wider field of resonant wireless power transfer. A brief overview of the history and recent developments was discussed together with the emergence of RWPT in consumer electronics and car charging infrastructure. We provided an overview of the most common wireless power transfer methodologies with a focus on the most viable technology, namely inductive power transfer. We discussed the most common types of resonant transmitter and receiver topologies for inductive WPT. The most important elements of WPT systems, such as discrete and parasitic capacitors and high frequency magnetic materials, were also treated in this chapter. The study of RWPT based motoring emerged only a decade ago. During the research activities that are presented in this thesis, other research groups initiated research regarding resonance based motoring. Section 1.4 positions the work of this thesis relative to these other research tracks.

The analysis of resonator based motoring systems can be approached from two different angles, namely by adapting existing electric motor models or by starting from the governing equations for WPT system design. In this thesis we decided to observe the resonators as a part of a general wireless power transfer system, while the resulting currents in the resonators generate forces and torques. In Chapter 2 we discussed the state of the art concerning wireless power transfer that allowed us to understand and improve the force and torque interactions between the resonators later in the thesis. The magnetic and electrical interaction between magnetically coupled coils was discussed and important figures of merit for WPT systems were introduced, such as the quality factor and the coupling factor. Classical analytic expressions were listed that describe the magnetic field of simplified coil shapes, the mutual induction and the forces between current carrying air coils. At the end of this chapter we discussed important design parameters of wound air coils, which affect their self-inductance and frequency dependent losses. An overview was given of the most viable AC capacitor types for use in RWPT motoring systems. The polypropylene film capacitor type was chosen for its favorable trade-off between stability, volume efficiency, dissipation factor and cost.

In Chapter 3, we derived the quasi-static models for RWPT based torque generation. First, we explained the rationale behind the motoring capability of two strongly coupled resonator receiver coils. An electrical state-space model was constructed based on Kirchoff's voltage law for magnetically coupled coils with reciprocal movement. By decomposing the instantaneous power balance, analytical expressions were derived for the torque on the rotor coil(s) for both a voltage controlled and current controlled power source. The torque profile of the RWPT system has a high variability with a peak value for the orientation for which the coupling between the receiver resonators (stator and rotor) is zero. An attempt was made to alleviate the torque ripple by adding a supplementary rotor coil. The single and dual rotor coil systems were compared in Section 3.2.7 and we concluded that the single rotor coil system has a significantly higher maximum and average torque for rising quality factors of the coils. A mostly 3D printed prototype was constructed to validate the analytical torque expressions. We showed that the simplified loss model in Chapter 2 is valid for the coils in the system. We derived that the performance of the RWPT motoring system is optimal when the Q factors of the coils are close to their peak value. The electrical model for the coil currents and torque model show a good correspondence to the sensor data. In this chapter we also explored the effect of adding magnetic material, namely a ferrite rotor core, to the RWPT system. While the heat dissipation results in additional losses for the same currents, the quality factor of the coils and the mutual inductance values improve, resulting in a 144% higher peak torque for the same transmitter current.

Chapter 3 detailed the torque interaction for two receiver resonators with the same resonance frequency which coincides with the frequency of the power source. We can identify two degrees of freedom when detuning the resonators from their resonance frequencies. In Chapter 4, we quantify the performance gain of the system when detuning the frequency and the stator capacitance. The electrical model and the torque expressions are expanded by adding the non-zero reactance terms of the resonators. The peak torque value and its corresponding orientation are now a function of both detuning parameters. The expanded models for the system currents and the torque were validated on the RWPT prototype for three stator capacitance values and a wide range of frequencies. We introduced two new performance metrics for RWPT motoring system, namely the torque efficiency (TE) and the torque capability (TC). Some electrical quantities are difficult or expensive to measure, while a good estimation of these quantities are often sufficient for optimal or safe operation. In Section 4.8, we discussed a robust methodology for estimating the rotor current based on offline measurements of electrical parameters, the rotor angle and sensor data.

The maximum values of both the TE and the TC strongly depend on the two detuning parameters. The frequency is easily adjusted by altering the frequency of the input signal of the amplifier. In Chapter 5, we explore three methods that allow online variation of the capacitor value. By intermittently charging and discharging an auxiliary switch controlled capacitor, we can continuously vary the equivalent capacitance of the RLC circuit. Intelligent control of the switching signals allows for zero voltage switching when engaging and disengaging the auxiliary capacitor. Analytical expressions are derived for the equivalent capacitance of series and parallel connected switch controlled capacitors. These analytical expressions assume a sinusoidal current in the resonator coil, which is acceptable for small variations in the total capacitance. The analysis of the TE and TC in Chapter 4 shows that we require an SCC with a wide range to reach close-to-optimal operating points for every rotor angle ($\pm$ 50%). For such a wide capacitance range, we cannot assume sinusoidal current waveforms. In Section 5.3.2 we proposed a semi-analytical approach to find the real waveform of a wide range SCC, by combining piecewise ODE solutions and a numerical minimization procedure. The simulated voltage and current waveforms were validated on an experimental setup with a parallel switch controlled capacitor. It was shown that the semi-analytical method was able to reconstruct the voltage and current waveforms, even for a non-negligible forward voltage drop of the bypass diodes in the AC switch. The analytical expressions for the equivalent capacitor are inaccurate for wide range SCC's. At the end of Chapter 5, we expanded the state estimation of Section 4.8 with an estimator for the stator impedance, which can be used to extract the equivalent capacitance for a resonator with an SCC in a 2 or 3 coil setup. A control loop is implemented that tracks the desired equivalent capacitance by adjusting the switching instance of the AC switch.

6.1 Discussion of thesis objectives

In Section 1.5, we set out four major categories of objectives that shaped the structure of this thesis. We will now revisit these objectives and discuss how the work in this thesis fulfilled these goals:

Insights and optimization

- In Chapter 2, we provided a thorough review of the literature regarding electromagnetic and physical coil-coil interactions. We discussed parametric electrical models that describe the electrical interactions between RLC resonators in an inductive wireless power transfer system. Additionally we introduced figures of merit, such as the coupling factor and quality factor, that describe the performance of RWPT systems. These performance indicators were adapted in Chapter 3 to quantify the efficacy of the RWPT motoring system.
- In Chapter 3 we derived analytical expressions for the torque profile of an RWPT motoring system, based on electrical and geometrical parameters. In Chapter 4, we discussed how the detuning of the resonators results in additional design parameters and we provided design guidelines in terms of the adapted performance indicators.
- In Chapters 3 and 4, we studied the performance gain that results from the addition of magnetic material in the system. The ferrite core increases the quality factors of the coils and the magnetic coupling between the coils. The addition of the cylindrical ferrite core in the rotor increased the peak torque of our prototype by 144%.

Experimental validation

- In Chapter 1, we set out to experimentally validate all of our core research results. We constructed a mostly 3D printed RWPT motoring prototype with one transmitter coil and two receiver resonators. In Chapter 3, we validated the electrical model and the quasi-static torque expressions for voltage and current controlled power sources. The same procedure was repeated for a rotor coil with a cylindrical ferrite core.
- In Chapter 4, we performed measurement campaigns that accurately validated the torque expressions for detuned systems, for a wide range of frequencies and three well-chosen stator capacitor values.
- The current and voltage waveforms of switch controlled capacitors are not accurately estimated by the derivations in literature. In Chapter

5, we constructed a semi-analytical approach to retrieve these waveforms. This procedure also incorporates the voltage drop over the bypass diodes. The simulated current and voltage waveforms were validated on a setup with silicon-carbide IGBT's with high voltage drop.

Tuning and control optimization

- In Chapter 4, we explored the effect of detuning of the resonators on the torque generation performance of the system. We identified two degrees of freedom in the detuning of the two resonators. Additionally, two performance indicators were introduced which were used to compare the torque efficiency and torque capability of detuned systems. We showed that we can increase the torque for all rotor angles by detuning the resonators, resulting in lower torque ripple. The active detuning strategy enables peak torque tracking for every rotor angle.

- In Section 4.7 it was shown that the optimal performance is reached for highly variable detuning settings (frequency and stator capacitor value). In Chapter 5, we explained how we can continuously detune the capacitor value over a wide range using a series or parallel switch controlled capacitor. The SCC was implemented on the setup and a control loop was constructed which estimates and tracks the desired equivalent capacitor value.

Increasing robustness

- In Section 4.7 we showed that the performance of an RWPT system is much more robust when at least one of the resonators is detuned. The torque efficiency and torque capability for detuned systems have a similar behavior, with the torque capability being a more stringent.

- It is difficult to accurately tune a capacitor value in a real setup. The SCC from Chapter 5 is capable of continuously adjusting its equivalent capacitance. A control loop allows for accurate tracking of the desired capacitor value.

- Some electrical quantities are inherently variable and difficult to model or measure. Capacitor values and coil resistances, for example, are affected by temperature. The equivalent capacitance of the SCC is difficult to accurately estimate by analytical models, while direct measurement of the rotor current would drastically increase the complexity and cost of the prototype. In Sections 4.8 and 5.4 we discussed methods that allows for the online estimation of electrical quantities, i.e. the stator coil impedance and the rotor current. The estimation of these quantities allows for active control of the stator capacitance, safeguarding of current limits and the estimation of the rotor torque.

6.2 Outlook on future research

This thesis focused on the optimization of the control of an exemplary RWPT motoring system. In Chapter 3, we constructed a prototype RWPT system to validate the electrical model and the torque profile expressions. The detuning settings for the frequency and the stator capacitor were optimized in Chapter 4. In Chapter 5, we discussed how the capacitor value can be adjusted continuously by the use of an AC switch. This focused approach resulted in a rounded definition of the thesis content and its structure. While we thoroughly explored and optimized the control of an arbitrary RWPT system, we can still identify additional research trajectories that can benefit from the foundation that is provided by this work.

- In Chapter 4, we enabled peak torque tracking for all rotor angles. However, the torque in a 3 coil setup is still variable for a full rotation. In [78–86], researchers proposed RWPT topologies with multiple poles of rotor and stator resonators. Intelligent spacing and control of these pole pairs can reduce the torque ripple on the rotor. The force interaction between the coils is more translational in nature [87,88] and can still be described by the expressions in Chapters 3 and 4. The control strategies from Chapter 4 and 5 can be applied to optimize the performance of these multi-pole topologies.

- While most research regarding RWPT motoring systems aims to eliminate magnetic materials and replace them by resonators, we encourage further integration of magnetic materials in addition to these resonators. Magnetic materials can lower the magnetic reluctance of the flux paths, direct the flux path to improve the magnetic coupling between coils and shield the environment from the alternating magnetic fields. In Section 3.7 we added a ferrite core and observed a peak torque gain of 144%. This drastic improvement in torque by the addition of a limited amount of magnetic material shows that there is still a large margin to improve the torque generation of RWPT systems even further. FEM based models can then be used to optimize the geometry of the ferrite cores.

- In this thesis, the transmitter generated forces in one receiver resonator pair. Multiple motors/actuators, with distinct resonance frequencies can be coupled with one transmitter. By varying the frequency of the transmitter current or by superimposing multiple frequencies, it is possible to selectively actuate the individual receiver pairs with varying intensities.

6.3 Acknowledgments

The final form of this thesis was made possible in part by the efforts of my colleagues. In this section I wish to acknowledge their contributions to the work presented in this thesis. Lab technician Tony Boone built my first two prototypes, which allowed me to demonstrate resonance based motoring early during my PhD. Tony and Vincent Gevaert also provided guidance when I used the tools in the workshop. Andries Daem built the 3D printer in the lab and taught me how to use it. Rikkert Van Durme introduced me to the Comsol finite element modeling software. Dimitar Bozalakov designed the inverter platform which allowed me to drive the transmitter with AC square waves and to implement the switch controlled capacitor. Hendrik Van Sompel, Arne De Keyser and Lynn Verkroost explained the operation of the dSpace 1104 and MicroLabBox and its integration in Matlab Simulink.

Bibliography

[1] Veronica Manescu, Gheorghe Paltanea, Horia Gavrila, Gheorghe Scutaru, and IOAN Peter. High efficiency electrical motors state of the art and challenges. *Rev. Roum. Sci. Techn. Électrotechn. et Énerg*, 62:14–18, 2017.

[2] Anibal T De Almeida, Fernando JTETE Ferreira, and Joao AC Fong. Standards for efficiency of electric motors. *IEEE Industry Applications Magazine*, 17(1):12–19, 2010.

[3] Anders Nordelöf, Mikael Alatalo, and Maria Ljunggren Söderman. A scalable life cycle inventory of an automotive power electronic inverter unit part i: design and composition. *The International Journal of Life Cycle Assessment*, 24(1):78–92, 2019.

[4] George Todorov and Bozhidar Stoev. Analytical model for sizing the magnets of permanent magnet synchronous machines. *Journal of Electrical Engineering*, 3(3):134–141, 2015.

[5] S Orlova, A Rassõlkin, A Kallaste, T Vaimann, Anouar Belahcen, et al. Lifecycle analysis of different motors from the standpoint of environmental impact. *Latv. J. Phys. Tech. Sci*, 53(6):37–46, 2016.

[6] Mbika Muteba. Optimization of air gap length and capacitive auxiliary winding in three-phase induction motors based on a genetic algorithm. *Energies*, 14(15):4407, 2021.

[7] Ismail Temiz. A study of different air gaps on the effect of torque and efficiency in induction machines.

[8] Mikko Valtonen, Asko Parviainen, and Juha Pyrhonen. Influence of the air-gap length to the performance of an axial-flux induction motor. In *2008 18th International Conference on Electrical Machines*, pages 1–5. IEEE, 2008.

[9] E Shamonina and L Solymar. Diamagnetic properties of metamaterials: a magnetostatic analogy. *The European Physical Journal B-Condensed Matter and Complex Systems*, 41(3):307–312, 2004.

[10] Bart Michiels, Ignace Bogaert, Jan Fostier, and Daniël De Zutter. Swiss roll ensemble homogenization by full-wave simulations. *Microwave and Optical Technology Letters*, 53(10):2268–2274, 2011.

[11] Yaroslav Urzhumov and David R Smith. Metamaterial-enhanced coupling between magnetic dipoles for efficient wireless power transfer. *Physical Review B*, 83(20):205114, 2011.

[12] Mustafa Boyvat and Christian V Hafner. Molding the flow of magnetic field with metamaterials: Magnetic field shielding. *Progress In Electromagnetics Research*, 126:303–316, 2012.

[13] Mustafa Boyvat and Christian V Hafner. Magnetic field shielding by metamaterials. *Progress In Electromagnetics Research*, 136:647–664, 2013.

[14] Romain Fleury and Andrea Alù. Cloaking and invisibility: A review. In *Forum for Electromagnetic Research Methods and Application Technologies (FERMAT)*, volume 1, 2014.

[15] William Yerazunis, Bingnan Wang, and Koon Hoo Teo. Metamaterials and resonant array wireless power systems. In *2014 IEEE Antennas and Propagation Society International Symposium (APSURSI)*, pages 1403–1404. IEEE, 2014.

[16] ALAK Ranaweera, Thuc Phi Duong, and Jong-Wook Lee. Experimental investigation of compact metamaterial for high efficiency midrange wireless power transfer applications. *Journal of Applied Physics*, 116(4):043914, 2014.

[17] Guy Lipworth, Joshua Ensworth, Kushal Seetharam, Da Huang, Jae Seung Lee, Paul Schmalenberg, Tsuyoshi Nomura, Matthew S Reynolds, David R Smith, and Yaroslav Urzhumov. Magnetic metamaterial superlens for increased range wireless power transfer. *Scientific reports*, 4(1):1–6, 2014.

[18] Gunyoung Kim, Taek-Kyu Oh, and Bomson Lee. Effects of metamaterial slabs applied to wireless power transfer at 13.56 mhz. *International Journal of Antennas and Propagation*, 2015, 2015.

[19] Zhen Zhang, Hongliang Pang, Apostolos Georgiadis, and Carlo Cecati. Wireless power transfer an overview. *IEEE Transactions on Industrial Electronics*, 66(2):1044–1058, 2018.

[20] Andre Kurs, Aristeidis Karalis, Robert Moffatt, John D Joannopoulos, Peter Fisher, and Marin Soljačić. Wireless power transfer via strongly coupled magnetic resonances. *science*, 317(5834):83–86, 2007.

[21] Grant A Covic and John T Boys. Inductive power transfer. *Proceedings of the IEEE*, 101(6):1276–1289, 2013.

[22] JT Boys, GA Covic, and A Williamson Green. Stability and control of inductively coupled power transfer systems. *IEE Proceedings-Electric Power Applications*, 147(1):37–43, 2000.

[23] Xun Liu, WM Ng, CK Lee, and SY Hui. Optimal operation of contactless transformers with resonance in secondary circuits. In *Applied Power Electronics Conference and Exposition, 2008. APEC 2008. Twenty-Third Annual IEEE*, pages 645–650. IEEE, 2008.

[24] Alanson P Sample, David T Meyer, and Joshua R Smith. Analysis, experimental results, and range adaptation of magnetically coupled resonators for wireless power transfer. *IEEE Transactions on Industrial Electronics*, 58(2):544–554, 2011.

[25] Shu Yuen Ron Hui, Wenxing Zhong, and Chi Kwan Lee. A critical review of recent progress in mid-range wireless power transfer. *IEEE Transactions on Power Electronics*, 29(9):4500–4511, 2014.

[26] Dukju Ahn and Songcheol Hong. Effect of coupling between multiple transmitters or multiple receivers on wireless power transfer. *IEEE Transactions on Industrial Electronics*, 60(7):2602–2613, 2013.

[27] Yiming Zhang, Ting Lu, Zhengming Zhao, Fanbo He, Kainan Chen, and Liang Yuan. Selective wireless power transfer to multiple loads using receivers of different resonant frequencies. *IEEE Transactions on Power Electronics*, 30(11):6001–6005, 2015.

[28] Olutola Jonah and Stavros V Georgakopoulos. Wireless power transfer in concrete via strongly coupled magnetic resonance. *IEEE Transactions on Antennas and Propagation*, 61(3):1378–1384, 2013.

[29] Ali Abdolkhani, Aiguo Patrick Hu, and Nirmal-Kumar C Nair. A double stator through-hole type contactless slipring for rotary wireless power transfer applications. *IEEE Transactions on Energy Conversion*, 29(2):426–434, 2014.

[30] Ping Si, Aiguo Patrick Hu, Simon Malpas, and David Budgett. A frequency control method for regulating wireless power to implantable devices. *IEEE transactions on biomedical circuits and systems*, 2(1):22–29, 2008.

[31] Riccardo Carta, Jef Thoné, and Robert Puers. A 3d ferrite coil receiver for wireless power supply of endoscopic capsules. *Procedia Chemistry*, 1(1):477–480, 2009.

[32] Wireless power consortium: Qi standard. `https://www.wirelesspowerconsortium.com/qi/`. Accessed: 2021-04-15.

[33] SY Hui. Planar wireless charging technology for portable electronic products and qi. *Proceedings of the IEEE*, 101(6):1290–1301, 2013.

[34] Chang-Gyun Kim, Dong-Hyun Seo, Jung-Sik You, Jong-Hu Park, and Bo-Hyung Cho. Design of a contactless battery charger for cellular phone. *IEEE Transactions on Industrial Electronics*, 48(6):1238–1247, 2001.

[35] Roy Want. An introduction to rfid technology. *IEEE pervasive computing*, 5(1):25–33, 2006.

[36] KV Seshagiri Rao, Pavel V Nikitin, and Sander F Lam. Antenna design for uhf rfid tags: A review and a practical application. *IEEE Transactions on antennas and propagation*, 53(12):3870–3876, 2005.

[37] Siqi Li and Chunting Chris Mi. Wireless power transfer for electric vehicle applications. *IEEE journal of emerging and selected topics in power electronics*, 3(1):4–17, 2015.

[38] Jaegue Shin, Seungyong Shin, Yangsu Kim, Seungyoung Ahn, Seokhwan Lee, Guho Jung, Seong-Jeub Jeon, and Dong-Ho Cho. Design and implementation of shaped magnetic-resonance-based wireless power transfer system for roadway-powered moving electric vehicles. *IEEE Transactions on Industrial Electronics*, 61(3):1179–1192, 2014.

[39] Adel El-Shahat, Erhuvwu Ayisire, Yan Wu, Mosfequr Rahman, and Dylan Nelms. Electric vehicles wireless power transfer state-of-the-art. *Energy Procedia*, 162:24–37, 2019.

[40] John M Miller, Perry T Jones, Jan-Mou Li, and Omer C Onar. Ornl experience and challenges facing dynamic wireless power charging of ev's. *IEEE cIrcuIts and systEms magazInE*, 15(2):40–53, 2015.

[41] Chirag Panchal, Sascha Stegen, and Junwei Lu. Review of static and dynamic wireless electric vehicle charging system. *Engineering science and technology, an international journal*, 21(5):922–937, 2018.

[42] Wireless power transfer for light-duty plug-in/electric vehicles and alignment methodology. `https://www.sae.org/standards/content/j2954`$_2$`02010/`. Accessed: 2021-04-15.

[43] Technology research that connects the dots. `https://omdia.tech.informa.com/`. Accessed: 2021-04-15.

[44] What the numbers tell us about the growing market of wireless charging technology. `https://www.iam-media.com/what-the-numbers-tell-us-about-the-growing-market-of-wireless-charging-technology`. Accessed: 2021-04-15.

[45] Runhong Huang, Bo Zhang, Dongyuan Qiu, and Yuqiu Zhang. Frequency splitting phenomena of magnetic resonant coupling wireless power transfer. *IEEE Transactions on Magnetics*, 50(11):1–4, 2014.

[46] Wim Bogaerts, Peter De Heyn, Thomas Van Vaerenbergh, Katrien De Vos, Shankar Kumar Selvaraja, Tom Claes, Pieter Dumon, Peter Bienstman, Dries Van Thourhout, and Roel Baets. Silicon microring resonators. *Laser & Photonics Reviews*, 6(1):47–73, 2012.

[47] Mingzhao Song, Ivan Iorsh, Polina Kapitanova, Elizaveta Nenasheva, and Pavel Belov. Wireless power transfer based on magnetic quadrupole coupling in dielectric resonators. *Applied Physics Letters*, 108(2):023902, 2016.

[48] Qian Zhao, Ji Zhou, Fuli Zhang, and Didier Lippens. Mie resonance-based dielectric metamaterials. *Materials today*, 12(12):60–69, 2009.

[49] Elisenda Bou Balust, Eduardo José Alarcón Cot, and Jordi Gutiérrez Cabello. A comparison of analytical models for resonant inductive coupling wireless power transfer. In *PIERS 2012: Progress in Electromagnetics Research Symposium: proceedings: Moscow, Russia: August 19-23, 2012*, pages 689–693. The Electromagnetics Academy, 2012.

[50] Ludvik Strauch, Mojca Pavlin, and Vladimir Boštjan Bregar. Optimization, design, and modeling of ferrite core geometry for inductive wireless power transfer. *International Journal of Applied Electromagnetics and Mechanics*, 49(1):145–155, 2015.

[51] Tushar Batra, Erik Schaltz, and Seungyoung Ahn. Effect of ferrite addition above the base ferrite on the coupling factor of wireless power transfer for vehicle applications. *Journal of Applied Physics*, 117(17):17D517, 2015.

[52] Byung-Chul Park and Jeong-Hae Lee. Enhanced efficiency for wireless power transmission using an auxiliary loop on ferrite in metallic environment. *Electronics Letters*, 51(24):2039–2041, 2015.

[53] Tushar Batra and Erik Schaltz. Magnetic field emissions for ferrite and non-ferrite geometries for wireless power transfer to vehicles. *Journal of Applied Physics*, 115(17):17E715, 2014.

[54] Fei Lu, Hua Zhang, and Chris Mi. A review on the recent development of capacitive wireless power transfer technology. *Energies*, 10(11):1752, 2017.

[55] Fei Lu, Hua Zhang, Heath Hofmann, and Chris Mi. A double-sided lclc-compensated capacitive power transfer system for electric vehicle charging. *IEEE Transactions on Power Electronics*, 30(11):6011–6014, 2015.

[56] Mitchell Kline, Igor Izyumin, Bernhard Boser, and Seth Sanders. Capacitive power transfer for contactless charging. In *2011 Twenty-Sixth Annual IEEE Applied Power Electronics Conference and Exposition (APEC)*, pages 1398–1404. IEEE, 2011.

[57] Michael P Theodoridis. Effective capacitive power transfer. *IEEE Transactions on Power Electronics*, 27(12):4906–4913, 2012.

[58] Hua Zhang, Fei Lu, Heath Hofmann, Weiguo Liu, and Chunting Chris Mi. A four-plate compact capacitive coupler design and lcl-compensated topology for capacitive power transfer in electric vehicle charging application. *IEEE Transactions on Power Electronics*, 31(12):8541–8551, 2016.

[59] Fei Lu, Hua Zhang, Heath Hofmann, and Chunting Chris Mi. An inductive and capacitive combined wireless power transfer system with lc-compensated topology. *IEEE Transactions on Power Electronics*, 31(12):8471–8482, 2016.

[60] Aristeidis Karalis, John D Joannopoulos, and Marin Soljačić. Efficient wireless non-radiative mid-range energy transfer. *Annals of physics*, 323(1):34–48, 2008.

[61] Vikash Choudhary, Satendar Pal Singh, Vikash Kumar, and Deepak Prashar. Wireless power transmission: an innovative idea. *International Journal of Educational Planning & Administration*, 1(3):203–210, 2011.

[62] Ki Young Kim. *Wireless power transfer-principles and engineering explorations*. IntechOpen, 2012.

[63] Kafeel Ahmed Kalwar, Muhammad Aamir, and Saad Mekhilef. Inductively coupled power transfer (icpt) for electric vehicle charging–a review. *Renewable and Sustainable Energy Reviews*, 47:462–475, 2015.

[64] Bingnan Wang, William Yerazunis, and Koon Hoo Teo. Wireless power transfer: Metamaterials and array of coupled resonators. *Proceedings of the IEEE*, 101(6):1359–1368, 2013.

[65] Junjun Deng, Weihan Li, Trong Duy Nguyen, Siqi Li, and Chunting Chris Mi. Compact and efficient bipolar coupler for wireless power chargers: Design and analysis. *IEEE Transactions on Power Electronics*, 30(11):6130–6140, 2015.

[66] YP Su, Xun Liu, and SY Ron Hui. Mutual inductance calculation of movable planar coils on parallel surfaces. *IEEE Transactions on Power Electronics*, 24(4):1115–1123, 2009.

[67] Jun-Han Choi, Sung-Ku Yeo, Seho Park, Jeong-Seok Lee, and Gyu-Hyeong Cho. Resonant regulating rectifiers (3r) operating for 6.78 mhz resonant wireless power transfer (rwpt). *IEEE journal of solid-state circuits*, 48(12):2989–3001, 2013.

[68] Valeria Boscaino, Filippo Pellitteri, La Rosa, and Giuseppe Capponi. Wireless battery chargers for portable applications: design and test of a high-efficiency power receiver. *IET Power Electronics*, 6(1):20–29, 2013.

[69] Amir Babaki, Sadegh Vaez-Zadeh, Mohammad Jahanpour-Dehkordi, and Ali Zakerian. Wireless motor drives with a single inverter in primary side of power transfer systems. In *2019 IEEE PELS Workshop on Emerging Technologies: Wireless Power Transfer (WoW)*, pages 125–128. IEEE, 2019.

[70] Chaoqiang Jiang, KT Chau, TW Ching, Chunhua Liu, and Wei Han. Time-division multiplexing wireless power transfer for separately excited dc motor drives. *IEEE Transactions on Magnetics*, 53(11):1–5, 2017.

[71] C Jiang, KT Chau, C Liu, et al. Wireless dc motor drives with selectability and controllability. energies, 10, 49, 2017.

[72] Motoki Sato, Giuseppe Guidi, Takehiro Imura, and Hiroshi Fujimoto. Model for loss calculation of wireless in-wheel motor concept based on magnetic resonant coupling. In *2016 IEEE 17th Workshop on Control and Modeling for Power Electronics (COMPEL)*, pages 1–6. IEEE, 2016.

[73] Chaoqiang Jiang, Kwok Tong Chau, Wei Liu, Chunhua Liu, Wei Han, and WH Lam. An lcc-compensated multiple-frequency wireless motor system. *IEEE Transactions on Industrial Informatics*, 15(11):6023–6034, 2019.

[74] Mustafa Boyvat, Daniel M Vogt, and Robert J Wood. Ultrastrong and high-stroke wireless soft actuators through liquid–gas phase change. *Advanced Materials Technologies*, 4(2):1800381, 2019.

[75] MS Mohamed Ali and K Takahata. Wireless microfluidic control with integrated shape-memory-alloy actuators operated by field frequency modulation. *Journal of Micromechanics and Microengineering*, 21(7):075005, 2011.

[76] MS Mohamed Ali and K Takahata. Selective rf wireless control of integrated bulk-micromachined shape-memory-alloy actuators and its microfluidic application. In *2011 IEEE 24th International Conference on Micro Electro Mechanical Systems*, pages 1269–1272. IEEE, 2011.

[77] Mustafa Boyvat, Je-Sung Koh, and Robert J Wood. Addressable wireless actuation for multijoint folding robots and devices. *Science Robotics*, 2(8), 2017.

[78] Yasutaka Fujimoto. Modeling and analysis of wireless electromechanical energy transfer and conversion using resonant inductive coupling. In *IECON 2015-41st Annual Conference of the IEEE Industrial Electronics Society*, pages 004905–004910. IEEE, 2015.

[79] Besong John Ebot and Yasutaka Fujimoto. A general framework for the analysis and design of a wireless resonant motor. In *2019 IEEE International Electric Machines & Drives Conference (IEMDC)*, pages 1966–1970. IEEE, 2019.

[80] Besong John Ebot and Yasutaka Fujimoto. A motor design based on wireless magnetic resonance coupling technology. In *2020 IEEE Energy Conversion Congress and Exposition (ECCE)*, pages 1140–1144. IEEE, 2020.

[81] Besong John Ebot and Yasutaka Fujimoto. A simulation method for a motor design based on magnetic resonance coupling technology. In *2020 23rd International Conference on Electrical Machines and Systems (ICEMS)*, pages 369–373. IEEE, 2020.

[82] Matteo F Iacchetti, Rajesh P Deodhar, Alexander C Smith, and Keisuke Mishima. Modelling and operating characteristics of air-cored resonant induction machines. In *2018 IEEE Energy Conversion Congress and Exposition (ECCE)*, pages 6468–6475. IEEE, 2018.

[83] Kazuto Sakai and Yuta Sugasawa. Ultralightweight motor design using electromagnetic resonance coupling. In *2016 IEEE Energy Conversion Congress and Exposition (ECCE)*, pages 1–7. IEEE, 2016.

[84] Kazuto Sakai, Kenta Takijima, and Kazuki Nihei. Principles and characteristics of an ultralightweight electromagnetic resonance coupling machine with a cage rotor. In *2017 IEEE Energy Conversion Congress and Exposition (ECCE)*, pages 1154–1160. IEEE, 2017.

[85] Kazuto Sakai and Kenta Takijima. Basic characteristics of an ultralightweight magnetic resonance coupling motor with various numbers of poles. In *2018 IEEE Energy Conversion Congress and Exposition (ECCE)*, pages 7342–7348. IEEE, 2018.

[86] Kazuto Sakai and Kenta Takishima. Frequency and operational characteristics of an ultra-lightweight machine converting energy by magnetic resonance coupling. *The Journal of Engineering*, 2019(17):4571–4575, 2019.

[87] Ming Liu, Ka Wing Chan, Jiefeng Hu, Qifang Lin, Junwei Liu, and Wenzheng Xu. Design and realization of a coreless and magnetless electric motor using magnetic resonant coupling technology. *IEEE Transactions on Energy Conversion*, 34(3):1200–1212, 2019.

[88] Mustafa Boyvat, C Hafner, and Juerg Leuthold. Wireless control and selection of forces and torques-towards wireless engines. *Scientific reports*, 4(1):1–9, 2014.

[89] Roman Bosshard and Johann W Kolar. Inductive power transfer for electric vehicle charging: Technical challenges and tradeoffs. *IEEE Power Electronics Magazine*, 3(3):22–30, 2016.

[90] Jie Hua, Hui-Zhen Wang, Yao Zhao, and Ai-Long Zou. Lcl resonant compensation of movable icpt systems with a multi-load. *Journal of Power Electronics*, 15(6):1654–1663, 2015.

[91] Hunter Hanzhuo Wu, Aaron Gilchrist, Ky Sealy, Paul Israelsen, and Jeff Muhs. Design of symmetric voltage cancellation control for lcl converters in inductive power transfer systems. In *2011 IEEE International Electric Machines & Drives Conference (IEMDC)*, pages 866–871. IEEE, 2011.

[92] Do-Hyeon Kim and Dukju Ahn. Self-tuning lcc inverter using pwm-controlled switched capacitor for inductive wireless power transfer. *IEEE Transactions on Industrial Electronics*, 66(5):3983–3992, 2018.

[93] Zhiyuan Hu, Yajie Qiu, Laili Wang, and Yan-Fei Liu. An interleaved llc resonant converter operating at constant switching frequency. *IEEE Transactions on Power Electronics*, 29(6):2931–2943, 2013.

[94] Navid Shafiei, Majid Pahlevaninezhad, Hosein Farzanehfard, and Seyed Reza Motahari. Analysis and implementation of a fixed-frequency $lclc$ resonant converter with capacitive output filter. *IEEE Transactions on industrial electronics*, 58(10):4773–4782, 2011.

[95] James Simpson, John Lane, Christopher Immer, and Robert Youngquist. Simple analytic expressions for the magnetic field of a circular current loop. *NASA technical documents*, 2001.

[96] John E Lane, Robert C Youngquist, Christopher D Immer, and James C Simpson. Magnetic field, force, and inductance computations for an axially symmetric solenoid. *National Aeronautics and Space Administration, Washington*, 2001.

[97] Ki-Bong Kim, Enrico Levi, Zivan Zabar, and Leo Birenbaum. Mutual inductance of noncoaxial circular coils with constant current density. *IEEE Transactions on Magnetics*, 33(5):4303–4309, 1997.

[98] Frederick W Grover. The calculation of the mutual inductance of circular filaments in any desired positions. *Proceedings of the IRE*, 32(10):620–629, 1944.

[99] Slobodan Babic, Frédéric Sirois, Cevdet Akyel, and Claudio Girardi. Mutual inductance calculation between circular filaments arbitrarily positioned in space: alternative to grover's formula. *IEEE transactions on magnetics*, 46(9):3591–3600, 2010.

[100] Slobodan I Babic and Cevdet Akyel. Calculating mutual inductance between circular coils with inclined axes in air. *IEEE Transactions on Magnetics*, 44(7):1743–1750, 2008.

[101] Edward Bennett Rosa and Louis Cohen. *On the self-inductance of circles*, volume 4. US Department of Commerce and Labor, Bureau of Standards, 1907.

[102] Edward Bennett Rosa and Frederick Warren Grover. *Formulas and tables for the calculation of mutual and self-inductance*. Number 169. US Government Printing Office, 1948.

[103] Marc C Thompson. Inductance calculation techniques-part ii: approximations and handbook methods, 1991.

[104] Frederick W Grover and Inductance Calculations. Working formulas and tables. *Calculation of Mutual Inductance and Self-Inductance: High Frequency Formulas*, pages 261–283, 1946.

[105] Harold A Wheeler. Simple inductance formulas for radio coils. *Proceedings of the institute of Radio Engineers*, 16(10):1398–1400, 1928.

[106] IEC 60287-1-1. Electric cables - calculation of current rating - part 1: Current rating equations (100General. Technical report, International Organization for Standardization, 2016.

[107] Jordi-Roger Riba. Analysis of formulas to calculate the ac resistance of different conductors' configurations. *Electric Power Systems Research*, 127:93–100, 2015.

[108] Cory James Liu. *Skin effect in large bi-media power conductors*. PhD thesis, The University of North Carolina at Charlotte, 2016.

[109] Claudio Carretero. Coupling power losses in inductive power transfer systems with litz-wire coils. *IEEE Transactions on Industrial Electronics*, 64(6):4474–4482, 2017.

[110] Charles R Sullivan. Optimal choice for number of strands in a litz-wire transformer winding. *IEEE transactions on power electronics*, 14(2):283–291, 1999.

[111] Charles R Sullivan and Richard Y Zhang. Simplified design method for litz wire. In *2014 IEEE Applied Power Electronics Conference and Exposition-APEC 2014*, pages 2667–2674. IEEE, 2014.

[112] Wenxing Zhong, Chi Kwan Lee, and SY Ron Hui. General analysis on the use of tesla's resonators in domino forms for wireless power transfer. *IEEE transactions on industrial electronics*, 60(1):261–270, 2011.

[113] CK Lee, WX Zhong, and SY Ron Hui. Recent progress in mid-range wireless power transfer. In *2012 IEEE Energy Conversion Congress and Exposition (ECCE)*, pages 3819–3824. IEEE, 2012.

[114] Tatsuki Ujihara, Quang-Thang Duong, and Minoru Okada. kq-product analysis of inductive power transfer system with two transmitters and two receivers. In *Wireless Power Transfer Conference (WPTC), 2017 IEEE*, pages 1–4. IEEE, 2017.

[115] Takashi Ohira. Extended kq product formulas for capacitive-and inductive-coupling wireless power transfer schemes. *IEICE Electronics Express*, 11(9):20140147–20140147, 2014.

[116] Ferroxcube. *Soft Ferrites and Accessories, Data Handbook*, 11 2017.

[117] Carpenter Electrification. *Datasheet: Silicon Core Iron A*, 5 2020.

[118] Carpenter Electrification. *Datasheet: Silicon Core Iron B*, 5 2020.

[119] Carpenter Electrification. *Datasheet: Silicon Core Iron C*, 5 2020.

[120] WF Brown. Magnetic materials, ch 8 in the handbook of chemistry and physics, condon and odishaw, eds, 1958.

[121] Fausto Fiorillo, Cinzia Beatrice, Oriano Bottauscio, and Enrico Carmi. Eddy-current losses in mn-zn ferrites. *IEEE Transactions on Magnetics*, 50(1):1–9, 2013.

[122] Samuel Dobák, Cinzia Beatrice, Fausto Fiorillo, Vasiliki Tsakaloudi, and Carlo Ragusa. Magnetic loss decomposition in co-doped mn-zn ferrites. *IEEE Magnetics Letters*, 10:1–5, 2018.

[123] Hideo Saotome and Yo Sakaki. Iron loss analysis of mn-zn ferrite cores. *IEEE Transactions on Magnetics*, 33(1):728–734, 1997.

[124] Yo Sakaki, Mitsunobu Yoshida, and Toshiro Sato. Formula for dynamic power loss in ferrite cores taking into account displacement current. *IEEE transactions on magnetics*, 29(6):3517–3519, 1993.

[125] Mihael Drofenik, Andrej Žnidaršič, and Igor Zajc. Highly resistive grain boundaries in doped mnzn ferrites for high frequency power supplies. *Journal of applied physics*, 82(1):333–340, 1997.

[126] F Fiorillo, Enzo Ferrara, Marco Coisson, Cinzia Beatrice, and N Banu. Magnetic properties of soft ferrites and amorphous ribbons up to radiofrequencies. *Journal of magnetism and magnetic materials*, 322(9-12):1497–1504, 2010.

[127] Jürgen Reinert, Ansgar Brockmeyer, and Rik WAA De Doncker. Calculation of losses in ferro-and ferrimagnetic materials based on the modified steinmetz equation. *IEEE Transactions on Industry applications*, 37(4):1055–1061, 2001.

[128] D Stoppels. Developments in soft magnetic power ferrites. *Journal of Magnetism and Magnetic Materials*, 160:323–328, 1996.

[129] T Kawano, A Fujita, and S Gotoh. Analysis of power loss at high frequency for mnzn ferrites. *Journal of Applied Physics*, 87(9):6214–6216, 2000.

[130] F Fiorillo, Cinzia Beatrice, Oriano Bottauscio, A Manzin, and M Chiampi. Approach to magnetic losses and their frequency dependence in mn–zn ferrites. *Applied physics letters*, 89(12):122513, 2006.

[131] Cinzia Beatrice, Oriano Bottauscio, and F Fiorillo. Eddy current and spin damping losses in mn-zn ferrites. *Journal of the Japan Society of Powder and Powder Metallurgy*, 61(S1):S208–S210, 2014.

[132] Harry Suhl. Theory of the magnetic damping constant. *IEEE Transactions on Magnetics*, 34(4):1834–1838, 1998.

[133] Yue-Long Lyu, Fan-Yi Meng, Guo-Hui Yang, Bang-Jun Che, Qun Wu, Li Sun, Daniel Erni, and Joshua Le-Wei Li. A method of using nonidentical resonant coils for frequency splitting elimination in wireless power transfer. *IEEE Transactions on Power Electronics*, 30(11):6097–6107, 2015.

[134] Abhilash Kamineni, Grant A Covic, and John T Boys. Self-tuning power supply for inductive charging. *IEEE Transactions on Power Electronics*, 32(5):3467–3479, 2016.

[135] Andrea Agnes, Edoardo Bonizzoni, Piero Malcovati, and Franco Maloberti. An ultra-low power successive approximation a/d converter with time–domain comparator. *Analog Integrated Circuits and Signal Processing*, 64(2):183–190, 2010.

[136] Henry Kennedy, Rares Bodnar, Teerasak Lee, and William Redman-White. A self-tuning resonant-inductive-link transmit driver using quadrature symmetric delay trimmable phase-switched fractional capacitance. *IEEE Journal of Solid-State Circuits*, 53(6):1694–1706, 2018.

[137] Jin Zhao, Jianzhong Zhang, and Yaodong Zhu. A flexible wireless power transfer system with switch controlled capacitor. *IEEE Access*, 7:106873–106881, 2019.

[138] Jianzhong Zhang, Jin Zhao, Yaqian Zhang, and Fujin Deng. A wireless power transfer system with dual switch-controlled capacitors for efficiency optimization. *IEEE Transactions on Power Electronics*, 35(6):6091–6101, 2019.

[139] Jun Osawa, Takanori Isobe, and Hiroshi Tadano. Efficiency improvement of high-frequency inverter for wireless power transfer system using series compensator. *Electrical Engineering in Japan*, 206(3):51–61, 2019.

[140] Wang Xusheng, Zhang Ming, Ren Xiaojiao, Francis Rodes, and Romain Deniéport. Auto tuning system for a half bridge resonant converter using a synchronous switched capacitor. In *2015 IEEE 13th International New Circuits and Systems Conference (NEWCAS)*, pages 1–4. IEEE, 2015.

Illustration: Nikola Tesla sitting in his Colorado Springs laboratory next to his 'magnifying transmitter' Tesla coil.